Powder based processing of novel dispersion strengthened copper alloys for fusion applications



Alasdair Morrison

Lincoln College

University of Oxford

A thesis submitted for the degree of

Doctor of Philosophy

Trinity 2017

Acknowledgements

This thesis was the product of extensive guidance from a number of people. Professor Patrick Grant must be thanked as the primary supervisor for his remarkable productivity in shaping the direction of this thesis and development of the ideas as well as the science undertaken. Professor Sergio Lozano-Perez as co-supervisor who has equally assisted extensively throughout especially in the development, processing and understanding of the electron microscopy used throughout this thesis. Dr Elizabeth Surrey and Dr Mike Gorley of Culham Centre for Fusion Energy without whom this project would not have been possible, and for invaluable guidance throughout. Within the wider associated groups of Processing of Advanced Materials and Nanoanalysis a number of individuals stand out for their assistance and discussions that resulted in the advancements of ideas and work presented herein. Namely; Dr Andrew London for his assistance in the general understanding of oxide dispersion strengthened materials and the nanoscale effects at play; Dr Thomas Aarholt for his assistance with electron microscopy and especially with data processing; Dr Zuliang Hong for his ever willing assistance in processing direction and understanding their effects and finally, Sarah Connolly for endless discussions on the science underpinning this thesis and the wider field of oxide dispersion strengthened materials processing. The work in this thesis was funded jointly by the Engineering and Physical Sciences Research Council (EPSRC) and Culham Centre for Fusion Energy (CCFE) through an Industrial Cooperative Award in Science & Technology (CASE) studentship.

Abstract

Cu has high thermal conductivity and is thus ideal for high heat flux, thermal heat sink applications in fusion power applications. Divertor designs for future fusion power plants will expose Cu alloys to extreme thermal ($>10\,\mathrm{MW\,m^{-2}}$) and neutron fluxes (200 dpa) that destabilise the microstructure of Cu. To improve stability, strength and creep resistance, alloying additions are used commercially, but these compromise thermal conductivity. Dispersed oxide particles may offer the opportunity for improved mechanical stability and creep resistance even at very low volume fractions (<1%) while avoiding large reductions in thermal conductivity. However there are few studies on the processing-performance of oxide dispersion strengthened Cu alloys.

In this thesis, novel oxide dispersion strengthened Cu alloys were prepared by room temperature mechanical alloying of Y_2O_3 and the mechanism of dispersion investigated. A small fraction of Y_2O_3, up to 1%, was shown to disperse effectively during mechanical alloying at room temperature in Cu. Both severe fragmentation and some local disassociation of the Y and O occurred, allowing for re-precipitation of fine nanoparticles <10 nm during consolidation and exposure to elevated temperatures. A model alloy of Cu-2 wt.% Y_2O_3 alloy had a mean oxide particle diameter of $7.1 \pm 6.0\,\mathrm{nm}$ and a mean particle number density of $8.24 \times 10^{22}\,\mathrm{m^{-3}}$ following consolidation.

Ternary Ti additions were investigated for nanoparticle refinement and best design alloy with a composition of Cu-0.25Y_2O_3-0.25Ti was produced that had a mean nanoparticle diameter of $3.2 \pm 1.5\,\mathrm{nm}$ and a mean particle number density of $2.36 \times 10^{23}\,\mathrm{m^{-3}}$, which after thermal ageing for 545 h at 350 °C, was largely unchanged

at $3.8 \pm 1.7\,\mathrm{nm}$, and $1.74 \times 10^{23}\,\mathrm{m}^{-3}$ respectively. Comparing favourably with commercial Al_2O_3 dispersion strengthened Cu, the alloy had a narrower particle size distribution and a higher particle number density. The fine dispersed oxide nanoparticles gave good grain boundary pinning, retaining an ultrafine mean grain size of 220 nm after thermal ageing. Thermal conductivity of the Ti-containing alloy was $332 \pm 16\,\mathrm{W\,m^{-1}\,K^{-1}}$, and the addition of Ti increased the thermal conductivity with increasing temperature. The creep resistance was evaluated by small punch testing and in-house produced alloys outperformed commercial alloys at 350 °C. The work in this thesis indicates that mechanically alloyed Cu-Y_2O_3 or Cu-Y_2O_3-Ti alloys, with further development and evaluation, have potential as thermal heat-sink materials for fusion divertor application.

Contents

1 Introduction **1**

2 Literature review **3**

2.1 Nuclear fusion 3

2.1.1 Magnetic confinement reactors 4

2.2 Divertor design 4

2.2.1 Plasma 5

2.2.2 Cooling 6

2.2.3 Heat flux and irradiation 6

2.3 Candidate materials for high heat flux environments 7

2.3.1 Cu and other alloys 8

2.3.2 Precipitation strengthening 8

2.3.3 Solution strengthening 10

2.3.4 Dispersion strengthening 11

2.4 Oxide dispersion strengthened Cu 12

2.4.1 Oxide selection 14

2.4.2 Microstructure 17

2.4.3 Mechanical properties 20

2.4.4 Thermal properties 21

2.4.5 Irradiation properties 24

2.5 Fabrication of oxide dispersion strengthened Cu 27

2.5.1 Internal oxidation 27
2.5.2 Mechanical alloying 29
2.5.3 Consolidation 31
2.6 Summary 37

3 Experimental methods **39**
3.1 Introduction 39
3.2 Processing 39
3.2.1 Raw materials 39
3.2.2 Mechanical alloying 40
3.2.3 Sintering 41
3.2.4 Accelerated isothermal ageing 43
3.3 Sample preparation 45
3.3.1 Powder materials 45
3.3.2 Consolidated materials 45
3.3.3 Focused ion beam liftout 46
3.4 Characterisation techniques 47
3.4.1 Optical microscopy 47
3.4.2 Scanning electron microscopy 47
3.4.3 Transmission electron microscopy 49
3.4.4 Atom probe tomography 52
3.4.5 X-ray diffraction 52
3.5 Physical properties 53
3.5.1 Chemical analysis 53
3.5.2 Laser flash analysis 54
3.6 Mechanical properties 54
3.6.1 Microhardness 54
3.6.2 Tensile testing 55

3.6.3 Small-punch testing 56

4 Dissolution and re-precipitation of Y_2O_3 in Cu **59**

4.1 Introduction 59

4.2 Planetary ball milling 60

4.2.1 Milling of Cu 60

4.2.2 Milling of Cu-Y_2O_3 62

4.3 Y_2O_3 71

4.3.1 Dispersion of Y_2O_3 73

4.3.2 Re-precipitation of Y_2O_3 83

4.4 Summary 94

5 Consolidation **97**

5.1 Introduction 97

5.2 Experimental procedure 98

5.3 Results and discussion 98

5.3.1 Extent of consolidation 101

5.3.2 Mechanical properties 101

5.3.3 Microstructure 105

5.4 Summary 116

6 The effect of Ti additions on Cu-Y_2O_3 **119**

6.1 Introduction 119

6.1.1 Ti addition 120

6.2 Results and Discussion 122

6.2.1 Addition route 122

6.2.2 Powder properties 125

6.2.3 Fully pre-alloyed powder 131

6.2.4 Consolidated Ti-Y_2O_3 containing alloys 133

6.2.5 Cu-0.5Ti partial pre-alloy particles 135
6.3 Summary 141
6.3.1 The effectiveness of Ti additions by mechanical alloying 141
6.3.2 The role of Ti in particle refinement 143
6.3.3 Conclusions 144

7 Evaluation of a Cu-ODS alloy of Cu-0.25Ti-0.25Y_2O_3 145
7.1 Introduction 145
7.2 Experimental procedure 145
7.2.1 Raw materials 145
7.2.2 Mechanical alloying 146
7.2.3 Sintering by FAST 146
7.2.4 Thermomechanical treatment 148
7.3 Results and discussion 150
7.3.1 Comparison with other Cu-ODS alloys 150
7.3.2 Effect of processing 150
7.3.3 Microstructure 151
7.3.4 Tensile properties 155
7.3.5 Thermal properties 158
7.3.6 Thermal stability 161
7.4 Summary 170

8 Conclusions and suggestions for further work 173
8.1 Conclusions 173
8.2 Suggestions for further work 177

Bibliography 180

List of Figures

2.1 Schematic drawing of the tokamak comparing limiter and divertor configuration. 5

2.2 Room temperature 0.2% proof strength from tensile testing versus thermal conductivity of fusion relevant Cu alloys 9

2.3 The effect of oxide additions on the electrical conductivity of ODS Cu alloys prepared by MA 18

2.4 Creep behaviour of fusion-relevant Cu alloys 22

2.5 The effect of increasing annealing temperature on hardness of Cu alloys. 23

2.6 TEM micrograph of dispersed particles in GlidCop AL-15 Cu-ODS . 28

2.7 Horizontal section schematic diagram of a planetary ball mill 30

2.8 Schematic representation of FAST machine. 33

3.1 Schematic representation of HIP set-up 42

3.2 Schematic diagram of cylindrical FAST die in cross-section 43

3.3 FIB liftout TEM sample preparation technique 48

3.4 Tensile test geometries 55

3.5 Schematic diagram of cylindrical cross-section of small-punch testing set-up 57

4.1 Effect of milling time on microhardness of Cu powder 62

4.2 Secondary electron micrographs of Cu powder morpholgy with increasing milling time 63

4.3 The Cu-Y phase diagram 64
4.4 Effect of milling time on Vickers microhardness with increasing Y_2O_3 content 65
4.5 Effect of milling time on microhardness, crystallite size and lattice strain of Cu-2Y_2O_3 and Cu-10Y_2O_3 66
4.6 Seconday electron micrographs of the effect of Y_2O_3 fraction in milled powders 68
4.7 Effect of increasing Y_2O_3 content on microhardness, crystallite size and lattice strain of Cu-2Y_2O_3 and Cu-10Y_2O_3 69
4.8 Comparison of calculated contribution to strength of cyrstallites compared with microhardness derived yield strength 71
4.9 Effect of milling speed on the powder hardness, crystallite size and lattice strain of Cu-2Y_2O_3 72
4.10 Variation in XRD signal of Cu-10Y_2O_3 with increasing milling time . 74
4.11 EDX surface analysis of Cu-2Y_2O_3 milled powder 75
4.12 Preparation of TEM lamella from powder materials by FIB liftout technique 76
4.13 Y N maps of Cu-2Y_2O_3 powder after 12 hours milling. 78
4.14 STEM micrographs of Cu-2Y_2O_3 powder after 12 hours milling 79
4.15 Low-loss EFTEM Y-N maps of Cu-2Y_2O_3 powder after 12 hours milling 80
4.16 Crystallographic indexing of a Y_2O_3 particle in Cu-2Y_2O_3 powder after 12 hours milling. 81
4.17 STEM-EDS analysis of Cu-2Y_2O_3 milled powder 82
4.18 FAST sintering of Cu-2Y_2O_3 powder 84
4.19 Low-loss EFTEM Y $N_{2,3}$ maps and particle size distribution of consolidated Cu-2Y_2O_3 85
4.20 EDS mapping of consolidated Cu-2Y_2O_3 showing Y oxides 86

4.21 APT of Cu-2Y_2O_3 prepared by FAST consolidation 88
4.22 PPB region highlighted at increasing magnification 89
4.23 EBSD of prior particle boundaries in Cu-2Y_2O_3 90
4.24 Particle diameter near the PPB 91
4.25 Schematic diagram of proposed method of PPB formation 93

5.1 Sintering profiles for HIP and FAST 99
5.2 Typical FAST sintering of Cu-2Y_2O_3 powder 100
5.3 Tensile response of materials consolidated by HIP and FAST 103
5.4 SE macrographs of fracture surfaces of FAST and HIP consolidated alloys 104
5.5 SE micrographs of fracture surfaces of FAST and HIP consolidated alloys 106
5.6 SE micrographs and EDS maps of HIP consolidated Cu-2Y_2O_3. . . . 108
5.7 STEM analysis of HIPed Cu-2Y_2O_3 109
5.8 EFTEM Y $N_{2,3}$ map and size distribution of Cu-2Y_2O_3 consolidated by HIP and FAST 110
5.9 SE micrographs of porosity in FAST consolidated Cu-2Y_2O_3 112
5.10 SE micrographs and EDS maps of FAST consolidated Cu-2Y_2O_3. . . 113
5.11 STEM analysis of FAST consolidated Cu-2Y_2O_3 114
5.12 EFTEM Y $N_{2,3}$ maps of Cu-2Y_2O_3 consolidated by FAST 115

6.1 The Cu-Ti phase diagram 121
6.2 Schematic representation of the four processing routes for the incorporation of Ti during MA 121
6.3 Size distribution of Cu and Ti powders 122
6.4 SE micrographs of Cu-1Y_2O_3-1Ti produced by MA of elemental powders. 123
6.5 SE micrographs of Cu-1Y_2O_3-0.36Ti produced by MA. 124
6.6 SE micrographs of Cu-1Y_2O_3-1Ti produced by MA of a partial pre-alloy. 125

6.7 Effect of milling time and Ti-addition route on Vickers microhardness of mechanical alloyed powders 126
6.8 Comparison of agglomerates observed between different Ti addition routes 127
6.9 EDS analysis of master alloy Ti-addition route 12 hour milled powder 128
6.10 EDS analysis of elemental alloy Ti-addition route 12 hour milled powder 129
6.11 Effect of milling time and Ti addition route on powder morphologies of Cu-Y_2O_3-Ti 130
6.12 EDS maps of Cu-0.5Ti pre-alloyed powder 132
6.13 Secondary electron micrographs of 12 hour milled fully pre-alloyed powder of Cu-0.5Ti-0.5Y_2O_3 132
6.14 EFTEM maps showing co-localisation of Y and Ti in HIPed Cu-0.25Y_2O_3-0.25Ti 134
6.15 EFTEM maps of Y and Ti in HIPed Cu-0.25Y_2O_3-0.25Ti 134
6.16 Particle size distribution obtained from low-loss EFTEM of HIPed Cu-0.25Y_2O_3-0.25Ti 135
6.17 HAADF-STEM micrograph of dispersed particles/clusters in sintered Cu-0.25Ti-0.25Y_2O_3 prepared from a Cu-0.5Ti pre-alloyed powder . . 136
6.18 EELS analysis of nanoclusters in sintered Cu-0.25Ti-0.25Y_2O_3 137
6.19 EELS analysis of an Fe-rich particle and nanoclusters in sintered Cu-0.25Ti-0.25Y_2O_3 138
6.20 EELS analysis of a large particle in sintered Cu-0.25Ti-0.25Y_2O_3 . . . 139
6.21 EELS analysis of nanoclusters in sintered Cu-0.25Ti-0.25Y_2O_3 140

7.1 Sintering of a 60 mm diameter die containing 299.15 g Cu-0.25Y_2O_3-0.25Ti powder with a dwell of 30 minutes at 900 °C under 50 MPa uniaxial load 147
7.2 Preparation of Cu-0.25Y_2O_3-0.25Ti sample for open-die forging . . . 149

7.3 Forged Cu-0.25Y_2O_3-0.25Ti segment 149
7.4 SE micrographs of Cu-0.25Y_2O_3-0.25Ti following consolidation and forging. 152
7.5 STEM imaging of FAST consolidated and cold forged Cu-0.25Y_2O_3-0.25Ti153
7.6 STEM imaging of FAST consolidated and cold forged Cu-0.25Y_2O_3-0.25Ti153
7.7 EELS analysis of nanoclusters in FAST consolidated and cold-forged Cu-0.25Ti-0.25Y_2O_3 154
7.8 Stress-strain curves of Cu-0.25Y_2O_3-0.25Ti and GlidCop alloys 156
7.9 SE fractography of Cu-0.25Y_2O_3-0.25Ti following RT tensile testing. . 157
7.10 Point EDS analysis of a FAST consolidated, cold-forged, and aged Cu-0.25Y_2O_3-0.25Ti fracture surface. 158
7.11 EDS maps of particle at tensile fracture surface of Cu-0.25Y_2O_3-0.25Ti 159
7.12 Thermal diffusivity and conductivity of Cu-ODS alloys from 300 to 825 K.160
7.13 Secondary electron micrographs of thermally aged Cu-0.25Y_2O_3-0.25Ti and GlidCop AL25 163
7.14 ADF-STEM of FAST consolidated and cold forged Cu-0.25Y_2O_3-0.25Ti prior to and after isothermal ageing. 164
7.15 STEM DF and HAADF imaging of Cu-0.25Y_2O_3-0.25Ti following isothermal ageing 164
7.16 STEM imaging of Cu-0.25Y_2O_3-0.25Ti following isothermal ageing, showing fine nanoparticles. 165
7.17 EELS analysis of nanoclusters in Cu-0.25Ti-0.25Y_2O_3 prepared by FAST consolidated,cold-forging and isothermal annealing 166
7.18 Nanocluster size distribution in as-sintered and aged Cu-0.25Y_2O_3-0.25Ti166
7.19 Small punch creep testing of Cu-0.25Ti-0.25Y_2O_3 at 350 °C; extension versus time. 168

7.20 Small punch creep testing of Cu-ODS alloys at 350 °C; - load versus failure time 169
7.21 Small punch testing failure surfaces 171

8.1 Room temperature 0.2% proof strength from tensile testing versus thermal conductivity of fusion relevant Cu alloys including in-house alloys 176

List of Tables

2.1 CuCrZr-IG composition 9

2.2 Reference CuAl25-IG composition. 11

2.3 Estimated strengthening contributions in Cu-ODS alloys 14

2.4 Physical properties of selected ceramic compounds for dispersion strengthening, ranked by enthalpy of formation 15

2.5 Contributions to electrical resistivity of Cu-Al_2O_3 produced by reactive ball milling. 20

2.6 Tensile properties of extruded GlidCop AL15 at room temperature. . 21

2.7 Properties of irradiated copper alloys 24

2.8 Properties of pure Cu prepared by FAST and VHP. 35

3.1 Compositions of milling pot and milling media 40

3.2 Major electron loss edges for elements of interest 52

4.1 Effect of Y_2O_3 fraction on hardening rate and plateau microhardness during milling 65

4.2 Estimation of the contribution of crystallite size to σ_y for different Y_2O_3 fractions, based on hardness and crystallite size measurements. 67

5.1 Sintering parameters for HIP and FAST consolidation 99

5.2 Density and hardness of materials consolidated by HIP and FAST . . 101

5.3 Tensile properties of materials consolidated by HIP and FAST 102

6.1 Effect of Ti addition route on hardening rate and plateau microhardness during milling 126
6.2 Effect of Ti addition route on agglomerate composition in powder from EDS analysis 129
6.3 Hardness of partial pre-alloyed and HIP consolidated Cu-Y_2O_3-Ti alloys compared with Cu-2Y_2O_3 133

7.1 Effect of milling pot & balls composition on Fe contamination in Cu-0.25Y_2O_3-0.25Ti 147
7.2 Density and hardness of Cu-0.25Y_2O_3-0.25Ti 151
7.3 Measured tensile properties of Cu-0.25Y_2O_3-0.25Ti, compared with Cu-2Y_2O_3 and GlidCop AL25. 155
7.4 Calculated contribution to thermal conductivity associated with presence of grain boundaries, particles, pores and Fe impurity solute atoms. 161
7.5 Effect of isothermal ageing on hardness on Cu-0.25Y_2O_3-0.25Ti, Cu-2Y_2O_3, and GlidCop AL25 162
7.6 Particle diameter, number density, and interparticle spacing for Cu-0.25Y_2O_3-0.25Ti, Cu-2Y_2O_3 and GlidCop AL25. 167

Chapter 1

Introduction

There is a requirement for improved materials for heat-sink application in the next generation of experimental nuclear fusion reactors. Dispersion strengthening of Cu, has been examined for at least 30 years for application as a heatsink material. GlidCop Al25 is the most explored Cu oxide dispersion strengthened (ODS) alloy, and a good baseline of understanding of the microstructure–property relationship has been achieved. However, even in this relatively well-explored system there are a number of areas with inconsistent results and/or limited understanding. ODS alloys made with oxides other than Al_2O_3 have received only limited study and usually without explanations for differences in the properties observed. In general, Y_2O_3 strengthened Cu alloys show particular promise owing to the stability of Y_2O_3 and there are opportunities for comparison of Y_2O_3 containing Cu alloys with the more well-explored Y_2O_3 containing Fe-ODS alloys.

The objectives of the work in this thesis are:

1. To investigate the relationship between the microstructure and properties, and their stability, in Cu-ODS alloys, with an emphasis on the dynamics and mechanism of any oxide dissolution and subsequent re-precipitation and ageing.

2. To investigate the relationship between the processing conditions and Cu-ODS microstructure in both as-milled powder and bulk consolidated material, and the effect of ternary alloying additions on microstructure.

3. To compare in-house produced materials with competitor Cu alloys and Cu-ODS products suitable for the divertor application and to explore the relationship between processing route and properties, with particular emphasis on the thermal stability of Cu-ODS alloys with respect to microstructure and creep.

This thesis will address these objectives as follows: the experimental methods are outlined in Chapter 3; the behaviour of oxides during mechanical alloying based processes will be examined in Chapter 4; the effect of sintering route on dispersed particles is presented in Chapter 5.; the role of Ti additions is described in Chapter 6; and a best design alloy, taking the new understanding into account, is investigated in Chapter 7. These results are summarised and further work suggested in Chapter 8.

Chapter 2

Literature review

2.1 Nuclear fusion

Nuclear fusion is the process of joining two atomic nuclei to produce a new, larger atomic nucleus, which will have lower mass than the combined mass of the original two nuclei. The lost mass is released as energy, which provides the basis for the use of nuclear fusion as an energy source.

The reaction for this process is:

$$ {}^{1}_{2}D + {}^{1}_{3}T \rightarrow {}^{2}_{4}He(3.5\,\mathrm{MeV}) + n^{0}(14.1\,\mathrm{MeV}) \tag{2.1} $$

For the fusion reaction to occur, the reacting nuclei must have sufficient energy that collisions may overcome the electric force allowing the strong nuclear force to take effect and bind the nuclei. The energy to overcome the electric force of the nuclei is provided thermally; the mixture of deuterium and tritium must be heated to around $200 \times 10^{6}\,^{\circ}\mathrm{C}$ at which point the reaction becomes self-sustaining [1].

There are two proposed techniques to obtain the requisite conditions for successful collisions to take place between deuterium and tritium, where the high temperature plasma that forms must be contained:

1. Inertial confinement, for example with a high power laser; and

2. Magnetic confinement

Magnetic confinement is closer to realisation as a power station technology, and is the focus of this thesis.

2.1.1 Magnetic confinement reactors

Magnetic confinement uses the principle that charged particles in a magnetic field will move in the direction parallel to the magnetic field with an additional force acting in the transverse direction caused by an electric current flowing through the plasma. This leads to the movement of charged particles in a spiral. By creating a ring of plasma, a torus, it is possible to create a continuously looping particle, that is replicated throughout the toroidal-shaped plasma to enable regular collisions and reactions.

Building on experimental devices such as the Joint European Torus (JET), the International Tokamak Experimental Reactor (ITER), due for first plasma in the 2020s, will allow self-sustaining DT plasmas to be studied in order to confirm the predicted behaviour of the reactions. Results from ITER will feed in to the development of the third step of fusion: commercial feasibility, which will be undertaken with the Demonstration Power Plant (DEMO). Significant challenges lie in many aspects of DEMO development, not least in materials selection due to an extremely limited palette of suitable materials and restricted testing of these in high irradiation environments [1, 2].

2.2 Divertor design

In an attempt to mitigate interactions of the plasma with the walls of the reactor, the plasma is diverted away from the magnetically confined region to a lower recess in the base of the tokamak known as the divertor, where the plasma interaction with the walls may be less damaging in terms of sputtered elements from the wall entering the confined plasma, and in some ways the divertor acts as the exhaust of the plasma to draw any undesired sputtered atoms away from the confined region, as shown

in Fig. 2.1. Sputtering events or "plasma strikes" risk sputtered atoms diluting the plasma and radiating plasma energy, known as "quenching", which lowers the plasma temperature and reduces the efficiency of the reactor.

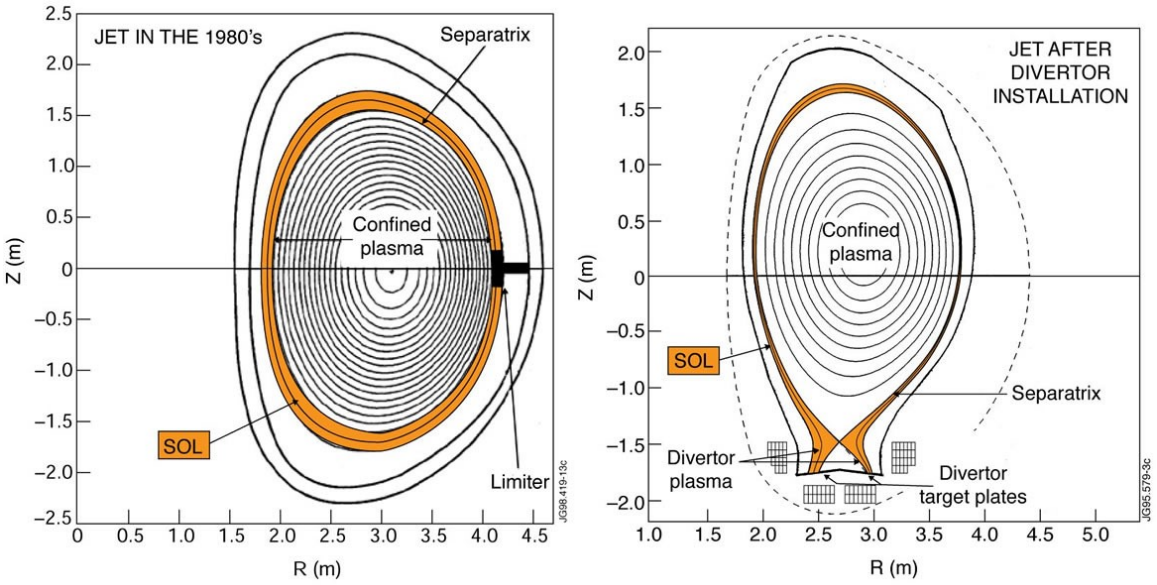

Figure 2.1: Schematic drawing of the vertical cross-section of the tokamak torus in JET comparing the plasma and scrape off layer (SOL) of the 1980's with a limiter (to give controlled plasma-wall interactions) to that with a divertor. The SOL is directed to a lower region of the reactor where it comes into contact with target plates at its base [2].

With respect to power plant reactors, the divertor's most important role will be for the removal of heat from the plasma, through cooling of the divertor with high-pressure water or helium. Excess thermal energy can be removed to a heat-exchanger system and converted to electricity [1]. Proposals for DEMO require a heat sink material in contact with a coolant and the plasma-facing material.

2.2.1 Plasma

Plasma interactions with the divertor material are expected and as such, plasma facing materials are necessitated in the design of fusion reactors. Plasma facing materials come from two groups of material, low Z-number and high Z-number. Low Z materials, such as carbon fibre composites and Be, have high sputtering rates and have more

limited effects on quenching the plasma. However, they retain relatively large amounts of radioactive tritium on re-deposition and they are also mobile in the plasma so they may re-deposit far from the plasma strike. High Z materials, such as W, sputter less but the heavy atoms quench the plasma more significantly; they typically have lower thermal conductivity, but do not retain as much tritium [3]. Current DEMO designs specify W armour [4, 5], which has limited potential for use as a heat-sink material due to its comparatively low thermal conductivity.

2.2.2 Cooling

The divertor serves as the primary thermal exhaust in current and future reactor designs and a water cooled divertor concept has been proposed. A number of designs are suggested requiring varying combinations of water temperature, water pressure and material operating temperature [4, 6–8]. An examination of the different designs is outside the scope of this thesis, but the most important parameters with reference to the material challenges faced are: a coolant temperature of 150 °C at a pressure of 5 MPa with the heat-sink material maintaining a steady state temperature of ∼250 °C with peak temperatures >350 °C [8]. The heat-sink material must interface successfully with the plasma-facing material.

2.2.3 Heat flux and irradiation

DEMO designs have required a gradual increase in the conditions plasma facing components (PFC) are expected to withstand. Current design conditions propose peak heat flux loadings of $10\,\mathrm{MW\,m^{-2}}$ quasi-stationary, with transient loadings of $>20\,\mathrm{MW\,m^{-2}}$ [5, 8].

During the fusion reaction high energy He atoms and neutrons are produced as outlined in Eq. 2.1. The high mass of the He atoms lead to rapid energy loss through collisions in the plasma and they are removed as “ash”. The high energy neutrons interact with the components of the reactor through collisions, scattering and causing

nuclear reactions within the materials. Direct collisions between neutron and atoms will knock the atom out of alignment on the crystal lattice, forming vacancies and self-interstitials. Current design conditions suggest structural materials in the divertor will be subject to >6 displacements per atom (dpa) per full plasma year due to neutron bombardment [8]. Neutrons also cause damage by neutron activation, where the impinging neutrons are captured in atomic nuclei to give an excited state. The resultant isotope will decay by nuclear decay emitting alpha, beta or gamma radiation, leading to long lifetime radioactive isotopes that present problems over the course of the reactor lifetime and especially for decommissioning [9]. A further problem associated with neutron activation is the accumulation of alpha particles in the lattice that form He bubbles and lead to embrittlement, swelling and blistering [10].

2.3 Candidate materials for high heat flux environments

The properties for consideration for heat sink materials for high heat flux environments are as follows with a particular emphasis on application in DEMO [9]:

Mechanical properties; strength, ductility, Young's modulus, and fracture toughness.

Thermal properties; conductivity and coefficient of thermal expansion.

Environmental resistance; creep, corrosion, and fatigue resistance.

Irradiation resistance; creep, swelling, and activation resistance.

Manufacturing considerations; joinability, coolant compatibility, armour/substrate compatibility, cost, and material availability.

Of the desirable properties, the most important for a commercial fusion power plant are: the mechanical properties, namely a high yield strength and fracture

toughness; excellent thermal conductivity; good irradiation resistance and long-term thermal stability (especially with regard to creep resistance); and finally producing a low-activation material [4, 9, 11]. These factors rule out many materials classes, for example Al alloys are not low-activation and present serious radioactivity issues after neutron irradiation, whilst steels are not suitable because of their low thermal conductivity when compared with other available materials.

2.3.1 Cu and other alloys

Cu alloys offer the greatest potential, in particular due to the high thermal conductivity of Cu of $398\,\mathrm{W\,m^{-1}\,K^{-1}}$ [12] and even once slightly alloyed to increase strength, conductivity remains 10 to 20 times greater than 316 stainless steel ($13\,\mathrm{W\,m^{-1}\,K^{-1}}$) [13]. Figure 2.2 shows the room temperature proof strength versus thermal conductivity of some Cu alloys suggested for fusion applications. The requirement is to maintain high thermal conductivity whilst also maintaining a stable microstructure under thermal and irradiative load. Pure Cu does not have sufficient strength for the application and also suffers significantly from irradiation damage and limited thermal stability; it suffers from high creep rates, neutron-induced swelling, irradiation hardening and shows some embrittlement by He [14]. The addition of alloying elements to pure Cu has the undesirable effect of reducing the thermal conductivity, so solutions are sought to provide improved mechanical properties and irradiation resistance with minimal alloying.

2.3.2 Precipitation strengthening

CuCrZr alloys are amongst the most mature Cu alloys for divertor application and have been selected for application in ITER. The reference composition is shown in Table 2.1, and the relative performance to other Cu alloys is shown in Fig. 2.2.

CuCrZr alloys are precipitation hardening and suffer from over-ageing at elevated temperature and under irradiation. A specific fusion grade of CuCrZr designed for

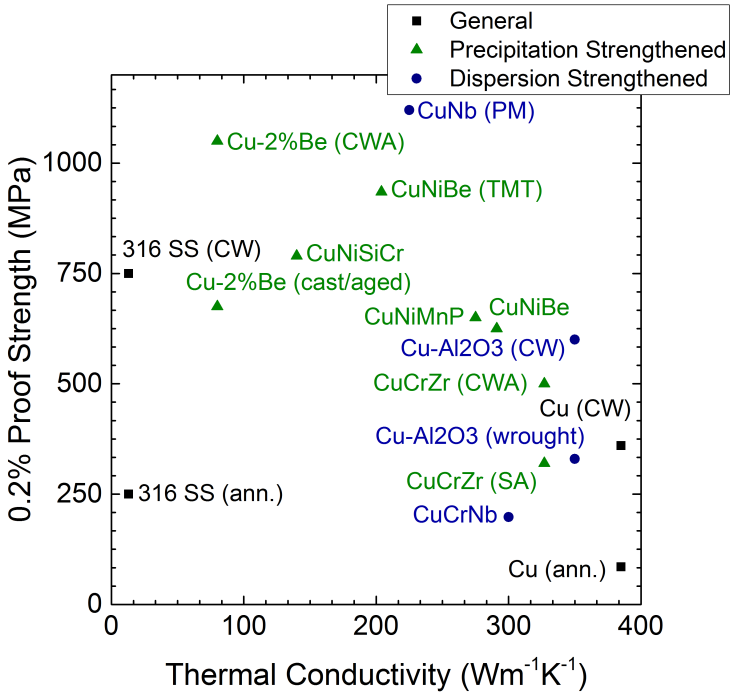

Figure 2.2: Room temperature 0.2% proof strength from tensile testing versus thermal conductivity of fusion Cu alloys [11].

Table 2.1: Composition of CuCrZr ITER-grade (IG) alloy (all values wt.%) [9].

Cu	Cr	Zr	Impurities
Balance	0.6-0.9	0.07-0.15	<0.01

divertor application in ITER, known as "ITER-grade" (IG) has been investigated. CuCrZr-IG's ultimate tensile strength (UTS) reduced from ∼275 to ∼175 MPa when the temperature was increased from RT to 400 °C – with a corresponding decrease in yield strength. Under irradiation (fission energy spectra neutrons and ions), CuCrZr showed similar damage to pure Cu with swelling at 300 °C and Otswald ripening of the precipitates [14]. The limited thermal and irradiation stability restrict the likely use of CuCrZr alloys for the expected conditions in DEMO, but remain adequate for the initial experiments planned for ITER. Irradiation enhanced creep at high temperature, and caused embrittlement at low temperatures, leaving a useful window of operation of only 250 to 350 °C, which was considered too narrow for DEMO [15].

Other precipitation strengthened alloys include those Cu-Be alloys that have a comparatively high 0.2% proof strength, as shown in Fig. 2.2, at the expense of thermal conductivity and with poor stability at elevated temperature [11]. Additionally, Be is undesirable due to its toxicity when in particulate form, which could be an issue in the event of high wear of the plasma strike surfaces or corrosion.

2.3.3 Solution strengthening

Solution strengthening of copper alloys is a relatively straightforward and, as with many alloys, usually requires significant additions (>2 wt.%) for meaningful effects. A number of alloying additions have been considered, in particular Mn, Cd and Sn in varying concentrations, for both binary and ternary alloys [13]. Cu alloyed with 0.5-5 wt.% Mn showed comparable thermal conductivity to CuCrZr-IG between 0.5 and 1 wt.% Mn, but in order to reach similar strengths, higher concentrations of Mn were required (up to 5 wt.%); but which reduced thermal conductivity from ∼350 to ∼100 $\mathrm{kW^{-1}\,m^{-1}\,K^{-1}}$ [14]. Cu-0.002 wt.%Mn-0.002 wt.%Se has shown an excellent thermal conductivity of 392 $\mathrm{kW^{-1}\,m^{-1}\,K^{-1}}$, close to that of pure Cu, but at the expense of useful mechanical properties, with a 0.2% proof strength of 248 MPa, compared with

463 MPa for CuCrZr-IG in a similar cold-worked state [13]. This suggests that solid-solution strengthening will be at the expense of thermal conductivity, while overall irradiation resistance is expected to remain similar to that of pure Cu. Also, the cold-worked microstructure would recrystallise at divertor operating temperatures [16, 17] and strength could not be maintained at the divertor operating temperatures, and with insufficient creep and irradiation resistance.

2.3.4 Dispersion strengthening

Promise is shown by dispersion strengthened (DS) Cu alloys and they have been considered for fusion application for over 20 years [13, 18]. DS materials offer potential for fusion because they exhibit excellent high temperature stability and improved mechanical properties (notably yield strength) for modest alloying additions. They also have good potential for irradiation resistance if the dispersoids act to stabilise grain structure and act as sinks for He. DS Cu may be strengthened by a number of hard ceramic particles, including oxides (e.g. Al_2O_3 and Y_2O_3), borides (e.g. TiB_2 and ZrB_2), nitrides (e.g. Si_3N_4 and BN) and carbides (e.g. SiC and WC). The main considerations for particle selection for DS Cu are thermal and chemical stability, ability to impart creep and thermal fatigue resistance, and finally stability under irradiation i.e. low activation elements. A commercially available Cu-Al_2O_3 oxide dispersion strengthened (ODS) alloy is currently being considered for DEMO, and an ITER grade alloy composition has been proposed, with the composition shown in Table 2.2, which has been the subject of the majority of studies on Cu-ODS alloys.

Table 2.2: Reference composition of ITER grade GlidCop alloy, CuAl25, a dispersion strengthened alloy using Al_2O_3 for strengthening. B is added as a deoxidiser to prevent embrittlement during processing (all values wt.%) [9].

Cu	Al (as Al_2O_3)	O (as Al_2O_3)	B (as B_2O_3)	Impurities
Balance	0.23-0.27	0.020-0.28	0.005-0.04	<0.035

2.4 Oxide dispersion strengthened Cu

Oxide dispersion strengthening uses oxide particles to enhance material properties and much of the challenge in their use lies in obtaining a homogeneous distribution of a low fraction of suitable fine-scale particles. Oxides are selected for their high melting points, hardness and thermal stability and especially for their limited interactions with the matrix metal due to their high chemical stability and minimal solubility.

Strengthening and other mechanical improvements such as creep resistance in DS materials result from two main mechanisms: direct retarding of dislocation motion by nanoparticles, and dislocation retardation by other induced microstructural features.

Dislocation retardation mechanisms may be considered to result from the additional applied stress needed for dislocation cutting of coherent nanoparticles, or the additional stress required for dislocations to bow around non-shearable nanoparticles, or climb to a different plane to bypass them [19]. The Orowan mechanism allows dislocations to move past impenetrable objects. As the dislocation reaches an object, it is impeded close to the object, while the rest of the dislocation moves past and is forced to "bow" around the pinning point. As the dislocation curves, it becomes energetically favourable for the dislocation to be drawn together on either side of the object and a loop is formed around the object. The rest of the dislocation then continues through the material and the loop left increases the stress required for the next dislocation to move past the object. This is the Orowan stress and describes the flow stress required for dislocations to bow around obstacles, given by:

$$\tau = \alpha_b G b / D_t \tag{2.2}$$

where α_b is the barrier strength coefficient (equal to 0.84 for a random array of impenetrable particles), G is the matrix shear modulus, b is the Burger's vector of the dislocation and D_t is the particle spacing. Assuming a constant volume fraction of

particles in the matrix, Orowan strengthening may be increased by reducing particle size, which reduces D_t.

Nonetheless, the microstructural features that contribute most strengthening in ODS materials are the ultrafine grain sizes (<500 nm diameter) that are induced due to grain boundary (Zener) pinning effects, giving rise to Hall-Petch strengthening; the increased density of grain boundaries results in increasing pile-up of dislocations per unit volume of material. The Hall-Petch relationship provides an estimate of the contribution of grain diameter to the yield strength, according to:

$$\sigma_y = \sigma_i + kd^x \tag{2.3}$$

where σ_i and k are the intrinsic strength (i.e. the resistance of the lattice to dislocation motion) and strengthening coefficient respectively, and d is the grain diameter. Historically, the exponent x is given as -0.5, although recently this was argued to be more accurately $x = 1$ [20].

A Cu-0.5Y_2O_3 alloy produced by a high temperature oxidation route evaluated the contribution of Orowan strengthening, coherent particle strengthening (where dislocations are able to cut through the particles), modulus mismatch strengthening and Hall-Petch strengthening and the results are summarised in Table 2.3. The particles were shown to be coherent with the matrix as a result of the processing method, and as such it was suggested that the majority of strengthening was provided through the particles by a combination of Orowan strengthening followed by particle cutting of the 3 to 5 nm particles [21]. The large grain sizes that resulted from the time spent at the liquidus temperature for oxidation gave rise to relatively large grain diameters and thus only a small strengthening contribution. Given an improvement in processing it was suggested that the UTS might be increased beyond 583 MPa. A similar approach to evaluation of strengthening was employed for ODS Cu-Al_2O_3 prepared by reactive mechanical alloying followed by hot extrusion at Al_2O_3 weight

fractions of 1 and 5 wt.%. The Hall-Petch strengthening at a grain size of 50 nm was suggested to be by far the largest contributing factor [22], and significantly larger than the direct effect of particles (by cutting or bowing), as shown in Table 2.3.

Table 2.3: The estimated contribution of strengthening mechanisms to Cu-0.5Y_2O_3 prepared by oxidation at the liquidus temperature [21], compared with Cu-Al_2O_3 at weight fractions of 1 and 5 wt.% prepared by reactive mechanical alloying and hot extrusion [22]. All given values are in MPa.

Mechanism	Cu-0.5 wt.% Y_2O_3	Cu-1 wt.% Al_2O_3	Cu-5 wt.% Al_2O_3
Orowan	174	101	200
Coherent particle	181	-	-
Modulus mismatch	26	-	-
Hall-Petch	12	381	381
Solid-solution (impurity)	-	6	6

2.4.1 Oxide selection

Table 2.4 gives the physical properties of a number of the most promising oxide dispersion additives (and other compounds). The compounds were compared and ranked theoretically according to suitability for the fusion ODS application, giving CeO_2, MgO and CaO as the strongest contenders, followed closely by Y_2O_3 [18]. These results were strongly influenced by the solubility and diffusivity of the metal oxide forming element in Cu, in order to consider the potential for dissolution of the nanoparticle during elevated temperature operation. The various oxide physical properties are shown in Table 2.4. The high enthalpy of formation of Y_2O_3 suggests it may be the least reactive system for alloying additions but some caution in these results is required owing to the significance of the large particles (30 nm diameter) used for calculation that do not conform to generally much finer particles (<10 nm diameter) expected in DS alloys in practice.

Table 2.4: Physical properties of selected ceramic compounds for dispersion strengthening, ranked by enthalpy of formation [18]. The melting point, coefficient of thermal expansion and enthalpy of formation allow prediction of likely particle stability in fusion applications.

Compound	T_m (°C)	$\Delta\alpha$ (10^{-6} °C^{-1})	ΔH_f (kJ mol^{-1})
Y_2O_3	2430	9.3	-1905.3
Al_2O_3	2050	7.6	-1667
Cr_2O_3	2435	8.2	-1140
CeO_2	2600	8.4	-1088.7
CaO	2572	4.8	-635.1
MgO	2800	3.8	-601.2
Be_3N_2	2240	8	-588.3
TiB_2	3200	8.5	-323.8
ZrB_2	3060	11	-322.6

Role of Ti in ODS alloys

In Fe-ODS alloys processed in the solid-state by mechanical alloying (MA), the final oxide particle size may be controlled through the use of minor alloying additions to give complex oxides. Ti reduces the oxide particle size drastically in Fe-ODS alloys, for example with a reduction of mean particle diameter from 15 to 2 nm in Fe-14Cr-0.25Y_2O_3 on the addition of 0.4wt.%Ti [23] and from 13 to 3 nm in Fe-14Cr-3W-0.4Ti-0.25Y_2O_3 (all wt.%) [24]. The smallest particles of 2 to 5 nm diameter had a comparatively high Ti and more modest Y fraction of between 0.1 and 0.6 wt.% [23]. MA of Ti-containing Fe-ODS promoted the formation of complex oxides of $Y_2Ti_2O_7$ and Y_2TiO_5 with average diameter of 5 nm, smaller than for alloys without Ti, as a result of Ti promoting the dissolution of Y_2O_3 to Y and O [25]. Small angle neutron scattering experiments identified Ti was responsible for altering the re-precipitation behaviour of oxide particles in Fe-ODS alloys, where the oxide particles were also more resistant to coarsening with Ti present than without [26]. The stability of these particles is thought to be additionally dependent on the Ti:Y ratio, with highest stability when this ratio is >1, and O is limited [27]; this likely results from the change in structure from coherent body-centered cubic (bcc) particles to incoherent

orthorhombic with reducing O content [28, 29]. It is suggested that Ti promotes the nucleation of Y-containing oxide particles by increasing the coherency of the nanoclusters with the matrix, allowing for lower energy interfaces [30].

In Cu-ODS alloys the effect of Ti is poorly understood. Early work on the effect of Ti on Cu-Al internally oxidised ODS alloys did not reveal if Ti was co-locating with Al in forming complex dispersed oxides [31], only $CuAlO_2$, Al_2O_3 and TiO_2 were found using X-ray diffraction (XRD). A change in the morphology of particles was observed between oxidised Cu-Al and Cu-Ti-Al, whereby large triangular, hexagonal or polygonal oxides were altered by the addition of Ti, resulting in slightly polygonal oxides particles. Particles in the Cu-Al-Ti system were a factor of three smaller than those in the Cu-Al system under the same oxidation conditions. Recently, high-resolution analytical transmission electron microscope (TEM) and density functional theory calculations have been used to further understand the role of Ti in internally oxidised Cu-Al-Ti alloy systems, revealing a reduction in particle/matrix interfacial energy. Additional improvements in properties, particularly ductility - rising to 21% elongation at failure at 280 MPa UTS - and electrical conductivity - 90% international annealed copper standard (IACS) versus 81% for comparable GlidCop, were realised by Ti also acting as an effective gettering agent for O, Al and other impurity elements [32].

The effect of Ti on Y-containing nanoparticles has not been examined in Cu-ODS alloys, although the wettability of Cu on Y_2O_3 was significantly improved by the addition of either Al or Ti [33], suggesting it may be beneficial in reducing the interfacial surface energy of Y-Ti-O particles compared with Y-O particles in contact with the Cu matrix.

Ti has positive effects on the thermal and electrical conductivity of Cu alloys. In Cu-Ti alloy systems, the low solubility of Ti in Cu promotes the formation of Ti-rich precipitates [34], and the effect of these particles is to increase the purity of the surrounding Cu matrix, so increasing thermal and electrical conductivity [35].

As Ti is more reactive than Cu, it has a stronger affinity for gettering O and other interstitial elements from the matrix. Additionally, through reduction of the interface energy between a Cu-matrix and C particles, Ti increased the thermal diffusivity of the composite with increasing temperature [36], which may arise from the increasing thermal conductivity of Ti with temperature [37].

2.4.2 Microstructure

The microstructural features of ODS alloys are dominated by two features. First, the presence of the dispersed particles themselves, and second the comparatively fine induced grain sizes. Powder processed Cu is normally characterised by large grain sizes on account of the comparatively high mobility of dislocations in the face-centered cubic (fcc) lattice that allows rapid recovery during powder consolidation. Nano-grains of the order of 100 nm and below may be obtained by extreme processing routes such as cryomilling [38] or equal channel angular pressing that induce very large strains in the material [17]; however these nanostructured materials recover quickly on exposure to elevated temperature [39, 40]. In contrast, a Cu-2Y_2O_3 alloy produced by MA in a rotary ball mill had a mean grain diameter of 35 nm (measured by TEM) with a distribution of diameters from 10 to 90 nm, and a modal grain diameter of approximately 30 nm [41]. Commercial GlidCop alloys typically have larger grains of 5 to 15 µm on account of the relatively prolonged thermal exposure during the internal oxidation step required to form the stabilising Al_2O_3 particles [42], Generally the resulting spatial and size distributions of oxide particles are considered to be qualitatively "inhomogeneous" [43]. A quantified definition of acceptable homogeneity in ODS alloys is not in wide operation.

Conductivity

The volume fraction of particles has a significant effect on the conductivity of Cu-ODS alloys. Cu alloys were prepared with 1, 2, 4 and 6 wt.% of ZnO, Y_2O_3, and

Al_2O_3 in a planetary ball mill and sintered by hot pressing for 30 min at 800 °C under 200 MPa [44]. The electrical conductivity was a maximum at ~4 wt.%, as shown in Fig. 2.3. The reduction in the conductivity was suggested to be due to the effect of the additions on the grain size, with smaller grains giving lower electrical conductivity as a result of increasing density of grain boundaries that impede electron flow. Cu-4ZnO had an electrical conductivity of ~48 MSv m^{-1}, approximately 80% of the conductivity of the International Annealed Copper Standard (IACS), compared with approximately 16 MSv m^{-1} for 1 wt.% oxide addition.

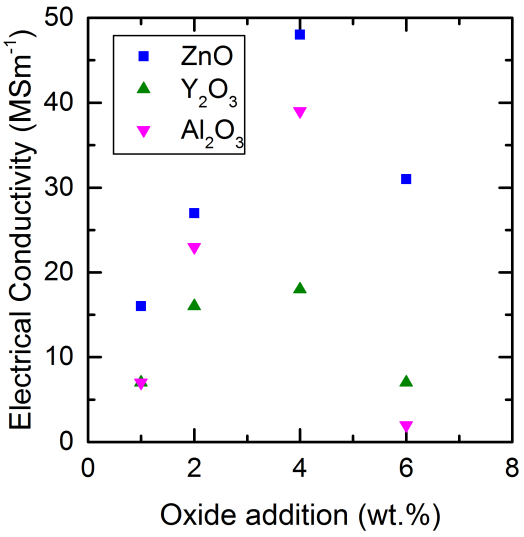

Figure 2.3: The effect of oxide additions on the electrical conductivity of ODS Cu alloys prepared by MA of ZnO, Al_2O_3 and Y_2O_3 at increasing wt.% [44].

According to the Wiedmann-Franz law, the electrical conductivity and thermal conductivity in metals are linked by:

$$\kappa/\sigma = LT \tag{2.4}$$

where κ is the thermal conductivity, σ is the electrical conductivity, L is the Lorenz number and T is the temperature [45].

The electrical conductivity - or its inverse, resistivity - is affected by changes in the material microstructure. The primary contributing changes are the grain boundary density, the dislocation density, the fraction of solute atoms, and the presence of non-matrix particles and their interfaces.

The effect of the grain boundary density on the resistivity, ρ_{gb}, of a metal may be calculated according to [46]:

$$\Delta\rho_{gb} = \frac{2}{3}\rho_0\frac{S}{V} \tag{2.5}$$

where ρ_0 is the intrinsic resistivity of bulk Cu caused by thermal scattering of phonons and $= 3.12 \times 10^{-16}\,\Omega\,\mathrm{m}^{-1}$, and S/V is the grain boundary surface area per unit volume, which may be approximated to $2.37/d_g$, where d_g is the mean grain diameter in the case of a tetradecahedral/equiaxed grain.

The effect of particles or pores on the resistivity, ρ_p, may be calculated using the modified Schroeder equation, for high resistivity particles (for example oxides and pores) [47]:

$$\Delta\rho_p = (\rho_0 + \Delta\rho_d + \Delta\rho_{gb})\frac{3V_f}{2(1-V_f)} \tag{2.6}$$

where $\Delta\rho_d$ is the effect of dislocations on the resistivity, given by $N \times 0.8 \times 10^{-25}\,\Omega\,\mathrm{m}^{-3}$ where N is the dislocation density, and V_f is the volume fraction of particles in the matrix.

The effect of solute impurity elements on resistivity due to the induced lattice strains, ρ_s, may be calculated according to [22]:

$$\Delta\rho_s = \beta f \tag{2.7}$$

where β is the change in electrical resistivity for a specific solute atom in a matrix material per wt.% (equal to $115 \times 10^{-9}\,\Omega\,\mathrm{m}$ for Fe dissolved in Cu, [22]), and f is the wt.% of solute atoms.

The total resistivity of the material may then be expressed as :

$$\rho = \rho_0 + \Delta\rho_{gb} + \Delta\rho_p + \Delta\rho_d + \Delta\rho_s \tag{2.8}$$

Applying the above approach to Cu-Al_2O_3, Table 2.5 summarises the results for Cu-1wt.%Al_2O_3 and Cu-5wt.%Al_2O_3 produced by reactive ball milling [22]. The largest single contributor to an increase in the electrical resistivity and hence the reduction in thermal conductivity is the presence of a solid-solution of Fe at ∼0.13 wt.%, leading to a reduction in the thermal conductivity of ∼190 $\mathrm{W\,m^{-1}\,K^{-1}}$ - a loss of almost 50%.

Table 2.5: Contributions to electrical resistivity, ρ, of Cu-Al_2O_3 produced by reactive ball milling. All values in $\mathrm{n\Omega\,m}$ at 20 °C [22].

Contribution	Cu-1Al_2O_3	Cu-5Al_2O_3
$\Delta\rho_{gb}$	2.5	5
$\Delta\rho_p$	0.33	1.76
$\Delta\rho_d$	-	-
$\Delta\rho_s$	15	15

2.4.3 Mechanical properties

The mechanical properties of particular interest for fusion heat-sink application of Cu-ODS alloys are the tensile strength, creep resistance, cyclic fatigue resistance and fracture toughness. GlidCop alloys have been subjected to more mechanical property testing than other Cu-ODS alloys, owing to their ready commercial availability.

Tensile properties

The tensile strength of Cu-ODS alloys is dependent on the nanoparticle type, number and fraction, which is also dependent on the processing route. UTS and proof strength (as Cu alloys do not show a distinct yield point) are typically lower than the precipitation hardening Cu alloys such as CuCrZr, but demonstrate a much

slower loss of tensile properties at elevated temperatures. Extruded GlidCop Al15 was tested in both the extrusion and perpendicular directions and the significant extrusion texture gave a large variation in the tensile properties, with better properties in the extrusion direction, as shown in Table 2.6. Anisotropy was also observed in the fracture toughness and cyclic fatigue resistance, with both lowered in the extrusion direction [42].

Table 2.6: Tensile properties (Young's modulus, E; 0.2% proof stress, σ_y; ultimate tensile strength, UTS; and, elongation at failure ϵ_f) of extruded GlidCop AL15 (Cu-$0.3Al_2O_3$) at room temperature. Testing was performed parallel and perpendicular to the extrusion direction.

Test direction	E (GPa)	σ_y (MPa)	UTS (MPa)	ϵ_f (%)
Parallel	100	325	401	47
Perpendicular	100	275	352	34

Fracture behaviour of GlidCop Al25-IG0 was compared with precipitation strengthened CuCrZr IG, where CuCrZr was more resistant to fracture at all temperatures tested. Fracture toughness decreased for both alloys with increasing temperature, although this was less pronounced in the CuCrZr-IG, which maintained a fracture toughness of 200 MPa $m^{1/2}$ up to 100 °C and then decreased rapidly [48]. Fracture in GlidCop Al25 was ductile fracture by void nucleation and coalescence up to 250 °C, where it became intergranular brittle fracture corresponding to a significant decrease in fracture toughness. It was suggested that the presence of large oxide nanoparticles (>100 nm diameter) preferentially located at grain boundaries were responsible for the relatively good ductile behaviour at lower temperatures [49], though no explanations for the high temperature behaviour was suggested.

2.4.4 Thermal properties

Creep resistance

There is little data on the creep strength of ODS Cu alloys and creep response appears poorly understood. Preliminary results indicate that creep strength is improved

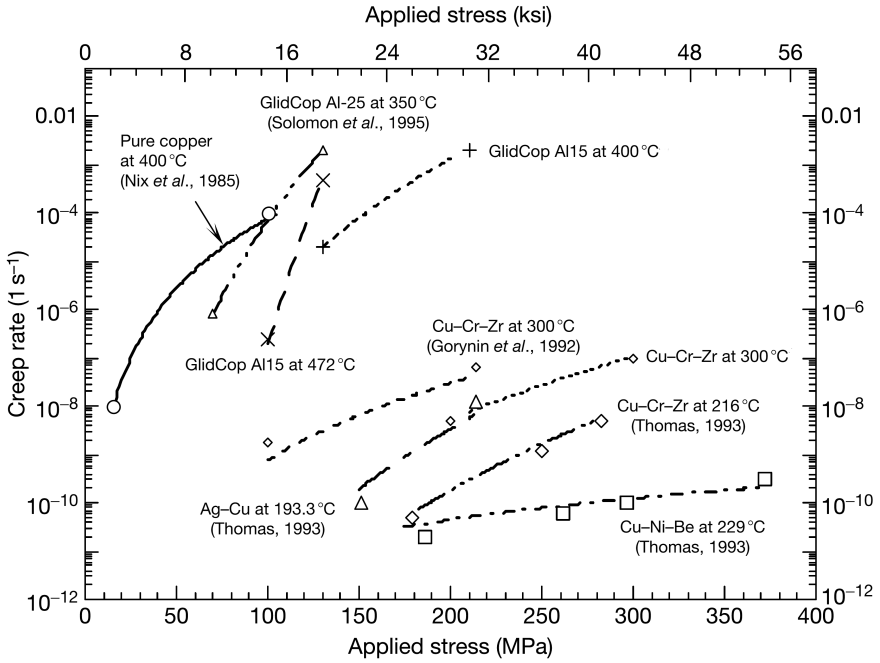

Figure 2.4: Steady state thermal creep behaviour of fusion-relevant Cu alloys - combination of modelling and experiment [51, 52]

on oxide addition, especially at elevated temperatures above 300 °C. For example, GlidCop AL60 retained significant creep strength to 800 °C, and even higher fractions of oxide particles gave improved creep strength [13].

GlidCop AL25 produced by hot isostatic press (HIP), hot extrusion, and extrusion with cross-rolling was evaluated for creep resistance at 350 °C. The effect of microstructure resulting from different processing routes yielded limited variation in secondary creep rates, and supported the assumption that yield strength governs creep [50]. However, Fig. 2.4 shows the creep resistance of GlidCop AL25 to be poor when compared with precipitation strengthened CuCrZr.

Thermal stability

Stability of the ODS alloys under elevated temperature (100 to 350 °C, as required for ITER and likely higher for DEMO [49]) and irradiation (up to 10 dpa), are essential for their application in fusion environments. The alloys must exhibit resistance to swelling, embrittlement and softening, to fracture toughness reduction and to fatigue,

whilst also maintaining their thermal conductivity, and without resorting to high activation element alloying additions.

The addition of ODS particles prevents grain growth through grain boundary pinning at elevated temperatures, preserving strengthening through Hall-Petch considerations, especially where the grain size is retained at ∼20 nm. Figure 2.5 shows the effect of annealing at 500 to 650 °C and for 1 h on the hardness of three Cu-ODS alloys prepared by MA, and compares them with three precipitation hardened Cu alloys prepared by conventional melt processing. In contrast to the precipitation alloys, the ODS alloys showed no softening after annealing at elevated temperature, suggesting that the microstructure was significantly stabilised, even under thermal exposure up to at least 650 °C [53].

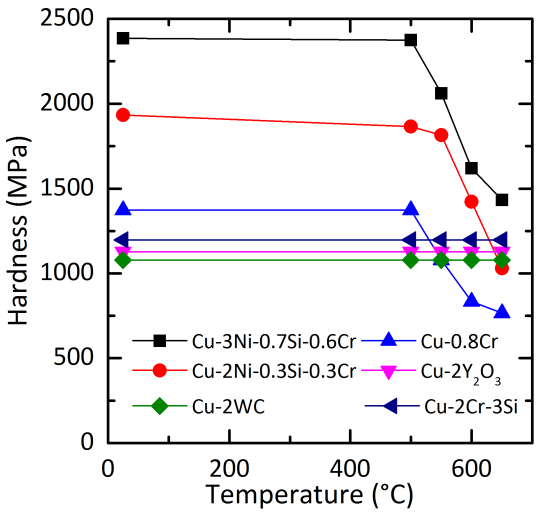

Figure 2.5: The effect of increasing annealing temperature on the hardness of precipitation and dispersion strengthened Cu alloys after 1 hour; the Cu-Y_2O_3, Cu-WC and Cu-Cr-Si alloys were dispersion hardened [53].

Abnormal grain growth has been widely reported in Fe-ODS and dispersion strengthened Cu alloys, and may present a particular problem for high temperature stability since a significant proportion of useful strengthening is attributed to stable,

fine-grain sizes. Abnormal grain growth results from the breakaway of one grain from its pinned state, which due to curvature considerations, is then relatively stable compared with its neighbours, which then shrink and disappear whilst the larger grain continues to grow. Cu-2.7Al_2O_3 prepared by internal oxidation and hot extrusion showed abnormal grain growth during annealing, compared with extruded Cu that demonstrated more "normal", homogeneous grain growth. Grains with a diameter of 1.1 ± 0.2 µm grew to 7.9 to 13.3 µm when exposed to temperatures ranging from 500 to 1000 °C for 4 h, with the volume fraction of abnormal grains increasing from 0.4 to 0.8 [54]. This behaviour could present a problem for fusion applications where materials will be exposed to high temperatures and further work is required to understand how abnormal grain growth might be mitigated.

2.4.5 Irradiation properties

Cu and various Cu alloys were subjected to irradiation in the Materials Open Test Assembly in the Fast Flux Test Facility during the mid-1980's and Table 2.7 details the changes in physical properties for pure Cu, a Cu-Mg-Zr-Cr (MZC) alloy and an ODS Cu alloy (GlidCop).

Table 2.7: Properties of various copper alloys irradiated to approximately 16 dpa (2.5×10^{22} n/cm^2 [E >0.1 MeV]) at 450 °C compared with thermally aged samples exposed to 400 °C for 1000 h [55].

			Conductivity (% IACS)	
Alloy	Composition (wt.%)	% swelling	Unirradiated	Irradiated
Cu	99.999% Cu	6.5	101	86
MZC	Cu-0.9Cr-0.1Zr-0.05Mg	1.03	84	73
GlidCop Al25	Cu-0.45Al_2O_3	0.13	83	77

	Yield strength (MPa)			Uniform elongation (%)		
Alloy	Unirradiated	Aged	Irradiated	Unirradiated	Aged	Irradiated
Cu	58	58	43	28	26	14
MZC	483	476	396	1.8	5.5	5.9
GlidCop Al25	450	401	267	2.5	6.2	8.7

Swelling was largest in the pure Cu, at 6.5% after irradiation and smallest for the GlidCop at 0.13%. All three alloys show a reduction in electrical conductivity, with GlidCop giving the smallest 7% reduction compared with 14% for both Cu and MZC-Cu. Yield strength decreased with irradiation damage as may be expected, and GlidCop showed the largest reduction of 40% compared with 18% for MZC-Cu. Pure Cu showed significant embrittlement with irradiation whereas the MZC-Cu and ODS Cu increased in ductility: no explanation for this behaviour was proposed and other alloys (solution strengthened and precipitation strengthened) also did not follow any obvious trends of strength and ductility [55]. It was separately reported that low-temperature embrittlement of GlidCop Al25 and pure Cu was reduced when irradiation took place at temperatures of 80 °C and then at 150 °C. The obstacle density was shown not to change during irradiation suggesting no Ostwald ripening or dissolution of the particles, so radiation hardening was attributed to the 'cascade-induced source hardening' (CISH) model, whereby migrating clusters of self-interstitial atoms attach themselves to dislocations and prevent motion. It was proposed that increasing the temperature would further alleviate hardening [56].

The increased swelling resistance associated with use of ODS and precipitate particles may be explained by the requirement for a threshold pressure, P, to be overcome to allow the nucleation of a He bubble at the particle/matrix interface given by

$$P = \frac{4\gamma \sin\theta}{\delta} \tag{2.9}$$

where γ is the surface tension of the Cu matrix, θ is the contact angle between the particle and matric and δ is the particle diameter. For small δ, this pressure becomes large and the bubbles remain small, preventing swelling [13]. Some GlidCop alloys suffer from swelling as a result of a low fraction of B deoxidiser (added to prevent the formation of deleterious CuO particles during internal oxidation), with swelling rates

of 1%/dpa owing to the high transmutation rate of B [56], leading to the development of B free alloys.

Irradiation of Cu-ODS alloys has continued since the early studies in order to compare Cu alloys for application in ITER focusing on CuCrZr, CuNiBe and Cu-Al_2O_3 alloys. The irradiation dose for the majority of studies has been set at 0.3 dpa as this was found to be the point at which maximum defect cluster density was reached and provided a reasonable indication of the effects of higher dose rates for ease of comparison between samples. Coarsening of precipitates was noted in CuNiBe, and in contrast to a slight size reduction of particles in Cu-Al_2O_3. CuCrZr and pure Cu suffered from a decrease in ductility at 0.3 dpa, and a significant reduction in yield strength, neither of which were observed in CuNiBe and Cu-Al_2O_3 when irradiated at 50 °C. At higher temperatures of >250 °C, there was embrittlement of CuNiBe [57].

Cu-0.45Al_2O_3 had a greater number of cycles to failure compared with CuCrZr under all conditions (0.3 dpa irradiated and unirradiated at 50 °C and 100 °C). Both alloys showed a reduction in fatigue life at higher temperatures of 250 °C and 350 °C. The high fatigue life was proposed to result from the difficulty of propagating dislocations as a result of the Al_2O_3 particle obstructions [57].

The toughness of Cu-ODS alloys reduced significantly from 100 MPa $m^{1/2}$ at room temperature during irradiation and heating [48]. For example, the fracture toughness of GlidCop Al25 decreased continuously with increasing temperature. A further reduction by a factor of 2-3 was noted from room temperature to 350 °C when GlidCop Al25 was subject to 0.3 dpa [57]. Fracture after irradiation was shown to be entirely brittle in nature [49].

2.5 Fabrication of oxide dispersion strengthened Cu

There are a number of techniques for the production of ODS alloys. The dominant techniques are powder metallurgy based and include mechanical alloying and internal oxidation, both of which are usually followed by powder consolidation through sintering or extrusion. There are considerable difficulties in the production of melt processed ODS alloys relating to clustering of the oxide additions and inability to achieve acceptable levels of dispersion. The low solubility of oxides in copper, particularly Y_2O_3 and Al_2O_3, prevents the possibility of solution processing followed by precipitation via any process in which near-equilibrium conditions prevail. Additionally, the lower densities of oxide particles, $\rho_{Y_2O_3} = 5.03\,\mathrm{g\,cm^{-3}}$ and $\rho_{Al_2O_3} = 3.97\,\mathrm{g\,cm^{-3}}$ for Al_2O_3, and their high melting points, T_m of 2703 K and 2323 K for Y_2O_3 and Al_2O_3 respectively, lead to the rapid formation of an oxide slag on the surface of molten Cu with $\rho_{Cu} = 8.02\,\mathrm{g\,cm^{-3}}$ at 1357 K (T_m) if they are mixed into the melt [58, 59]. As such, direct mixing of oxides into Cu and Cu alloy melts is generally considered not possible and non-equilibrium solid-state processing routes are preferred.

2.5.1 Internal oxidation

Internal oxidation is achieved by controlled oxidation of a reactive alloying element in solid solution at elevated temperature after powder production. A molten alloy of the major component and the metal cation for the desired oxide is prepared and during either cooling or subsequent heat treatments the alloy is exposed to oxygen to produce metal oxide particles dispersed in a metallic matrix. Internal oxidation is a diffusion-controlled process and requires the diffusion of oxygen into the powder particles and also the diffusion of the metal species atoms that will form the cation of the oxide. The control of and final size and distribution of dispersed particles is key

and a degree of control can usually be provided by the choice of specific processing parameters.

GlidCop is a commercial Cu-ODS alloy that is prepared by internal oxidation. A Cu-Al alloy is melted and water atomized and the powder then oxidised in an air flow at 1 hour at 900 °C to give dispersed Al_2O_3 particles in/on the Cu powder and surface CuO that forms during the oxidation step is removed by reduction in H_2 at 800 °C for 1 hour. Typically, the powder is then compacted by cold-pressing at 500 MPa, and then hot extruded at 900 °C under Ar [42], although it may also be HIPed effectively. Figure 2.6 shows a typical microstructure produced by internal oxidation of Cu-Al, to give Cu-0.3Al_2O_3 (Trade name: GlidCop Al15). The particles ranged in size from 3 to 12 nm with an interparticle spacing of 30 to 100 nm, giving a particle density of $\sim 5 \times 10^{22}\,\mathrm{m}^{-3}$ [42]. For effective creep resistance and density of irradiation sinks a particle density of $>1 \times 10^{22}\,\mathrm{m}^{-3}$ is considered sufficient for DEMO divertor application [11], although this assumes particles are "homogeneously" dispersed.

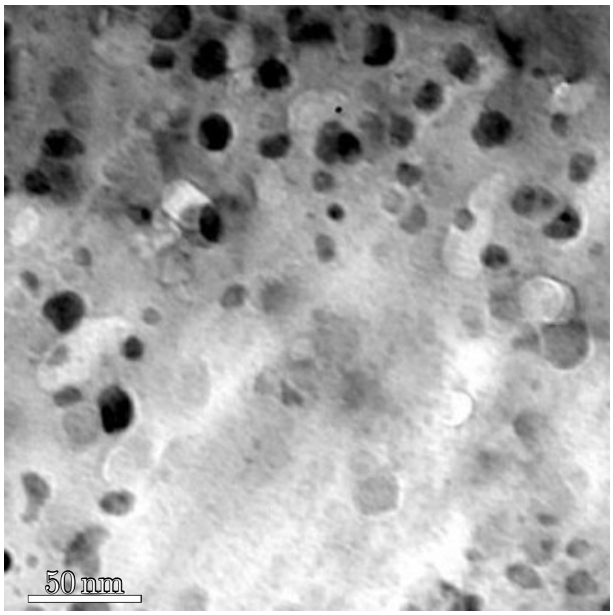

Figure 2.6: TEM micrograph showing dispersed particles in GlidCop AL-15 Cu-ODS (Cu-0.3Al_2O_3) [42].

2.5.2 Mechanical alloying

Mechanical alloying (MA) is a solid-state technique for producing both equilibrium and non-equilibrium alloy phases. Originally developed in 1966 for the development of dispersion strengthened Ni-superalloys, MA is now widely used for the production of nanostructured alloys [60]. MA takes place through the repeated working, fracture and cold-welding of pre-alloyed or elemental powders together with one-another so that over time an acceptably homogeneous mixture is developed. Collisions between milling balls and the pot walls or other milling balls, as shown in Fig. 2.7, will trap a small amount of milling powder at the point of collision. It is the high energy of these collisions that leads to the atomic transfer of material. The powder is subject to high energy impacts and there is local work hardening, an increase in the local defect density and eventual micro-fracture to facilitate material exchange and mixing.

The primary concern in mechanical alloying is reaching an acceptably homogeneous powder, where the desired elements or phases are distributed acceptably evenly in the material. However, as described earlier the definition of "homogeneous" for the oxide dispersion appears entirely qualitative. There are a large number of interlinked variables that govern the effectiveness of MA, of which the dominant variables include [61]:

Mill type - e.g. attritor mill, planetary ball mill, shaker mill

Milling media - size, shape, mass, material

Milling time - to include pauses and pause length for cooling

Milling speed - which directly controls impact energy

Starting powders - morphology, diameter, hardness

Ball-to-powder weight ratio (BPR)

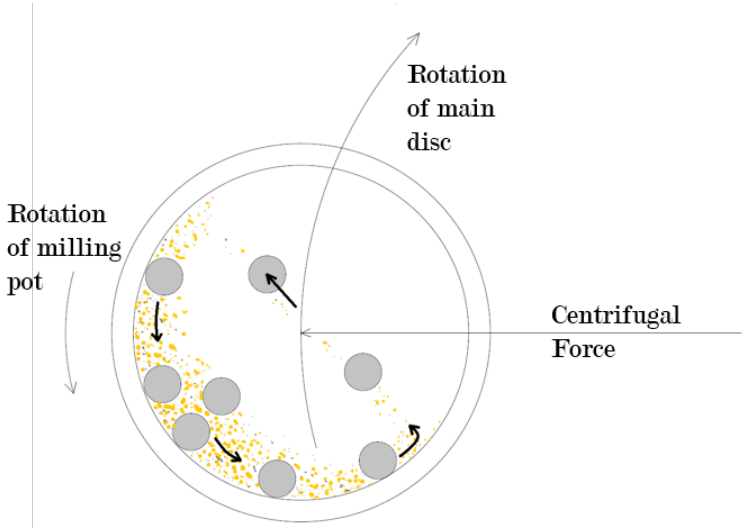

Figure 2.7: Horizontal section schematic diagram of planetary ball mill, showing direction of travel of milling balls and powder [61].

Milling atmosphere

Milling temperature

A steady state condition in MA is widely reported and is defined as the point when the rate of particle fracture is the same as the rate of particle welding, and the desired composition, microstructure (through grain size and alloy distribution homogeneity) and maximum level of cold-work is met. To determine when a steady state is reached variations in powder microhardness, crystallite size and lattice strain (as measured through XRD) with milling time are widely used. With increasing milling time, microhardness and lattice strain increase to a plateau, while crystallite size reduces to a plateau, and these changes progress in tandem. It is important that the steady state is just reached during MA to prevent over milling, beyond which contamination from the milling pot and media steadily increase.

Cryomilling

Cryomilling is increasingly used for MA in order to promote grain refinement in ductile materials, such as Al and Cu alloys, and to increase the rate of particle fracture by

reducing particle ductility [60]. Cyromilling is undertaken by the addition of a cryogen to the milling container directly, or through external cooling of the milling container.

Grain refinement takes place during cryomilling of Cu powders by the generation of very high dislocation densities because the low temperature prevents grain recovery. The dislocation density in pure Cu showed a rapid increase with cryomilling time, reaching $50 \times 10^{16}\,\mathrm{m}^{-2}$ in 20 hours, whereas room temperature milling of pure Cu reached only $3.5 \times 10^{16}\,\mathrm{m}^{-2}$ after 50 hours. There was a corresponding increase in the number of stacking faults [62], suggesting that grain refinement during cyromilling was a result of structural decomposition without significant recrystallisation. Whilst cryomilling offers opportunity for improved milling and MA of ductile materials, scale-up to industrial levels of output is difficult due to the complexity and small size of currently available cryomills.

2.5.3 Consolidation

Consolidation of powder materials to form a bulk is undertaken by sintering. The sintering process requires the application of heat, and is often accompanied by the application of an isostatic or uniaxial pressure.

Conventional sintering techniques for the production of powdered Cu and Cu alloys are in line with standard powder metallurgical processing routes and vary according to the alloy and application. Current Cu alloys produced by powder metallurgy are consolidated by several methods: cold powder compaction, solid state sintering and liquid phase sintering.

Commercial Cu-ODS alloys may be consolidated using HIP, powder extrusion or hot pressing to obtain >99% theoretical density. A significant limitation for processing by these methods is the time required (often several hours) at high temperatures that promotes usually undesirable recovery, recrystallisation and grain growth.

A Cu-3Al_2O_3 as-milled powder had an average grain size of 35 nm following 20

hours of milling in air in a planetary ball mill with a ball-to-powder weight ratio (BPR) of 35:1. Following 1 hour treatment at 400 °C in an H_2 atmosphere to remove surface oxides, the powder was compacted in a hot press at 800 °C for 1 hour and 35 MPa, which led to an increase in the average grain size to 90 nm. After 5 hours exposure at 800 °C in an Ar atmosphere the grain size increased to 120 nm. This grain size increase reduced the microhardness from 2100 MPa after compaction to 730 MPa after thermal treatment [63]. A significant factor in the rate of recrystallisation is the size of the particles, with smaller particles providing greater grain boundary pinning. Internal oxidation of Cu-1Al by milling in air was said to give finer particles than direct milling of Cu with Al_2O_3 although measurements of the oxide particle size were not explicitly reported [63].

Melt spun ribbons of CuY and CuZr alloys were internally oxidised to give Cu-$1Y_2O_3$ and Cu-$1ZrO_2$ and then consolidated, following pulverisation of the ribbons to form a powder, by hot pressing at 600 °C under 53 MPa [64]. Fine grains <5 µm were produced, along with particles of 5 to 20 nm diameter. The particles had a repeatable orientation relationship with the matrix, and appeared coherent [64]. High levels of particle-matrix coherency would be expected to allow easier cutting of dislocations and so reduce strength when compared with mechanically alloyed alloys where the particle orientation is suggested to be random (overall a lower tendency for coherency). Hot pressing gave rise to significant recrystallisation of Cu-$3Y_2O_3$ prepared by ball-milling: after 800 °C for 1 hour, the recrystallised regions formed in the sinter necks [63], and comprised a local region of comparatively large grains, suggested to result from recrystallisation of the Cu rapidly due to high local strain at the contact points.

Field assisted sintering technique

The Field assisted sintering technique (FAST) - also known as spark plasma sintering (SPS), or pulsed electric current sintering (PECS) - uses electrical current to activate or accelerate sintering mechanisms (diffusion is enhanced), and has been investigated

for a range of "difficult to sinter" materials, from refractory metals and superalloys, through intermetallic materials to conventional ceramics and metals [65]. The powders to be sintered are placed in a conductive die and subjected simultaneously to an applied pressure (typically $<100\,\mathrm{MPa}$) and electrical current (typically $<5\,\mathrm{V}$ and $\gg 1\,\mathrm{kA}$). The applied pressure ensures good electrical contact allowing joule heating that leads to rapid sintering. Figure 2.8 shows a schematic drawing of a typical FAST machine with its primary design features, namely current supply directly through the uniaxial press punches in a controlled environment chamber (vacuum or dynamic inert gas flow).

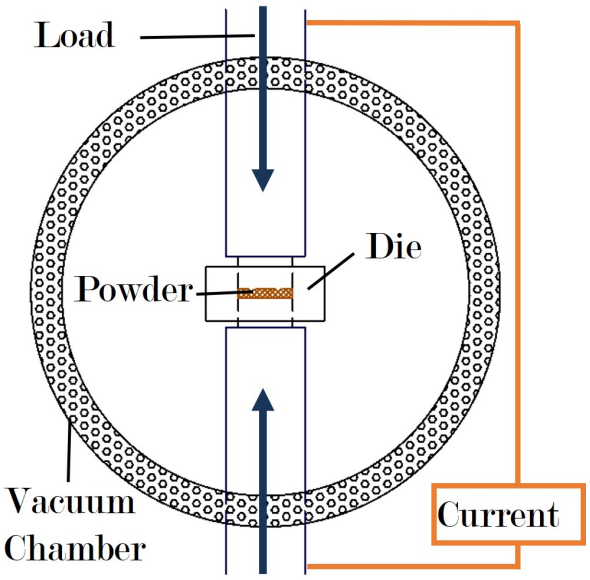

Figure 2.8: Schematic representation of FAST machine.

The major difference between HIP and FAST is the resulting rapid heating rate: FAST allows heating rates in excess of $1000\,^{\circ}\mathrm{C\,min^{-1}}$, which contrasts with heating rates up to approximately $100\,^{\circ}\mathrm{C\,min^{-1}}$, but typically of the order of $10\,^{\circ}\mathrm{C\,min^{-1}}$, in HIP and vacuum hot press (VHP) [65]. Some controversy persists in the specific role of the high current in this family of processes. Initially it was thought that the dielectric breakdown of insulating powders and the formation of micro-plasmas between particles was needed [66], but then metals were shown to also show accelerated consolidation [67].

That the current flows both through the retaining die and through the sample adds to the complexity. It was suggested that the Branly effect - an enhanced reduction in the resistivity between grains as a result of sparks [68] - occurs in conductive materials, identified by local melting at the surfaces of powder particle during the initial stages of sintering [69]. Most recently it has been shown that consolidation can be achieved even without a die or pressure, only the electric current [70]. Direct effects of the current flow on diffusion through electromigration and defect mobility enhancement are also suggested as critical [71, 72].

Regardless of the precise mechansism(s), consolidation by FAST typically takes place over much shorter time scales than VHP or HIP so that the same or higher density consolidated materials are sintered in an order of magnitude shorter times [71].

Ultra-fine grained Cu (99.95% purity) was prepared by FAST using spherical powder with an average particle diameter of 1 µm that was sintered at 750 °C for 360 s at 50 MPa. The consolidated Cu had significantly improved properties over the same material prepared by VHP under identical conditions, as shown in Table 2.8. The largest difference was the reduction in grain growth that occurred during sintering; VHP gave an average grain size of 15 µm, compared with 2.2 µm by FAST [73]. Using a pure Cu powder with sub-micron grain diameter allowed retention of sub-micron grains after sintering [74]. It is possible that the grain size difference between VHP and FAST was indirectly due to the more efficient joule heating in the die and in the compact during FAST, that helped to reduce temperature gradients between the die and the powder compact central regions - i.e. it is simply the inhomogeneity of heating in VHP that mandates longer consolidation times.

A range of dispersion strengthened materials have been consolidated by FAST. FAST and HIP consolidated Fe-14Cr-0.3Y_2O_3 was sintered for 240 s at 1100 °C and 36 MPa and 7200 s at 1100 °C and 200 MPa respectively. FAST consolidation material had a lower yield strength of 600 MPa compared with HIP consolidation of 1100 MPa

Table 2.8: Properties of pure Cu prepared by FAST and VHP, sintered at 750 °C for 360 s under a 50 MPa load with a heating rate of 80 °C min^{-1} under vacuum. The starting powder was 99.95% pure spherical Cu powder of 1 µm mean diameter [73].

	FAST	VHP
% of theoretical density	99.9	94.4
Young's modulus (MPa)	125	102
Mean grain size (µm)	2.2	15.0
Ultimate tensile strength (MPa)	280	203
Elongation to failure (%)	50	32

at room temperature. The FAST material had a higher residual porosity and an increased volume fraction of martensite attributed to C diffusion from the graphite dies [75]. Conductive dies are necessary for FAST, with graphite the conventional material of choice, which limits the maximum pressure to 40 to 70 MPa. A hybrid die using tungsten carbide and silicon carbide punches inside a graphite die providing conduction allowed pressures up to 1 GPa to be applied [76], and through the use of metal foils carbon contamination may be avoided.

Cu-ODS powder prepared by an internal oxidation method with Al was consolidated using FAST under conditions of 300 s at 900 °C and 40 MPa, and a density of 99% theoretical density (TD) was achieved [77]. The ODS mean particle diameters were comparatively large at 27 nm which was attributed to internal oxidation, as opposed to the consolidation technique itself.

FAST may also allow the relatively straightforward production of functionally graded materials that are useful for joining materials with dissimilar properties. For example, FAST was used to produce a three layered W/Cu functionally graded material with a density of 96.5% TD by stacking layers of 20 mm thick W-75Cu, W-50Cu and W-25Cu milled powders and then cold-pressing, before sintering for 300 s at 1050 °C and 40 MPa. A thermal conductivity of 140 W m^{-1} K^{-1} was achieved, approximately 35% and 81% the thermal conductivity of pure Cu and W respectively [78]. No mechanical properties were evaluated, nor the effect of thermal expansion coefficient

mismatch at the interfaces of the different grades.

2.6 Summary

The requirement for high conductivity materials for future fusion reactors and the recent work in the development of Fe-based ODS alloys presents an opportunity to enhance decades-old work in Cu-ODS alloys with the improved process understanding and knowledge now available.

This thesis will explore the processing and properties of Cu-ODS alloys prepared by MA. The objectives are:

1. To investigate the relationship between the microstructure and properties, and their stability, in Cu-ODS alloys, with an emphasis on the dynamics and mechanism of any oxide dissolution and subsequent re-precipitation and ageing.

2. To investigate the relationship between the processing conditions and Cu-ODS microstructure in both as-milled powder and bulk consolidated material, and the effect of ternary alloying additions of Ti on microstructure.

3. To compare in-house produced materials with commercial Cu alloys and Cu-ODS products suitable for the divertor application and to explore the relationship between processing route and properties, with particular emphasis on the thermal stability of Cu-ODS alloys with respect to microstructure and creep.

Chapter 3

Experimental methods

3.1 Introduction

In this chapter the experimental methods for processing and characterisation of samples examined in this thesis are described. All alloy compositions are in the form E_1-nE_2-mE_3, where E represents any element and n and m give the weight percentage (wt.%), unless otherwise stated.

3.2 Processing

3.2.1 Raw materials

The primary raw materials used were Cu powder, Y_2O_3 powder, and Ti or Ti-containing powder.

- Cu 99.5% purity with mean powder particle size 300 µm, Alfa Aesar Ltd, UK
- Cu 99.9% purity with mean powder particle size 70 µm, Alfa Aesar Ltd, UK
- Y_2O_3 99.999% purity with stated powder particle size 20 to 40 nm, PI-KEM Ltd., UK
- Cu-10Ti 99.9% purity with mean powder particle diameter 45 µm prepared by gas atomisation, Goodfellow Ltd., UK

- Cu-0.5Ti of 99.95% and 99.6% starting purities and mean powder particle diameter 45 µm prepared by Ar gas atomisation, Nanoval GmbH & Co. KG, Germany

3.2.2 Mechanical alloying

Mechanical alloying was undertaken using planetary ball mills Fritsch Pulverisette models 5 and 6. The model 6 is a single mill station with counterweight, the model 5 is a four-station mill requiring an even number of pots to balance.

Milling was undertaken in FeCr alloy milling pots, with the material code X210CrW12. Milling media were AISI 52-100 steel balls of 10 mm diameter weighing 8.00 g each and were used throughout, apart from a limited number of experiments that used a stabilised-ZrO_2 pot and stabilised-ZrO_2 milling balls of identical dimensions. The compositions are given in Table 3.1. All milling was undertaken under a dry argon atmosphere.

Table 3.1: Composition of milling pot and milling media [suppliers data], all wt.%

	X210CrW12 pot	AISI 52-100 balls
Fe	Bal	Bal
C	2-2.3	0.98-1.1
Cr	11-13	1.3-1.6
Si	0.1-0.4	0.15-0.3
Mn	0.3-0.6	0.25-0.45
P	< 0.03	< 0.03
W	< 0.6-0.8	< 0.03

	ZrO_2 pot & balls
ZrO_2	Bal
HfO_2	1-2
MgO	3.5
SiO_2	0.1
Al_2O_3	0.1

In order to reduce contamination during milling, a "cleaning" experiment using high purity (99.5%) Cu powder was used between each sample run. This is something of a misnomer because rather than remove the material, the Cu infiltrated any surface micropores and produced a thin Cu coating on the surface of the milling pot and milling media with the aim of reducing contamination from direct milling of the pot and media into the powder [79]. The cleaning procedure had the same time

duration, powder mass and milling speed as a typical experiment (see later). After this procedure, the pots had a comparatively smooth inner surface finish, and a mirror finish with tint of rose colouring.

3.2.3 Sintering

Vacuum hot press

Vacuum hot press (VHP) was performed using in-house designed and built equipment utilising a 12 kW induction heater together with a 60 ton hydraulic press. The sintering of cold-pressed compacts took place in a vacuum chamber that was pumped by dual-stage pump consisting of a rotary pump for roughing and a diffusion pump. A charge of 20 g was loaded into a graphite foil lined graphite mold, and degassed in the chamber between the dies at 400 °C for 4 hours at $<5 \times 10^{-4}$ mbar. The compact was then heated at a rate of approximately 100 °C min^{-1} dropping to 20 °C min^{-1} as the dwell temperature of 900 °C was approached. The dwell temperature was calibrated by use of a thermocouple inserted in the centre of the Cu powder in a prior calibration experiment, such that at the final dwell temperature the temperature at the die centre was known to ±4 °C.

A load of 50 MPa was applied once the sample reached 800 °C and only removed once the temperature dropped below 600 °C, after 1 hour at the dwell temperature. During this period, the vacuum was maintained as high as possible, typically maintaining a level below 5×10^{-4} mbar.

Hot isostatic pressing

Hot isostatic press (HIP) was performed by the University of Birmingham at the Advanced Manufacturing and Processing Laboratory using an EPSI laboratory scale HIP. Powders were canned in mild steel and degassed at 200 °C for 24 hours prior to sealing and sintering. A schematic drawing of the HIP set-up is shown in Fig. 3.1.

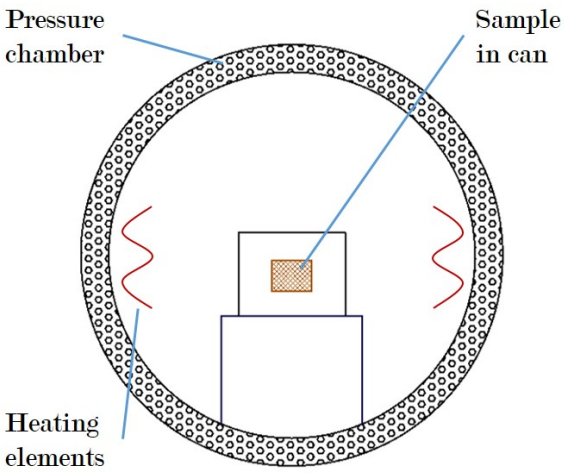

Figure 3.1: Schematic representation of HIP set-up.

The equipment allowed a maximum heating rate from room temperature of $10\,^{\circ}\mathrm{C\,min^{-1}}$, a maximum dwell temperature of 1450 °C (which was not necessary for Cu-based alloys), and a maximum pressure of 200 MPa.

Field assisted sintering

Field assisted sintering technique (FAST) was performed in-house using a Dr Fritsch GmbH DSP-507, consisting of a vacuum chamber capable of achieving 5×10^{-2} mbar by means of a rotary pump while heating was provided by means of passing a DC current of <4.2 V and <13 kA through die electrodes either side of the powder compact that were connected to a hydraulic press. A schematic drawing of the equipment is shown in Fig. 2.8.

The machine was equipped with instrumentation to record the sintering behaviour including: vacuum gauge; load cell; 6 thermocouples; positional transducer for the electrode (ram) displacement (accuracy ±100 µm); closed loop Hall effect sensor surrounding the electrode bus bars to record the current; voltmeter; and flowmeter for maintaining a dynamic atmosphere of N_2.

Figure 3.2 schematically shows the cylindrical die arrangement used for consolidation of samples. Dies with punch diameters of 20 mm, 40 mm, 60 mm and 80 mm

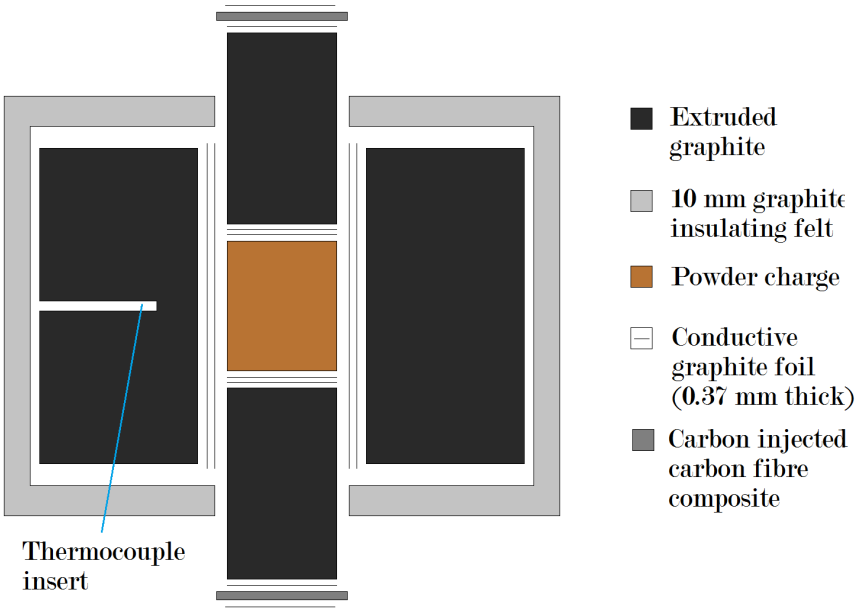

Figure 3.2: Schematic diagram of cylindrical FAST die in cross-section. Punch length was 35 mm, the die walls were 20 mm thickness and the dies were 40 mm in height. The thermocouple was located centrally with respect to the die height and maintained at a depth of 15 mm.

were available. Samples were produced in the range of 5 to 15 mm in height.

Heating of the sample was controlled by automatically varying the current and voltage using a proportional–integral–derivative (PID) controller. The machine was set to operate according to a prescribed programme to give appropriate and safe heating, cooling, sample loading and atmospheric control. Specific conditions are given for each experiment subsequently.

3.2.4 Accelerated isothermal ageing

Due to time constraints, it was necessary to accelerate isothermal ageing processes on consolidated material in order to assess how the microstructure responded to prolonged thermal exposure. By assuming that any changes in microstructure were governed by diffusion processes, an Arrhenius relationship may be used to express the diffusion coefficient D of the process as a function of temperature:

$$D = D_0 \exp\left(\frac{-Q}{kT}\right) \tag{3.1}$$

where D_0 is an experimentally derived diffusion coefficient, Q is the activation energy of diffusion, T is the absolute temperature, and k is the Boltzmann constant ($1.38 \times 10^{-23}\,\mathrm{J\,K^{-1}}$).

Comparing two different temperatures and assuming that D_0 is independent of temperature for small changes in temperature [80]:

$$D_1 = D_0 \exp\left(\frac{-Q}{kT_1}\right) \text{ and } D_2 = D_0 \exp\left(\frac{-Q}{kT_2}\right) \tag{3.2}$$

Taking logs and equating for D_0:

$$ln(D_1) + \frac{Q}{kT_1}1 = ln(D_2) + \frac{Q}{kT_2} \tag{3.3}$$

Which may be re-arranged to

$$ln\left(\frac{D_2}{D_1}\right) = \left(\frac{Q}{k}\right)\left(\frac{1}{T_1} - \frac{1}{T_2}\right) \tag{3.4}$$

So the rate of change in the diffusion coefficient, ΔD is given by:

$$\Delta D = \exp\left(\left(\frac{Q}{k}\right)\left(\frac{1}{T_1} - \frac{1}{T_2}\right)\right) \tag{3.5}$$

For Cu, Q for self-diffusion is $\sim 3.51 \times 10^{-19}\,\mathrm{J}$ [80, 81] so that applying Eq. 3.5 shows that an increase of 10 °C is approximately equivalent to doubling the diffusion rate, in the range 280 to 400 °C. This approach allows accelerated ageing to be performed by halving the exposure time for every 10 °C temperature increase.

3.3 Sample preparation

3.3.1 Powder materials

Powders were analysed using secondary electron microscope (SEM) (for powder size, morphology and microstructural analysis), microhardness and X-ray diffraction (XRD). For XRD, powders were randomly sprinkled on a Si substrate. To obtain samples for SEM characterisation of surface morphology and particle size, the powders were distributed on a carbon sticky pad on a stub. To ensure a random distribution of the particles, a tapping method was used to obtain samples from 10 ml Eppendorf tubes.

For microhardness and microstructural analysis, the samples were cold mounted with Struers Specifix-20 epoxy resin inside 12.5 mm diameter sections of Cu pipe and allowed to cure over 24 hours. The powders were then ground and polished as per the polishing procedure below.

3.3.2 Consolidated materials

Sectioning

Samples were sectioned according to the required dimensions by a combination of waterjet cutting (Global Jet Model 1212 with a position tolerance of 0.05 mm and cut width of ∼0.8 mm), and gravity fed diamond slow saw (Buehler IsoMet low speed saw with a position tolerance of 0.005 mm and a cut width of 0.3 mm) to reduce sample damage away from the waterjet cuts.

Polishing procedure

As with many composite materials, the properties of hard particles in a soft matrix raised difficulties for surface preparation, and a bespoke preparation procedure was developed.

Grinding:

- 12 s for two perpendicular grinds on 320, 600, 1200 grit SiC grinding papers

- 20 s for two perpendicular grinds on 2500 grit SiC paper
- 40 s for two perpendicular grinds on 4000 grit SiC paper

Polishing:

- 1 min manual polishing with Struers DP-Suspension 3 µm polycrystalline diamond suspension on MetPrep Trounoire cloth
- 1 min manual polishing with Metprep 1 µm polycrystalline diamond suspension on MetPrep Trounoire cloth
- 1 min minute manual polishing with Struers DP-Suspension 0.25 µm polycrystalline diamond suspension on MetPrep Trounoire cloth
- 1 min manual polishing with Struers OP-S NonDry, 0.04 µm colloidal silica suspension on MetPrep Chemicloth followed by 2 minute of manual polishing on the same polishing cloth with de-ionised water

Between each polishing step the samples were cleaned for 2-3 minutes in de-ionised water in an ultrasonic bath to remove the polishing media from the sample surface.

3.3.3 Focused ion beam liftout

Samples were prepared for transmission electron microscope (TEM) imaging by the focused ion beam (FIB)-liftout technique from powder and consolidated samples [82]. Initial trenching and thinning of a foil to ∼1 µm thickness was performed using a FEI FIB200 microscope. Trenches were cut to a depth of ∼12 µm with a beam current of 5000 pA 2 µm either side of a deposited Pt layer of 20 µm×2 µm×1.5 µm depth. The edge of the trench was then polished at 3000 pA and 1000 pA using Ga ions, gradually cutting in until the foil was thin enough, shown in Fig. 3.3(a) with the polished face of the liftout shown in Fig. 3.3(b). The foils were lifted out using a Kleindiek micromanipulator in a Zeiss Auriga dual-beam SEM-FIB microscope. Foils

were bonded to an ion-polished, flat surface on a Mo grid by Pt deposition over the joint, as shown in Fig. 3.3(c). Thinning was undertaken by progressive reductions in the beam current of a 30 keV ion beam until at 7 keV using the SEM secondary electron (SE) signal the sample was partially electron transparent. Final polishing was completed with the ion beam reduced to 2 keV and 200 pA until the sample was transparent to electrons of 5 keV using the SEM SE signal, as shown in Fig. 3.3(d).

3.4 Characterisation techniques

3.4.1 Optical microscopy

Optical microscopy was undertaken using a Reichert Polyvar Met instrument, operated in bright field. Optical microscopy was used for initial inspection of polished materials and particularly for examination of undesirable Fe-based inclusions or CuO/Cu_2O particles, which had a significant contrast. However, the low magnification available was insufficient for the majority of useful microstructural investigations.

3.4.2 Scanning electron microscopy

SEM was used extensively, with all imaging and analysis undertaken using a Zeiss Merlin unless otherwise stated. An accelerating voltage of 5 keV was used throughout for imaging, at a working distance of 8.0 mm and a probe current of 500 pA. SE imaging used an Everhart-Thornley detector and an In-Lens SE detector; all SEM figures presented in this thesis show SE-imaging, as, in general, backscattered electron imaging did not provide additional useful information. Grain size measurement was performed using a linear grain boundary intersection approach at angles of 0°, 30°, 60° and 90° across the image.

Energy dispersive X-ray spectroscopy

Energy dispersive X-ray spectroscopy (EDS) was performed on the Zeiss Merlin equipped with an Oxford Instruments X-Max^n 150 mm^2 silicon drift detector. This

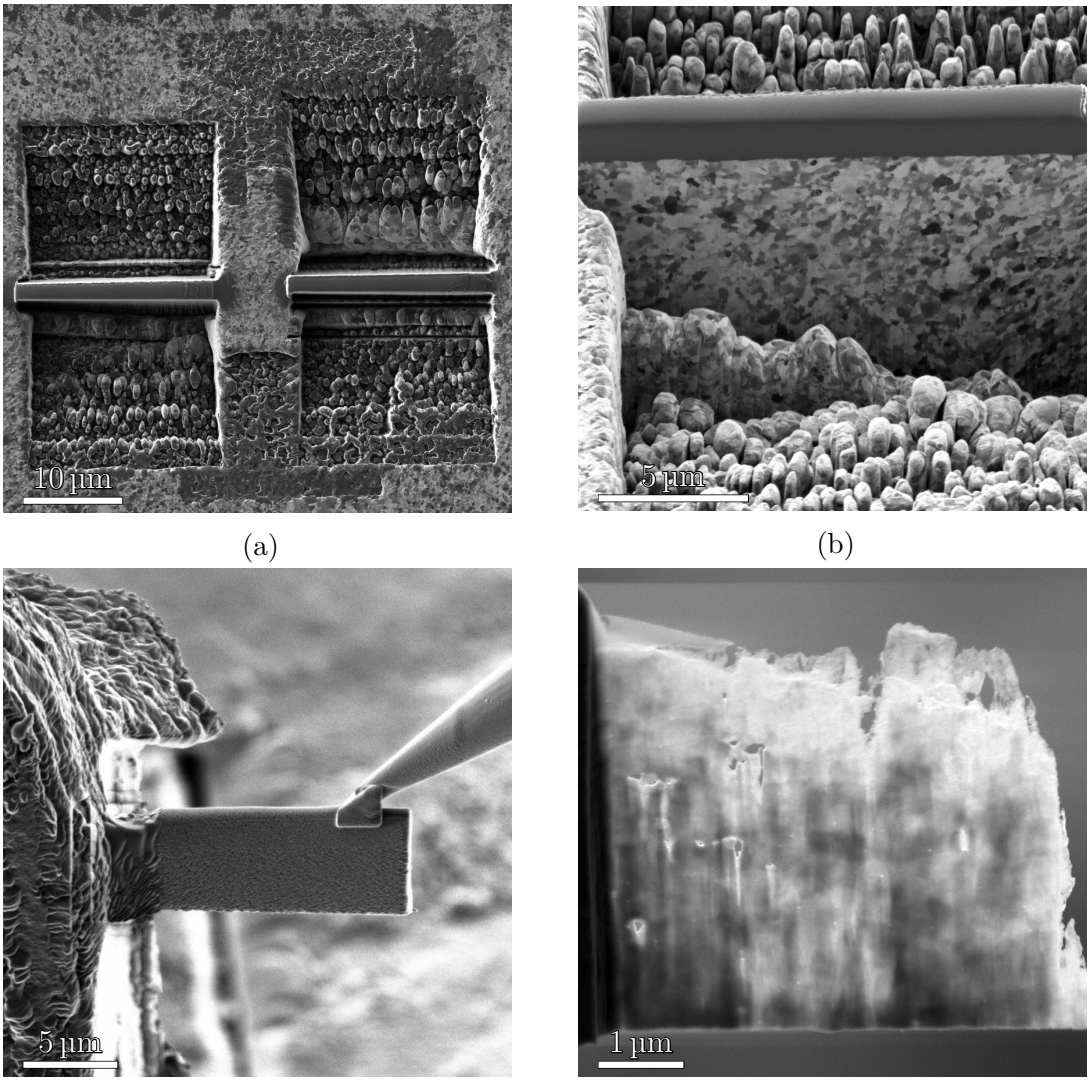

(a) (b)

(c) (d)

Figure 3.3: Stages of FIB liftout for TEM sample preparation; **(a)** cut trenches and thinned foil prior to liftout (FIB-SE micrograph), **(b)** foil surface following thinning to 1 µm (FIB-SE micrograph), **(c)** bonding of foil to polished Mo grid using Pt with micromanipulator attached (SEM-SE micrograph), and **(d)** SEM-SE micrograph at 5 keV in partial transmission, showing electron transparency of liftout.

allowed for elemental mapping, line profiles and point analysis of polished surfaces. Excitement of the sample was using a beam of 5 keV, except for Ti-containing samples where 10 keV was used, with a probe current of 1000 pA.

Analysis of EDS data was undertaken using Oxford Instruments Aztec software. Background subtraction and peak deconvolution summed the contributions of the α and β peaks above the background where necessary. To increase contrast in maps, K and L line contributions were summed manually and as indicated in each figure. All EDS maps presented are shown in the inverse i.e. dark represents a higher count/concentration.

Electron backscatter diffraction

Electron backscatter diffraction (EBSD) was performed using a JEOL JSM-6500F equipped with a field emission gun. EBSD maps were obtained at an accelerating voltage of 15 keV, a working distance of 15 mm and were tilted to an angle of 70° with respect to the phosphor screen of the camera. Typical maps were taken over a 40 µm square region, with a point spacing of 60 nm which was determined as the minimum for the excitation conditions by simulation of the interaction volume. Maps were obtained and analysed using EDAX Inc, TSL OIM software. Individual grains were identified by a misorientation angle of >5° with at least three points per grain and a confidence index of >0.1, coupled with an image quality index >100. EBSD data was used to verify grain size measurements and to examine texture.

3.4.3 Transmission electron microscopy

TEM characterisation was used for analysis of fine scale microstructure and particles. The specific techniques used with the TEM or scanning transmission electron microscope (STEM) are outlined below. Two TEMs were used for analysis:

Oxford-JEOL 2200MCO - a dual-aberration corrected field emission gun (FEG) TEM/STEM system equipped with a high angle annular dark field

(HAADF) detector, an Oxford Instruments X-max^n 100 mm^2 energy dispersive X-ray detector and an Omega-type electron energy filter with a Gatan 4k by 4k Ultrascan CCD camera.

JEOL ARM 200F - a spherical aberration corrected cold-FEG TEM/STEM system equipped with a JEOL 100 mm^2 Centurio EDS detector and Gatan GIF Quantum 965 ER with Dual electron energy loss spectroscopy (EELS) and energy filtered transmission electron microscopy (EFTEM) capabilities.

All analysis with these instruments was undertaken at 200 keV.

Energy-filtered transmission electron microscopy

EFTEM allows for the analytical examination of the constituent elements of a sample. Low-loss region EFTEM was extensively used for analysis of Y and Ti-containing particles, on account of their relatively defined energy loss edges. The Y $N_{2,3}$-edge is located at a loss of 26 eV, the Ti $M_{2,3}$-edge is at a loss of 35 eV [83].

Low-loss EFTEM mapping was completed using the Oxford-JEOL 2200MCO system, using a slit width of 3 eV and a step size of 1 eV for energy losses from 10 to 80 eV which covered the Y and Ti edges described above.

Elemental maps were extracted using Gatan Digital Micrograph's multiple linear least squares (MLLS) approach. The Y reference signal was taken from large Y_2O_3 particles whose thickness equalled that of the foil and the Ti reference signal was obtained from a Ti standard. Following MLLS analysis, the residuals were examined to ensure that no information was lost. Thickness, t, of the region of interest was measured using $t = \lambda \ln(I_t/I_0)$ where λ is the wavelength, I_t is the intensity of the total spectra and I_0 is the intensity of the zero-loss peak, the thickness is expressed as a fraction of the mean free path (mfp), which for Cu was taken as 39 nm [84]. This method introduce a relative error of ± 10 % which is carried over to all further analysis such as volume estimation. Prior to undertaking EFTEM mapping, the thickness of

the region of interest was evaluated and if greater than $\sim 0.5 \pm 0.2$ mfp the region was not characterised. All EFTEM maps presented are shown in the inverse i.e. dark represents a higher concentration of the element of interest.

STEM imaging

STEM imaging was performed using the JEOL ARM 200F, using annular dark field (ADF) and HAADF detectors; ADF covers a smaller angular scattering range, allowing for diffracted beams to contribute to the image. STEM imaging was also undertaken using a HAADF detector on the Oxford-JEOL 2200MCO exclusively for imaging in association with EDS.

Energy dispersive X-ray spectroscopy

EDS in the STEM was undertaken using the Oxford-JEOL 2200MCO system described above. Data acquisition was undertaken with Oxford Instruments Aztec software, equipped with drift correction. Data analysis was undertaken on the same software, as for the SEM-EDS analysis.

Electron energy loss spectroscopy

EELS spectrum were acquired on the JEOL ARM 200F system. EELS spectrum were obtained with a dispersion of 0.25 eV at a camera length of 2 cm. Low-loss and core-loss regions were collected at a dispersion of 0.25 eV/channel from 10 to 500 eV and 400 to 900 eV respectively. To maximise output intensity, probe size 3C was used with condenser lens aperture 2 set at 3 to prevent sample damage. A convergence angle of 40 mrad and a collection angle of 60 mrad were used with an aperture of 2.5 mm.

Analysis of EELS images was undertaken using the HyperSpy library for Python. Principal component analysis was used to identify the non-noise components of the EELS spectrum and blind source separation was used to show a more physical

Table 3.2: Major electron loss edges for elements of interest [83].

Element	Edge	Electron-loss (eV)
Y	$N_{2,3}$	26
Ti	$M_{2,3}$	35
Fe	$M_{2,3}$	54
Y	$M_{4,5}$	157
Ti	L_3	456
Ti	L_2	462
O	K	532
Fe	L_3	708
Fe	L_2	721

representation. Extraction of the respective peaks of Y, Ti, Fe, O, with the major edges given in Table 3.2, was completed by multiple linear least squares fitting using the EELS standards library and compared with the blind source separated factors for confirmation.

In the case of Y $N_{2,3}$-edge in low-loss spectroscopy, due to overlap with the plasmon excitation peak, blind source separation was used to identify the Y components.

All EELS maps presented are shown in the inverse i.e. dark represents a higher concentration of the element of interest.

3.4.4 Atom probe tomography

Atom probe tomography (APT) was used for analysis of one sample, and was obtained using an Imago local electrode atom probe 3000X HR system. The sample preparation of electropolishing and FIB polishing and the APT run was completed by Dr Andrew London of the Department of Materials, and data analysis was completed collaboratively.

3.4.5 X-ray diffraction

X-ray diffraction was undertaken using a Bruker D8 Advance system with a Cu Kα source between 2Θ angles of 10° and 90°.

Crystallite size

An approximation for crystallite size may be made according to the amount of line broadening at the full width at half maximum (FWHM), β, observed for a particular X-ray peak using the Scherrer formula [85]:

$$\beta = \frac{K\lambda}{L\cos\theta} \tag{3.6}$$

where K is a constant for shape factor (close to 1), λ is the wavelength of the incident X-rays, L is the crystallite size and θ is the Bragg angle.

Rietveld refinement

Further evaluation of crystallite size and lattice strain can be made using Rietveld refinement to calculate broadening across a whole XRD profile. Rietveld refinement was undertaken using the Maud program [86], using a Marquadt least squares fitting approach in stages of fitting as follows:

1. Refine background and instrument broadening
2. Refine for phase concentration
3. Refine for microstructural features (lattice strain, cyrstallite size)

3.5 Physical properties

3.5.1 Chemical analysis

Chemical analysis of samples was obtained using inductively coupled plasma mass spectroscopy (for Al, B, Cr, Cu, Fe, Mg, Mn, Ni, P, Pb, Sn, Ti, V, Zr, Zn), inductively coupled plasma optical emission spectroscopy (for Y) and infrared inert gas fusion analysis (for O). All chemical analysis was completed by AMG Superalloys UK Ltd, Analytical Services, of Rotherham.

3.5.2 Laser flash analysis

Laser flash analysis (LFA) was used to obtain measurements of thermal diffusivity, α, by flashing a laser pulse of known energy on one face of a disc of material and measuring the time for a thermal response on the opposite face of the disc [87]. Calculations of the specific heat capacity, C_p, may be made by:

$$C_p = \frac{Q}{L\rho T_m} \tag{3.7}$$

where Q is the known pulse energy on the incident face, L is the sample thickness ρ is the sample density, and T_m is the maximum thermal response temperature at the opposing face. This allows determination of the thermal conductivity, κ according to:

$$\kappa = \alpha C_p \rho \tag{3.8}$$

LFA was undertaken by Dr Shahin Mehraban of the MACH1 centre at Swansea University using a Netzch LFA 457 MicroFlash on a ⌀12.5 mm sample of 3.0 mm thickness with a sputtered graphite coating to ensure efficient absorbance of the laser energy.

3.6 Mechanical properties

3.6.1 Microhardness

Room temperature microhardness measurements were obtained using a Wolfson Instruments 402MVD Microindentor with a Vickers indenter diamond tip. The indenter tip was loaded with 100 g and allowed to dwell for a period of 20 s. A minimum of 10 indentations per sample were made; in bulk materials these were made from a surface finished to at least a 1 µm polish in a 2 by 5 array with spacing of 250 µm. Mean values and standard deviations are given for all measurements. In powder materials, the indentations were made on the polished surface (finished as

above) in at least 10 powder particles, though owing to the variation in particle size and the epoxy mounting medium (see Section 3.3.1), an element of operator bias was included where small particles may be untested, with the size of the smallest testable particle depending on the alloy composition and condition. Microhardness measurements were converted from units of HV to MPa throughout.

3.6.2 Tensile testing

Tensile testing was undertaken by two methods. First ASTM E8 specification tensile tests were performed by Westmoreland Mechanical Testing and Research Ltd of Banbury, Oxfordshire. Cylindrical samples were prepared to the geometry shown in Fig. 3.4(a) by lathe, and testing was undertaken at a strain rate of $0.015\,\mathrm{min}^{-1}$ until yield, and then at $0.4\,\mathrm{min}^{-1}$, strain was measured using a dual averaging extensometer.

Small dogbone specimens were prepared by waterjet cutting and tested by Mr. André Nemeth using an Instron ETMT8800 electrothermal mechanical testing system (ETMT) which allows joule heating of samples under testing conditions from room temperature to elevated temperature tensile tests >1000 °C. Strain was measured using video recording and digital image correlation of a speckle pattern painted on the sample surface.

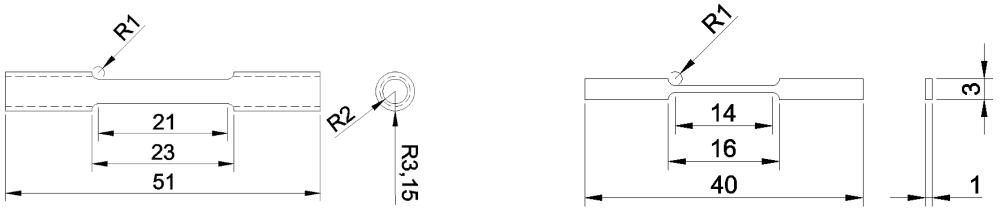

(a) (b)

Figure 3.4: Tensile test geometries, all dimensions in mm, **(a)** ASTM specification TETRE 160 round specimen with threaded ends, **(b)** ETMT dogbone for vice grip.

3.6.3 Small-punch testing

Small-punch testing was used to investigate creep behaviour, according to ASTM E 643-15 working standard [88]. In this procedure, a thin disc of diameter 8.0 ± 0.5 mm and thickness 500 ± 5 µm is loaded using a 4 mm diameter spherical indenter and displacement of the opposing sample face measured with respect to time. Samples were prepared by cutting to a thickness of ∼600 µm using a gravity-fed slow-saw and then thinned by grinding with 600 grit and finished to 1200 grit SiC paper. To ensure parallel surfaces were maintained, the discs were thinned using a heavy brass polishing mount with isolated sample feed.

The small-punch testing was carried out using the MeT1 system at the Culham Centre for Fusion Energy (CCFE), manufactured by Phoenix Calibration and Service Ltd for the specific application. A schematic drawing of the set-up is shown in Fig. 3.5: the sample was clamped between the upper and lower dies by means of a threaded overlap of the top die to the bottom die to provide a constant clamping force which was set by applying a pre-set torque.

The sample, dies and punch were then heated by means of infra-red heaters surrounding the set-up. The temperature of the sample was maintained using a PID controller using thermocouples located in the upper die, lower die and above the punch tip. To prevent oxidation of the sample at elevated temperature, the set-up was in a controlled atmosphere chamber under flowing Ar.

The procedure used for creep testing was to heat the sample to the desired test temperature at a rate of $5\,^{\circ}\mathrm{C\,min^{-1}}$, and then allow for stabilisation by holding for 1 h. Once stabilised, a constant hydraulic load was applied to the indenter (maintained by a PID controller), and the displacement of the lower plane of the sample disc was measured by a low-friction alumina probe connected to a positional transducer which was free to move in the vertical plane. Temperatures of the upper and lower dies, and

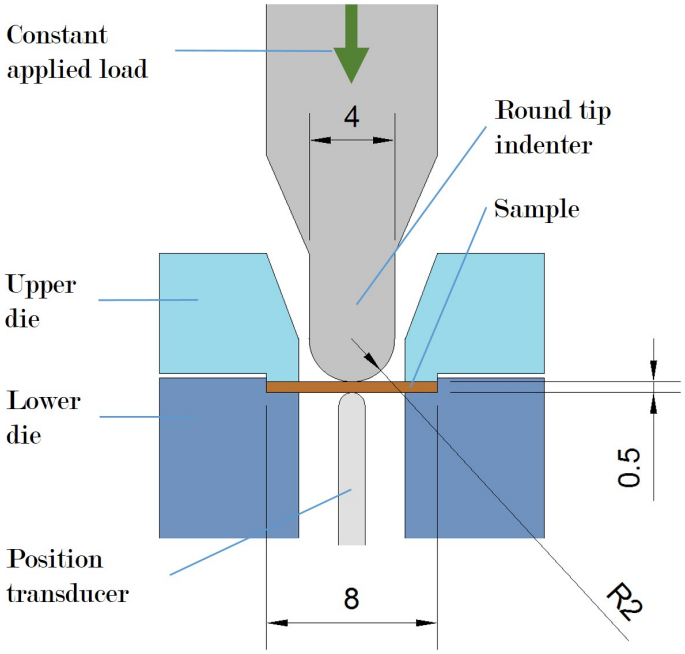

Figure 3.5: Schematic diagram of cylindrical cross-section of small-punch testing set-up, all dimensions shown in mm.

the indenter were measured by thermocouples. All data was recorded at a rate of 1 Hz for the full duration of the test.

All creep testing was undertaken by Dr. Mark Richardson of UKAEA on-site at CCFE.

Chapter 4

Dissolution and re-precipitation of Y_2O_3 in Cu

4.1 Introduction

Unlike the much more heavily studied Fe-based oxide dispersion strengthened (ODS) alloys, comparatively little information was available for the behaviour of Y_2O_3 and Cu during mechanical alloying (MA), and if the same Y_2O_3 fracture or dissolution and re-precipitation behaviour might be readily achieved. Instead, as described in the literature review, commercial processing routes to obtain Cu-ODS alloys rely upon chemical reaction during processing, such as internal oxidation or direct reaction of two elements in solution (see Section 2.5.1). To address the perceived inhomogeneity and coarse microstructural scale of alloys obtained by these methods, the potential of room temperature MA was explored. The principal differences of MA Cu compared with MA Fe-based ODS alloys is that the Cu is either only lightly alloyed or is unalloyed, it is face-centered cubic (fcc) rather than body-centered cubic (bcc), and it has a significantly lower melting point. These effects combine to suggest that Cu will provide a much lower degree of work-hardening and dislocation accumulation, which can then be expected to lead to significantly different milling behaviour.

4.2 Planetary ball milling

Planetary ball milling is a high energy milling process that utilises the collisions between milling media, the pot walls and the powder to cause large deformations of the material and work-hardening leading to particle fracture (see Section 2.5.2). In conjunction with simultaneous cold welding, across-powder mixing of the alloying constituents occurs [61]. The hypothesis to be investigated is that the high energy nature of the collisions may allow metastable states of solution of Y to be reached in Cu as observed in other alloy systems, such as in Fe and Y_2O_3 containing ODS alloys [89–91].

4.2.1 Milling of Cu

Consistent with previous reports, it was soon found that Cu (exceeding 99.5% purity) did not refine during milling because of its high ductility, so that cold-welding dominated over work-hardening and fracture of the powder, leading to large (>1 mm diameter) spherical, hollow powder particles [92, 93]. This did not prevent the formation of highly-deformed material within these shells/particles with ultra-fine grain sizes (<200 nm mean diameter) [39], but the hollow particles presented difficulties for effective subsequent consolidation owing to the disconnected and isolated nature of the internal pores. The formation of ultra-fine grained but larger Cu powder particles during room temperature milling resulted from several simultaneous processes (see Section 2.5.2) including the formation of stacking faults and twins that inhibit dynamic recrystallization, promoting high dislocation densities that combine to form sub-grain and grain boundaries [62, 93–95]. To obtain both an ultrafine grain size *and* a fine particle size powder a process control agent (PCA) might be considered. A PCA reduces the welding between powder particles by acting as a lubricant or surfactant [60] - however, PCAs also have the deleterious effect of reducing the energy imparted during collisions, slowing or preventing the dissolution/break-up of the

alloying additions [96, 97]. Therefore, milling was undertaken without the aid of a PCA.

Figure 4.1 shows the hardness of milled Cu (99.5% purity) with increasing milling time. Prior to milling, the as-received powder had a mean hardness (1020 ± 290 MPa), approximately double that expected for similar purity, annealed Cu (approximately 490 MPa [59]), due to Hall-Petch strengthening from the fine grains, estimated at 130 ± 60 nm, resulting from the rapid cooling during gas atomisation manufacture of the powder. The mean crystallite size was measured by XRD at 173 ± 23 nm, which agreed well with the Hall-Petch estimates based on the powder hardness. An initial rapid increase in hardness to ∼2000 MPa after a few minutes of milling was likely associated with an increase in the dislocation density. Interactions between dislocations led to entanglement and many were unable to slip past one another. Following this, a steady state was expected where the rate of work-hardening and fracture equals that of the cold welding and the dislocation density (and hardness) cannot be increased further [62, 91, 98]. However, in this instance there was a reduction in hardness after 24 h. This was likely due to the increasing size of the powder particles themselves (>3 mm diameter), as shown in Fig. 4.1. With increasing particle size, there was more variation in the hardness, contributing to a range of hardness for the milled powder that is expressed as a standard deviation here. In this regime there may be some local recovery in the internal regions of the particles as these regions were no longer exposed to the collision induced strains, but still receive significant thermal energy from the repeated collisions and friction between the milling pot and media, and the powder particles [99]. Milling temperatures of >200 °C have been recorded and help promote recovery in central regions of the larger particles [92, 93, 99].

The powder morphology changes observed in Fig. 4.2(a) show the initial formation of flakes within the first hour, where cold welding exceeded the rate of fracture resulting from work-hardening [93, 100]. With progressive milling, the flakes cold

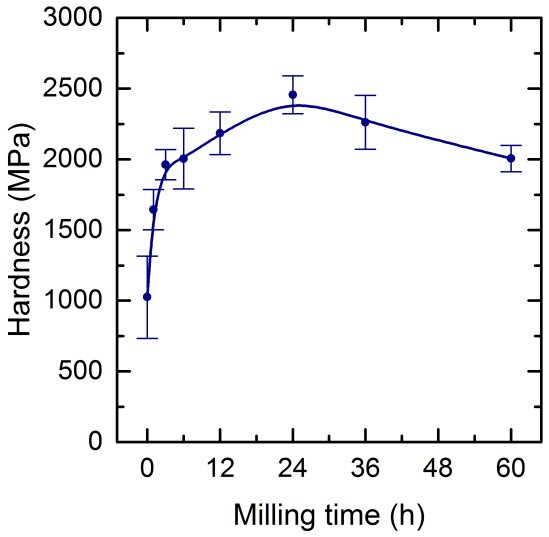

Figure 4.1: Effect of milling time on Vickers microhardness of Cu powder (99.5% purity) during planetary ball milling.

welded (Fig. 4.2(b)) leading to the formation of large spheres (Fig. 4.2(c)).

4.2.2 Milling of Cu-Y_2O_3

It is the aim of this work to determine a processing route to disperse and refine Y_2O_3 within a Cu matrix, however, as may be seen in the Cu-Y phase diagram in Fig. 4.3, Y is largely immiscible in Cu thus preventing use of conventional ODS production routes (such as internal oxidation) that involve a liquid phase, unless rapid solidification routes are used that might allow for some meta-stable solid solution formation. Therefore MA is proposed as a method to introduce Y_2O_3 directly into the Cu and the associated hardening may also provide a route to improve Cu deformation behaviour during milling, since the addition of Y_2O_3 may provide dislocation pinning and facilitate an increase in the work-hardening capacity. A more defective meta-stable Cu matrix may in turn help to promote the dissolution, severe fragmentation or disassociation of the Y_2O_3.

In order to elucidate whether Y_2O_3 may be dispersed/dissolved in Cu during MA,

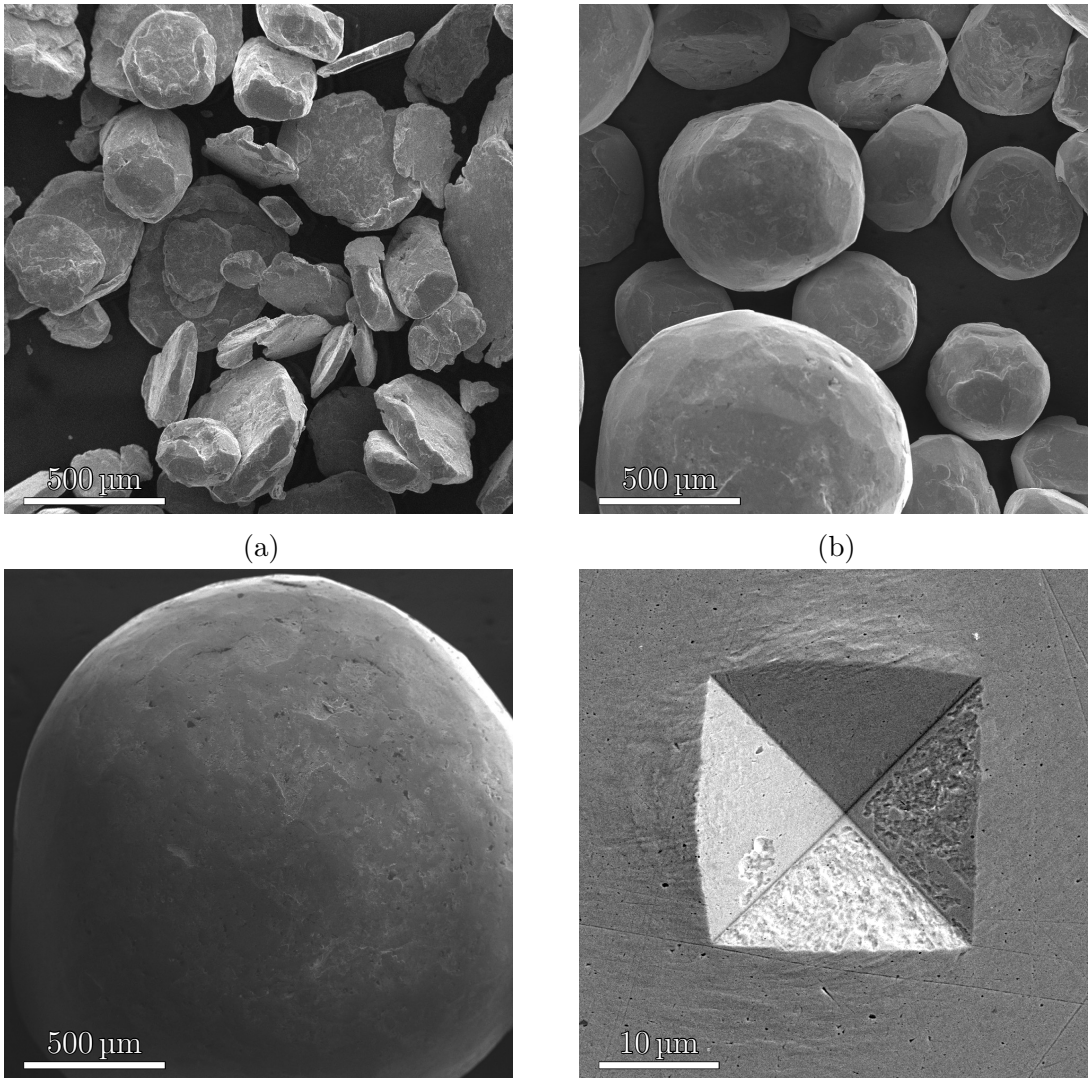

(a) (b)

(c) (d)

Figure 4.2: Secondary electron micrographs of Cu (99.5% purity) powder after milling as a function of time, **(a)** 1 hour, **(b)** 12 hours, and **(c)** 24 hours. **(d)** Vickers microhardness indent in the powder showing pile-up at the top and left edges.

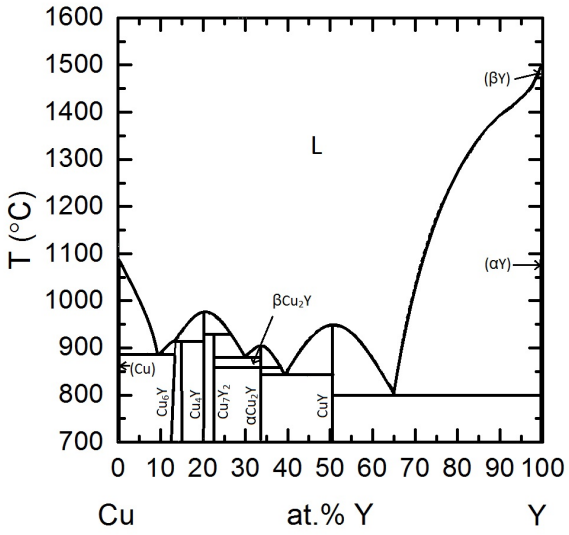

Figure 4.3: The Cu-Y phase diagram, reproduced from [101].

and the mechanism by which this is achieved, high purity Y_2O_3 (99.999%) with a powder particle diameter in the range of 20 to 40 nm and an average crystallite size of 23.5 ± 0.3 nm (measured from peak broadening in XRD analysis) was added to the milling pot under an Ar atmosphere in various weight percentage (wt.%) additions at a constant charge weight of 80.0 ± 0.1 g.

Effect of milling time

Milling time is an important parameter in MA: short milling times do not allow complete distribution and break-up/dissolution of the Y_2O_3, long milling times increase the risk of contamination from the milling media, milling atmosphere and milling pot material (particularly O and Fe) [61]. Long milling times also risk increasing powder particle size and the formation of hollow spheres as previously described.

The effect of Y_2O_3 fraction in the range 0 to 10 wt % Y_2O_3 with increasing milling time on powder microhardness is shown in Fig. 4.4. The hardness increased with increasing fraction of Y_2O_3 as might be expected when mechanically alloying hard particles in to a ductile matrix. The time taken to reach a steady state was insensitive to

the Y_2O_3 fraction, between 6 to 12 h. Table 4.1 gives the microhardnesses in the plateau region. Increasing the fraction of Y_2O_3 increased the plateau microhardness, either by allowing a higher dislocation density and/or a direct rule-of-mixtures "composite" behaviour; however, the initial hardening rate also increased with increasing Y_2O_3 fraction.

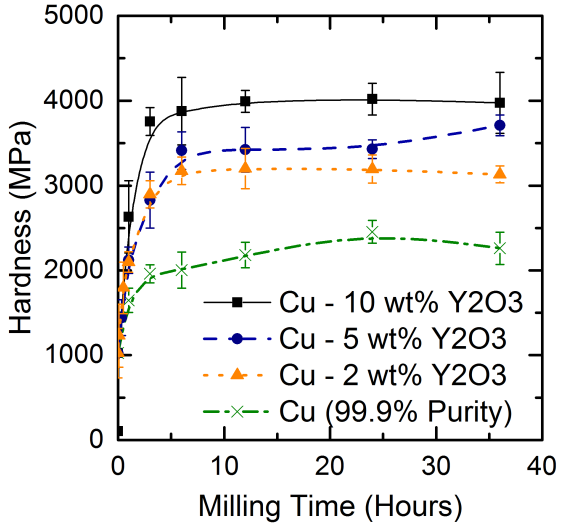

Figure 4.4: Effect of milling time on Vickers microhardness with increasing Y_2O_3 fraction.

Table 4.1: Effect of Y_2O_3 fraction on the initial hardening rate (IHR) (during the first three hours of milling) and the Vickers microhardness in the plateau region beyond 12 hours of MA.

Composition	IHR (MPa s^{-1})	Plateau microhardness (MPa)
Cu (99.9% Purity)	0.08	2220 ± 260
Cu-$2Y_2O_3$	0.16	3180 ± 90
Cu-$5Y_2O_3$	0.16	3540 ± 230
Cu-$10Y_2O_3$	0.30	4000 ± 340

The milled powders were investigated by XRD after 1, 3, 6, 12, 24 and 36 hours of milling. Figure 4.5 shows changes in the crystallite size, lattice strain (calculated using Rietveld refinement, Section 3.4.5) and microhardness for Cu-$2Y_2O_3$ and Cu-$10Y_2O_3$. The Cu-$2Y_2O_3$ hardness stabilised at 3180 ± 90 MPa compared with 4000 ± 340 MPa

for Cu-10Y_2O_3. There was a reduction in the stable crystallite size from 21.8 ± 0.2 nm to 14.5 ± 0.1 nm with the increasing Y_2O_3 fraction. The reduction of crystallite size from the as-received powder (173 ± 23 nm) was similar to the order of crystallite size reduction in a Fe-0.132Y_2O_3 alloy [89], where the crystallite size reduced from 138 nm to ~10 nm. This suggested that the hardness increase was primarily due to a reduction in the effective grain size.

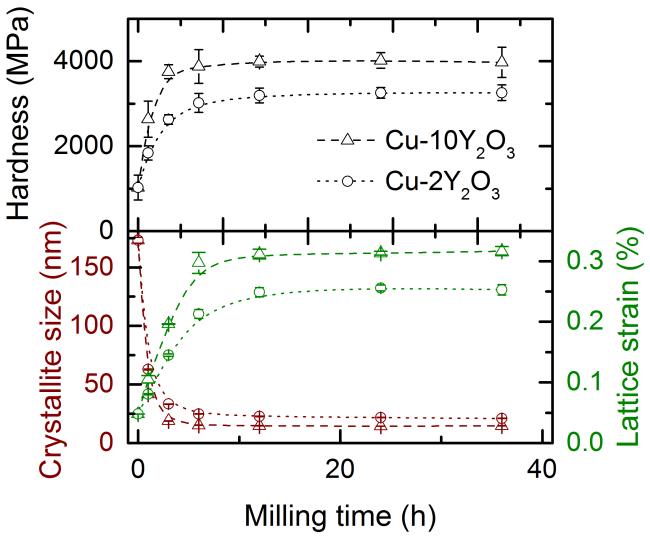

Figure 4.5: Effect of milling time on Vickers microhardness, crystallite size and lattice strain (calculated by Rietveld analysis) of Cu-2Y_2O_3 and Cu-10Y_2O_3 during MA at 250 rpm, in an argon atmosphere with a ball-to-powder weight ratio (BPR) of 10.

Assuming that the crystallite size was equivalent to the grain size in the heavily deformed microstructure, the contribution of grain size reduction to strengthening was estimated as follows. Assuming that the deformed powder microstructures follow the relationship $\sigma_y = 1/3 \times$ hardness [102], the approximation of the yield strength may be compared to the predicted yield strength obtained from the Hall-Petch equation $\sigma_y = \sigma_i + k \times d^{-1/2}$ where σ_i and k are the material properties intrinsic strength and strengthening coefficient respectively, d is the grain diameter. Comparative estimations of the yield strength are summarised in Table 4.2. Both approaches estimated a similar increase in σ_y as the Y_2O_3 fraction was increased from 2 to 10 wt.% Y_2O_3, giving

support to the interpretation that the majority of increased microhardness was due to reduced crystallite size. For comparison, the maximum dislocation density was reached significantly faster than Fe-ODS, at 12 h for pure Cu to Cu-10Y_2O_3 compared with 30 h for Fe-14Cr-10Y_2O_3 [91] for identical MA conditions. In the case of Fe-14Cr-10Y_2O_3 a lattice strain >0.8% was reported, compared with 0.32% for Cu-10Y_2O_3 here (Fig. 4.5). Assuming that the capacity of the metallic matrix to absorb ceramic additions is limited to its maximum work-hardened capacity - its defect capacity - the lower accumulated strain may suggest that there was a lower "solubility limit" for Y_2O_3 in fcc Cu compared with bcc Fe. The defect capacity may be considered to result from the microstrain in the system where a higher induced microstrain improves accommodation of defects, or foreign oxides, as the overall strain can be reduced. Higher work hardening results in higher microstrain of the matrix, and so more accommodation of defects, or ceramic additions. An alternative way to express this is that the higher microstrain makes the material more metastable i.e. shifted from thermodynamic equilibrium. Free energy is released if oxide is dissolved into this metastable structure (a requirement for any microstructural change). On account of their greater workhardening response, bcc materials can achieve greater deviations from equilibrium and thus offer a higher solubility, even in the case of usually insoluble oxides.

Table 4.2: Estimation of the contribution of crystallite size to σ_y for different Y_2O_3 fractions, based on hardness and crystallite size measurements.

	σ_y microhardness (MPa)	σ_y Hall-Petch (MPa)
Cu-2Y_2O_3	1080	770
Cu-10Y_2O_3	1330	940
Difference	250	170
Percentage increase	23.1%	22.1%

From these results, a milling time of 12 hours was selected as an optimum time to reach the plateau of dislocation density for milling conditions of 250 rpm, Ar

atmosphere, BPR of 10, using 10 mm spherical milling media, and with a 20:40 minute on:off milling time (to allow cooling of the powder, milling pot and milling media).

Effect of increasing Y_2O_3 fraction

In order to understand the effect of Y_2O_3 on Cu during milling at lower, more practical Y_2O_3 fractions, further alloys with 0.5 to 2.5 wt.% Y_2O_3 were prepared using the milling conditions above.

Figure 4.6 shows the effect of increasing Y_2O_3 fraction in the range 0 to 10 wt % on powder morphology. With increasing Y_2O_3 fraction, the average particle diameter reduced: at 2 wt.%Y_2O_3, the powder diameter was approximately constant after only 1 hr; conversely, at 5 and 10 wt.%Y_2O_3, the powder diameter continued to reduce with further milling. Consistent with earlier results, the increasing Y_2O_3 fraction increased the maximum dislocation density achievable and altered the balance point between work-hardening and cold welding.

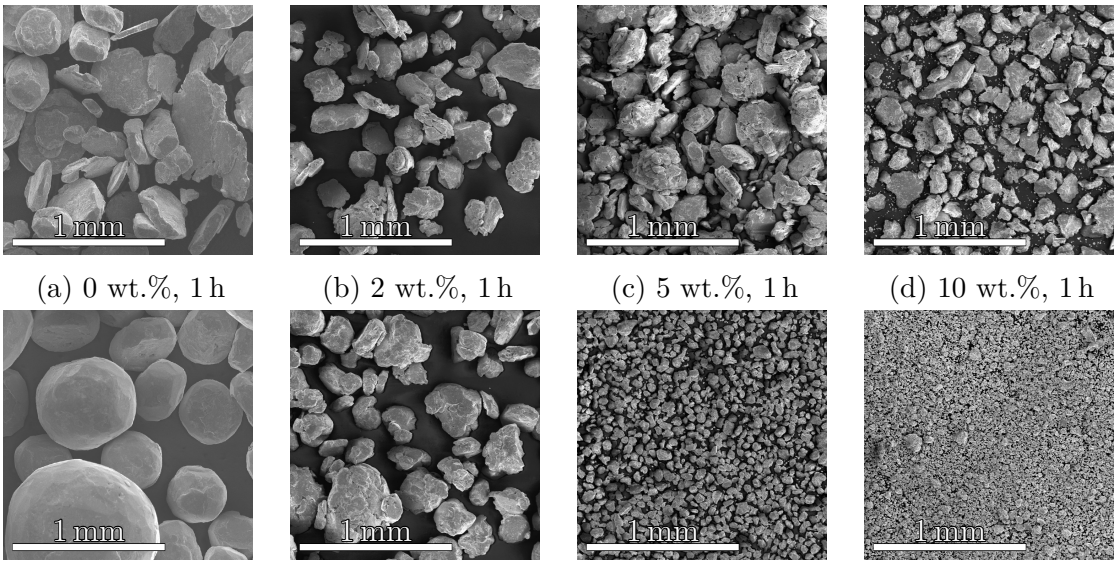

(a) 0 wt.%, 1 h (b) 2 wt.%, 1 h (c) 5 wt.%, 1 h (d) 10 wt.%, 1 h

(e) 0 wt.%, 12 h (f) 2 wt.%, 12 h (g) 5 wt.%, 12 h (h) 10 wt.%, 12 h

Figure 4.6: Secondary electron micrographs of Cu-Y_2O_3 powders after milling for 1 hour and 12 hours at different Y_2O_3 fractions.

Figure 4.7 demonstrates the effect of increasing Y_2O_3 fraction on 12 h milled powders hardness, crystallite size and lattice strain. There was a rapid, 50% increase

in hardness after 12 h for 0 to 1 wt.% additions of Y_2O_3. At higher fractions, there was a reduction in the hardening effect of the Y_2O_3 and a corresponding reduction in the induced lattice strain from 4.8×10^{-4} % in Cu, to 2.55×10^{-3} % at $1Y_2O_3$ to 2.92×10^{-3} % at $2.5Y_2O_3$.

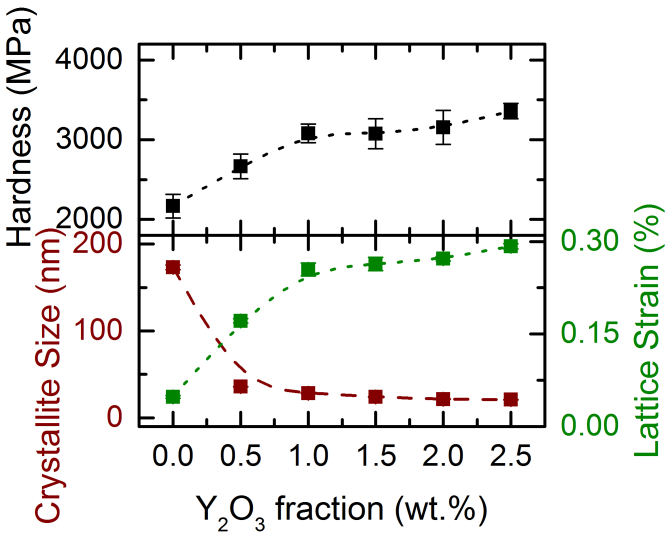

Figure 4.7: Effect of increasing Y_2O_3 content from 0 to 2.5 wt.% on Vickers microhardness, crystallite size and lattice strain (calculated as per Section 3.4.5 from the Cu [111] peak) during MA at 250 rpm for 12 hours.

The crystallite size reduced between 0 and 0.5 Y_2O_3, from 173 ± 3 nm to 35 ± 1 nm, but with a smaller 42% reduction to 20 ± 1 nm on addition of a further $2Y_2O_3$. Taking the approach for the data in Table 4.2, it was suggested that there was again only a limited contribution to strength increase from factors other than a grain size effect. Figure 4.8 shows a plot of calculated yield strength as a function of Y_2O_3 fraction from the measured microhardnesses, the measured crystallite size (using the Hall-Petch relationship), and from the difference between them - equivalent to the work hardening of the 12 h milling procedure. In the situation where the oxide nanoparticle size remained constant with increasing Y_2O_3 fraction, such that only the particle number density increased with volume fraction, the Orowan strengthening model can be applied to allow an estimation of the strengthening provided by an increasing

fraction of 30 nm Y_2O_3 nanoparticles, as shown in Fig. 4.8.

The difference between the estimated yield strength from microhardness and crystallite (from XRD refinement) measurements remained constant at $\sim 315 \pm 62$ MPa, assuming a linear best-fit as the Y_2O_3 fraction increased. This contrasts with the estimated Orowan strengthening effect of the increasing Y_2O_3 particles which at low fractions had limited strengthening, but at higher fractions exceeded the measured difference. This might suggest significant error in the simple assumption that the nanoparticle size was constant for all Y_2O_3 fractions. For example, a single particle size varying from 10 to 40 nm diameter would result in Orowan strengthening contribution varying from 640 to 160 MPa in Cu-2Y_2O_3. Indeed, as shown later, significant refinement of at least some of the Y_2O_3 particles diameter was evident and which can be expected to provide a greater potential for dislocation pinning and thus work-hardening. Whilst this is not an accurate model for the prediction of strengthening afforded by Y_2O_3 additions, it supports the hypothesis that Y_2O_3 particle size reduction is likely to be contributing to the yield strength increase, while the work-hardening contribution is approximately constant for all Y_2O_3 fractions, as shown by an approximately constant difference between crystal size strengthening effects and measured microhardness in Fig. 4.8.

Effect of milling speed

Milling speed is directly linked to the effectiveness of milling through the proportion of collisions of maximum possible energy between milling media [103]. Too high a speed may increase contamination from milling media and pot, whilst too low a speed may not impart sufficient energy for MA to occur, or require such a long time as to allow unacceptable, progressive atmospheric contamination by O. A balance is sought between minimising contamination from the media/pot and atmosphere while maximising the energy of collisions,. Nonetheless interrupted milling is usually

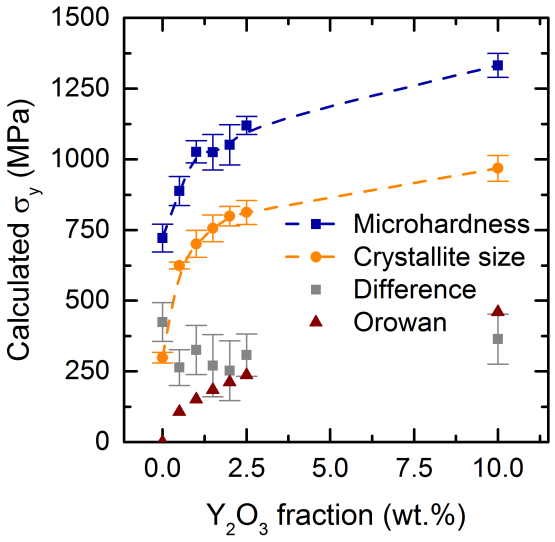

Figure 4.8: Estimated contribution to σ_y from crystallites compared with microhardness derived σ_y for increasing Y_2O_3 content.

needed to manage the temperature of milling and ensure a low temperature to prevent recovery and recrystallisation [61, 99].

Figure 4.9 shows the effect of increasing milling speed on powder hardness and crystallite size in Cu-2Y_2O_3. Increasing the milling speed increased the plateau microhardness and the plateau lattice strain, and reduced the plateau crystallite size. At all milling speeds the plateau microhardness, crystallite size and lattice strain tended to the same, with the notable exception of 150 rpm. The primary effect of increasing the milling speed was to reduce the time required to reach the plateau region.

4.3 Y_2O_3

The milling studies suggested that some of the Y_2O_3 was fragmenting and dispersing in the Cu powder, analogous to behaviours well-known in Fe-ODS alloys.

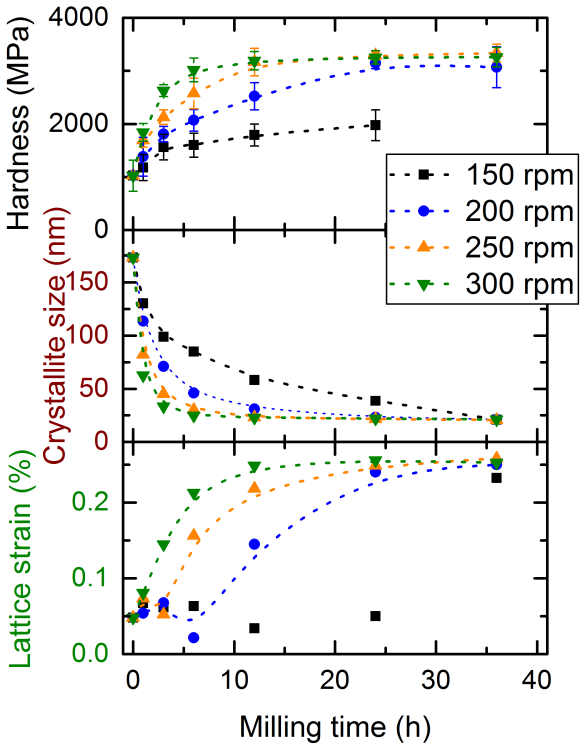

Figure 4.9: Effect of milling speed on Cu-2Y_2O_3 the powder hardness, crystallite size and lattice strain in a Fritsch P6 mill.

4.3.1 Dispersion of Y_2O_3

The Y_2O_3 may be dispersing through the Cu matrix by means of direct dissolution, severe fragmentation and/or amorphisation, or disassociation of the Y and O followed by dissolution. To determine which mechanisms might operate, Y and O distribution Cu-2Y_2O_3 milled for 12 hours was investigated in detail.

Unfortunately, laboratory XRD did not provide much useful information on account of the low fraction of Y_2O_3. Figure 4.10 shows laboratory XRD measurements of Cu-10Y_2O_3 with increasing milling time from 1 to 60 h, where a deliberately high fraction of Y_2O_3 was used to promote XRD detectability. The Y_2O_3 [222] peak shown in Fig. 4.10(a) showed only limited changes in the peak relative intensity, shape and position, in distinct contrast to Fe-ODS alloys where even 10 wt.% Y_2O_3 showed a progressively weakening Y_2O_3 peak, eventually becoming undetectable by both X-ray and neutron diffraction [90, 91]. Nonetheless, despite the weaker changes, the relative peak intensity above the background reduced by ∼30% over 60 h, which assuming no preferred orientation, might suggest that the fraction of Y_2O_3 of a detectable size was reducing. There was no corresponding peak broadening as shown by the FWHM data in Fig. 4.10(b). A corresponding peak broadening would suggest that the Y_2O_3 was reducing in crystallite size simultaneously as implied by the Scherrer formula, Eq. 3.7. However, laboratory X-ray sources are generally insufficiently energetic and spectra too noisy to resolve and quantify any subtle peak broadening variations.

Figure 4.11(a) shows a typical microstructure of Cu-2Y_2O_3 powder with 20 to 40 nm Y_2O_3 particles appearing dark due to atomic number contrast. Electron channelling contrast revealed an ultrafine grained microstructure with grains of approximately the same size as the particles (∼20 nm), which corresponded well with the calculated crystallite size from the XRD traces in Fig. 4.7 of 21.5 ± 0.2 nm. The particles had a mean diameter of 22.6 nm with a mean inter-particle spacing of 210 nm. Assuming all the particles had a mean diameter of 22.6 nm and were homogeneously distributed,

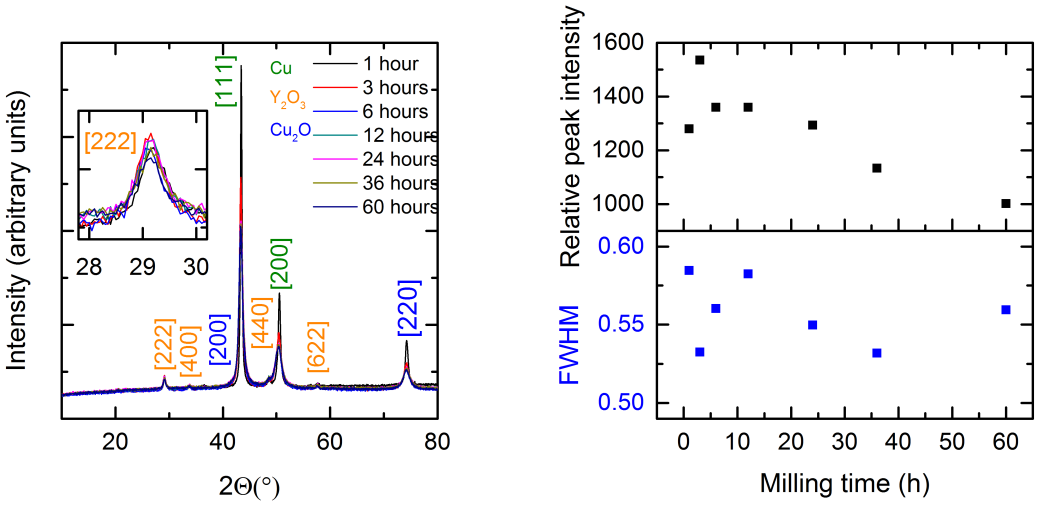

(a) (b)

Figure 4.10: **(a)**XRD of Cu-10Y_2O_3 with increasing milling time, with inset detail of the Y_2O_3 [222] peak. **(b)** Variation in the peak intensity above the background and peak FWHM with increasing milling time from laboratory XRD of Cu-10Y_2O_3, obtained from analysis of the Y_2O_3 [222] peak from 27 to 32° shown in part inset in (a).

and knowing the volume fraction, the expected mean inter-particle spacing would be 14.3 nm [19]. The difference between measured and expected inter-particle spacing suggests a large fraction of the added Y_2O_3 particles were not resolved by electron channelling contrast. Figures 4.11(b) to 4.11(d) show SEM-EDS maps of Cu-2Y_2O_3 with a typical density of 20 to 40 nm particles. It was not possible to obtain chemical information on all particles and only those with diameters >40 nm showed resolvable Y and O presence. Point analysis of 18 distinct particles revealed a mean Y:O ratio of 0.56 ± 0.24, with a median Y:O ratio of 0.65 ± 0.24 suggesting that these particles had a composition consistent with Y_2O_3, but with some significant outliers, likely due to matrix contributions within the interaction volume.

In order to understand the changes in the Y_2O_3 during milling without resorting to neutron diffraction or high intensity X-ray sources, it was necessary to examine the microstructure by higher resolution techniques. Therefore TEM lamella were prepared using the FIB liftout technique [82], directly from powder particles as shown

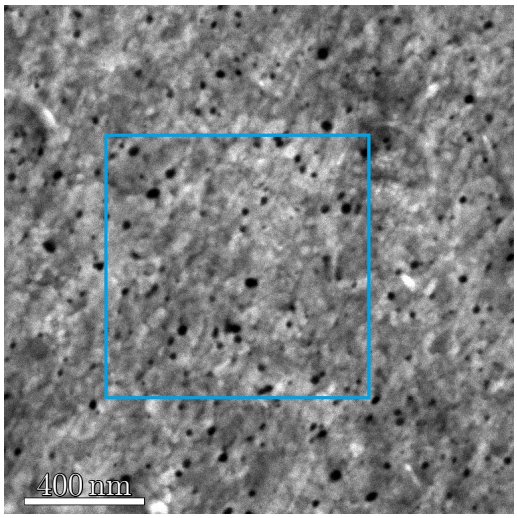

(a)

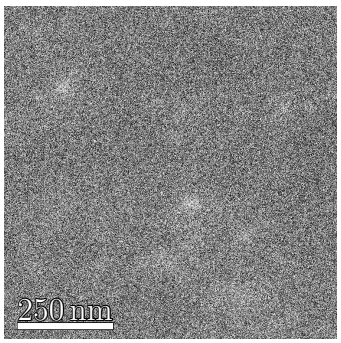

(b) Cu L

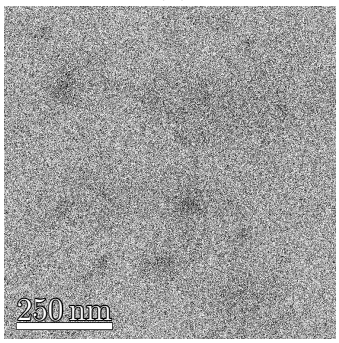

(c) O K

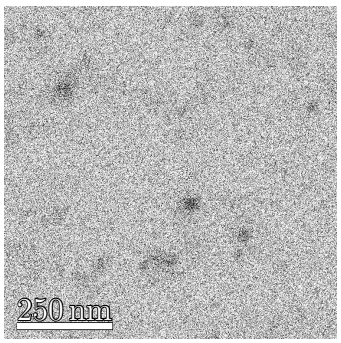

(d) Y L

Figure 4.11: SEM-EDS analysis of Cu-2Y_2O_3 milled powder. **(a)** Secondary electron micrograph of powder showing the region of the EDS map. **(b)** Inverse Cu L map. **(c)** Inverse O K map. **(d)** Inverse Y L map.

in Fig. 4.12, both from internal regions of the powder particles prepared as per Section 3.3.1 in Figs. 4.12(a) and 4.12(b), and directly from the powder surface in Figs. 4.12(c) and 4.12(d).

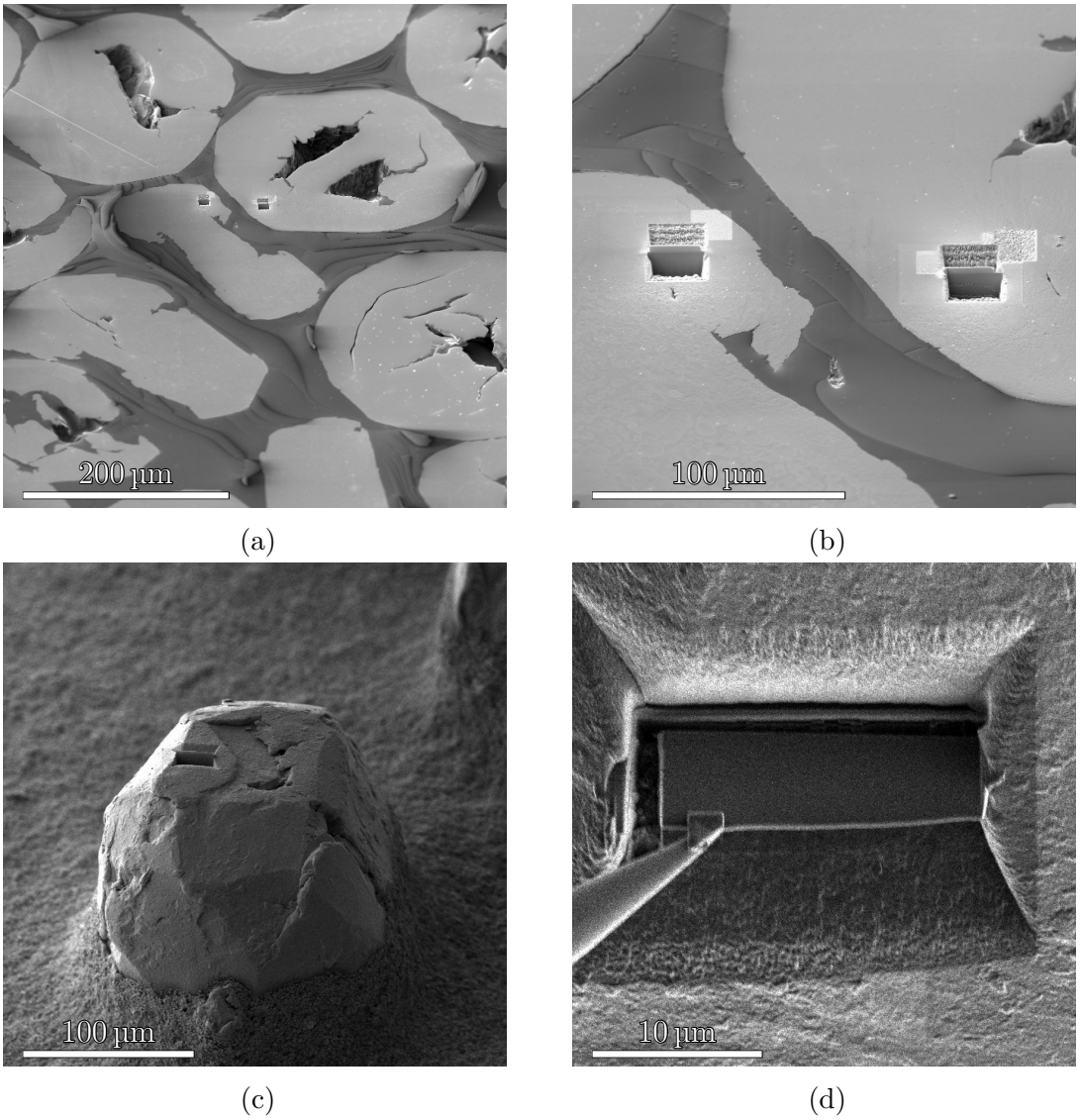

Figure 4.12: Secondary electron micrographs of the preparation of TEM lamella by the FIB liftout technique from powdered materials. **(a)** From the polished surface of interior regions of powder. **(b)** Lamella shown in (a) **(c)** Preparing a sample from the powder surface region. **(d)** Micromanipulator in position to remove lamella from the powder surface in (c).

Yttrium

Cu-2Y_2O_3 milled powder TEM lamella were thinned to ∼20 nm (half the mfp of Cu of ∼39 nm) and analysed at 200 keV by low-loss EFTEM and STEM-EDS. Figure 4.13 shows low-loss Y $N_{2,3}$ maps, revealing a spatially heterogeneous distribution of particles. There were particles of diameter 20 to 40 nm with relatively high Y concentrations, with smaller Y-rich clusters in the range 2 to 5 nm diameter in between the more distinct, larger particles. In addition to the fine clusters, there were striations of Y, typically aligned with one another in a region, such as those shown in Figs. 4.13(a) and 4.13(b).

Figure 4.14(a) shows an example of a typical HAADF-STEM micrograph with Z-contrast between the constituent elements/compounds (Z numbers: Cu-29, Y-39, Y_2O_3-25.2 (effective)). There were dark striated regions in grain/crystallite boundary regions, shown in Fig. 4.14(b), along with particles <10 nm in diameter. The contrast between striated regions, particles and the Cu matirx indicated that the Y_2O_3 has not fully disassociated into Y and O, but some dissolution was evident. The location of dark regions along the grain/crystallite boundaries also suggested fragmentation of the Y_2O_3.

Significant difficulties were faced in obtaining high-quality TEM and STEM analysis of the Y within the powder. The high defect density in the Cu matrix gave rise to a lack of stability in the FIB liftouts, resulting in difficulty thinning to ∼20 nm to obtain good transparency without sample folding. This was further exasperated by the high sputter rate of Cu that resulted in re-deposition during low-current polishing of the sample surfaces.

Despite the difficulties, further characterisation of the Y-containing striations showed that these regions formed from a combination of indistinct Y-rich clusters with halo-like regions and finer striations around and between them, shown in Fig. 4.15(b). The diffuse nature of the <5 nm Y-rich clusters contrasted with the larger >20 nm

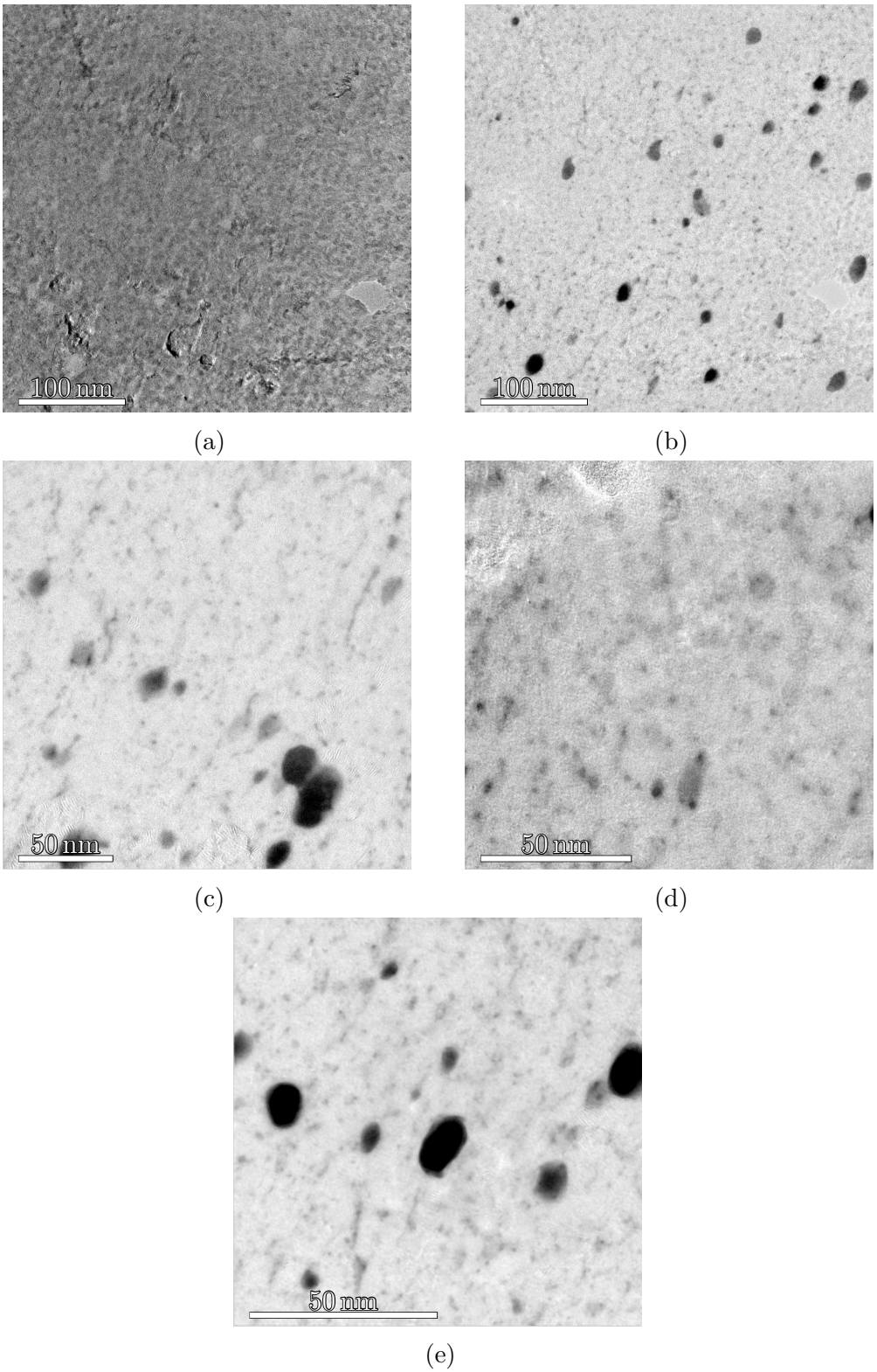

Figure 4.13: Micrograph of Cu-2Y_2O_3 powder after 12 hours milling. **(a)** TEM bright field. **(b)** Inverse Y $N_{2,3}$ map from EFTEM of (a). **(c-e)** Further typical inverse Y $N_{2,3}$ maps.

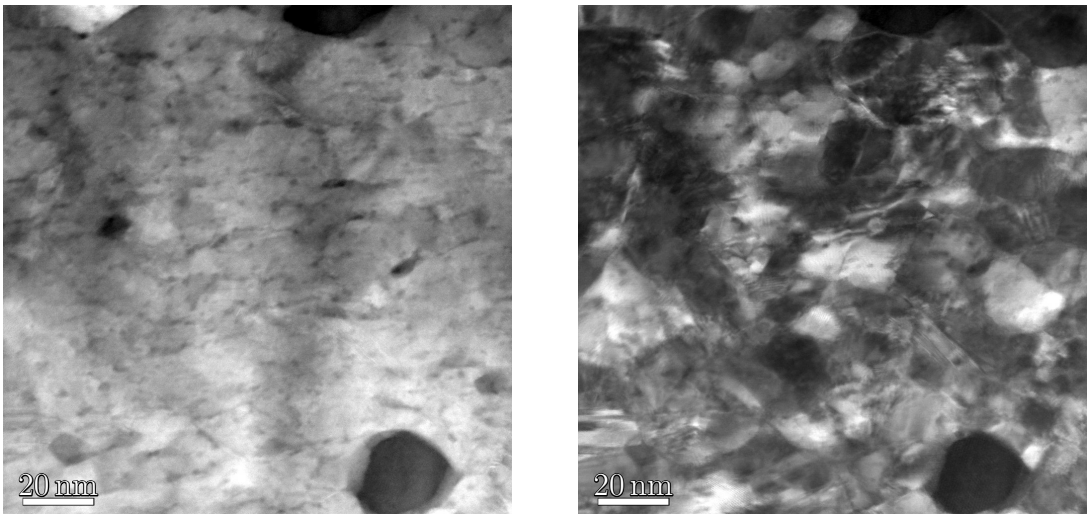

(a) (b)

Figure 4.14: STEM micrographs of Cu-2%Y_2O_3 powder after 12 hours milling, the same region **(a)** HAADF showing Z-contrast, and **(b)** ADF showing diffraction contrast.

Y-rich particles, which had resolvable crystallinity, as seen in Fig. 4.15(c), which was identified as cubic-Y_2O_3 in the [110] orientation . Converse to the observations in HAADF-STEM, the Y-rich clusters showed a decreasing Y concentration as a function of distance away from the cluster centre.

Oxygen

An O signal could not be collected in low-loss EFTEM, so STEM-EDS at 200 keV was utilised. The striated regions shown in the lower right hand of Fig. 4.17(a) contained a resolvable increase in O concentration (Fig. 4.17(c)) that corresponded to regions comparatively denuded in Cu (Fig. 4.17(b)) and an increase in Y (Fig. 4.17(d)). It was not possible to obtain robust Y:O concentration ratios from these regions, however it could be concluded that the Y and O were strongly co-located, rather than either element preferentially segregating to the matrix. High concentrations of O not co-located with Y were associated with surface Cu-oxides on the TEM foil.

To summarise, examination of the MA powder by analytical TEM techniques showed that some of the Y_2O_3 reduced in size but was unlikely to be disassociating

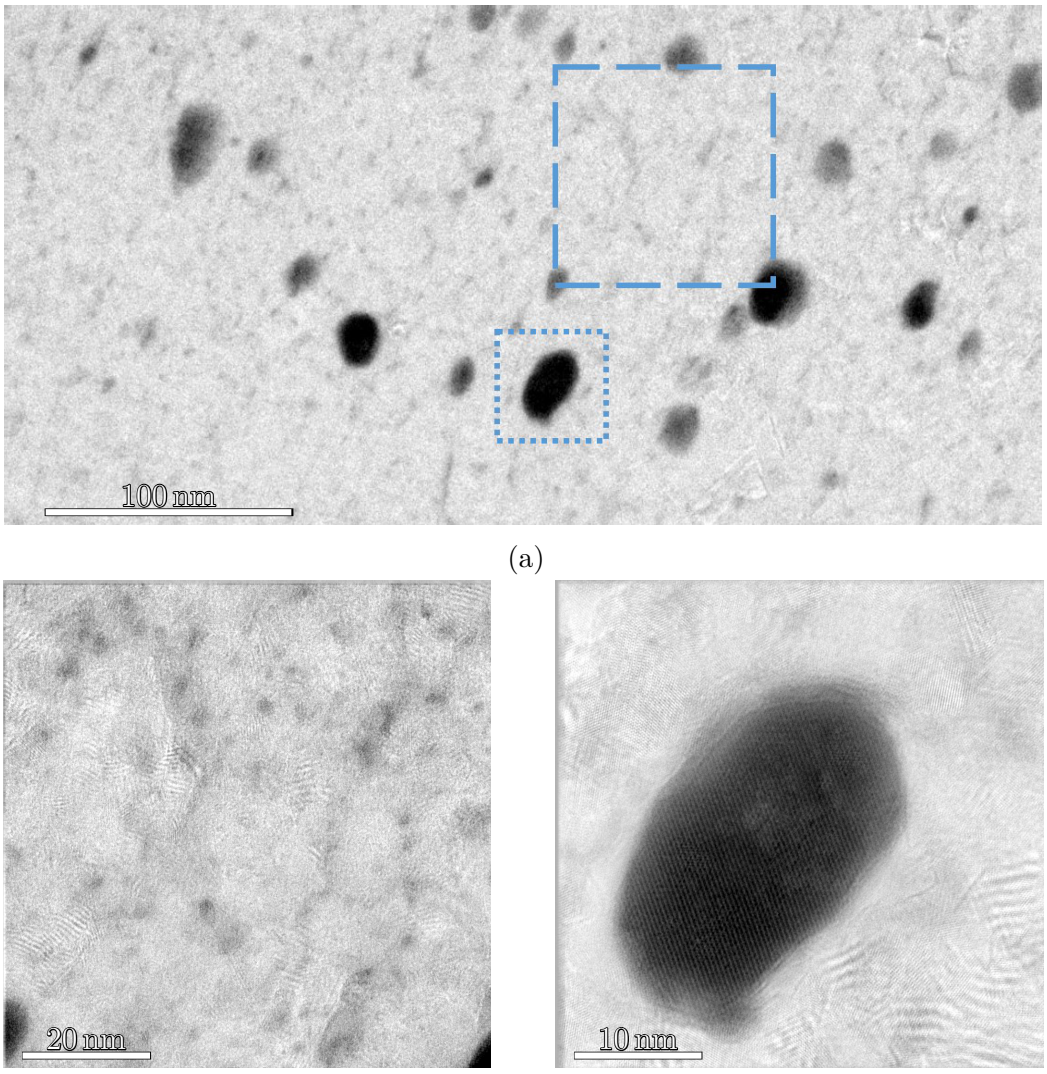

Figure 4.15: Inverse Y $N_{2,3}$ maps from low-loss EFTEM of Cu-$2Y_2O_3$ powder after 12 hours milling, **(a)** typical region of distributed 20 to 40 nm particles with striations of Y, **(b)** topmost highlighted region of (a) showing striations and 3 to 4 nm clusters with halo-like Y, **(c)** lower highlighted region of (a) showing detail of a 40 nm mean diameter particle with distinct crystallinity.

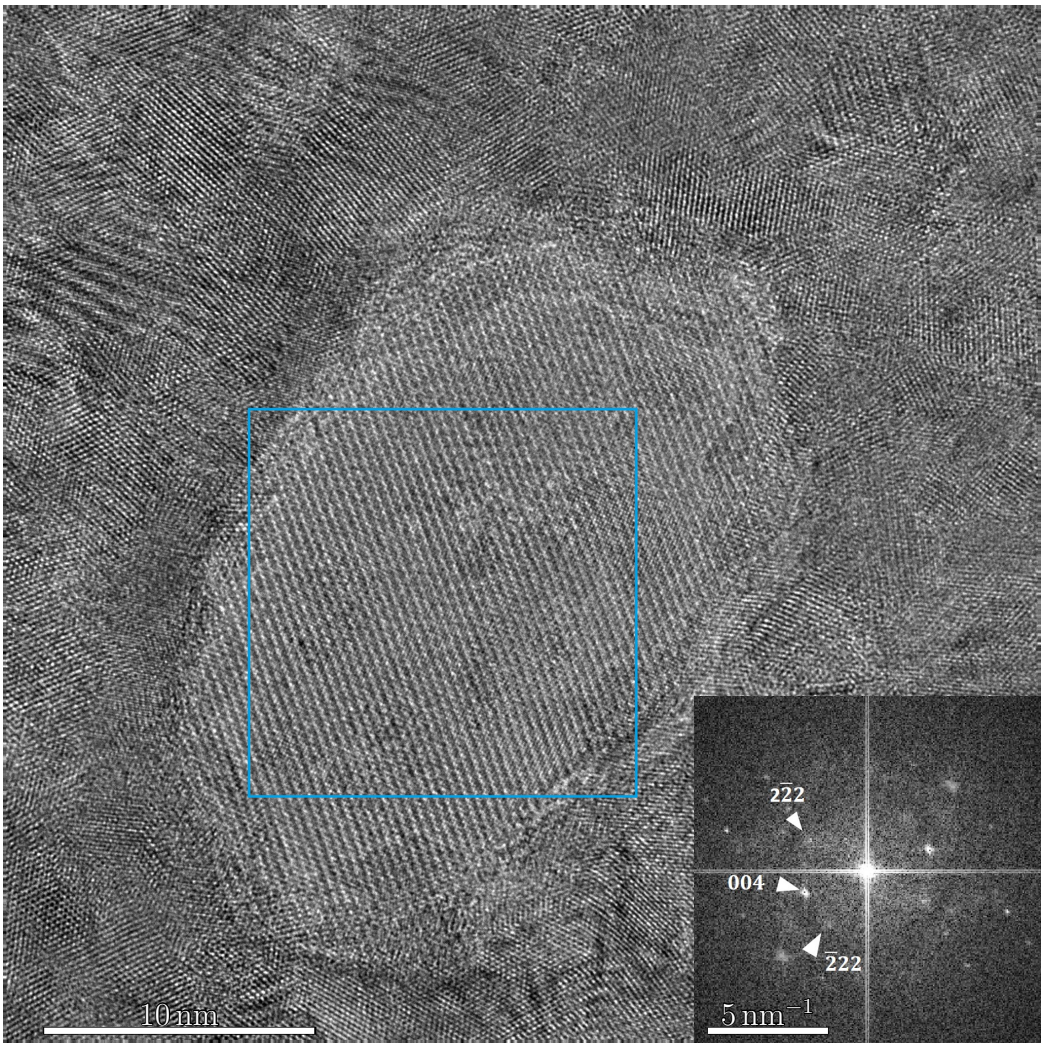

Figure 4.16: Unfiltered TEM micrograph of the particle in Fig. 4.15(c). Inset: indexed fast fourier transform (FFT) of the highlighted region, indicating the particle is cubic-Y_2O_3 of space group $Ia\bar{3}$ viewed in the [110] orientation.

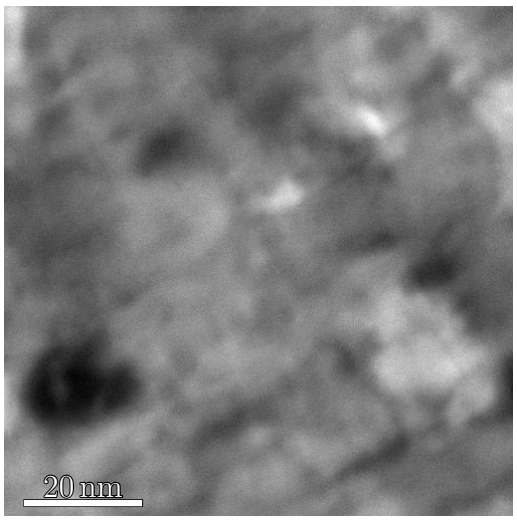

(a)

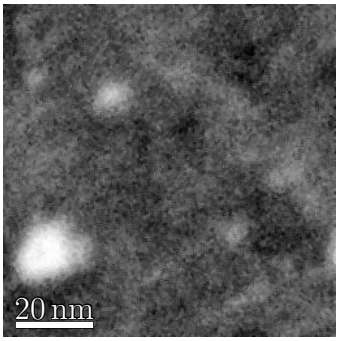

(b) Cu K+L

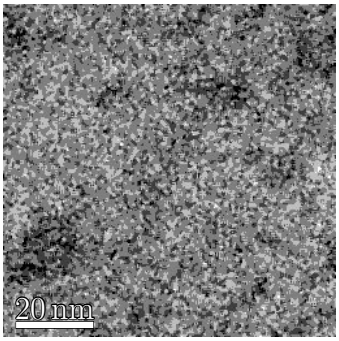

(c) O K

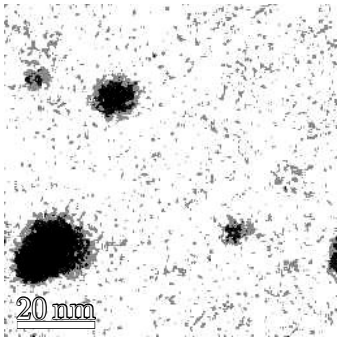

(d) Y K+L

Figure 4.17: STEM-EDS analysis of Cu-2Y_2O_3 milled powder. **(a)** ADF micrograph of powder, showing the region of EDS mapping. **(b)** Inverse Cu K+L map showing regions denuded of Cu, particularly the striations in the lower right-hand corner. **(c)** Inverse O K map. **(d)** Inverse Y K+L map.

into distinct regions of Y and O. Instead dispersion proceeded by fragmentation and/or dissolution of Y_2O_3. This dispersion is broadly in line with most (but not all) current understanding of the process of Y_2O_3 break-up in Fe-ODS which is suggested to be diffusion assisted intermixing of Y and O following severe fragmentation [104].

4.3.2 Re-precipitation of Y_2O_3

A large driving force exists for the re-precipitation of any dissolved Y and O as the high dislocation density from MA is subsequently eliminated leading to enhanced recovery and recrystallisation, coupled with the affinity for Y and O for each other, and metastability of the Cu-Y solid solution. As part of the processing of the powder into bulk by sintering, the heating provides energy to activate diffusion for the formation of particles from within the regions of Y and O observed in Section 4.3.1.

Cu-2Y_2O_3 was sintered by FAST for 30 min, under a uniaxially applied load of 40 MPa at 900 °C, and key process parameters as a function of time are shown in Fig. 4.18. During the initial heating phase at 100 °C min^{-1} to 800 °C, there was significant outgassing of the powder, starting at 350 °C, but at all times the vacuum was below 1.0 mbar, eventually recovering to <0.1 mbar. Above 600 °C, measurable reductions in the sample height were observed as a low pressure of 12.5 MPa was applied. Upon reaching 800 °C the heating rate was reduced to 50 °C min^{-1} and the applied pressure was ramped to 50 MPa. All further compression of the sample was completed as the pressure was increased, suggesting the majority of sintering occurred during the first minute or so after the application of the uniaxial load. The compression rate fell to ∼0 mm min^{-1} after this period, when the resolution limit of the positional transducer was too low (±100 µm) to measure any further reductions in the height of the compact. The FAST electrodes were water cooled so post consolidation cooling was rapid, which may have helped to inhibit recrystallisation.

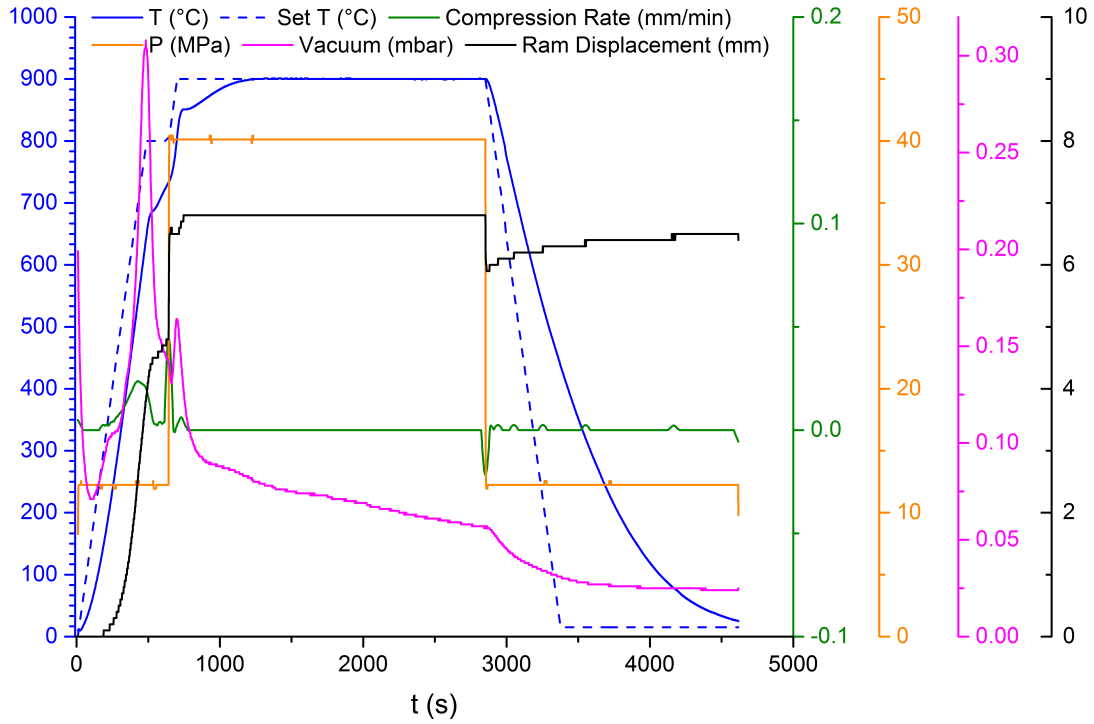

Figure 4.18: Sintering of a 60 mm diameter die containing 260 g Cu-2Y_2O_3 powder with a dwell of 30 minutes at 900 °C under 40 MPa uniaxial load.

Particles

Sintered Cu-2Y_2O_3 exhibited a fine dispersion of nano-precipitates in the prior particles as shown in Figs. 4.19 and 4.20. Examination of the particles by TEM revealed particles of near-spherical shape without obvious faceting. The coarser nanoparticles of 20 to 40 nm, presumably enduring from the as-milled powder, remained but they were now surrounded by a near-homogeneous dispersion of much finer particles with diameters of 2.0 ± 0.7 to 15.0 ± 0.7 nm. Measurement of 1120 of these Y-rich particles by EFTEM revealed the particles to have a mean diameter of 7.1 nm and a mean inter-particle spacing of 23 nm, with the particle diameter distribution shown in Fig. 4.19(c). Particles larger than approximately 20 nm were typically at grain boundaries, with finer particles again at grain boundaries but also within grains as shown in Fig. 4.19(b).

Figure 4.20 shows a region analysed by STEM-EDS containing fine Y and O-rich clusters in the range of 2 to 10 nm (31 particles, mean diameter 5.6 ± 0.8 nm). The

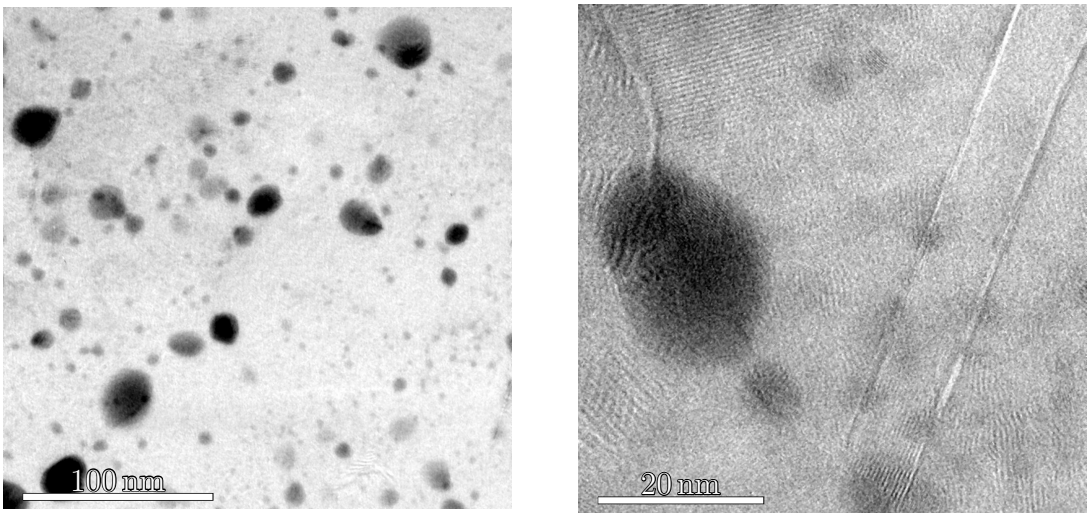

(a) (b)

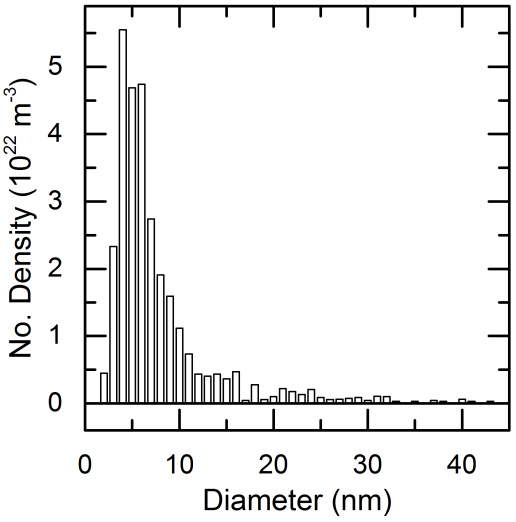

(c)

Figure 4.19: Low-loss EFTEM analysis of FAST consolidated Cu-2Y_2O_3, **(a+b)** inverse Y $N_{2,3}$ maps, and **(c)** particle size distribution of 1120 Y-containing particles from multiple sites of three FIB liftouts.

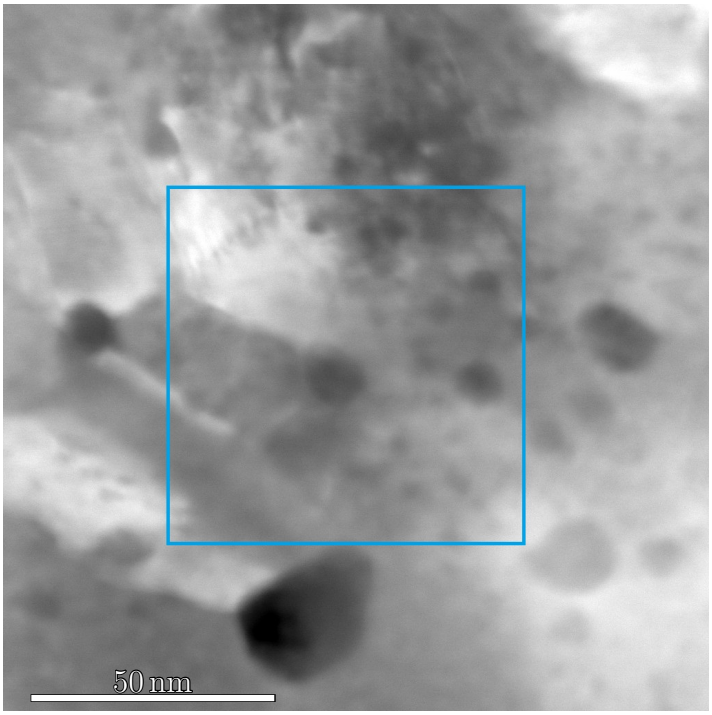

(a) HAADF

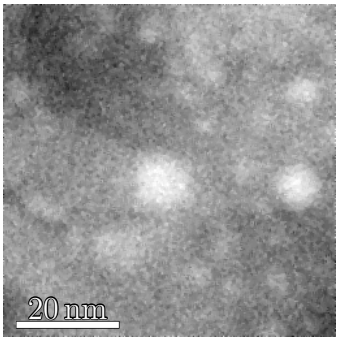

(b)

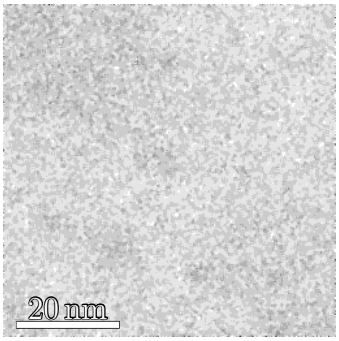

(c)

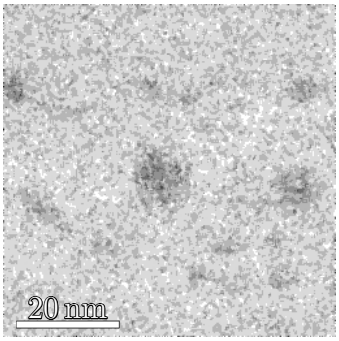

(d)

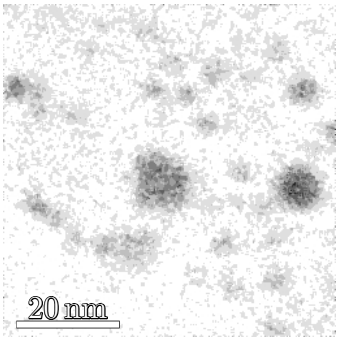

(e)

Figure 4.20: STEM analysis of consolidated Cu-2Y_2O_3, **(a)** HAADF micrograph, **(b)** inverse Cu K+L map, **(c)** inverse Fe K+L map, **(d)** inverse O K map, and **(e)** inverse Y K+L map.

clusters were on a twin boundary and within the grains. As described earlier, Fe contamination from the milling process may be problematic, but only a small number of the clusters showed a (weak) Fe signal such as Fig. 4.20(c), and were co-located with Y and O-rich areas.

APT analysis of sintered Cu-2Y_2O_3 shown in Fig. 4.21 revealed a wide range of cluster diameters and variation in the cluster Y:O ratio. Only a single sample was analysed with a total of 245 clusters identified within $\sim$650 000 nm^3 (calculated from Cu lattice spacing of total atoms detected). The Y:O ratio ranged from 0.45 to 1.90 with a mean ratio of 1.02 and a median ratio of 1.00 (N.B. Y:O ratio of Y_2O_3 is 0.67). A possible, but unlikely, explanation for a Y:O ratio of 1.0 may be the formation of YO, which has recently been produced directly by sputtering of Y_2O_3 [105], but has not been reported in previous Y_2O_3 studies in ODS materials. Broadly, cluster composition was comparable with the EFTEM and EDS observations of predominantly Y and O, with co-located Fe in some instances, C was not found in concentrations above 0.3 at.%. The cluster size measured by APT was consistent with TEM observations.

Prior-particle boundaries

During sintering, diffusion of atoms from the near-surface to the powder surface provides the reduction of free surface energy that drives the elimination of porosity and densification of the powder. In sintered Cu-2Y_2O_3 a bimodal grain structure was observed after sintering. The regions surrounding the prior-powder-particles that previously constituted the void at the triple point between three powder particles had a much coarser grain structure than the regions inside the prior-powder-particles, as shown in Fig. 4.22. These structures appear comparable to those observed in a Cu-3Al_2O_3 alloy sintered at 800 °C for 1 h without pressure [63].

Figure 4.22 shows images of the PPB and triple-point voids regions of consolidated Cu-2Y_2O_3. Figure 4.22(a) shows an incompletely consolidated triple-point obtained

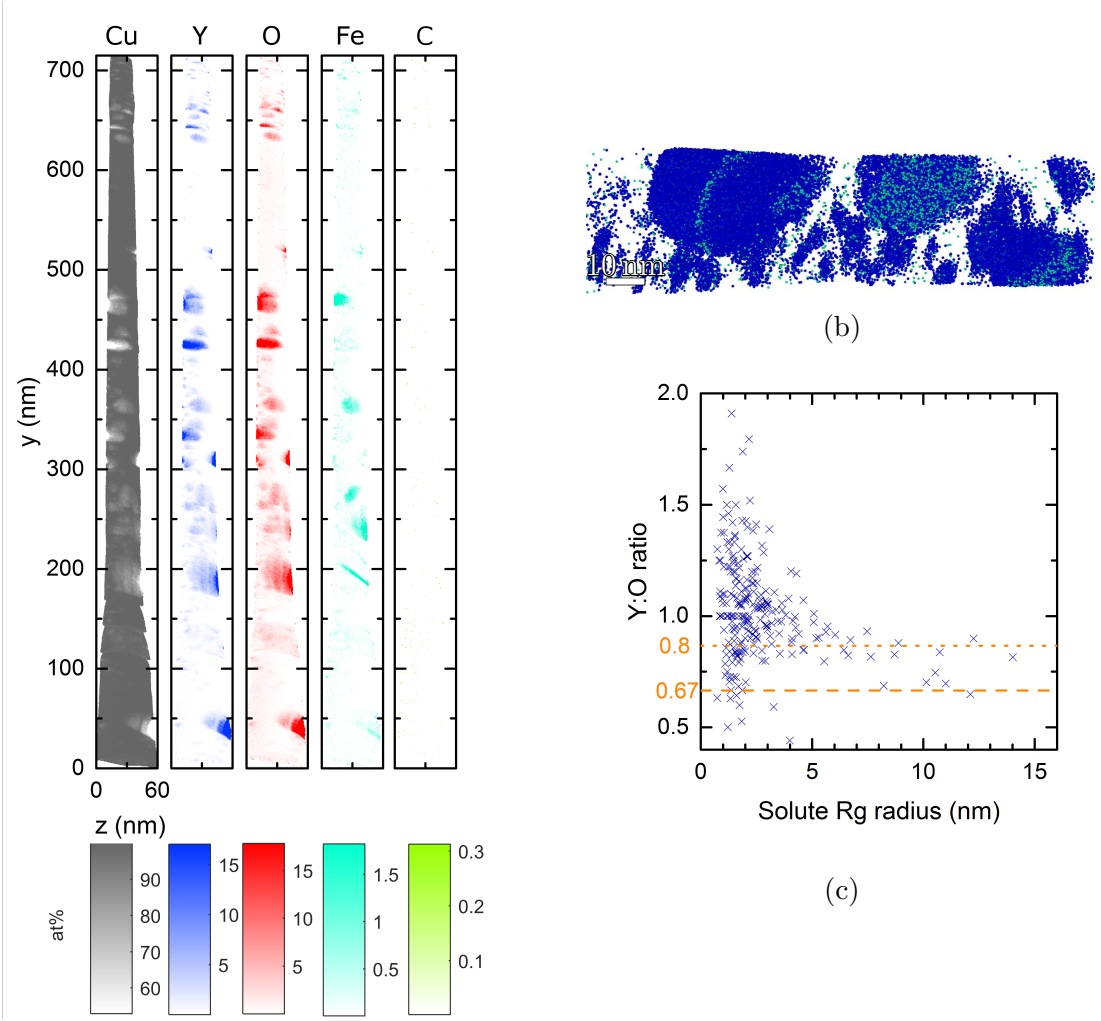

(a) (b) (c)

Figure 4.21: APT of Cu-$2Y_2O_3$ prepared by FAST consolidation, **(a)** projection in x of atomic concentrations Cu, Y, O, Fe, and C, **(b)** 3d projection of segments containing clusters of Y and Y-O ions (blue) and Fe ions (green), and **(c)** estimated Y:O ratio versus radius of gyration (Rg) from 245 Y-containing clusters measured by APT of a 650 000 nm^3 volume.

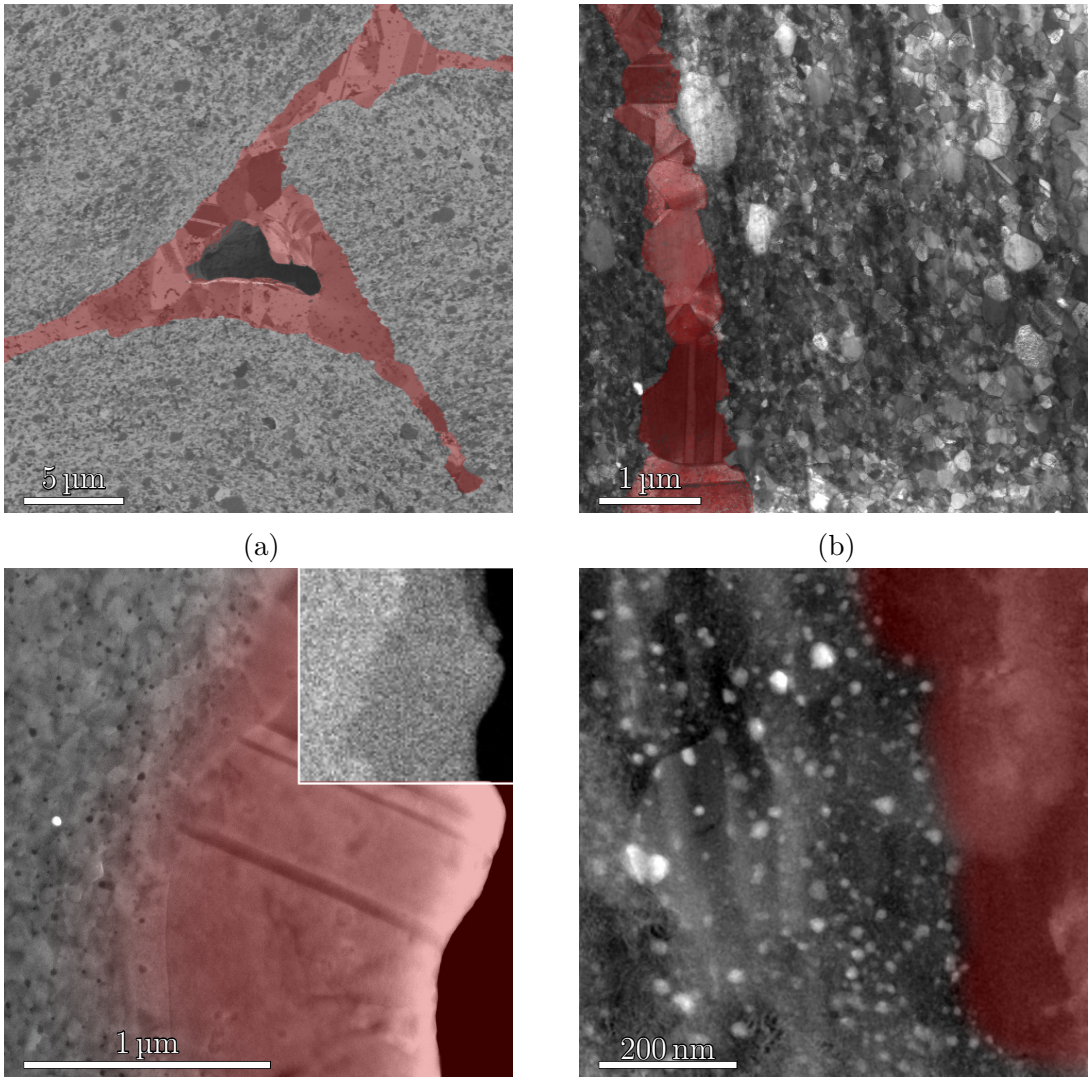

Figure 4.22: Prior-particle-boundary (PPB) region highlighted in red at increasing magnification, **(a)** Channelling contrast micrograph of incomplete sintering where the sintering time was deliberately shortened to retain a small degree of porosity, showing a triple point of prior particles and growth of large grains beyond the PPB, **(b)** Bright field STEM with diffraction contrast showing grain structure alongside a PPB, **(c)** Secondary electron micrograph at a triple point edge, with inset Y K SEM-EDS map inset, and **(d)** Y $N_{2,3}$ map obtained by EFTEM across PPB, showing Y-rich particles (bright) within prior-particles and a region denuded of Y beyond the PPB.

from interrupted sintering. Surrounding the residual pore there were highly twinned ~1 µm Cu grains. Within the prior-particles themselves, the microstructure was much finer, with 50 to 250 nm grains largely free of twins. Figure 4.22(b) shows a PPB of ~1 µm width between two regions of 50 to 250 nm grains. Figure 4.22(c) shows an enlarged view with an inset indicating the Y distribution, which showed a markedly lower concentration in the region beyond the PPB, next to the pore. The low-loss EFTEM image in Fig. 4.22(d) revealed the absence of Y-containing particles within the region, and a distinct interface between the fine-grained, particle rich regions within the prior-particle, and the particle free region beyond the PPB.

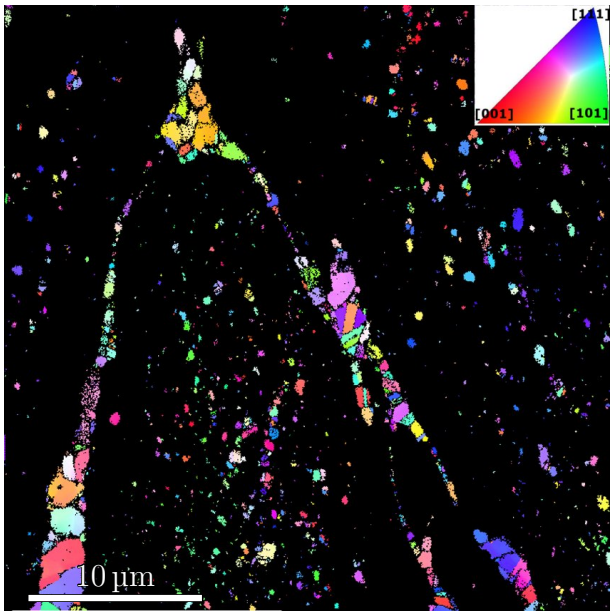

Figure 4.23: EBSD inverse pole figure coloured map showing resolvable fine grains only in the region of PPBs in Cu-2Y_2O_3.

Figure 4.23 shows an EBSD inverse pole figure false coloured map of PPB regions in Cu-2Y_2O_3. The finest grain structure of the internal regions of the prior particles were not resolved due to the high defect (dislocation) density and resulting low confidence in indexing the EBSD patterns, and only the largest recovered/recrystallised grains >1 µm in the region of the PPBs were resolved.

Further analysis of the PPB region in Fig. 4.22(d) revealed that there was an

increase in the particle diameter and a decrease in number density with increasing distance from the PPB into the particle. Figure 4.24(b) confirmed a high concentration of small Y-rich particles within the first 200 nm of the edge (rough position, marked in blue in Fig. 4.24(a)), after which the trend was for fewer, larger particles. Figure 4.24(c) shows that the volume fraction of particles peaked at a distance of approximately 200 nm then reduced.

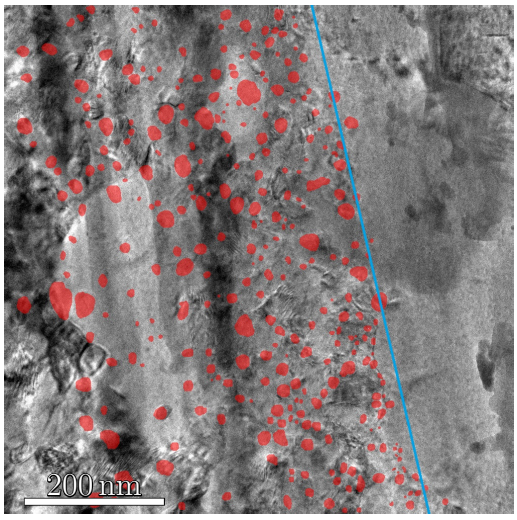

(a)

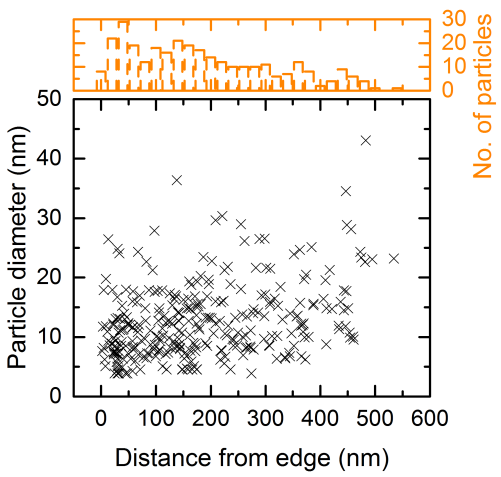

(b)

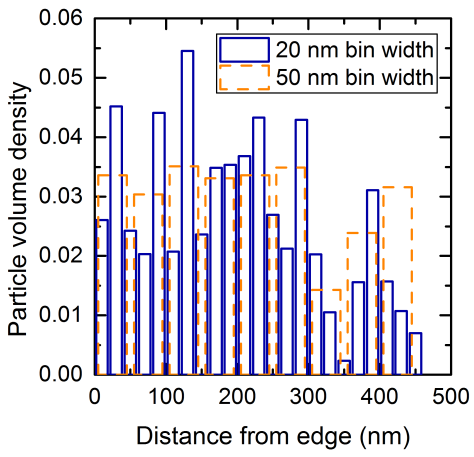

(c)

Figure 4.24: Particle diameter near the PPB **(a)** overlay of Y map (false colour, red) on the TEM bright-field image in Fig. 4.22(d), **(b)** measured particle diameter vs distance from PPB edge region shown by line in (a), and **(c)** volume density of particles vs distance from PPB edge.

The formation of regions depleted of Y-rich particle regions beyond the PPB that contained 1 to 4 µm diameter grains suggested that Cu readily diffused into the sinter neck region and that Y_2O_3 fragments, or Y and/or O in solid solution, had much more limited or no mobility. In the case of Y having dissociated from O, Y atoms have a significantly larger atomic radius than Cu (1.797 Å compared to 1.276 Å [106]) and so can be expected to be a relatively slow diffuser in Cu. It was also likely that, despite best efforts, a Cu-containing oxide film formed on Cu powder to define the prior particle surface (during milling, storage or die loading in the FAST) and any diffusing Y would replace Cu in the oxide film (Gibbs free energy of formation of oxide $Y_2O_3 \sim -510\,\mathrm{kJ\,mol^{-1}}$, $Cu_2O \sim -85\,\mathrm{kJ\,mol^{-1}}$ at 900 °C [107]) to form particles. In the case that the Y_2O_3 was not disassociated or dissolved (i.e. it had only been severely fragmented) then it is sensible that the Y_2O_3 fragments would be too large to diffuse, thus leading to the preferential diffusion of Cu from the bulk to the sinter neck surfaces.

The proposed mechanism of neck formation is shown schematically in Fig. 4.25 whereby the powder particles are mechanically forced into close, neck-like contact with one another during initial uniaxial loading at room temperature (see Fig. 4.18) but do not deform significantly on account of their work-hardened, elevated yield strength (∼1000 MPa, see Table 4.2) under the relatively low load. During sintering, necks form at the contact points from mobile diffusing Cu, that leaves behind an increasing volume concentration of immobile Y_2O_3 fragments in a narrow band close to the PPB. The diffused Cu in the consolidated sinter neck is thus comparatively free of grain-boundary pinning particles allowing grain growth to occur largely unheeded; resulting in a microstructure consisting of regions of larger Cu-grains denuded of oxide particles surrounding well defined prior particles.

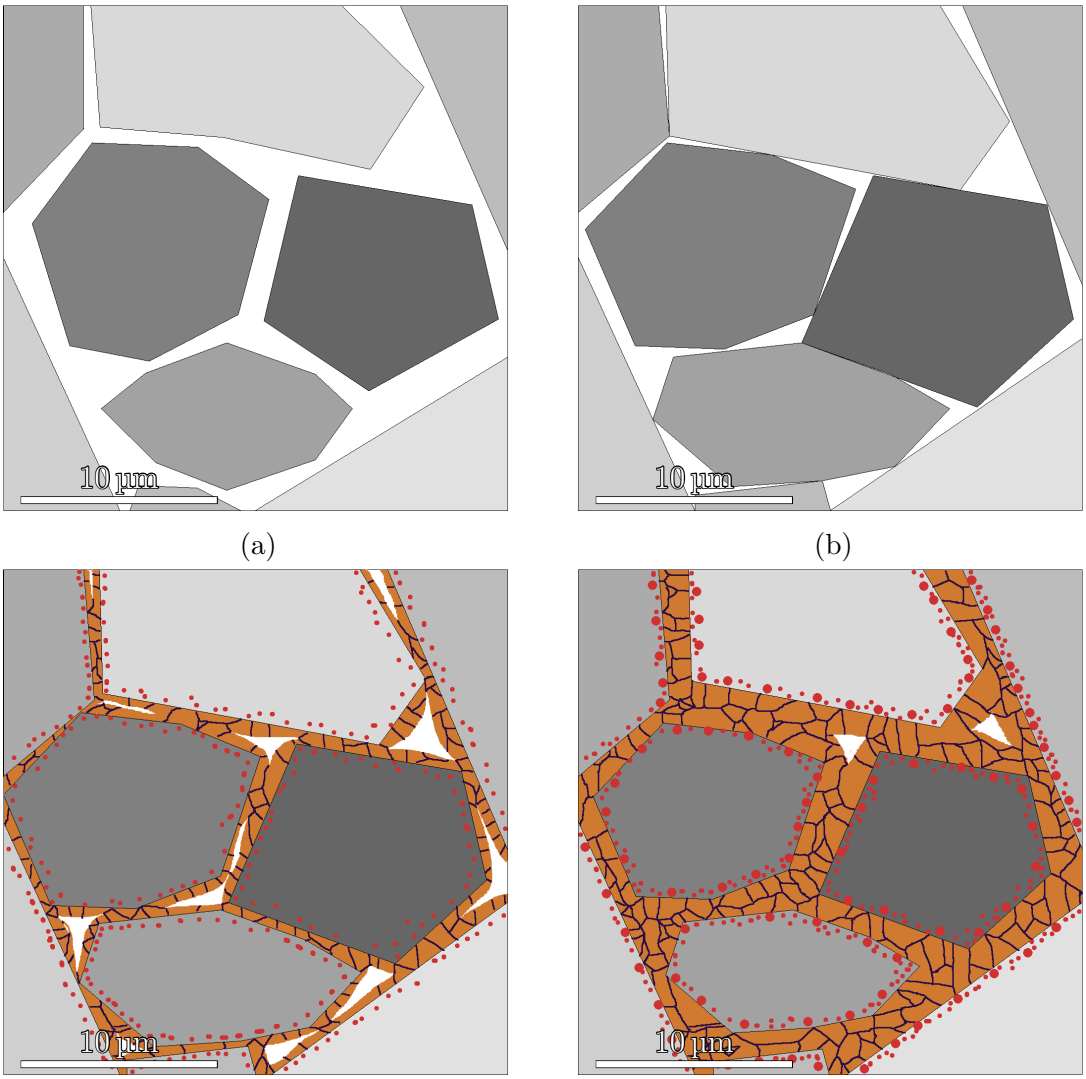

Figure 4.25: Schematic diagram of proposed method of PPB formation. **(a)** Powder particles loaded in die (grey). **(b)** Powder particles under uniaxial load (top-to-bottom) forced into contact. **(c)** Sintering (by application of heat and pressure) provides driving force for volume diffusion of Cu (orange) from powder to pore boundaries to reduce free surface energy. Y or Y_2O_3 (red) left at prior particle surface. **(d)** Coarse grained (∼2 µm diameter) Cu left in PPB regions, with a decorative layer of Y-containing particles around the prior particle surfaces.

4.4 Summary

Mechanical alloying of Cu with Y_2O_3 by planetary ball milling, with a focus on a Cu-2Y_2O_3 model alloy, was performed in order to investigate the feasibility of using mechanical alloying as a route to Cu-ODS alloys containing Y_2O_3. It was found that:

- MA by planetary ball milling allowed for Y_2O_3 to be distributed within the Cu matrix and precipitation of Y_2O_3 significantly finer than the feedstock Y_2O_3 could be brought about by means of applying thermal energy during sintering.
- Systematic milling studies suggested a lower solubility of usefully refined Y_2O_3 in fcc Cu when compared with the MA of bcc Fe-ODS alloys, which was suggested to relate to the lower work hardening capacity of the Cu matrix.
- The Y_2O_3 was distributed effectively during MA but with a bimodal distribution of particle diameters comprising unrefined feedstock particles and some strongly fragmented/dissolved Y-O particles.
- Prior void regions were consolidated by the diffusion of Cu atoms but were denuded in Y_2O_3, and a proposal for their formation was suggested that favoured fragmentation only as the mechanism for Y_2O_3 distribution during MA.
- Taking the various findings together, the proposed mechanism of distribution of Y_2O_3 in Cu by MA is a combination of fragmentation (primary) and partial dissolution of Y_2O_3 (secondary) that is consistent with the formation of particle free, coarse Cu grained regions in prior voids and Y-rich particles with non-stoichiometric ratios of Y:O.

Overall, MA provided a feasible processing route for the production of Cu-Y_2O_3 ODS alloys, but refinement and Y_2O_3 dispersion and subsequent homogeneity of microstructure were more challenging than in Fe-based ODS alloys. Encouragement

was provided for oxide dispersions considerably finer than in commercial Cu-based ODS alloys.

Chapter 5

Consolidation

5.1 Introduction

Consolidation is the process by which a powder material is transformed to a bulk, by promoting bonding between the powder particles. There are numerous methods to achieve consolidation and the most widely practised in industry is sintering. Energy is applied in the form of heat, sometimes together with pressure, to promote diffusion of atoms to reduce specific free surface area and so to give densification. Key technologies in the consolidation of metal powders for bulk production are hot extrusion, VHPing and HIPing.

Within the context of the Cu-2Y_2O_3 alloys developed in Chapter 4, there is a requirement to reduce the amount of time and heat exposure during consolidation in order to control the development of the Y-containing nanoparticles, and avoid over-ageing or excessive grain growth. In Fe-ODS alloys the standard procedure for consolidation is HIPing followed by thermomechanical treatments such as rolling, extrusion or forging [108].

The thermal exposure (sintering temperature and time) should ideally be minimised to prevent grain growth (starting at ∼210 °C for heavily deformed Cu [16, 17]). Significant recrystallisation and recovery of Cu-ODS alloys has been observed at temperatures above 400 °C, with the fast coarsening of the microstructure between 600 °C and 700 °C, with some remnant retention of subgrain structures by ODS particles at

higher temperatures [109, 110]. So-called abnormal grain growth is an associated risk of dispersion strengthened powder consolidation and heat treatment [19], as reported for Fe-ODS alloys [111–113], and also reported in Cu-ODS alloys containing Al_2O_3 particles produced by internal oxidation [54].

In this chapter, the effect of consolidation on model Cu and Cu-2Y_2O_3 alloys is investigated, with particular reference to the re-precipitation and/or behaviour of Y_2O_3.

5.2 Experimental procedure

Three powders were sintered by HIP and FAST:

- As-received Cu (99.9% purity) with a mean particle diameter of 70 µm.
- Milled Cu (99.9% purity) with a mean particle diameter of ∼700 µm.
- Cu-2 wt.% Y_2O_3 prepared by MA with a mean particle diameter of ∼180 µm.

Micrographs of the powders following milling were shown earlier in Fig. 4.6, with the powder hardnesses of (1020 ± 290) MPa, (2220 ± 260) MPa and (3180 ± 90) MPa respectively, prior to any thermo-mechanical treatment.

Sintering was undertaken at 850 °C ($0.82T_m$) following the sintering profiles shown schematically in Fig. 5.1 according to the parameters outlined in Table 5.1. Previous work on sintering of hard Cu and Cu-ODS-like alloys indicated that consolidation at 850 °C gave ∼100% theoretical density by HIPing [114, 115]. FAST consolidation in comparable Fe-ODS alloys has shown that near 100% theoretical density may be readily achieved at $<0.81T_m$ in <5 min [75, 108].

5.3 Results and discussion

Figure 5.2 shows the FAST sintering data of Cu-2Y_2O_3, which was typical of data for the sintering of as-supplied Cu and milled Cu. The temperature of the die, measured

Table 5.1: Sintering parameters for HIP and FAST consolidation of Cu, milled Cu and Cu-2Y_2O_3.

	HIP	FAST
Die material	mild steel can	graphite
Die size (mm)	∅22 × 60	∅60 × 12
Heating rate (°C min^{-1})	10	100
Dwell temperature (°C)	850	850
Dwell pressure (MPa)	150	40
Dwell time (minutes)	120	10
Vacuum (mbar)	$<5 \times 10^{-2}$	$<5 \times 10^{-1}$
Cooling rate (°C min^{-1})	furnace cool ∼10	100

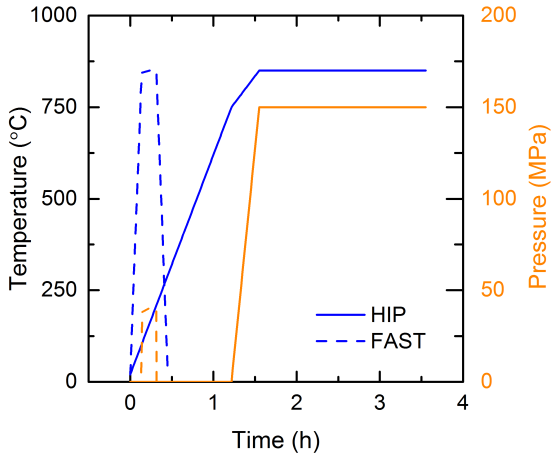

Figure 5.1: Approximate sintering profiles for consolidation of Cu, milled Cu and Cu-2Y_2O_3. by HIP and FAST. The HIP samples were furnace cooled.

by a thermocouple at a distance of 5 mm radially from the powder compact, followed the set profile closely except for a slowing in the range 800 to 850 °C as the plateau temperature was approached. This produced an effective dwell period of ∼15 min once the pressure was raised to 50 MPa. During the heating phase, the current and voltage rose steadily to increase the heating power; during the dwell period, the current remained approximately constant at 3 kA; with the voltage reducing slightly. This voltage reduction may signify a progressive reduction in the electrical resistivity of the powder as the number of powder particle interfaces and remnant pores were reduced. The principal reduction in the height of the powder compact occurred during the application of the uniaxial load, with no resolvable changes during the dwell period.

The total time spent above the recrystallisation temperature of Cu (∼210 °C for heavily work-hardened Cu) for HIP and FAST consolidation were a factor of 10 different at $>1.5 \times 10^4$ s and $<2.3 \times 10^3$ s respectively.

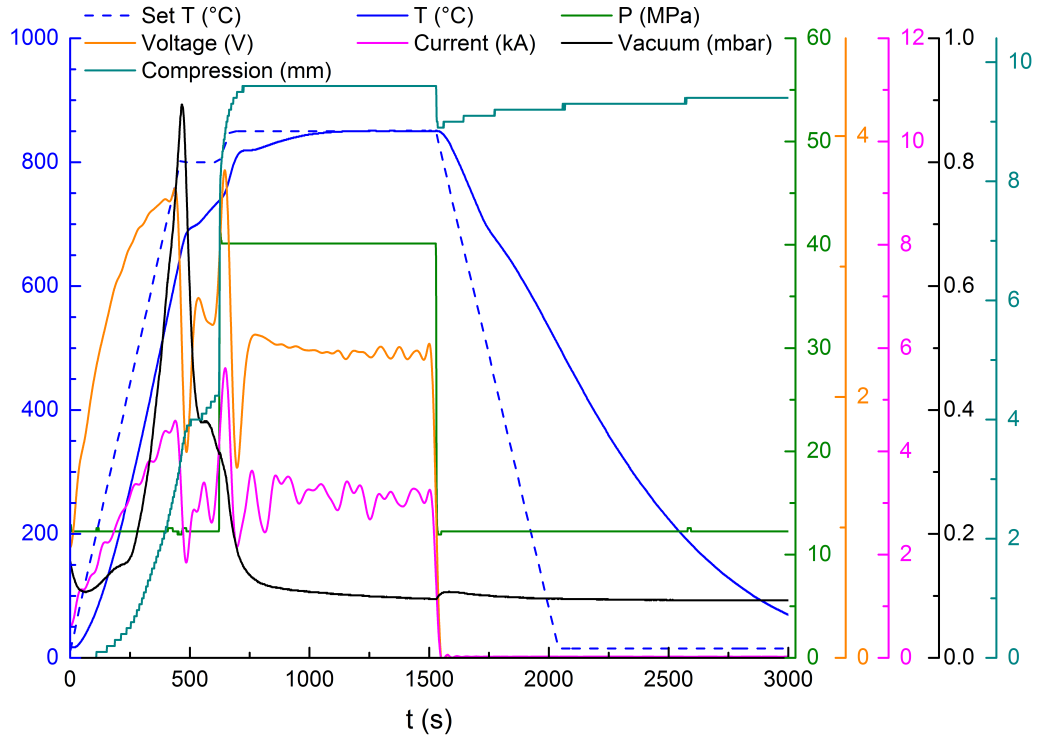

Figure 5.2: Typical FAST sintering data during consolidation of 260 g of Cu-2Y_2O_3 powder in 60 mm diameter die with a dwell of 10 minutes at 850 °C under 40 MPa uniaxial load.

5.3.1 Extent of consolidation

Table 5.2 details the densities of the sintered materials, as measured by the Archimedes method. The density achieved by HIP consolidation of milled Cu was $<8.59 \pm 0.09\,\mathrm{g\,cm^{-3}}$, which represents a relative density of 0.96, given a theoretical density of $8.96\,\mathrm{g\,cm^{-3}}$. The density of Cu-$2Y_2O_3$ was comparable with another high-Y_2O_3 containing HIPed Cu alloy at a relative density of 0.95 [14]. It was not possible to obtain a density measurements for HIPed as-received Cu due to asymmetric deformation of the sample during consolidation, which prevented the removal of the can and any further evaluation.

Table 5.2: Effect of consolidation route on density and hardness of materials consolidated by HIP and FAST, measured by the Archimedes method, fully dense Cu is assumed to be $8.96\,\mathrm{g\,cm^{-3}}$.

	Density ($\mathrm{g\,cm^{-3}}$)	Relative density (%)	Hardness MPa
HIP Cu (as received)	-	-	670 ± 20
FAST Cu (as received)	8.69 ± 0.09	97.0	610 ± 40
HIP Cu (milled)	8.59 ± 0.09	95.9	900 ± 210
FAST Cu (milled)	8.47 ± 0.12	94.3	1020 ± 130
HIP Cu-$2Y_2O_3$	8.38 ± 0.07	94.4	1180 ± 160
FAST Cu-$2Y_2O_3$	8.48 ± 0.05	95.5	2440 ± 110

The surprisingly low densities by both routes were not easily understood but were ascribed to the large $>400\,\mu\mathrm{m}$ diameter, milled prior-particles, so that the powder had a relatively low specific surface area, and thus reduced the driving force for consolidation.

5.3.2 Mechanical properties

Table 5.2 gives the room temperature microhardness of the consolidated alloys. HIP and FAST consolidated as-received Cu powder showed a 40% reduction in the hardness over the as-received powder, as previously reported in Section 4.2.1 at $1020 \pm 290\,\mathrm{MPa}$, which was due to the rapid coarsening of the fine-scale atomised microstructure. The two consolidation techniques gave a similar hardness of 600 to 700 MPa, suggesting

similar grain sizes despite the difference in time spent above the recrystallisation temperature. The hardness remained ∼20% greater than that of fully annealed Cu (490 MPa) [59]. FAST consolidated milled Cu retained ∼45% of the milled powder hardness. HIP consolidation resulted in a wide variation in hardnesses associated with regions of different microstructure, with an average hardness of 1180 ± 160 MPa. Microstructures resembling the consolidated as-received powder, had a minimum hardness 780 MPa, and others resembling the FAST consolidated regions of retained fine grains had a maximum hardness of 1590 MPa. HIPed Cu-2Y_2O_3 retained ∼38% of the milled powder hardness. Compared with a ∼77% microhardness retention in FAST Cu-2Y_2O_3.

Table 5.3: Tensile properties of materials consolidated by HIP and FAST from Fig. 5.3

	E (GPa)	σ_y (MPa)	UTS (MPa)	ϵ_f (%)
FAST Cu (as received)	83	119	254	24.3
HIP Cu (milled)	59	163	237	6.1
FAST Cu (milled)	83	207	279	5.8
HIP Cu-2Y_2O_3	85	297	345	3.1
FAST Cu-2Y_2O_3	40	-	490	0.40

Figure 5.3 shows the stress-strain curves from room temperature tensile tests of HIP and FAST consolidated alloys; three samples of each were tested and the mean behaviour is shown. The FAST materials had a higher 0.2% proof strength and ultimate tensile strength (UTS), than HIPed counterparts, but had lower ductility, as demonstrated by the reduction in elongation at failure, and shown in Table 5.3. There was significantly less necking in the FAST consolidated alloys, for example as shown by sudden failure once the UTS was reached.

Table 5.3 summarises the tensile properties. The Young's modulus was low for all alloys in the range 40 to 85 MPa, compared with a typical Cu databook Young's modulus of >115 MPa, and for strengthened alloys >125 MPa [52]. The Young's modulus of the FAST consolidated Cu-2Y_2O_3 was approximately half that of HIPed

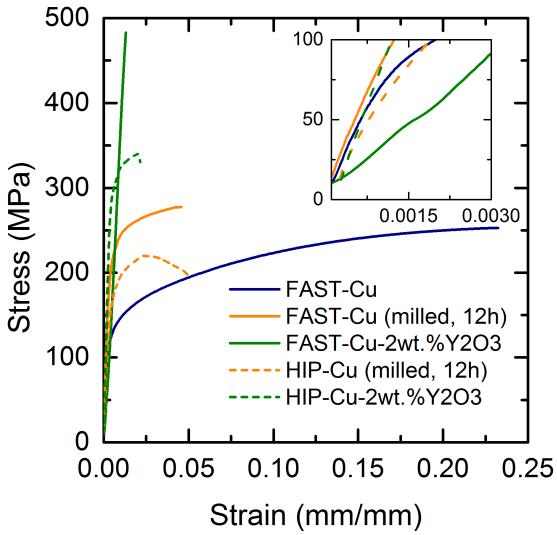

Figure 5.3: Tensile response of materials consolidated by HIP and FAST, averaged from three room temperature tensile tests performed to ASTM E8 standard on TETRE 160 round specimens, shown in Fig. 3.4. Samples were tested at a strain rate of $0.015\,\mathrm{min}^{-1}$ until yield and then at $0.4\,\mathrm{min}^{-1}$. Inset: the initial response. Engineering stress and engineering strain are presented.

material, which coupled with the low elongation at failure suggested incomplete sintering - i.e. even where apparent bonding between particles was suggested, under stress, these prior particle boundaries failed. These failure points are apparent in Fig. 5.4 that shows the necked failure surfaces of typical tensile samples. Those samples with the lowest estimated Young's modulus had apparent porosity at prior particle triple points, for example the HIP Cu (milled) in Fig. 5.4(b), where the largest powder particles did not sinter effectively despite deformation of the particles around one another, and FAST Cu-2Y_2O_3 in Fig. 5.4(e), which has finer porosity but sintering was again only partially complete. Figure 5.4(c) of FAST Cu (milled) shows some evidence of particle boundary failure, but of less severity. Unmilled Cu, processed by FAST, demonstrated conventional ductile failure with evidence of cup and cone fracture surfaces, in Fig. 5.4(a).

It is widely accepted that fine, closed porosity reduces both strength and Young's

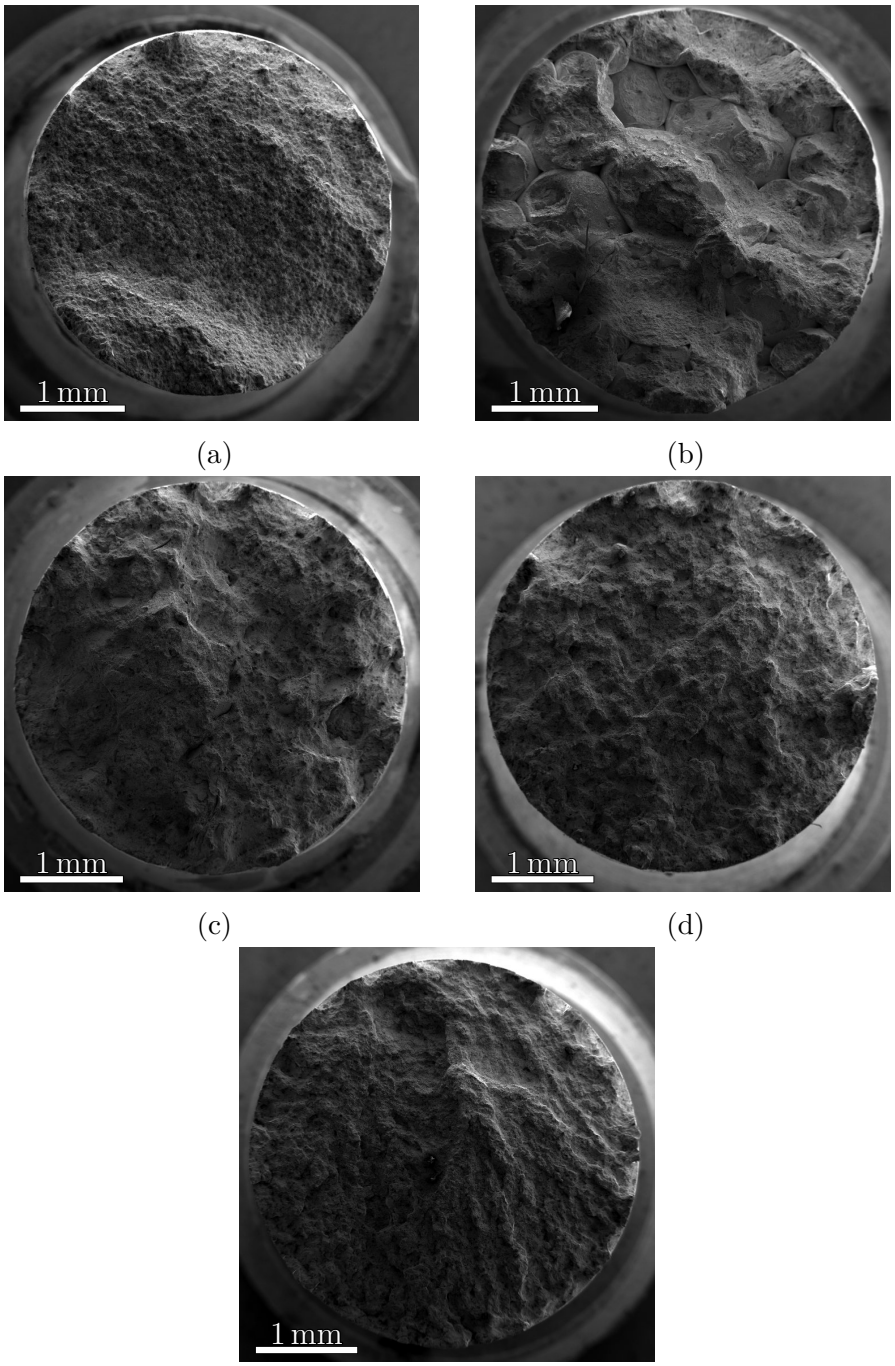

Figure 5.4: SE macrographs of typical tensile fracture surfaces. **(a)** FAST consolidated as-received Cu. **(b)** HIP consolidated 12 h milled Cu. **(c)** FAST consolidated 12 h milled Cu. **(d)** HIP consolidated 12 h milled Cu-2Y_2O_3. **(e)** FAST consolidated 12 h milled Cu-2Y_2O_3.

modulus, and there are a multitude of expressions that attempt to determine the relationship [116]. Using for example the adjusted Spriggs relationship $E = E_0 \exp -(bp + cp^2)$ where E_0 is the modulus of the bulk material, p is the porosity level, and $b = 2$ and $c = 4$ are material constants [117], the FAST consolidated Cu-2Y_2O_3 had a fraction of porosity >25%. From archimedes measurement of density, the porosity of FAST consolidated Cu-2Y_2O_3 was ∼5%, thus the reduction in modulus is likely to result from a combination of poor/weak bonding of the PPBs regions and porosity. The proof strength of HIP consolidated Cu-2Y_2O_3, 297 MPa was comparable to the recorded properties of commercial GlidCop AL25 and CuCrZr, of 310 MPa and 330 MPa respectively [52]. Whereas the FAST consolidated Cu-2Y_2O_3 showed a significantly higher UTS at the expense of ductility, no measurement of the proof strength was possible.

Figure 5.5 shows the typical fracture surfaces of the tensile samples. All surfaces bore evidence of ductile failure throughout with dimpled surfaces evident, inferring void formation. The scale of the dimples varied with the different materials: in the unmilled Cu, Fig. 5.5(a), dimples were evenly sized and spaced at typically 2 to 4 µm, contrasting with 5 to 10 µm in the HIP consolidated milled Cu. Consolidation by FAST tended to give a wider range of dimple size, with 1 to 10 µm in milled Cu and 0.1 to 20 µm in Cu-2Y_2O_3. This was considered to result from failure at or away from the PPBs, where fine grained regions give rise to finer dimples away from the PPBs and larger dimples formed at the coarse grained boundary regions.

5.3.3 Microstructure

Microstructural analysis focused on Y_2O_3 containing alloys, and in particular the effect of sintering on the nanoparticles.

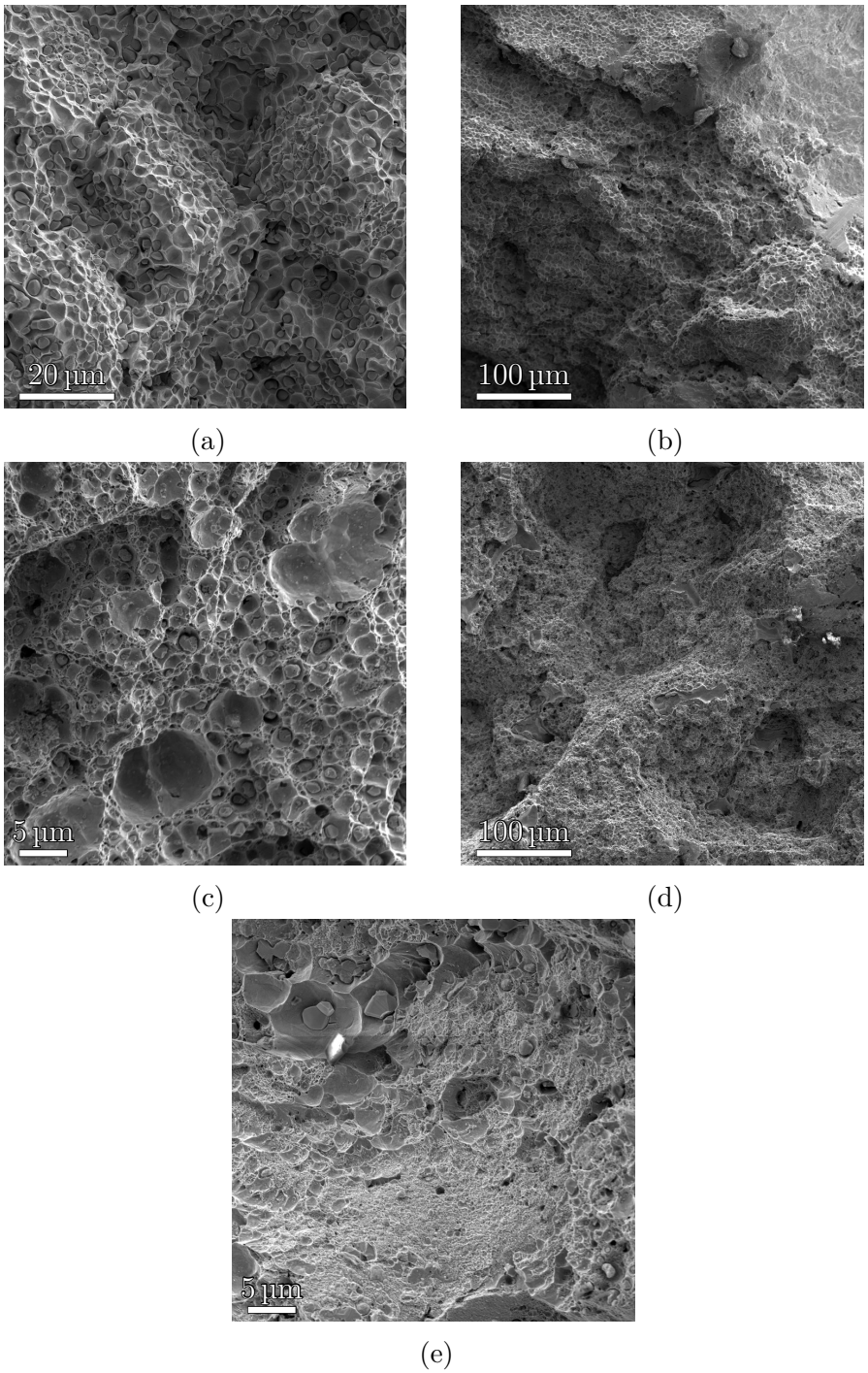

Figure 5.5: SE micrographs of typical tensile fracture surfaces. **(a)** FAST consolidated as-received Cu. **(b)** HIP consolidated 12 h milled Cu. **(c)** FAST consolidated 12 h milled Cu. **(d)** HIP consolidated 12 h milled Cu-2Y_2O_3. **(e)** FAST consolidated 12 h milled Cu-2Y_2O_3.

HIP consolidated Cu-2Y_2O_3

Figure 5.6 shows the typical microstructure of HIPed Cu-2Y_2O_3. Figure 5.6(a) shows large Y-rich particles (confirmed by EDS in Fig. 5.7(d)) with diameters of >500 nm, and the largest of these particles appeared to be polycrystalline. Fe contamination, shown in Fig. 5.7(e), was limited to the largest particles >250 µm. There were O-rich particles of typically 20 to 80 nm in diameter predominantly at grain boundaries, or in distinct lines indicating the prior grain or sub-grain boundaries. Evidence of abnormal grain growth was also apparent in Fig. 5.6(b), where there were relatively large grains, 500 nm diameter, denuded of fine particles. There were also annealing twins, with typical relatively large spacings of >200 nm, which were also often pinned by Y-rich particles as seen in Figs. 5.6(b) and 5.7(a).

Abnormal grain growth in Fe-ODS alloys has been suggested to result from heterogeneity - particularly the dispersoid spatial distribution - in the milled powder [111], rather than difficulties in precipitation of the oxide nanoparticles. In Fe-ODS alloys consolidated by FAST at 0.81T_m for 360 s abnormally large grains reached ∼30 µm diameter [108] and up to ∼150 µm in milled powder annealed at 0.78T_m for >2000 s [113]. A Cu-2.7Al_2O_3 alloy similar to that studied here, produced by internal oxidation had an average grain size of ∼60 µm after 7.2×10^3 s annealing at 700 °C, including significant abnormal grain growth with a critical grain diameter for grain breakaway of 0.8 µm suggested [54]. Although abnormal grain growth was less marked in the alloys here, it was likely that further heating of the HIP consolidated Cu-2Y_2O_3 would eventually promote more severe abnormal grain growth.

EDS analysis indicated that Y and O was at a 0.39:0.61 ratio in the resolvable particles (>100 nm), and therefore supporting the presence of Y_2O_3. The particles containing Fe had a ratio of Fe:Y:O of ∼0.18:0.24:0.58, suggesting a combination of Fe_2O_3 and Y_2O_3. These impurities were interpreted as pick-up from damage to the milling pot and media during milling.

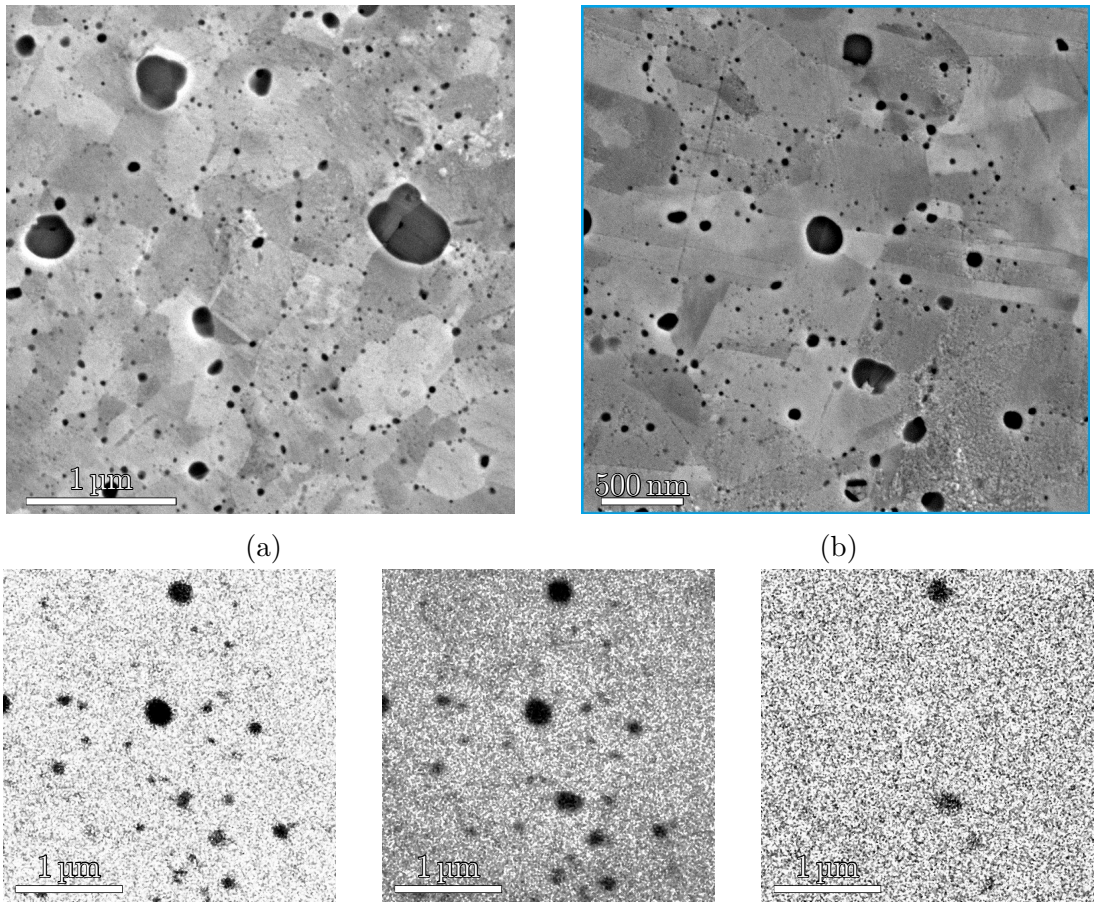

Figure 5.6: SEM-SE micrographs and EDS maps of Cu-2Y_2O_3 consolidated by HIP, **(a)** SE micrograph, **(b)** SE micrograph of EDS analysis region, **(c)** inverse O K map, **(d)** inverse Y L map, and **(e)** inverse Fe L map

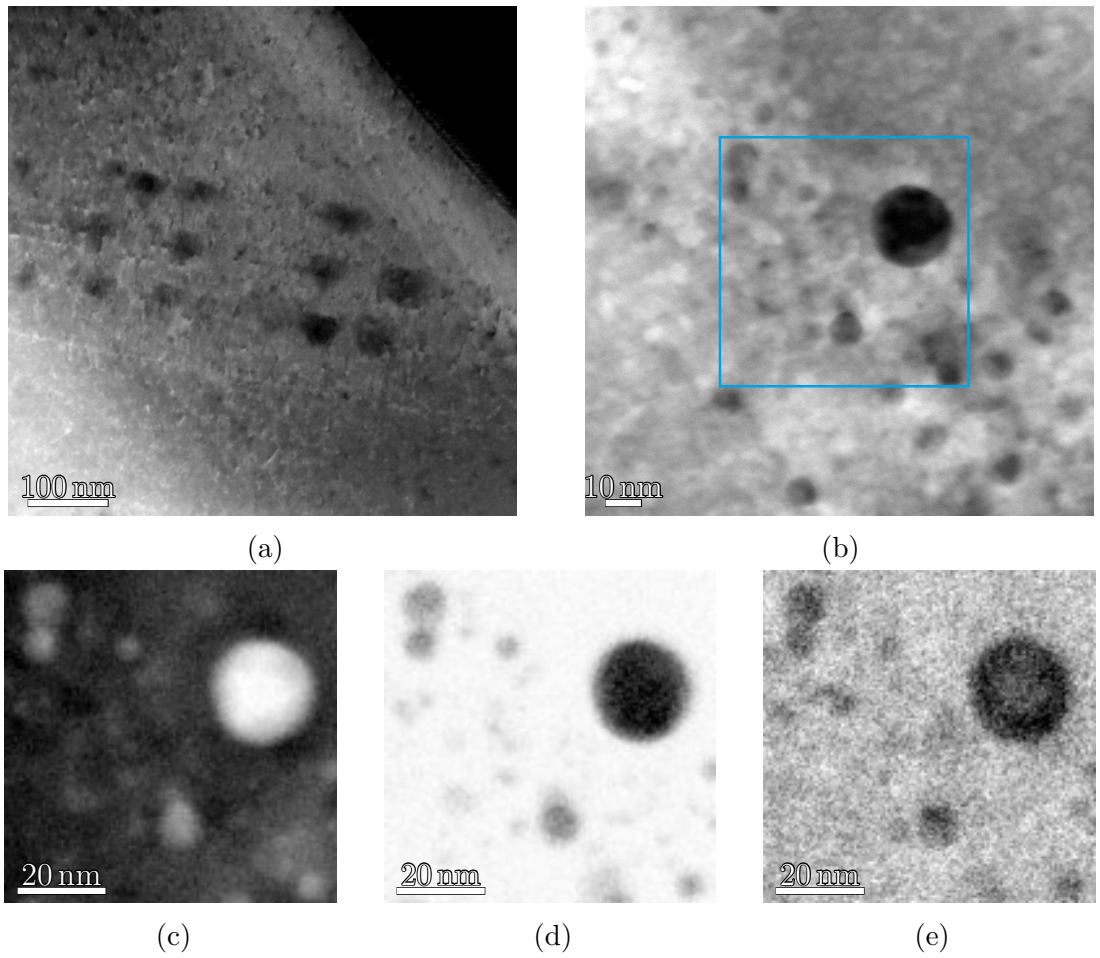

Figure 5.7: STEM analysis of Cu-$2Y_2O_3$ consolidated by HIP **(a)** HAADF image of twins with large precipitates along the twin boundaries, **(b)** HAADF Typical region of precipitates within a grain, with EDS region highlighted, **(c)** inverse Cu K+L map, **(d)** inverse Y K+L map, and **(e)** inverse O K map.

Figure 5.7 shows the typical microstructure observed after consolidation by HIP, with annealing twins already discussed shown in Fig. 5.7(a). Figure 5.7(b) shows a HAADF-STEM micrograph of fine oxide particles in Cu-2Y_2O_3 consolidated by HIP. EDS analysis revealed fine particles with a mean diameter of 7.0 ± 4.0 nm (obtained from 30 particles from 4 regions of 2 samples) that were rich in Y and O, as shown in Figs. 5.7(d) and 5.7(e) respectively. It was not possible to measure robust concentration ratios for either element due to surface oxidation of the thin samples, and it was unclear if Cu was present in the oxide particles or not since contributions from the Cu matrix could not be excluded.

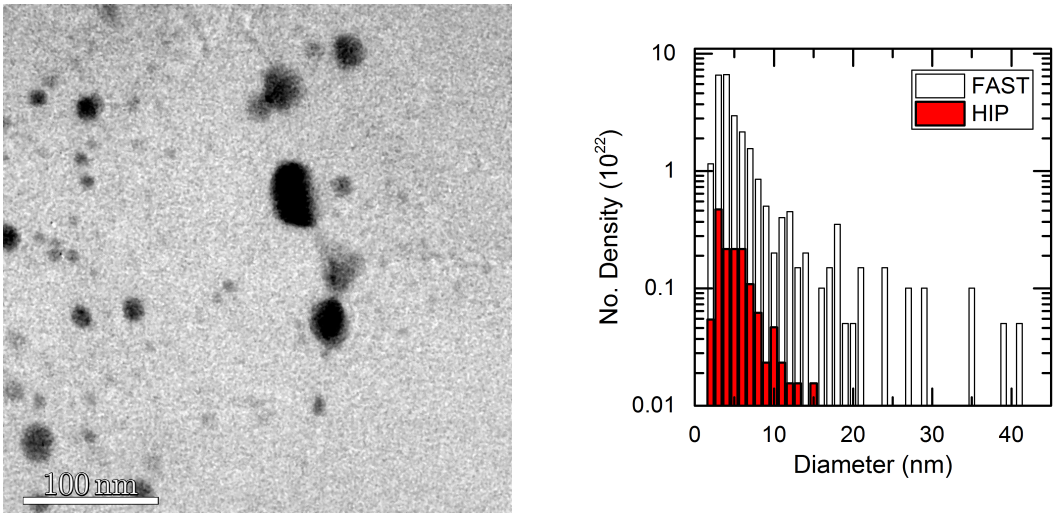

(a) (b)

Figure 5.8: EFTEM analysis of Cu-2Y_2O_3, **(a)** Y $N_{2,3}$ map showing segregation of Y to a grain boundary with one adjacent grain free of resolvable particles, and **(b)** particle size distributions for Cu-2Y_2O_3 consolidated by HIP and FAST from Y $N_{2,3}$ maps.

Statistical information on the nanoparticle size distribution was obtained from low-loss EFTEM analysis of the Y $N_{2,3}$ edge contribution, a typical example of which is shown in Fig. 5.8(a) where there were a combination of coarse >40 nm, and fine >10 nm nanoparticles. Three regions from two liftout samples were analysed with 194 Y-rich particles identified with a mean diameter of 4.8 nm and a mean inter-particle spacing of 40.5 nm. The size distribution of particles from EFTEM was comparatively

narrow and asymmetric with a large population of <7 nm diameter particles, as shown in Fig. 5.8(b). The mean particle number density was $1.5 \times 10^{22}\,\mathrm{m}^{-3}$ and nearly an order of magnitude smaller than that estimated in Section 4.3.2 for FAST consolidated Cu-$2Y_2O_3$ that had a mean particle number density of $8.24 \times 10^{22}\,\mathrm{m}^{-3}$.

The lower density of nanoparticles observed in EFTEM was attributed to the coarsening of oxide particles at grain boundary locations and triple points by Ostwald ripening aided by grain boundary mobility of any disassociated Y and O [46, 118], as shown in Fig. 5.6.

FAST consolidated Cu-$2Y_2O_3$

Figure 5.9 shows porosity in Cu-$2Y_2O_3$ consolidated by FAST, with macro-scale porosity of the order 20 µm (Fig. 5.9(a)) resulting from incomplete sintering between powder particles, and micro-scale porosity of the order 1 µm that is suggested to result from local melting. These latter pores were characterised by typically a more rounded morphology and surrounded by comparatively coarse grains (>1 µm diameter) exhibiting extensive twinning and without obvious particle pinning of grain boundaries. Larger >200 nm Y and O-rich particles were confirmed by EDS to be located in the solidified region. Overall, the porosity was higher than the HIP consolidated sample, with relative densities of 0.94 versus 0.95 respectively.

As previously described, the effect of the large applied current (∼3 kA) in FAST and the increase in sintering rate is not fully understood in terms of the combination of electromigration mass transport and joule heating effects [65]. Joule heating is expected to give rise to large localised heating effects due to field concentrations. It is hypothesised that as sintering progresses the powder consolidates and concentrates heating effects further in the more poorly consolidated areas - promoting the tendency for local overheating and melting.

Figure 5.10 shows more typical microstructural features of the FAST consolidated Cu-$2Y_2O_3$, including the prevelance of PPBs. The reduction in time spent above the

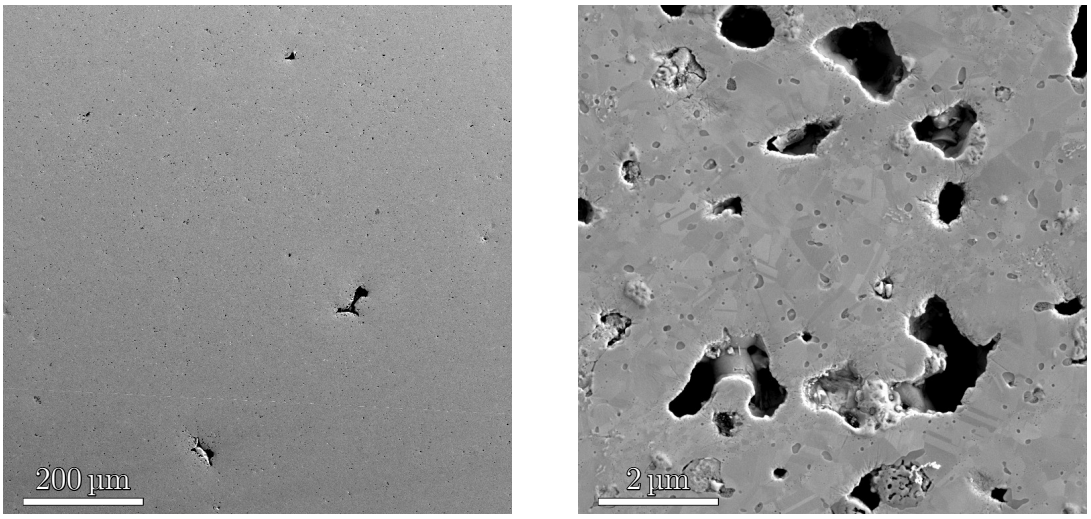

(a) (b)

Figure 5.9: SE micrographs showing porosity in Cu-2Y_2O_3 consolidated by FAST, **(a)** macro-porosity, and **(b)** region of localised melting leading to micro-porosity.

recrystallisation temperature in FAST compared with HIP limited opportunities for the ultrafine, highly deformed as-milled microstructure to recover, recrystallise and coarsen. Figure 5.10(a) shows that after FAST the grain diameter was ∼100 nm, with Y-rich particles of >40 nm diameter at grain boundaries and triple points. Similar HIP processed material had a grain diameter of 800 nm (Section 5.3.3).

Figure 5.10(b) again shows a typical PPB, which was a feature of both HIP and FAST consolidated Cu-2Y_2O_3 A distinct border region of large (>50 nm diameter) Y_2O_3 particles (estimated composition from EDS, not shown) are shown pinning the edge of the PPB. Pores and Fe-rich impurities were also located at PPB regions, as seen in Fig. 5.10(c) with large Y-O rich particles alongside Fe-O rich inclusions (Figs. 5.10(d) to 5.10(g)).

The ultrafine grains in Fig. 5.10 where confirmed by STEM imaging and Fig. 5.11(a) shows <100 nm diameter grains pinned by particles of 8 to 30 nm in diameter, which were confirmed Y and O-rich by EDS. STEM analysis using HAADF and EDS suggested >20 nm diameter particles at grain boundaries, as well as some particles <8 nm marking subgrain boundaries and distributed evenly within grains. These particles were also Y

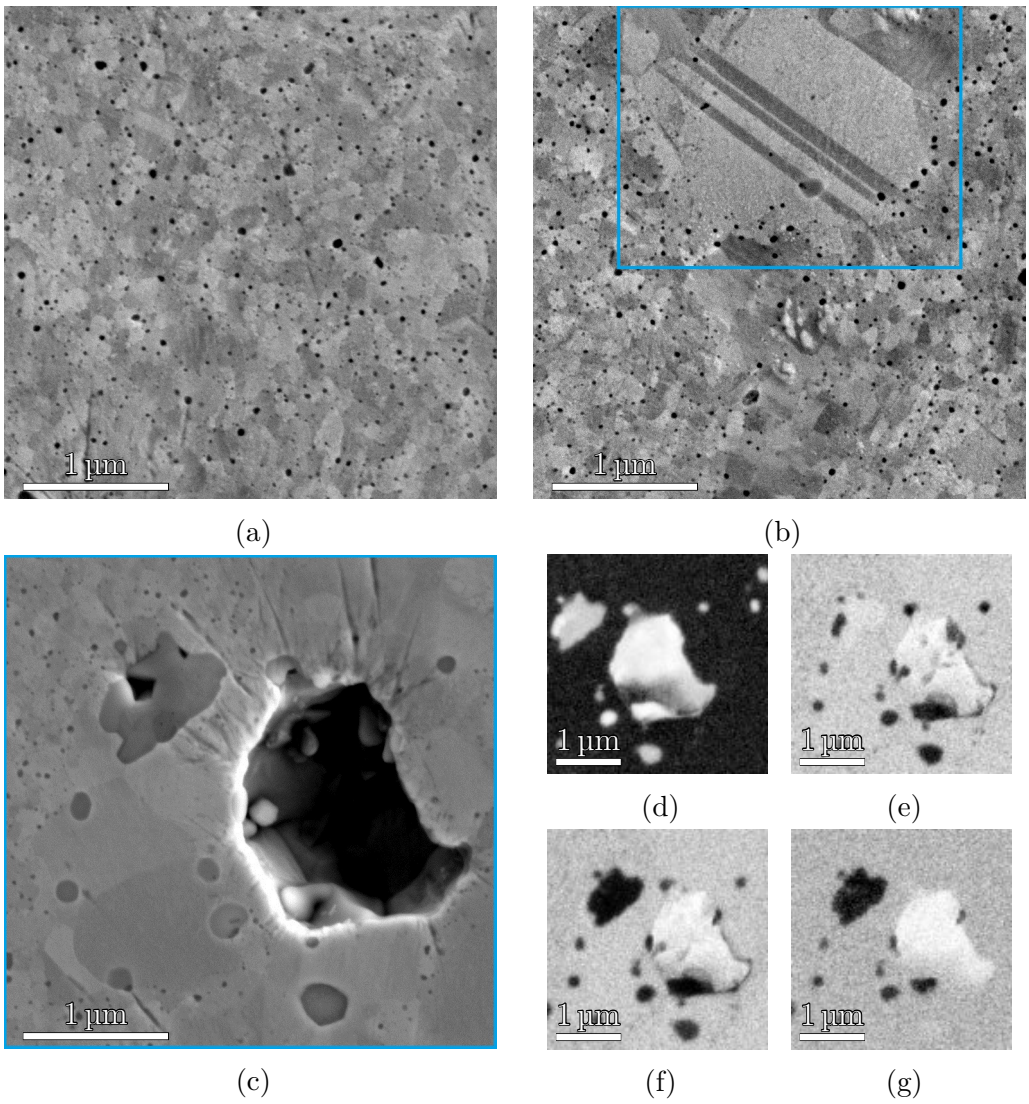

Figure 5.10: SE micrographs and EDS maps of FAST consolidated Cu-2Y_2O_3, **(a)** SE micrograph of prior-particle microstructure consisiting of fine grains and oxide particles (dark), **(b)** SE micrograph of PPB region denuded of particles and with large twins, **(c)** SE micrograph of pore at PPB, and region of EDS analysis, **(d)** inverse Cu L map, **(e)** inverse Y L map, **(f)** inverse O K map, and **(g)** inverse Fe L map

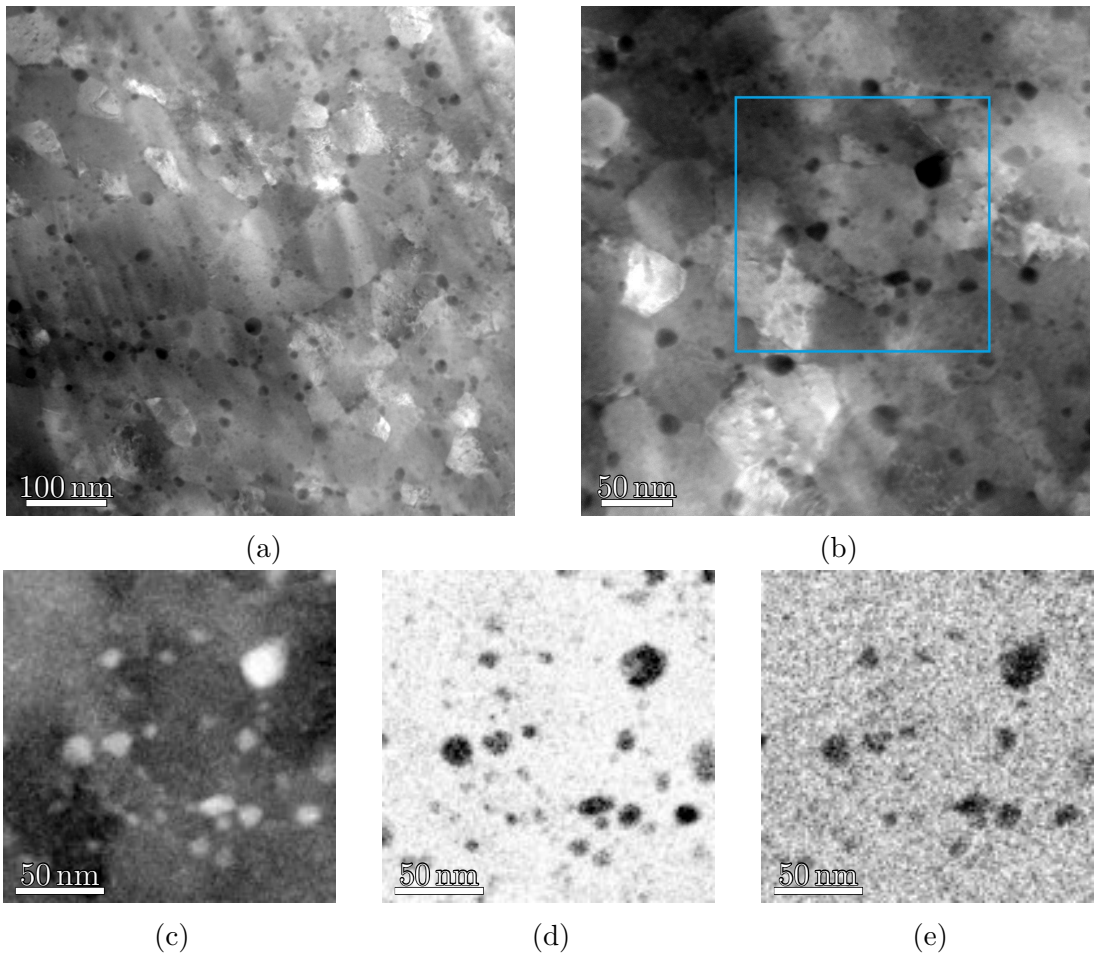

Figure 5.11: STEM analysis of Cu-$2Y_2O_3$ consolidated by FAST, **(a)** HAADF micrograph of typical region showing ultrafine microstructure, **(b)** HAADF micrograph of typical region of precipitates pinning grain boundaries, with EDS region highlighted, **(c)** inverse Cu K+L map, **(d)** inverse Y K+L map, **(e)** inverse O K map.

and O-rich according to EDS shown in Figs. 5.11(c) to 5.11(e). These fine nanoparticles were more prevalent in grains >100 nm. No reliable quantification of the Y:O ratio could be performed on these particles

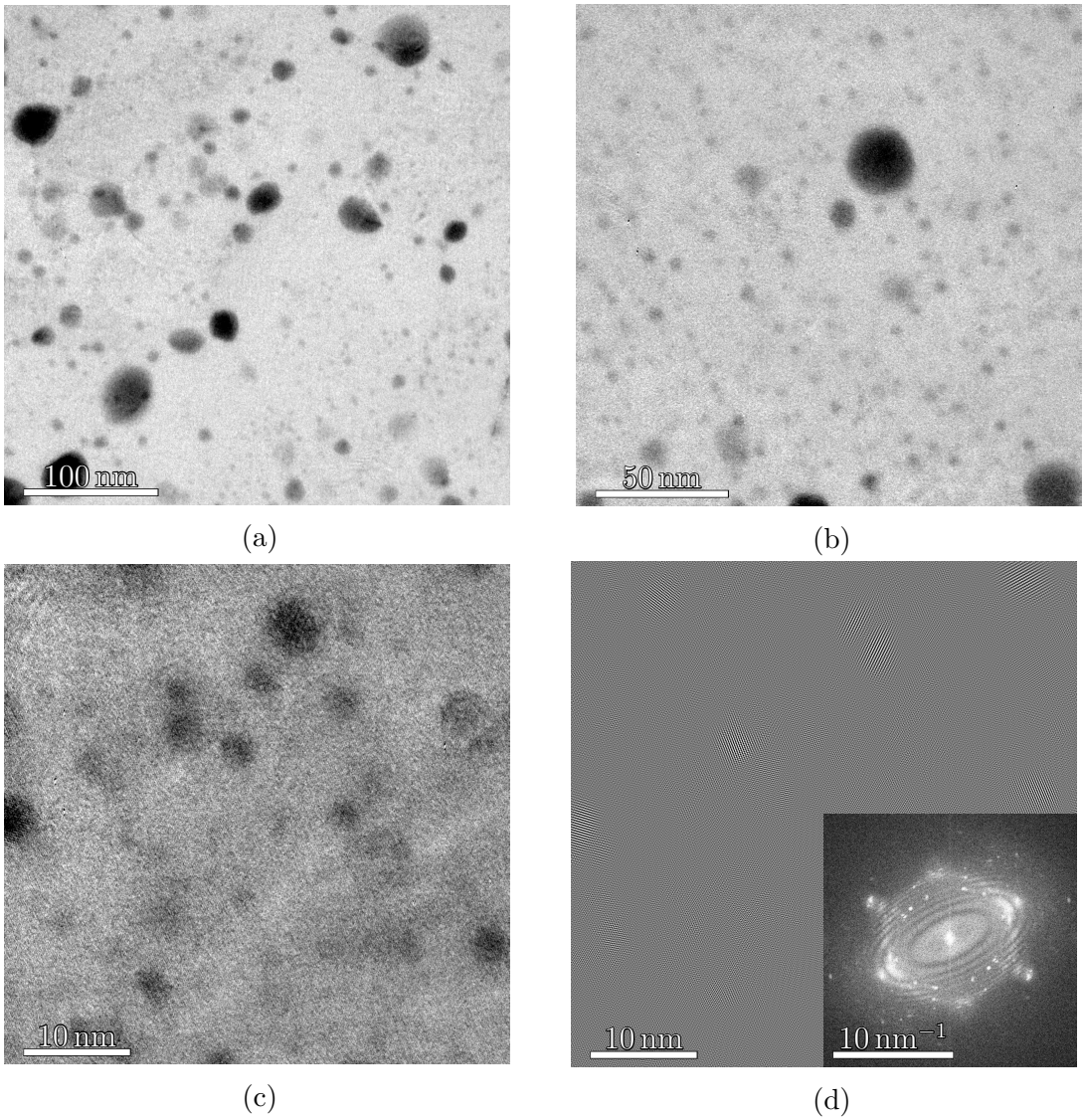

Figure 5.12: EFTEM Y $N_{2,3}$ maps of Cu-2Y_2O_3 consolidated by FAST ,**(a)**, **(b)**, **(c)** different regions at increasing magnifications, and **(d)** Fourier filtered micrograph showing crystalline particle contributions from bright-field (BF) micrograph of (c), with inset: Fourier transform.

Figures 5.12(a) to 5.12(c) show low-loss EFTEM maps of the Y-distribution in Cu-2Y_2O_3 prepared by FAST. EFTEM revealed a tendency for the Y-rich nanoparticles/clusters to align into striations with a spacing comparable with those in powder

prior to consolidation (Section 4.3.1, Fig. 4.13(c)) at ∼10 nm. This suggested that FAST consolidation did not lead to much direct deformation (resulting from the applied load) of the prior particle regions and that the Y and O did not diffuse far (<1 nm) during consolidation.

The particles in four regions from two liftout samples were analysed and 502 Y-rich particles were identified with a mean diameter of 5.4 nm and a mean inter-particle spacing of 15.8 nm. The size distribution of particles by EFTEM in FAST material was wider than similar measurements for HIP material previously shown in Fig. 5.8(b). Furthermore, the mean particle number density was $2.5 \times 10^{23}\,\mathrm{m}^{-3}$ for particles 1 to 40 nm in diameter, an order of magnitude greater than after HIP consolidation. It is proposed that the rapid heating rate and shorter time spent above the recrystallisation temperature resulted in a higher rate of nucleation of Y_2O_3 without allowing for diffusion led processes such as Ostwald ripening and particle coarsening. A higher number density of particles with diameters >10 nm was also suggested in the TEM examination of FAST consolidated material.

Figure 5.12(c) shows a region of Y-rich clusters <5 nm in diameter in a region free of grain boundaries. Figure 5.12(d) shows the same region with Fourier filtering of the Y contribution to the inset Fourier transform of the unfiltered TEM micrograph. Y-rich nanoclusters appeared semi-coherent or incoherent with the Cu matrix, with a random orientation relationship with the grain.

5.4 Summary

Consolidation of as-recieved Cu, milled Cu and MA Cu-2Y_2O_3 was investigated by HIP and FAST. The two techniques present opportunities and challenges for the manipulation of Cu-ODS alloy microstructures during consolidation.

Although HIP consolidation is considered a standard industrial powder processing technique, and is widely implemented, in this instance, the slow heating and cooling of

the powder compact due to the furnace limitations led to poor quality consolidation, and a low final bulk density. The microstructures showed significant coarsening from the as-milled microstructure with respect to grain size and Y and O-rich nanoparticles. Although full density was also problematic by FAST, a significantly higher number density of Y and O-rich nanoparticles was obtained by FAST which in turn stabilised grain diameters to <100 nm in FAST compared with >700 nm in HIP.

Mechanical properties were undermined by the residual porosity, especially with respect to room-temperature ductility and elongation to failure. There was limited necking at failure. Raising the consolidation temperature, or increasing the sintering time were not explored for HIP consolidation in part due to time/cost considerations and to avoid deleterious abnormal grain growth. Instead, lengthening sintering time in FAST consolidation is proposed, and initial results (not shown) using a smaller diameter die (20 mm) suggested this had a positive effect on the final density. However, scaling up to larger, more industrially relevant die sizes was not explored in the current work. Finally, it should be noted that 2 wt.% Y_2O_3 represents a very significant loading when the broader literature is considered. While useful in preliminary stages of optimisation to make nanoparticle identification easier, such high loadings likely also presented problems in ensuring sufficient densification and consolidation of the Cu under the parameters explored here. Indeed, industrial practice for many ODS alloys relies on the more aggressive (but harder to access) powder extrusion route.

From the results presented in this chapter, several considerations for consolidation of Cu-ODS materials are apparent:

- Neither HIP nor FAST consolidation gives complete densification of the Cu-$2Y_2O_3$ powder using typical sintering conditions based on the literature.
- HIP consolidation resulted in comparatively coarse grains and nanoparticles when compared with FAST consolidation.

- Significantly reoptimised FAST parameters and/or further thermomechanical treatment is required to obtain full density and the improvement in room temperature tensile mechanical properties required.

- Controlling the thermal exposure of the milled microstructure gives some control on the formation and coarsening of oxide nanoparticles and a significant number density of $\sim 10^{23}\,\mathrm{cm}^{-3}$ of $<10\,\mathrm{nm}$ particles was achievable.

Chapter 6

The effect of Ti additions on Cu-Y_2O_3

6.1 Introduction

Within the context of ODS Cu alloys for divertor applications, minimising the total fraction of solid-solution or precipitate/dispersion strengthening alloying additions is key to limiting losses in thermal conductivity [11] and the required mechanical enhancement and stability are instead provided by a low volume density but very high number density of small insoluble particles that act as pinning points and defect sinks. Ideally, pinning/sink particle size in the Y_2O_3-containing Cu-ODS alloys should be tailored such that any alloying additions are minimised or removed while achieving the required balance of strength, creep resistance and thermal properties. The addition of Ti as a refining agent for nanoparticles has been explored extensively in Fe-ODS alloys [24, 25, 27, 30, 108, 119]. As discussed in Section 2.4.1, the role of Ti in promoting the nucleation of Y-containing oxide particles has been suggested to be either through aiding in the coherency of the nanoclusters with the matrix allowing lower energy interfaces [30], or by assisting directly in the pre-nucleation clustering during re-precipitation [119]. The Cu-ODS alloys presented thus far contain a comparatively large weight fraction of 2 wt.% Y_2O_3, equivalent to >3.5 vol.% Y_2O_3. It is hypothesised that, based on its effect in steels, Ti may offer a route to

refine the oxide nanoparticle diameters in Cu-ODS alloys. If so, a reduction in the total fraction of oxide additions may be achieved while maintaining a high number density of particles. The mean number density of oxide nanoparticles in Cu-2Y_2O_3 analysed in Chapter 4 was $8.2 \times 10^{22}\,m^{-2}$ and the mean particle diameter was 7.1 nm. On the basis of particle strengthening according to the Orowan model [19], if the Y_2O_3 concentration is to be reduced from 2 wt.% to 0.5 wt.% while maintaining the same inter-particle spacing, the particle number density should be increased to $3.8 \times 10^{23}\,m^{-2}$ and the average particle diameter reduced to ∼3.6 nm.

This chapter investigates how Ti might be introduced to Cu-ODS alloy effectively so that it may react with Y, and studies the resulting effect of Ti additions on the microstructure.

6.1.1 Ti addition

Ti has limited solid-solubility in Cu of <0.1 wt.% at room temperature, as shown in the equilibrium Cu-Ti binary phase diagram in Fig. 6.1. Nonetheless, Ti is significantly more soluble than Y (0 wt.% Y, Fig. 4.3) at room temperature. An extension in Ti solubility to ∼1.5 wt.% in mechanical alloying has been reported [120].

To ensure that the Ti is distributed within the Cu matrix to react with Y during MA or subsequently, various potential milling strategies were investigated, building on previous work on the dissolution of Ti in Cu [122], and are shown schematically in Fig. 6.2:

(a) Elemental addition - Ti powder is added to the Cu and Y_2O_3 powder blend during mechanical alloying.

(b) Master alloy - Ti is mechanically alloyed with Y_2O_3 to form an alloy or mixture first, which is then mechanically alloyed with Cu powder.

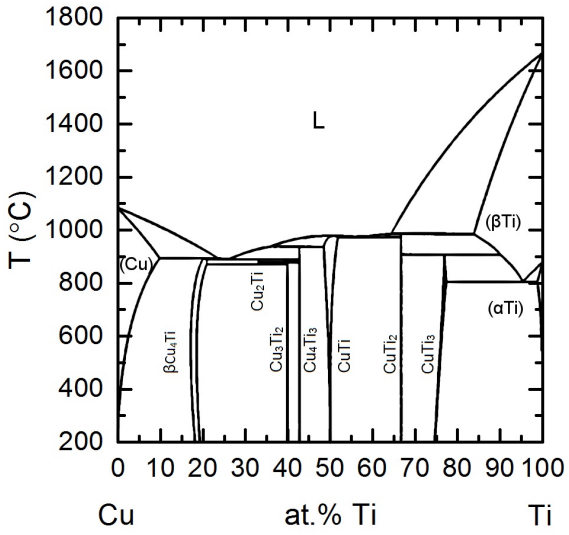

Figure 6.1: The Cu-Ti phase diagram, reproduced from [121]

(c) Partial pre-alloy - Cu is alloyed in the melt with a moderate concentration of Ti, gas atomised into a powder, and then mechanically alloyed with Cu and Y_2O_3 powder.

(d) Pre-alloy - Cu is alloyed in the melt with the required concentration of Ti and gas atomised to give a powder which is then mechanically alloyed with Y_2O_3 powder.

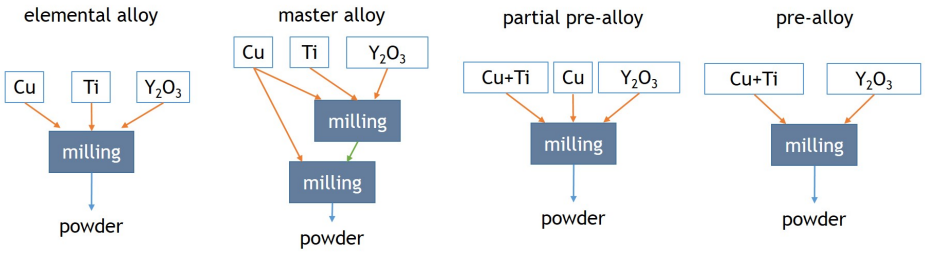

(a) (b) (c) (d)

Figure 6.2: Schematic representation of the four processing routes for the incorporation of Ti into Cu-Y_2O_3 ODS alloys by MA.

6.2 Results and Discussion

6.2.1 Addition route

The evolution of the powder microstructure and other properties, for each of the routes in Fig. 6.2, was investigated as a function of time. Selected powders that showed promise were chosen for sintering and further characterisation. In all cases, best efforts were used to minimise O contamination from air. The various powder blends were milled for 36 hours and their microstructure examined after 12 and 36 hours.

Elemental Ti addition

Elemental additions of Ti directly during the MA of Cu-Y_2O_3 were made using a fine Ti powder of 99.9% purity, with a mean powder diameter of 35 µm, as shown in Fig. 6.3. The Cu, Ti and Y_2O_3 powders were milled directly under the MA conditions identified in Chapter 4, hereafter referred to as standard conditions (Fritsch P5 planetary mill, 250 rpm, 10:1 BPR, 20:40 running:pause time during milling).

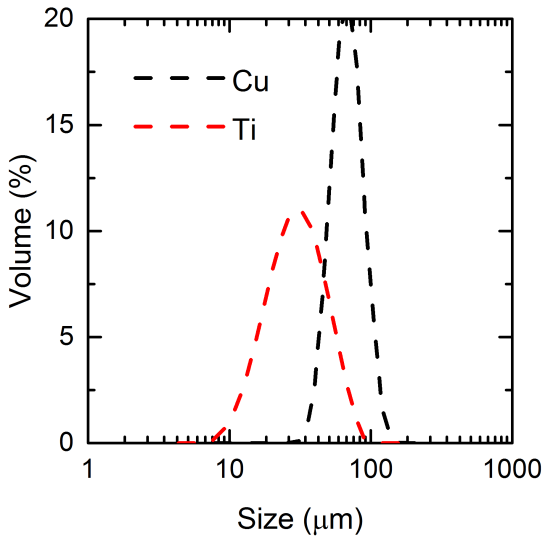

Figure 6.3: Size distribution of Cu and Ti powders measured by laser diffraction.

The Ti powder was refined and partially dissolved into the matrix Cu, with no obvious Ti-only particles persisting after 12 hours of milling. However, it was remarked

in every experiment that the addition of Ti led to agglomeration of the Y_2O_3 powder, which inhibited Y_2O_3 dissolution. Figure 6.4(a) shows large particles/agglomerates (>1 µm diameter) rich in Ti and Y (confirmed by EDS, not shown), with finer particles (<50 nm) also present after 12 hours milling. Further milling to 36 hours provided some additional break-up of the larger particles Fig. 6.4(b), but a distribution of >200 nm diameter oxide particles/agglomerates persisted.

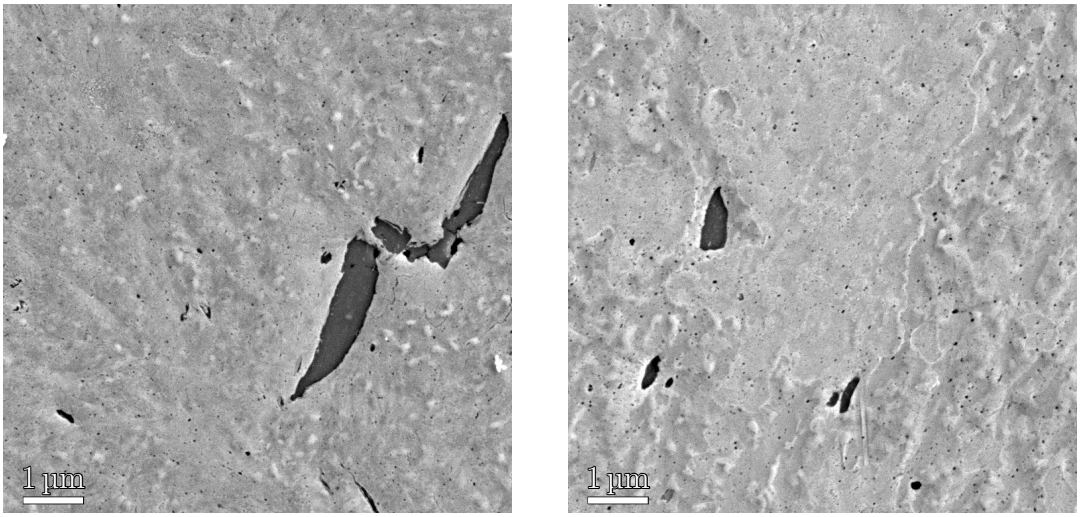

(a) 12 hours of milling (b) 36 hours of milling

Figure 6.4: SE micrographs from Cu-1Y_2O_3-1Ti powder produced by MA of elemental Ti powder with Cu and Y_2O_3 powders. Agglomerates of of Y, Ti, and O appear dark due to Z-contrast.

Master-alloy addition

First, a Ti and Y_2O_3 containing master-alloy powder was MAed, with a composition of Cu-36Y_2O_3-13Ti, for 12 hours in a stabilised ZrO_2 pot with ZrO_2 spherical milling balls. The alloy composition was chosen as it provides equimolar amounts of Ti and Y atoms, and may favour the formation of $Y_2Ti_2O_7$, as observed in Ti-containing Fe-ODS alloys [25].

The Cu master-alloy powder was then milled with Cu under the standard conditions for 36 h. However, MA was comparatively slow to refine the Ti and Y_2O_3 containing master-alloy powder particles, as shown in Fig. 6.5(a). Large particles greater than

1 µm were obvious within the microstructure, though interspersed with some finer particles below 100 nm. The larger particles in Fig. 6.5 contained a relatively high concentration of Ti, Y and O, with some also containing a significant (occasionally dominant) concentration of Fe.

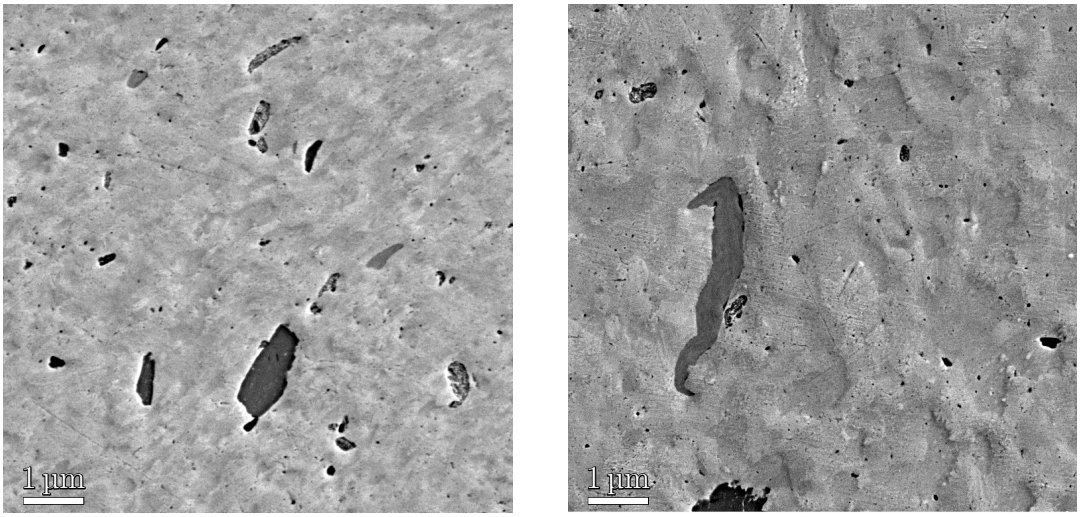

(a) 12 hours of milling (b) 36 hours of milling

Figure 6.5: SE micrographs from the master-alloy Cu-1Y_2O_3-0.36Ti powder produced by MA of a MA Cu-36Y_2O_3-13Ti powder with additional Cu. Agglomerates of of Y, Ti, and O appear dark due to Z-contrast.

Partial pre-alloyed addition

A pre-alloyed Cu-10Ti powder was milled with Y_2O_3 and additional Cu to give a final composition of Cu-1Y_2O_3-1Y_2O_3Ti, using the standard milling conditions for up to 36 h.

After 12 hours of milling there were >2 µm diameter Y, O and Ti-rich agglomerates shown in Fig. 6.6(a) (confirmed by EDS, not shown). Between the larger agglomerates, there was a finer distribution of smaller (<100 nm) agglomerates. After 36 hours of milling, the agglomerate diameter reduced to <1 µm as shown in Fig. 6.6(b). Although milling for 36 h was generally not preferred because of Fe and O contamination issues, it demonstrated the potential for long-term milling and partial pre-alloying in terms of promoting more even Ti and Y_2O_3 distributions.

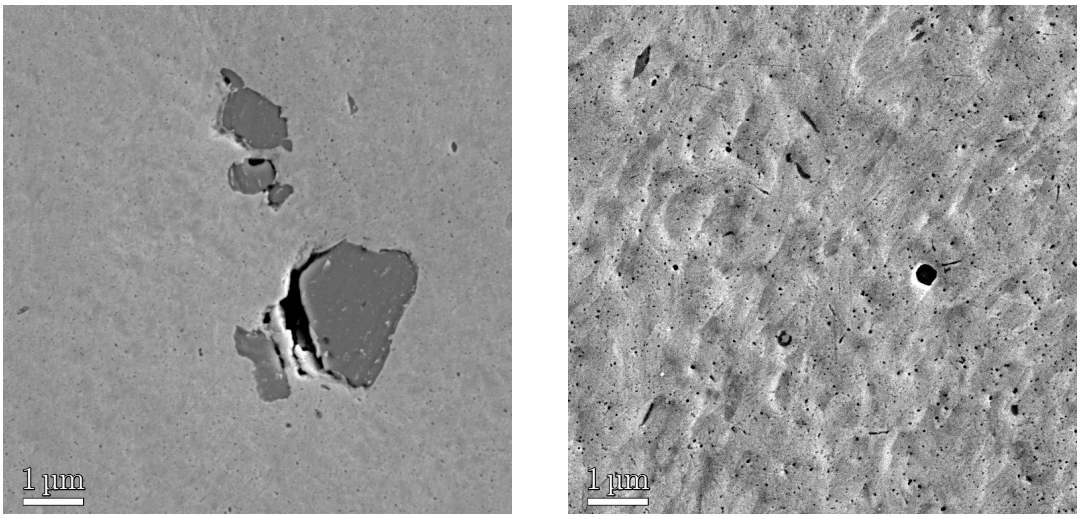

(a) 12 hours of milling (b) 36 hours of milling

Figure 6.6: SE micrographs from Cu-1Y_2O_3-1Ti powder produced by MA of a pre-alloyed Cu-10Ti powder with Cu and Y_2O_3 powders. Agglomerates of of Y, Ti, and O appear dark due to Z-contrast.

6.2.2 Powder properties

Powder hardness

To evaluate the effectiveness of the dissolution and mixing of the various powders, the microhardness of the powder was taken from polished cross-sections and investigated as a function of milling time, as shown in Fig. 6.7.

The alloy without any Ti additions but $2Y_2O_3$ hardened most rapidly at $0.16\,\mathrm{MPa\,s^{-1}}$ (best linear fit to hardness evolution at times $\leq 3\,\mathrm{h}$), followed by the partial pre-alloyed Cu-Ti-Y_2O_3 at $0.10\,\mathrm{MPa\,s^{-1}}$. A higher initial hardening rate may be attributed to an improvement in dislocation pinning, allowing an increase in the amount of work hardening that may be achieved [98, 99]. It should be noted that a higher initial hardening rate does not necessarily correlate with a higher plateau hardness: Table 6.1 summarises the effect of addition route on the powder hardness with milling time and shows the similar plateau hardnesses that were recorded for the elemental alloy and partial pre-alloy approaches.

Beyond 12 hours of milling, there was apparent powder softening in Fig. 6.7, most

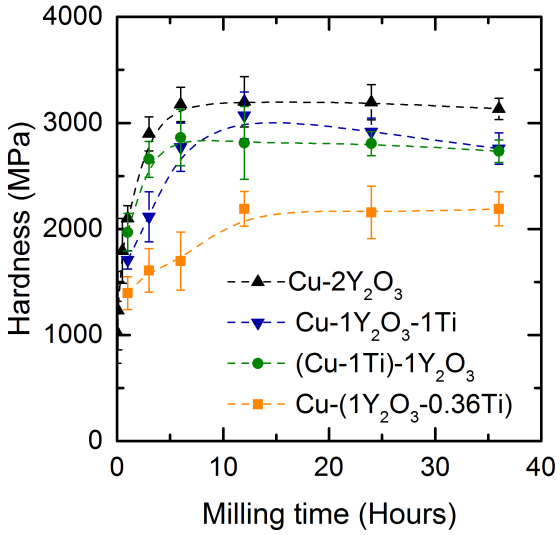

Figure 6.7: Effect of milling time on Vickers microhardness of powders during mechanical alloying of elemental addition (Cu-1Ti-1Y_2O_3), partial pre-alloyed addition ((Cu-1Ti)-1Y_2O_3), and master-alloy addition (Cu-(1Y_2O_3-0.36Ti)), compared with Cu-2Y_2O_3

Table 6.1: Effect of Ti and the addition route on the initial hardening rate (IHR) during the first three hours of milling, and the Vickers microhardness in the plateau region beyond 12 hours of MA.

Composition	IHR ($MPa\,s^{-1}$)	Plateau microhardness (MPa)
Cu-2Y_2O_3	0.16	3180 ± 90
Cu-1Ti-1Y_2O_3	0.06	2890 ± 170
Cu-(1Y_2O_3-0.36Ti)	0.03	2180 ± 190
(Cu-1Ti)-1Y_2O_3	0.10	2770 ± 180

strongly in the elemental powder. Although the mechanism of softening was not clear, it may relate to gradually increasing contaminants from the milling pot and milling media. In particular, there was Fe contamination into the larger particles, which were often associated with Ti, Y and O pick-up. It has been speculated that this may have the effect of reducing the matrix defect density and so reduces the total amount of work-hardening [19].

Agglomeration of Ti, Y, O and Fe

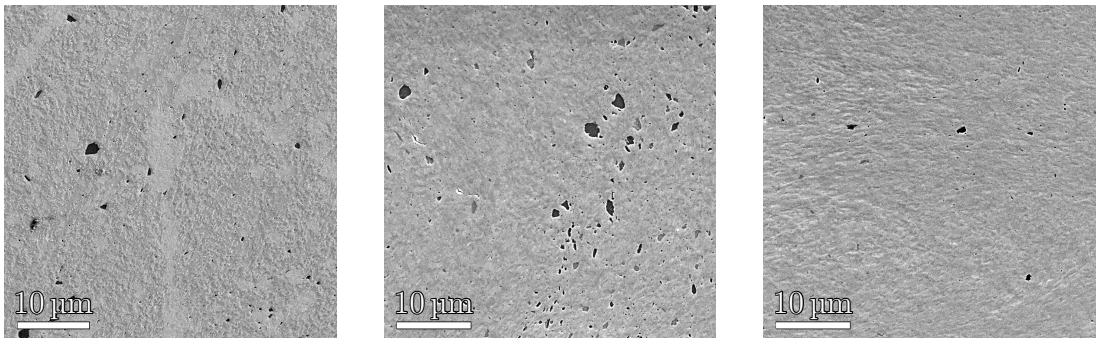

(a) (b) (c)

Figure 6.8: Secondary electron micrographs showing comparatively large (>1 µm) agglomerates in powders of the different Ti addition routes after 12 hours of milling. **(a)** Elemental alloy. **(b)** Master alloy. **(c)** Partial pre-alloy (from Cu-10Ti).

Ready agglomeration of Ti and Y presented a significant problem for the effective dissolution of Ti into Cu. The ductile nature of Cu meant that without prior hardening additions, i.e precipitates or oxide dispersions, there was insufficient work-hardening and limited fracture of the powder particles and hence distribution of any subsequently introduced alloying elements will be poor [123]. Figure 6.8 shows agglomerates (dark) in powders after 12 h using the different Ti addition routes. The elemental and master alloy addition routes, shown in Figs. 6.8(a) and 6.8(b) respectively, both had relatively high number densities of larger agglomerates (>0.5 µm), which supported the low plateau hardnesses in Fig. 6.7 and Table 6.1, since grain boundary and dislocation pinning effects were reduced. The partial pre-alloy route in Fig. 6.8(c) suggested a

comparatively low concentration of agglomerates.

Figure 6.9 shows the extent of agglomeration of Ti and Y in the master-alloy mechanical alloying route. There were agglomerates of 0.5 to 5 µm in powders after 12 h, and after 24 h and 36 h, there were both Fe-based flake-like particles and co-locations of Y, Ti and O in spherical particles. It is proposed that the two separate rounds of MA significantly increased the alloy contamination by additional erosion of the milling pot and media.

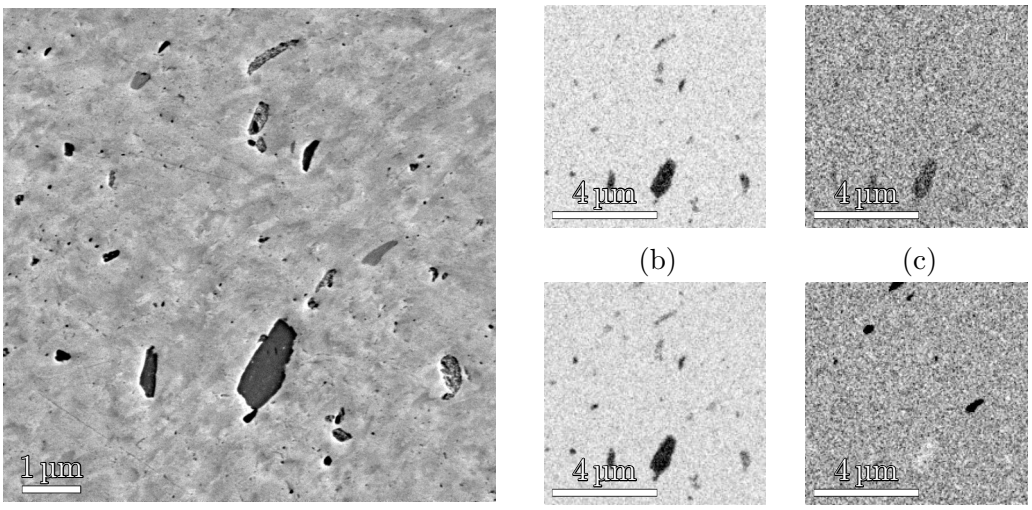

Figure 6.9: Inverse EDS maps from Cu-1Y_2O_3-0.36Ti powder after 12 h of milling **(a)** Secondary electron micrograph. **(b)** Y L map. **(c)** Ti L map. **(d)** O K map. **(e)** Fe L map.

EDS analysis of agglomerates >1 µm in diameter revealed a Y:Ti:O ratio of ∼2:5:9 in the partial pre-alloy and elemental powders, as shown in Table 6.2. The agglomerates may be a mixture of Y_2O_3 with Ti in various states/fractions of oxidation, as well as a minor Cu component. Conversely, the nominal master-alloy Y:Ti:O ratio was close to $Y_2Ti_2O_7$.

Fe contamination was limited to particles >200 nm and generally not co-located with Ti and Y, as seen in Fig. 6.10. In particular, Fe-rich regions tended to be located alongside the Y and Ti-rich agglomerates, as shown in Figs. 6.10(b) to 6.10(e).

Table 6.2: Effect of Ti addition route on the composition of agglomerates of Y-Ti-O in milled powders (both 12 and 36 hours), from EDS analysis. All values are shown as wt.% (at.%).

Route	Y	Ti	O
Elemental	0.32 ± 0.02 (0.13)	0.42 ± 0.01 (0.31)	0.19 ± 0.00 (0.56)
Master	0.40 ± 0.04 (0.16)	0.41 ± 0.09 (0.31)	0.18 ± 0.02 (0.53)
Partial pre-alloy	0.31 ± 0.02 (0.12)	0.42 ± 0.04 (0.31)	0.19 ± 0.01 (0.56)

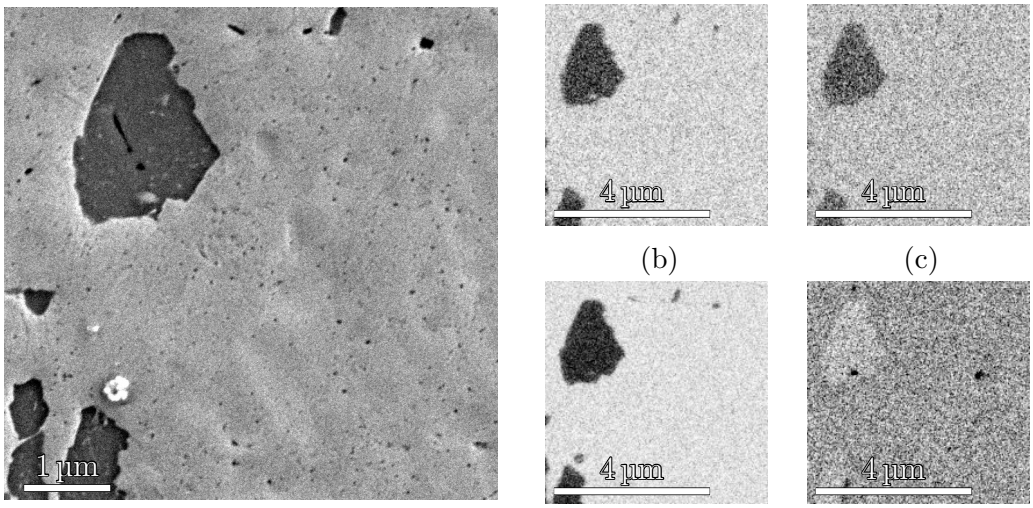

Figure 6.10: Inverse EDS maps of Cu-1Y_2O_3-1Ti powder after 12 hours of milling **(a)** Secondary electron micrograph. **(b)** Y L map. **(c)** Ti L map. **(d)** O K map. **(e)** Fe L map.



(a) Elemental 1 h (b) Elemental 12 h (c) Elemental 36 h

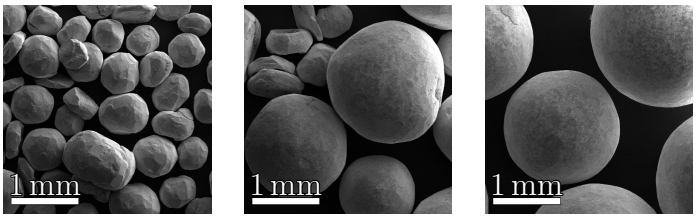

(d) Master-alloy 1 h (e) Master-alloy 12 h (f) Master-alloy 36 h



(g) Partial pre-alloy 1 h (h) Partial pre-alloy 12 h (i) Partial pre-alloy 36 h

Figure 6.11: Effect of milling time and Ti addition route on powder morphologies of Cu-Y_2O_3-Ti after 1, 12 and 36 hours of milling.

Effect of Ti addition route on powder morphology

As previously described, because of the comparatively high ductility and low work-hardening rate of Cu, when the added Y_2O_3 fraction was reduced to more typical levels, there was a reduction in the powder refinement that could be achieved. There was an increased tendency for cold-welding of flakes to dominate over fracture, as described earlier in Section 4.2.1. In general, the levels of Ti additions that were pursued here did not provide sufficient solute hardening to compensate for the lower Y_2O_3 fraction.

Figure 6.11 shows the change in morphology of the powders for each Ti addition route. Figures 6.11(a) to 6.11(c) show the elemental route and the initial formation of a distribution of powder particles, with a proportion of particles around 200 µm

in diameter and other particles of ∼1.2 mm diameter after 12 h, and then continued welding which resulted in very large >1.5 mm diameters after 36 h. The master-alloy route shown in Figs. 6.11(d) to 6.11(f) produced the most obvious particle welding, with smooth powder particles formed after 12 h that coarsened with further milling. The partial pre-alloyed route, shown in Figs. 6.11(g) to 6.11(i), was the least effective initially, but after 12 h particles with diameters between 500 µm and 2 mm were formed. The partial pre-alloy powder was considered suitable for further exploration, with other routes showing insufficient mixing of elements and dispersion of Y_2O_3, along with significant Fe pick-up.

6.2.3 Fully pre-alloyed powder

The pre-alloyed route based on Cu-10Ti gas atomised powder offered further promise for Ti dispersion into Cu prior to consolidation, although these powders always started with inevitable inter-dendritic microsegregation of Ti. During milling, the Ti again tended to promote reaction with Y and O but was less than in other routes. The initial selection of the relatively concentrated Cu-10Ti was based on quick and commercial availability of this powder for proof of concept, but given the imperative to reduce the Ti to more "normal" ODS concentrations, a bespoke fully pre-alloyed Cu-0.5Ti powder was then ordered and prepared by gas atomisation by Nanoval GmbH, Germany, with a mass mean diameter of ∼45 µm [124].

Figure 6.12 shows a typical Cu-0.5Ti powder particle with just-resolvable inter-dendritic microsegregation of Ti at sub-micron length scale (Fig. 6.12(b)). Figure 6.12(c) shows no obvious O pick-up other than the inevitable oxide shell.

Following MA with 0.5wt.% Y_2O_3, Fig. 6.13 shows significant grain refinement and complete destruction/recrystallisation of the as-solidified dendrite structure, which was replaced by polygonal grains of ∼500 nm. There was again evidence of persisting larger Y_2O_3 particles and possible Fe-rich agglomerates, but in general, their length-scale was

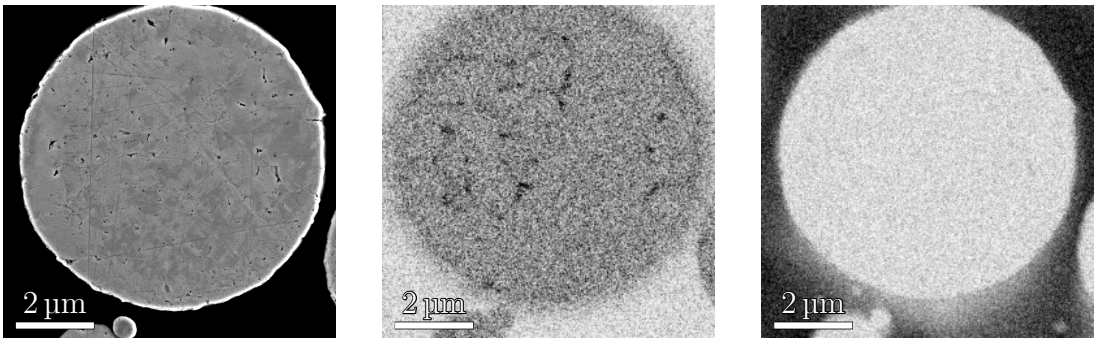

(a) (b) (c)

Figure 6.12: EDS maps of Cu-0.5Ti pre-alloyed powder before milling. **(a)** Secondary electron micrograph. **(b)** Inverse Ti L map. **(c)** Inverse O K map.

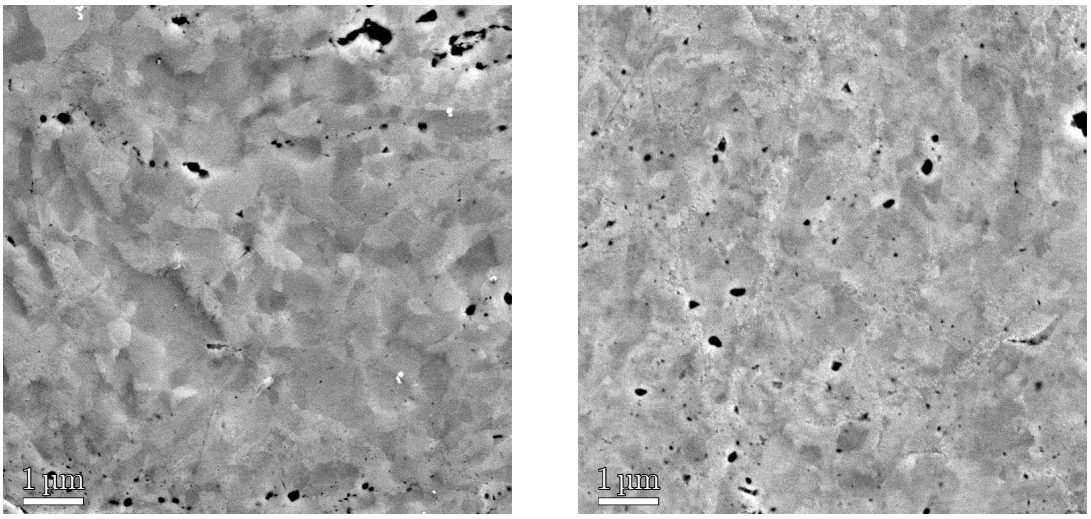

Figure 6.13: Secondary electron micrographs of 12 hour milled fully pre-alloyed powder of Cu-0.5Ti-0.5Y_2O_3

reduced when compared with Cu-10Ti and the other Ti-incorporation experiments.

6.2.4 Consolidated Ti-Y_2O_3 containing alloys

The partial pre-alloyed and fully pre-alloyed powders showed the better distributions of Ti after MA, which might allow refinement in the subsequent formation of Y_2O_3-based nanoparticles.

Partial pre-alloyed powders with final nominal composition Cu-0.25Y_2O_3-0.25Ti and Cu-0.5Y_2O_3-0.5Ti were produced with 12 h total milling from Cu-10Ti pre-alloyed powder and additional Cu powder. The powders were canned under vacuum in mild steel and HIPed at the University of Birmingham under conditions of: 4 h vacuum degas at 200 °C and then 850 °C for 2 h and 150 MPa. Table 6.3 shows that the alloy hardness following HIP was 1400 ± 190 MPa and higher than 1180 ± 160 MPa for Cu-2Y_2O_3 sintered under the same conditions (Chapter 5).

Table 6.3: Hardness of partial pre-alloyed and HIPed Cu-Y_2O_3-Ti alloys compared with Cu-2Y_2O_3 subject to identical processing (all compositions in wt%)

Alloy	Hardness (MPa)
Cu-0.25Y_2O_3-0.25Ti	1400±190
Cu-0.5Y_2O_3-0.5Ti	1370±100
Cu-2Y_2O_3	1180±160

In order to investigate if the Ti was having any effect on the Y distribution in the consolidated material, low-loss EFTEM covering Y $N_{2,3}$ and Ti $M_{2,3}$ edges was used, as shown in Fig. 6.14. Figure 6.14(a) shows Y-containing particles which were predominantly >20 nm in diameter while Fig. 6.14(b) shows Ti-containing nanoparticles predominantly <15 nm within grains. Figure 6.14(c) shows regions that had a greater number of counts for either Y or Ti across the same length of edge decay, indicating that whilst some particles were predominantly rich in one or the other of the alloying elements, the majority contained a co-location of both of Y and Ti.

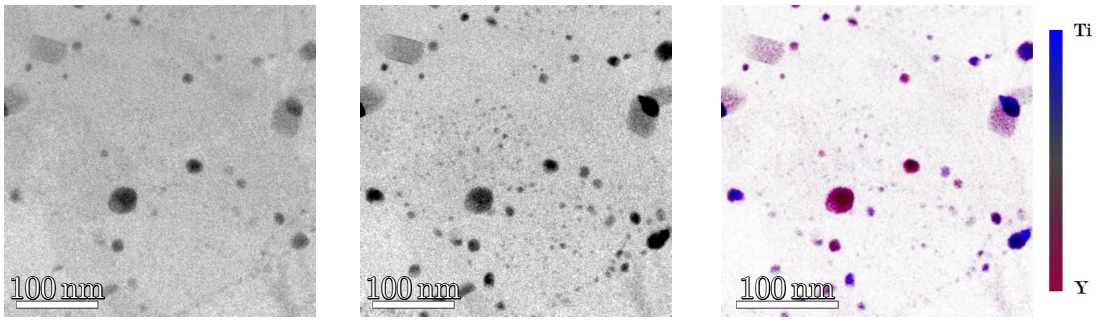

(a) (b) (c)

Figure 6.14: EFTEM maps of Cu-0.25Y_2O_3-0.25Ti after HIPing, showing **(a)** Y $N_{2,3}$ map, **(b)** Ti $M_{2,3}$ map, and **(c)** co-localisation showing differences in the counts for Y and Ti.

Figure 6.15 shows grain boundary pinning by >30 nm Y-Ti-rich particles located at grain boundary triple-points and significantly coarser than particles <10 nm within grains. As shown in Chapter 5, the use of FAST allowed some retention of the fine MA microstructures whereas HIP involved greater thermal exposure so that the oxides coarsened comparatively quickly perhaps because the grain boundaries provided fast diffusion paths for Y, Ti and O [118].

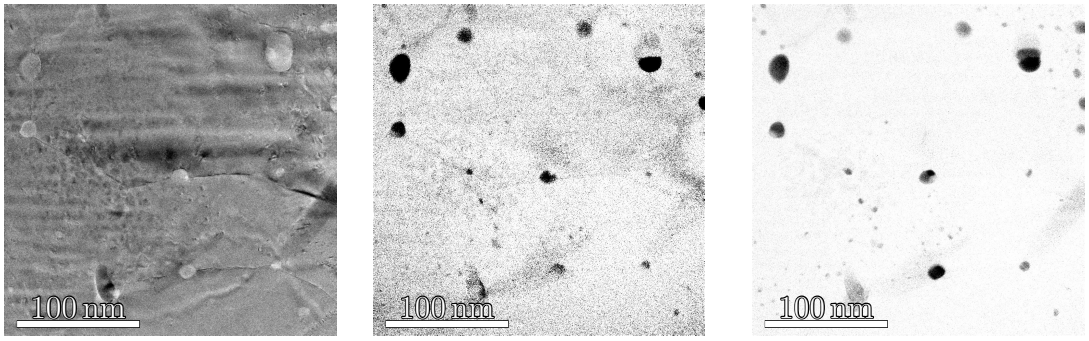

(a) (b) (c)

Figure 6.15: HIPed Cu-0.25Y_2O_3-0.25Ti, **(a)** Bright field TEM micrograph of a ~200 nm diameter grain. **(b)** Inverse Y $N_{2,3}$ map. **(c)** Inverse Ti $M_{2,3}$ map.

Figure 6.16(a) shows the particle size distribution obtained from Y and Ti-rich particles from EFTEM maps. A total of 423 particles from 7 regions on two liftouts from the HIPed Cu-0.25Y_2O_3-0.25Ti were counted. The nanoparticles had a mean diameter of 7.7 nm and a median diameter of 5.0 nm, with a mean interparticle spacing

of 39 nm. Figure 6.16(b) shows the particle volume distribution from the same counts, with a peak in the distribution at ∼20 nm and anomalous individual >30 nm particles. There was a slight reduction in the nanoparticle mean and median diameters on the addition of Ti when compared with Cu-Y_2O_3 alloys by using a fully pre-alloyed powder. Nonetheless, the particle number density, $1.8 \times 10^{22}\,m^{-3}$, was not significantly improved and the overall volume fraction of additions was probably too high from a thermal conductivity point of view.

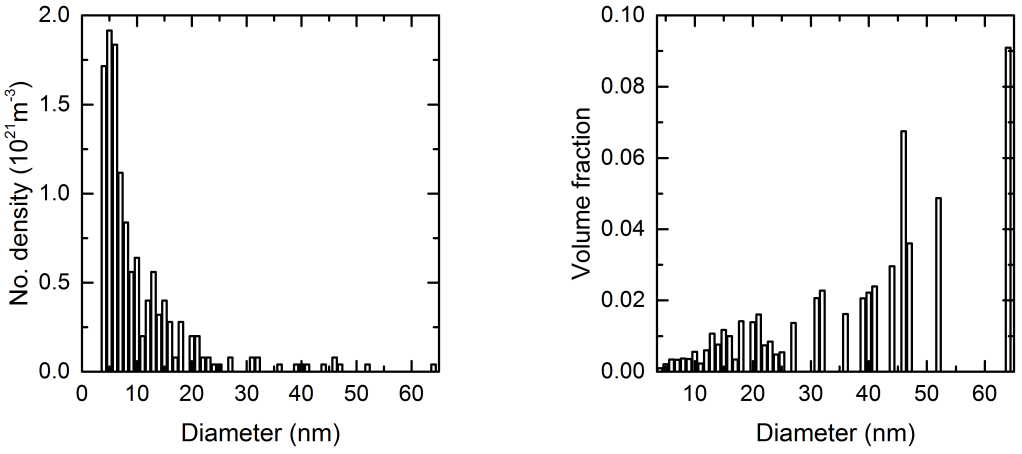

(a) (b)

Figure 6.16: Particle size distribution obtained from low-loss EFTEM of HIPed Cu-0.25Y_2O_3-0.25Ti **(a)** Particle number density distribution. **(b)** Particle volume fraction distribution. Caution must be taken in interpretation of volume fraction results where diameters exceeded the thickness of the sample at ∼25 nm, these particles were likely partially sectioned.

6.2.5 Cu-0.5Ti partial pre-alloy particles

Pre-alloyed powders were used to prepare Cu-0.25Y_2O_3-0.25Ti by MA of Cu-10Ti or Cu-0.5Ti pre-alloyed powder with Cu and Y_2O_3. The Cu-0.5Ti based powder had a reduced milled powder particle size distribution, the mean diameter was 0.4 mm compared with 1.5 mm for the Cu-10Ti based milled powder. Additionally, the powder hardness was better retained by Cu-0.5Ti over Cu-10Ti based alloys after consolidation

by FAST for 30 min at 900 °C and 50 MPa; the powder hardness was reduced by 30% and 50% respectively.

As alloys produced from Cu-0.5Ti showed the greatest promise for retention of desirable properties after sintering, the oxide nanoparticles were further investigated by STEM with HAADF and by EELS.

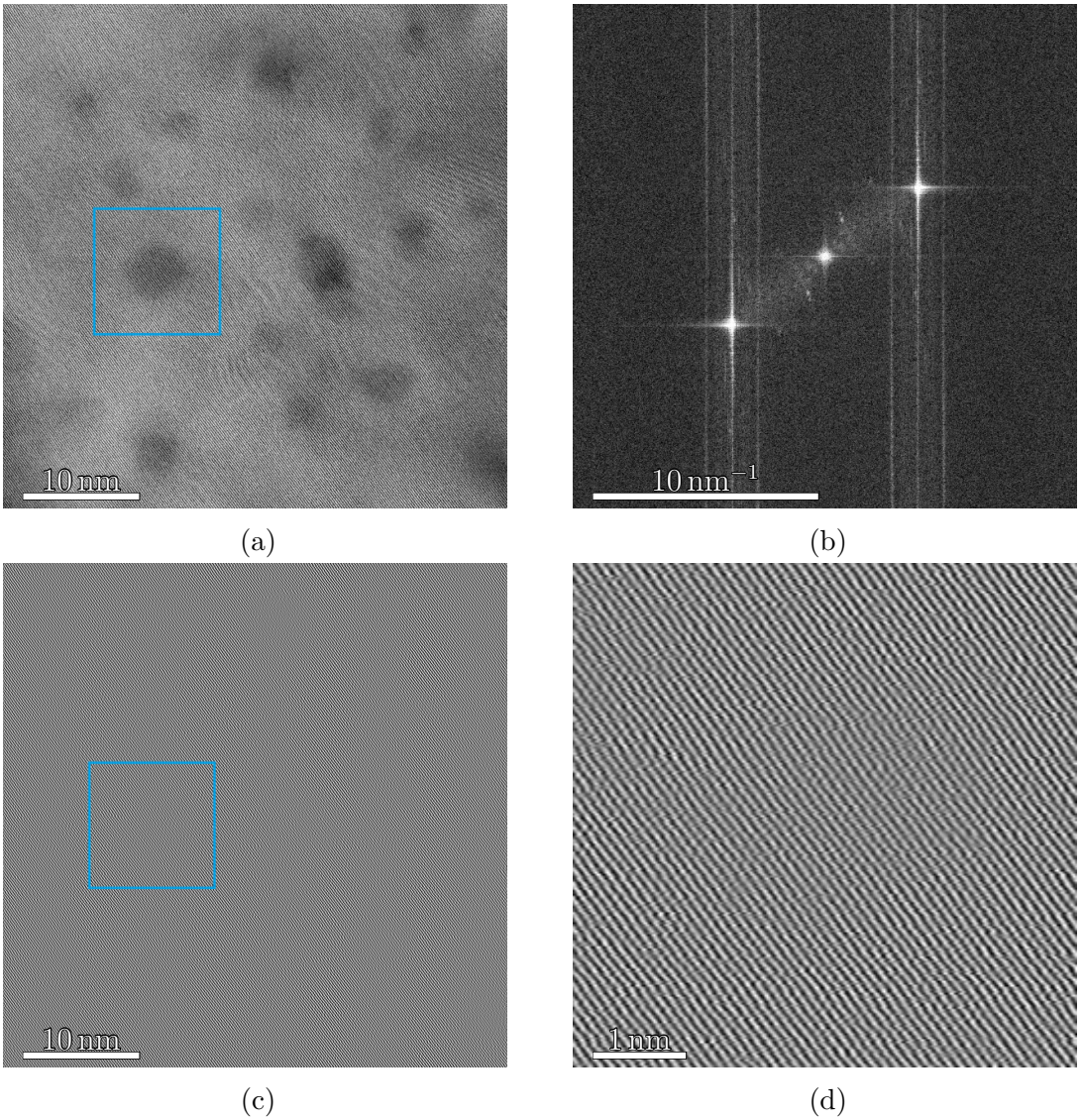

Figure 6.17: Coherent dispersed particles/clusters within a grain of sintered Cu-0.25Ti-0.25Y_2O_3 prepared from Cu-0.5Ti pre-alloyed powder. **(a)** HAADF-STEM micrograph. **(b)** Fourier transform. **(c)** Fourier filtered micrograph showing Cu matrix lattice. **(d)** Fourier filtered micrograph showing detail of cluster highlighted in (a) and (c)

Figure 6.17 shows STEM analysis of sintered Cu-0.25Ti-0.25Y_2O_3 prepared from

Cu-0.5Ti that exhibited a distribution of clusters/particles of 3.4 to 7.1 nm diameter, with a mean diameter of 5.0 nm (Fig. 6.17(a)). Figure 6.17(b) shows the Fourier transform of the HAADF micrograph with bright spots. Separating the matrix contributions from the Fourier transform (i.e. removing the Z-contrast from the Y-rich regions by masking the FFT and then transforming out of K-space) showed the Cu-matrix lattice planes (Fig. 6.17(b)), which were continuous in the region of interest and were indexed as $[1\bar{1}1]$. Figure 6.17(d) shows the filtered lattice of the highlighted particles, where there was no resolvable change in the lattice spacing between the particle and either near (<1 nm) or far (>5 nm) matrix regions. Thus, the clusters were considered to be fully or near-fully coherent with the Cu-matrix, which complements the observations in Ti containing Fe-ODS alloys of NaCl-type coherent nanoparticles which aligned with the bcc Fe matrix [30]. It was not possible to resolve the particle crystal structure from the Fourier transform.

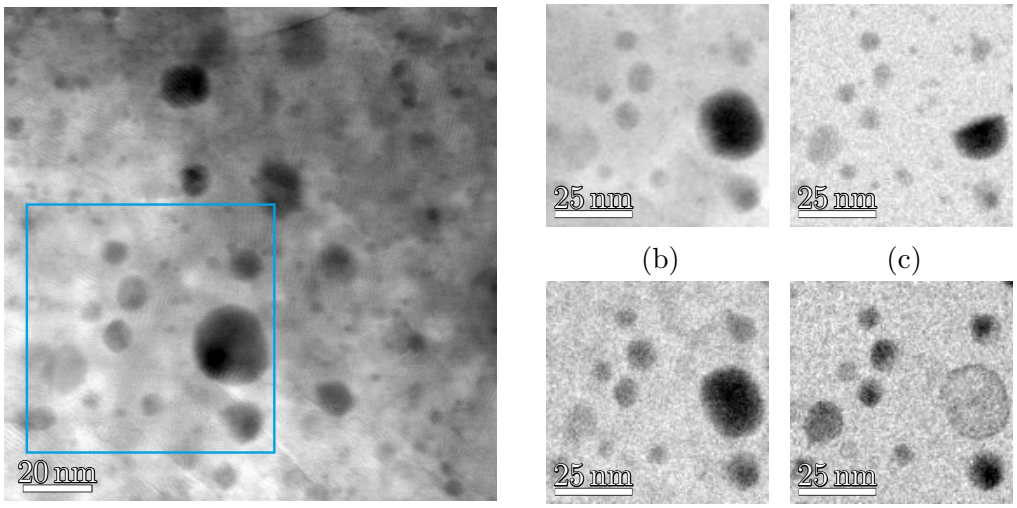

Figure 6.18: EELS analysis of particles in sintered Cu-0.25Ti-0.25Y_2O_3 prepared from a Cu-0.5Ti pre-alloyed powder.**(a)** dark-field (DF) STEM showing the region of interest for EELS, the average thickness of the matrix in this region is 0.41 ± 0.03 mfp. **(b)** Inverse Y $N_{2,3}$ map. **(c)** Inverse Ti $L_{2,3}$ map. **(d)** Inverse O K map. **(e)** Inverse Fe $L_{2,3}$ map.

b

Figure 6.18(a) shows a DF micrograph of a typical region of particles in consolidated

Cu-0.25Ti-0.25Y_2O_3. The region had a particle density of $3.75 \times 10^{23}\,m^{-3}$ and a mean inter-particle spacing of 14 nm. The mean and median particle diameters were 4.5 nm and 3.4 nm respectively. The inter-particle spacing and diameter are close to those suggested for achieving an increased particle density whilst reducing the fraction of additions, as described earlier in Section 6.1 [11]. EELS analysis of a 72 nm edge-length region revealed a strong correlation between the presence of Y (Fig. 6.18(b)), Ti (Fig. 6.18(c)) and O (Fig. 6.18(d)) in the <10 nm particles, with Fe (Fig. 6.18(e)) also showing a comparatively high concentration. The ∼20 nm particle was predominantly Y-O with an Fe-shell and Ti present in only half the particle. From the Y $N_{2,3}$ edge map, the edges of the ∼20 nm particle appeared diffuse, suggesting that Fe replaced Y, forming an Fe oxide.

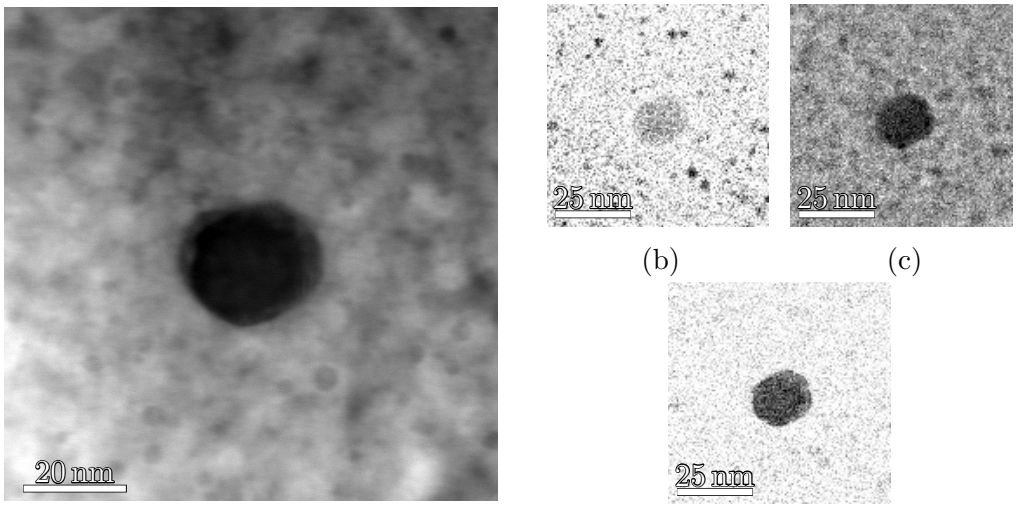

Figure 6.19: EELS analysis of particles in sintered Cu-0.25Ti-0.25Y_2O_3 prepared from Cu-0.5Ti.**(a)** DF STEM. **(b)** Inverse Ti $L_{2,3}$ map. **(c)** Inverse O K map. **(d)** Inverse Fe $L_{2,3}$ map.

Figure 6.19 shows a large (>30 nm diameter) particle with some finer ∼5 nm particles in the surrounding regions. EELS showed a comparatively high concentration of Fe (Fig. 6.19(d)) and O (Fig. 6.19(c)) in the large central particle and a relatively low concentration of Ti (Fig. 6.19(b)). The smaller particles had a lower concentration

of Fe, but higher concentrations of Ti and O, as shown in Fig. 6.19(d). The small Ti-rich oxides had a mean diameter of 4.5 ± 1.4 nm. It was not possible to obtain convincing information on the distribution of Y in these particles from the low-loss spectrum.

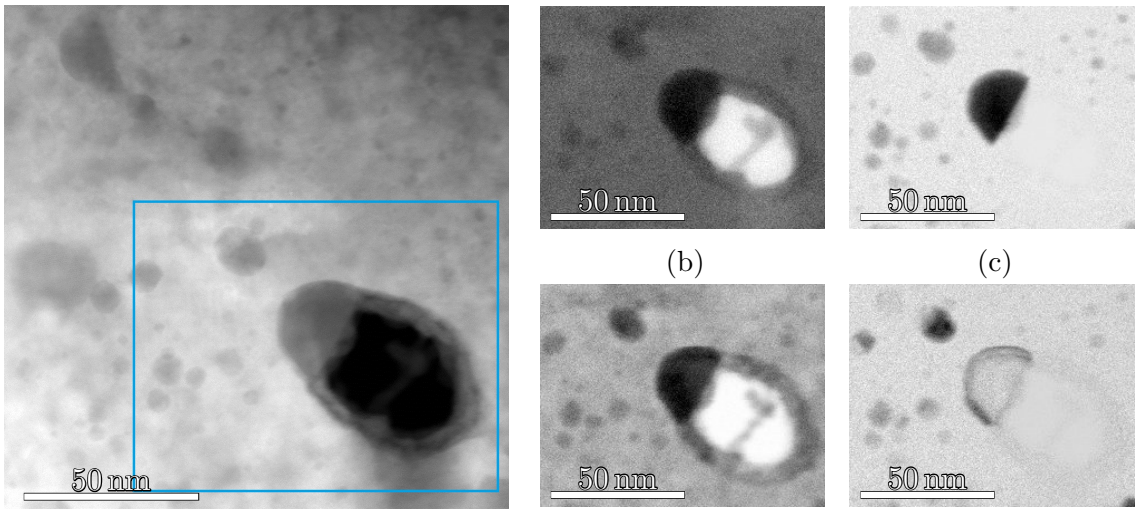

Figure 6.20: EELS analysis of particles in sintered Cu-0.25Ti-0.25Y_2O_3 prepared from a Cu-0.5Ti pre-alloyed powder.**(a)** DF STEM showing the region of interest for EELS. **(b)** Inverse Y $N_{2,3}$ map. **(c)** Inverse Ti $L_{2,3}$ map. **(d)** Inverse O K map. **(e)** Inverse Fe $L_{2,3}$ map.

Figure 6.20(a) shows a >40 nm diameter particle (partially removed by FIB damage), with nearby particles of <10 nm diameter. EELS analysis of the highlighted region showed the presence of Y shown in Fig. 6.20(b), Ti shown in Fig. 6.20(c), O shown in Fig. 6.20(d), and Fe shown in Fig. 6.20(e). The particle consisted of Ti, Y, O and Fe. At the north-western end of the particle there was a strong co-location of Ti, Y and O with an Fe shell. The particle had an Y and O-rich outer surface or shell as seen in Figs. 6.20(b) and 6.20(d), with a small concentration of Fe in the same region. Further information on the composition of the particle could not be determined due to FIB damage during thinning resulting in the central part of the particle being preferentially removed, and difficulty in deconvolution of the Y $N_{2,3}$ edge from the plasmon peak. The smaller particles containing Ti detectable by EELS

had a mean diameter of 6.0 ± 3.0 nm and showed strong co-location with both Fe and O, and a weaker co-location with Y. Macro-scale wetting experiments showed that Ti drastically enhanced the wettability of Cu with Y_2O_3 by forming various Ti-O phases, removing O from Y_2O_3 [33]. Thermodynamic arguments suggest this situation could also occur during sintering, which would allow for the partial dissociation of Y from O and preferred association with Ti suggested in Fig. 6.20(b).

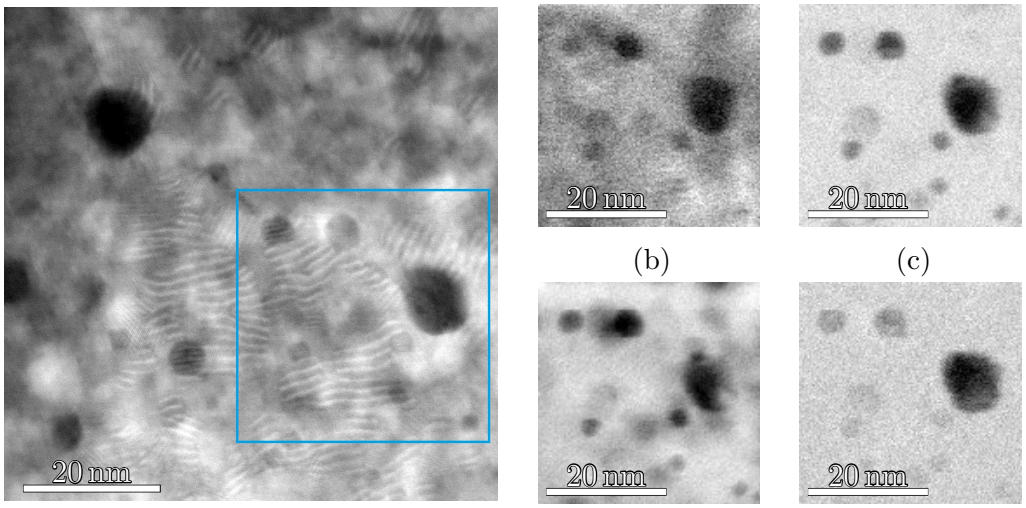

Figure 6.21: EELS analysis of particles in sintered Cu-0.25Ti-0.25Y_2O_3 prepared from a Cu-0.5Ti pre-alloyed powder.**(a)** DF STEM showing the region of interest for EELS. **(b)** Inverse Y $N_{2,3}$ map.**(c)** Inverse Ti $L_{2,3}$ map. **(d)** Inverse O K map. **(e)** Inverse Fe $L_{2,3}$ map.

Figure 6.21 shows particles <10 nm diameter with 10 particles exhibiting strong co-location of Ti and Y, all of which were also comparatively Fe-rich to varying degrees. O was again most strongly associated with Ti, although this may have been affected by surface oxides formed during surface preparation, as seen in the DF STEM micrograph that shows moiré fringes.

EELS data confirmed the formation of nanoparticles and nanoclusters of Ti-Y-O, with some likely Ti-O and as Y-O containing particle. The nanoparticles showed an affinity for Fe, particularly to combine with Ti. The Y distributions in/near particles were often diffuse in nature.

6.3 Summary

6.3.1 The effectiveness of Ti additions by mechanical alloying

Three routes for adding Ti to Cu based powders were investigated: master, elemental and pre-alloy. The pre-alloy route subdivided into two: partial and full, signifying if the final pre-alloyed powder contained the final desired ratio of Cu:Ti.

All routes had significant agglomerates of Y_2O_3 and Ti-rich oxides. Ti-based oxides were somewhat unexpected on account of Y having a higher affinity for O than Ti, and the comparatively low temperature of milling (standard Gibbs free energy of formation of oxides: $Y_2O_3 \sim -1250\,\mathrm{kJ\,mol^{-1}}$, TiO_2 $-889\,\mathrm{kJ\,mol^{-1}}$ [107]). The agglomeration of Y and Ti suggested the formation of a Y-Ti-O compound during the early stages of MA that was not subsequently broken down. The feedstock 20 to 40 nm Y_2O_3 powder had significant >1 µm agglomerates of particles prior to milling, and it is speculated that the interactions with Ti had a role in stabilising the agglomerates and thus minimising surface energy. The larger agglomerates provided only weak pinning effects in the Cu-based powders and thus could not promote the work hardening that makes MA effective.

Extended milling did not significantly reduce the size and distribution of agglomerates (Fig. 6.7) or increase powder hardness. The total amount of work-hardening that could be achieved in the Ti-containing alloys was lower than that of the only Y_2O_3 containing alloys examined in Chapter 4. The addition of Ti alone produced only a slight increase in hardness and the work-hardening, and the Ti-rich oxides (or more complex compounds e.g. with Fe) that also formed were not as effective as Y_2O_3 in promoting hardening.

A master alloy addition route produced MA powders with a plateau hardness similar to that based on milled Cu only (2180 ± 190 MPa compared with 2220 ± 260 MPa respectively). Full and partial pre-alloy addition routes improved the milled powder hardness, but had lower hardness after 12 hours than Cu-1Y_2O_3 (2890 ± 170 MPa and

2770 ± 180 MPa versus 3080 ± 180 MPa respectively) despite having the same total addition of Y_2O_3. Broadly, Ti additions in conjunction with Y_2O_3 lead to MA powder softening due to unexpected agglomeration of Ti and Y_2O_3. A low concentration of elemental Ti could not be effectively MAed into Cu using planetary ball milling because cold-welding of ductile Cu particles dominated over work-hardening and thus powder fracture and mixing [100].

A fully pre-alloyed Cu-10Ti powder was not as advantageous for effective incorporation of Ti into the Cu matrix as expected, or when compared with the partial pre-alloy route and stringers of agglomerations of Y, Ti and O and coarse grains resulted. It was expected that pre-alloying with 10 wt.% Ti would provide significant solute strengthening and improved work-hardening rate but the interaction with Y_2O_3 negated these benefits. However, reducing Ti concentration in the pre-alloyed powder from Cu-10Ti to Cu-0.5Ti had a significant positive effect on reducing agglomeration. Alloys with 0.25Ti and $0.25Y_2O_3$ based on Cu-0.5Ti retained a high hardness after consolidation by FAST, which was associated with restricted grain growth by the succesful incorporation of Y and Ti-rich pinning particles.

Despite the difficulties in achieving the levels of Ti homogeneity during milling using Cu-10Ti, after HIP Cu-$0.25Y_2O_3$-0.25Ti had a higher hardness than Cu-$2Y_2O_3$ due to Ti-O particle formation and associated pinning effects. Typical examples of these particles were shown in Figs. 6.14 and 6.15 and comprised primarily Ti and Y-rich nanoparticles at grain boundaries and triple-points. The central regions of grains were relatively denuded of these particles perhaps due to the higher mobility of solute atoms at grain boundaries [30]. Preferential pinning at grain boundaries may encourage so-called abnormal grain growth, because with larger particles, once grain boundaries break free they are difficult to re-pin [19]. Nonetheless, larger particles located at grain boundaries may be desirable for inhibiting creep and grain boundary sliding, and have been described by Zinkle as a design requirement for a Cu divertor

alloy [11]. EELS analysis of oxide nanoparticles in FAST consolidated Cu-0.25Y_2O_3-0.25Ti revealed occasional disparity in the co-location of Y and Ti, suggesting that Ti may remove O from Y during sintering to preferentially form a Ti-O based compound. The addition of Ti in the partial pre-alloyed route gave small diameter nanoparticles of both Y and Ti oxides and ternary or quaternary oxides constituted of Y-Ti-O and Fe. The wide variation in the nanoparticles stoichiometry might suggest they had not yet reached their equilibrium compositions because of the relatively short and possibly inhomogeneous thermal exposure during FAST consolidation.

6.3.2 The role of Ti in particle refinement

It is clear that Ti plays a role in particle refinement of Y-containing Cu-ODS, where the addition of nanoparticles was shown to increase the number density of <10 nm diameter particles very significantly as well as the overall number density. Not all oxide particles contained Ti and not all oxide particles contained Y, however, the finest particles were shown likely to contain both Y and Ti. As discussed in Section 2.4.1, Ti may affect particle refinement by either aiding nucleation or slowing down coarsening [26]. Slowing down coarsening may be considered to result from effects that make the particles more thermodynamically stable (i.e. greater interfacial coherence), reducing the rate of Ostwald ripening. Prior work in Al-based Cu-ODS has suggested, through *ab-initio* modelling coupled with high-resolution TEM imaging, that Ti promotes the formation of more regularly shaped particles, lowering the interfacial energy with the Cu matrix and reducing coarsening through their stability [32]. However, the Al-O particles characterised before addition of Ti tend to have planar or irregular shapes, whereas the observations in Chapters 4 and 5 suggest that the Y-containing particles are largely spherical in nature and distinctly incoherent as shown in Fig. 5.12, so this hypothesis is not complete for the Ti-Y-O system. Ti may aid nucleation and two effects may be considered: the Ti either clusters to form a nucleation point for the

precipitation of Y and O [119], or through the formation of an intermediate complex oxide phase with other elements in the alloy leading to coherency with the matrix [30]. EELS and EFTEM analysis of the particles identified co-location of Y and Ti in fine particles together with some <5 nm particles containing no Y - despite high O and Ti contents. There was no evidence of core-shell type particles that would indicate Ti clustering to aid nucleation. The change of oxide particles from incoherent to coherent on Ti addition suggests that the Ti promotes the formation of complex oxides in Cu such as $Y_2Ti_2O_7$ or Y_2TiO_5, as found simultaneously in Fe-ODS alloys [29], that have closer matching lattice spacing with the matrix, and similar to findings in Cu-Al_2O_3 [32].

6.3.3 Conclusions

Key conclusions relating to the effect and effectiveness of Ti additions in Cu are:

- Ti is most effectively introduced prior to milling by means of partial or full pre-alloying with Cu.
- The addition of Ti leads to (i) some unavoidable agglomeration with Y_2O_3 when added in small (<1 wt.%) additions, along with (ii) some dissolution of the Ti into the Cu matrix.
- Adding Ti leads to a reduction in the size of oxide nanoparticles, which may be attributed to Ti improving the coherency of these particles with the Cu matrix.
- Ti additions lead to an increase in the contamination by Fe from the milling pots and media, which were observed as either in Fe-rich flakes or preferentially separated to Ti/Fe-rich clusters.

Chapter 7

Evaluation of a Cu-ODS alloy of Cu-0.25Ti-0.25Y_2O_3

7.1 Introduction

From amongst the Cu-ODS alloys described so far, Cu-0.25wt.%Y_2O_3-0.25wt.%Ti fabricated by MA from pre-alloyed Cu-0.5T + Cu powder was chosen for further exploration of properties. The objective was to investigate the effect of microstructure on tensile properties, creep resistance, thermal stability, and thermal conductivity.

7.2 Experimental procedure

The alloy was produced by mechanical alloying of powders followed by consolidation by FAST and subsequent thermomechanical treatments.

7.2.1 Raw materials

Starting materials for mechanical alloying were: Cu powder (99.9% purity) , Cu-0.5Ti partial pre-alloyed powder (99.95% Cu and 99.6% Ti purity), and Y_2O_3 powder (99.999% purity), see Sections 3.2.1 and 6.2.3 for further details of source and powder size.

7.2.2 Mechanical alloying

Four pots with a powder charge of 80 g were milled in two batches at an ambient temperature below 20 °C to prevent overheating and excessive powder welding, as per the standard milling conditions. 99.7 % of the milling charge by weight was recovered from the milling process.

Effect of milling pot and media composition

To address issues of Fe-contamination in Chapter 6, a comparison of 12 h milling using Fe-based milling pots and media and ZrO_2-based milling pots and media was performed and 5 g of powder chemically analysed. Table 7.1 gives the measured composition from inductively coupled plasma mass spectroscopy (for Al, B, Cr, Cu, Fe, Mg, Mn, Ni, P, Pb, Sn, Ti, V, Zr, Zn), inductively coupled plasma optical emission spectroscopy (for Y) and infra-red inert gas fusion analysis (for O). It was hoped that the stabilised ZrO_2 pots and balls would be sufficiently tough and stable to prevent contamination. However, the Zr concentration was considered unacceptably high at 2.23%, which may lead to a high propensity for the formation of brittle Cu-Zr inter-metallic phases because of the low room temperature solid-solubility of Zr in Cu (<0.1 wt.%) [125]. The Fe contamination was 0.3 wt.%, (cf. a solid solubility of 0.26 wt.% in Cu at room temperature) for powders milled in steel pots, and can be expected to reduce thermal conductivity [22].

7.2.3 Sintering by FAST

Sintering was undertaken in a 60 mm diameter graphite die, thermally insulated with carbon-fibre composite and graphite felt. The temperature was measured throughout using a K-type thermocouple inserted in the die wall 5 mm radially from the powder compact. The powder was set to be heated at 100 °C min^{-1} until 800 °C was reached, at which point the heating rate was reduced to 50 °C min^{-1} to reach the final dwell

Table 7.1: Effect of milling pot & balls composition on Fe contamination in Cu-0.25Y_2O_3-0.25Ti, in wt.%, **(a)** X210CrW12 pot & AISI 52-100 balls, and **(b)** ZrO_2 milling pot and milling media.

	(a)	**(b)**
Cu	Bal	Bal
Y	0.163	0.159
Ti	0.23	0.31
O	0.285	0.300
Fe	0.32	<0.02
Mg	<0.02	0.04
Zr	<0.02	2.23
Cr	<0.02	<0.02

temperature of 900 °C without overshooting. A pressure ramp from 2.5 MPa to 50 MPa was set during the second heating ramp.

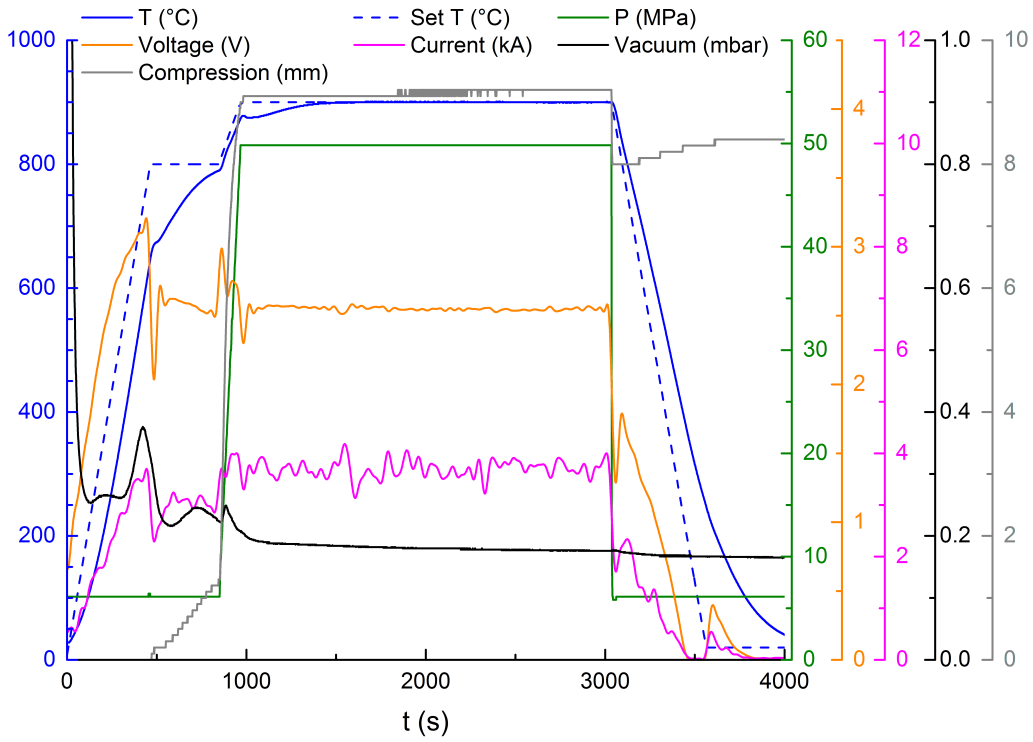

Figure 7.1: Sintering of a 60 mm diameter die containing 299.15 g Cu-0.25Y_2O_3-0.25Ti powder with a dwell of 30 minutes at 900 °C under 50 MPa uniaxial load

Figure 7.1 shows the programmed and actual sintering cycle. The die temperature followed the set temperature closely. The large thermal mass of the die required a cautious PID setting which forced slower heating approaching the dwell temperature,

but prevented overshooting. This increased the time spent above the Cu recrystallisation temperature to ∼4000 s, an increase of 20% from the planned heating profile. The loading of the die was set at 6 MPa during the initial heating to 800 °C after which it was ramped at a rate of 22 MPa min^{-1} once the powder had softened with temperature. The compression of the sample followed correspondingly, starting at 658 °C, at a compression rate of ∼15 µm s^{-1}, that increased to 65 µm s^{-1} on the application of higher pressure. During the dwell period, further compression of 0.1 mm was recorded, which was at the resolution limit of the positional transducer. The voltage and current remained approximately constant throughout the dwell period, indicating that no major changes in the resistivity of the powder occurred during the dwell period, supporting previous suggestions that most consolidation occurred during the ramp stages. The current and voltage had a 20 s smoothing Fourier transform operation applied to improve readability. A vacuum was applied throughout which stabilised at 0.16 mbar after some initial outgassing of the powder.

7.2.4 Thermomechanical treatment

Following sintering, additional mechanical work was applied to assist closure of residual porosity.

Forging

The sample was cold forged by means of a uniaxial hydraulic press at >750 MPa in an open die as shown in Fig. 7.2(c). The sample was prepared by skimming and facing on a lathe and then grinding to 4000 grit surface finish to remove any surface defects and ingression of graphite foil (Fig. 7.2(a)). In order to achieve this pressure with the 100 t hydraulic press available, the disc was cut into equal surface area segments by a waterjet (Fig. 7.2(b)), which were then forged separately. The sample had a thickness of 11.70 ± 0.02 mm prior to forging and the open die had a minimum closure gap of 10.00 mm. After compression to close to 10 mm, the samples elastically recovered

to 10.60 mm giving a retained compression of ∼9 %. A pressure of ∼800 MPa was required to plastically deform the sample during this operation.

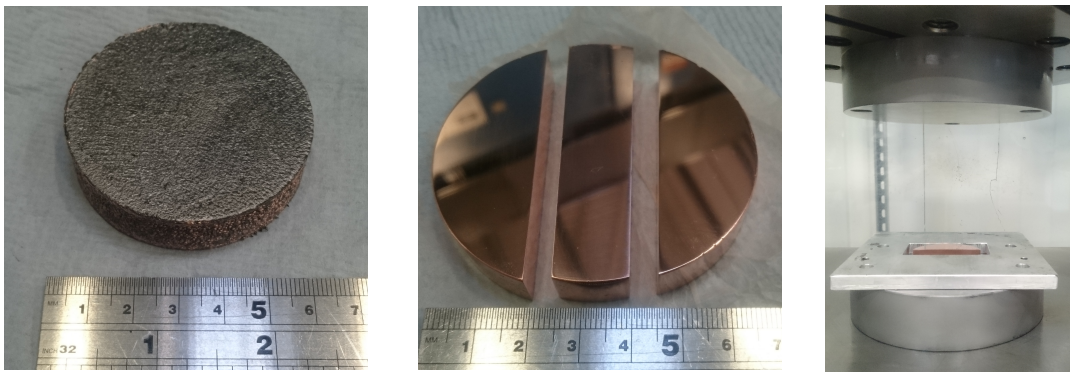

(a) As-sintered (b) Skimmed & sectioned (c) Die

Figure 7.2: Preparation of Cu-0.25Y_2O_3-0.25Ti sample for open-die forging

Figure 7.3 shows the surface finish of a section of the sample after forging. The faces parallel to the forging direction showed minor bulging, and prior-powder-particle pop-out indicating higher deformation in the PPB regions.

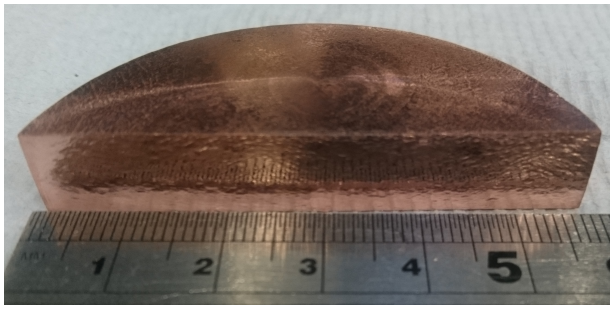

Figure 7.3: Forged Cu-0.25Y_2O_3-0.25Ti segment

Isothermal annealing and ageing

In line with other powder processed Cu-ODS alloys [50, 126–128], the forged samples were annealed at 900 °C for 1 h to relieve cold-work prior to mechanical property evaluation.

To evaluate the stability of the microstructure and nanoparticles isothermal ageing was undertaken. The proposed temperature for operation of the heatsink region of

the divertor for DEMO varies from 200 to 350 °C depending on the proposed heat flux, divertor design, and materials properties [4, 7–9] - with the primary limit being that of avoiding softening and embrittlement of irradiated CuCrZr that provides an operating window of 250 to 300 °C [8]. Without exposing the sample to multiple years of isothermal ageing due to time constraints, ageing at 350 °C for 545 h was chosen to simulate 2 years at 300 °C, as calculated in Section 3.2.4. Ageing was performed with the samples under vacuum in sealed quartz tubes although an exact measure of the vacuum quality was not possible on the equipment used for sealing.

7.3 Results and discussion

7.3.1 Comparison with other Cu-ODS alloys

The Cu-0.25Y_2O_3-0.25Ti alloy was compared with GlidCop AL25 (Cu-0.5Al_2O_3 prepared by internal oxidation, hot extrusion and annealing), and Cu-2Y_2O_3 as described in Chapters 4 and 5. These alloys will be hereafter referred to as CuYOTi, AL25, and CuYO respectively. The CuYOTi and CuYO were subjected to identical processing as outlined above, the AL25 was isothermally aged simultaneously with the CuYOTi and CuYO where appropriate for direct comparison.

7.3.2 Effect of processing

The effectiveness of processing of CuYOTi was considered through changes in density and hardness after each processing step. Table 7.2 shows the density increasing with each step of processing, reaching >99 % of the theoretical density of 8.94 g cm^{-3} (estimated using rule of mixtures). The hardness decreased on sintering due to recovery of the microstructure. The cold forging introduced a small amount of work giving an increase in hardness of ∼9 % and isothermal ageing caused a further hardness increase of ∼13 % associated with either reduction of micro-porosity in the structure,

a refinement of the microstructure during recrystallisation, and further precipitation of fine-scale Y, Ti and O rich particles.

Table 7.2: Density and hardness of CuYOTi

Condition	Density ($\mathrm{g\,cm^{-3}}$)	Hardness (MPa)
Powder	-	2110 ± 190
FAST consolidated	8.62 ± 0.04	1540 ± 240
Forged	8.78 ± 0.00	1680 ± 200
Isothermally aged	8.87 ± 0.00	1900 ± 140

7.3.3 Microstructure

Figure 7.4 shows PPBs between the CuYOTi prior-powder-particles following FAST consolidation and forging. The PPB regions showed μm-scaled Fe and Y containing oxide particles, as shown inset in Fig. 7.4. Either side of the PPB region, the microstructure was comparable with CuYO with a grain size of 100 to 500 nm, with some larger grains up to 1 µm.

The Fe presence was attributed to the reaction of dissolved Fe picked up during milling with the unavoidable powder particle surface O layer.

Figure 7.5(a) shows the deformed microstructure typical of cold-forging, imaged parallel to the forging direction, with the presence of deformation twins, and flake-like grains associated with compression of near-equiaxed grains during forging. The grains were of the order ∼200 nm height in the forging direction, and up to ∼1500 nm in length perpendicular to the forging direction. Figure 7.5(b) shows the larger nanoparticles (>20 nm diameter resolvable) of which the majority were located at grain boundaries and can be considered to be pinning points.

Figures 7.6(a) and 7.6(b) show the presence of fine (<10 nm diameter) particles within the elongated grains shown in Fig. 7.5(a). A single particle of 25 nm diameter (top-centre) is shown surrounded by particles of between 2 nm and 6 nm which had a number density of $2.27 \times 10^{23}\,\mathrm{m^{-3}}$, typical of the bulk. 3489 particles were analysed

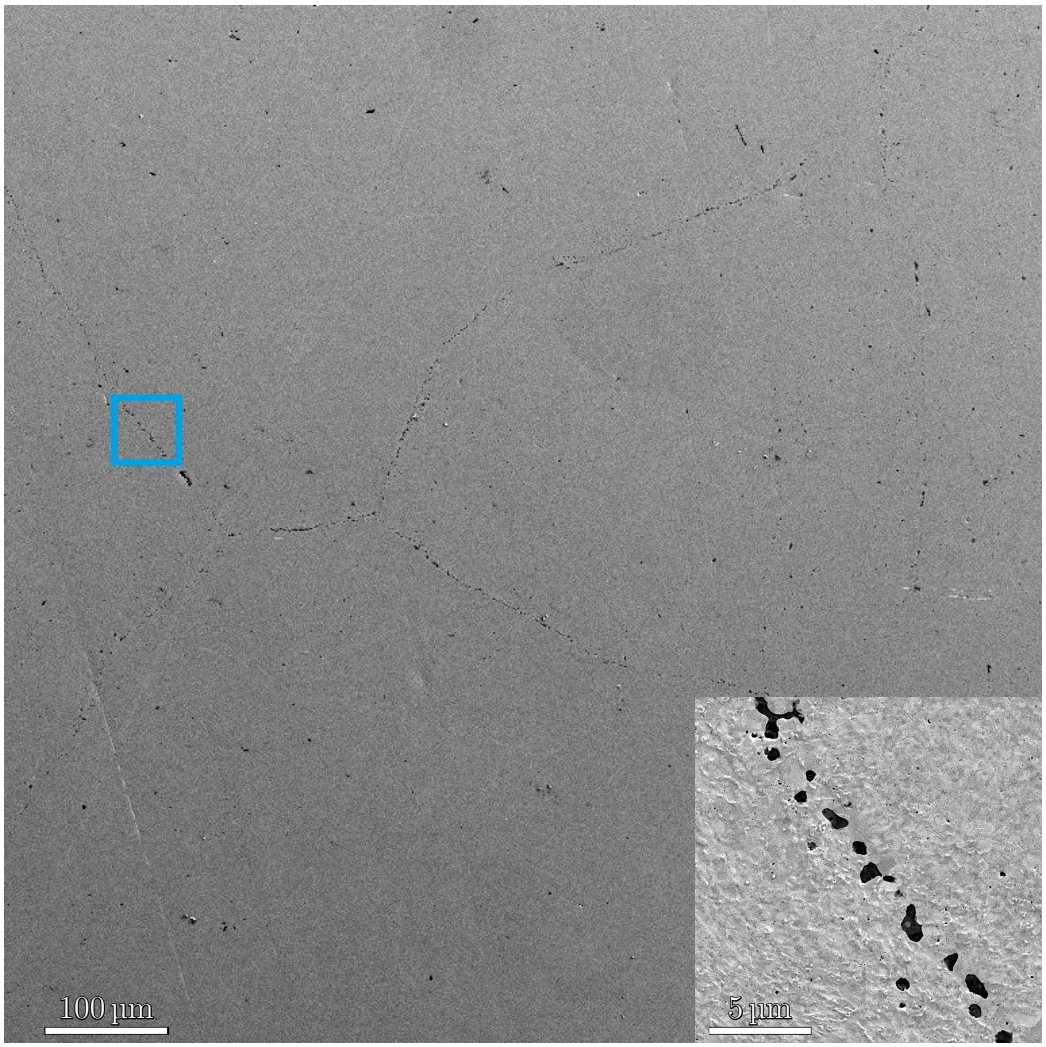

Figure 7.4: SE micrograph of CuYOTi prepared by FAST consolidation and cold-forging showing PPBs. Inset: highlighted PPB showing particles with significant Z-contrast.

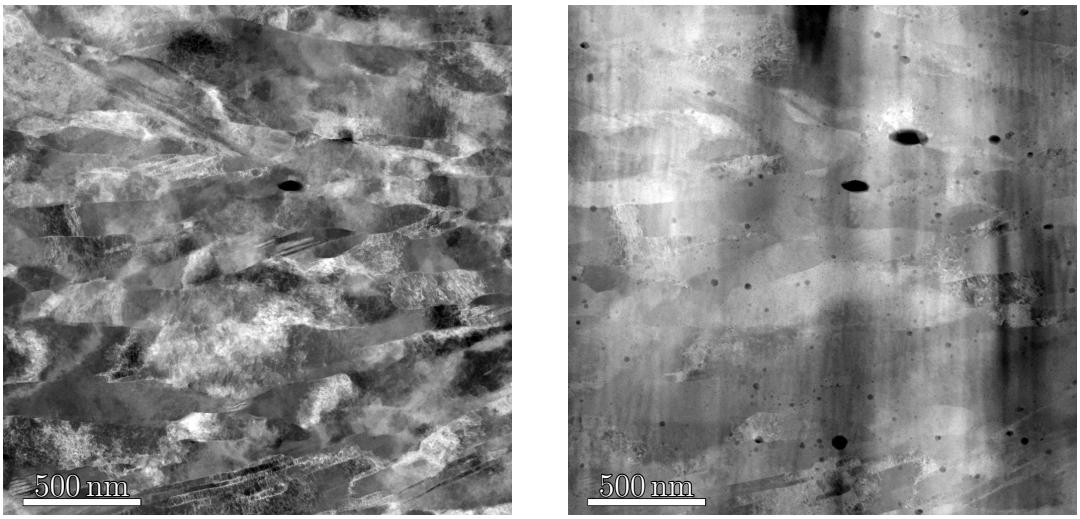

(a) (b)

Figure 7.5: STEM imaging from FIB liftouts of FAST consolidated and cold-forged CuYOTi, imaged parallel to the forging direction, **(a)** DF micrograph showing grain structure with typical forged texture, and **(b)** HAADF micrograph showing the larger nanoparticles at grain boundaries.

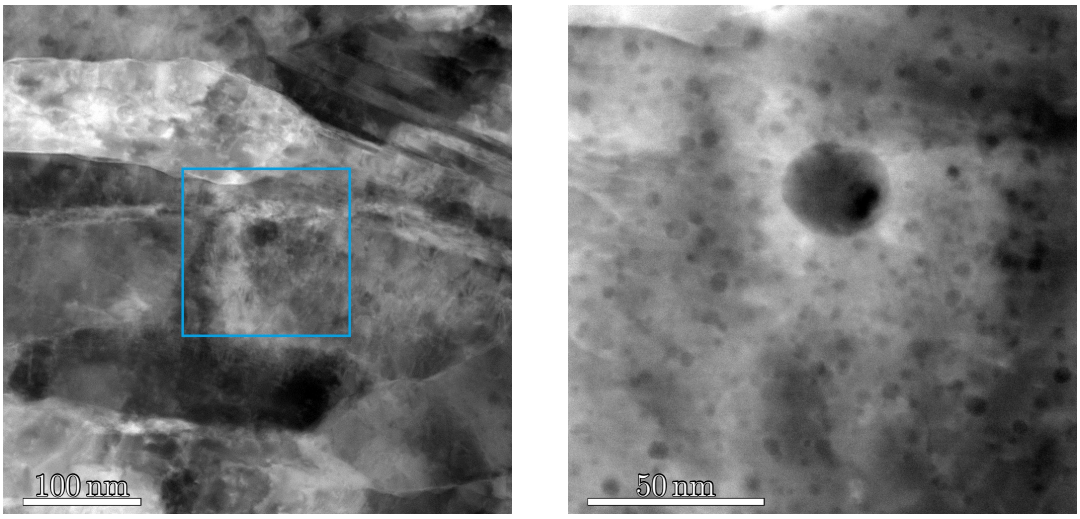

(a) (b)

Figure 7.6: STEM imaging from FIB liftouts of FAST consolidated and cold-forged (forging direction vertical in plane of image) CuYOTi, **(a)** DF micrograph showing grain structure, and **(b)** HAADF micrograph showing nanoparticles within the region highlighted in (a).

from a combination of DF and EELS images from a sample volume of $1.48 \times 10^{-20}\,\mathrm{m}^3$, from 5 regions prepared from two FIB liftout samples. The overall particle number density was $2.36 \times 10^{23}\,\mathrm{m}^{-3}$, the mean particle diameter was $3.2 \pm 1.5\,\mathrm{nm}$ and the mean interparticle spacing was 16.2 nm. Shown later, Fig. 7.18 indicates the overall particle size distribution.

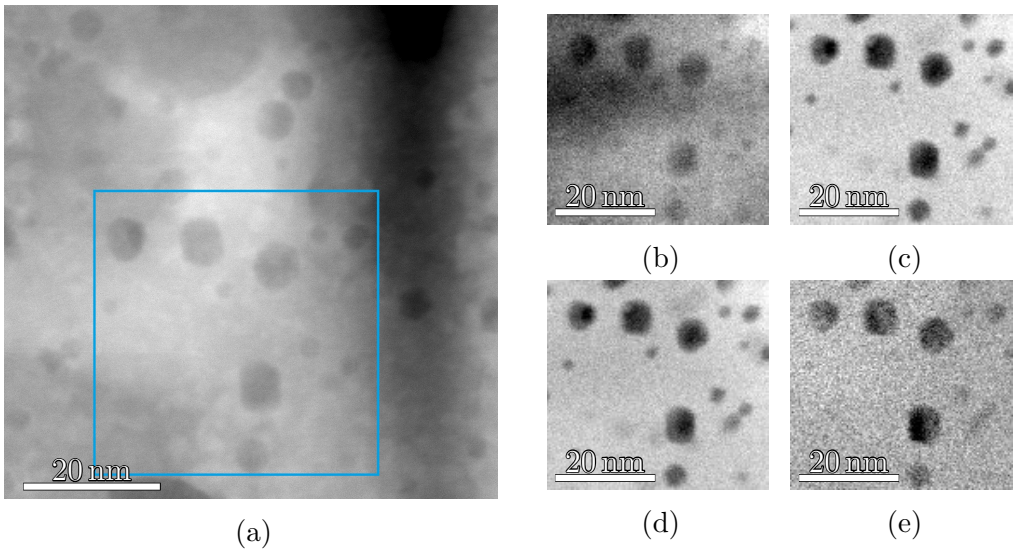

Figure 7.7: EELS analysis of particles in FAST consolidated and cold-forged CuYOTi, **(a)** DF STEM showing the region of interest for EELS, the average thickness of the matrix in this region is 0.32 ± 0.03 mfp. **(b)** Inverse Y $N_{2,3}$ map obtained from principal component analysis. **(c)** Inverse Ti $L_{2,3}$ map. **(d)** Inverse O K map. **(e)** Inverse Fe $L_{2,3}$ map.

Figure 7.7 shows examples of EELS analysis of 1.8 to 6.5 nm nanoclusters and nanoparticles. The particles were again Y, Ti, O and Fe-rich. Ti was present in all particles and showed no local intensity variation within each particle, conversely, the Fe showed significant intensity variation with Fe-rich and Fe-depleted regions within each of the ∼6 nm diameter particles, that correlated spatially with relatively high O concentrations. Particles <3 nm in diameter were predominantly free of Fe, appearing as only Y, Ti and O-rich.

7.3.4 Tensile properties

Tensile tests were performed on samples in the annealed and aged condition after cutting by waterjet to planar dog-bones (see Fig. 3.4) with 1 mm^2 cross-sectional area. The small cross-sectional area was chosen to enable multiple test samples to be taken from the limited volume and disc geometry of the forged samples. Figure 7.8(a) shows the resulting stress-strain curves. The annealed CuYOTi failed below 320 MPa in two out of three samples, before any significant yield occurred. The aged samples showed some signs of yielding before failure, but insufficient to obtain a 0.2% proof stress. Figure 7.8(b) shows the stress-strain curves for the GlidCop alloys AL15, AL25 and AL60. The curves have similar features with tan increasing Al_2O_3 fraction resulting in reduced ductility, increased UTS and increased 0.2% proof stress. AL25 is the closest comparable alloy with CuYOTi in terms of the oxide fraction and as shown in Table 7.3 that summarises the tensile data, AL25 had a slightly higher Young's modulus (∼8%), a lower 0.2% proof stress (14%), a comparable UTS, and substantially better elongation to failure.

Table 7.3: Measured tensile properties of CuYOTi, compared with CuYO and AL25.

Sample	E (GPa)	σ_y (MPa)	UTS (MPa)	ϵ_f (%)
Annealed 1	99	-	292	0.33
Annealed 2	102	461	498	0.92
Annealed 3	101	-	334	0.36
Aged 1	95	432	443	0.70
Aged 2	89	440	465	0.83
Aged 3	95	-	425	0.58
CuYO	-	-	490	0.40
GlidCop AL25	107	380	468	24.1

Figure 7.9 shows a selection of CuYOTi failure surfaces perpendicular to the tensile direction. In Fig. 7.9(a) the failure mode appeared brittle, with a mosaic of relatively large planar surfaces at the scale of the prior-powder-particles. At higher magnification, there were 1 to 5 µm dimples such as those shown in Fig. 7.9(b) each

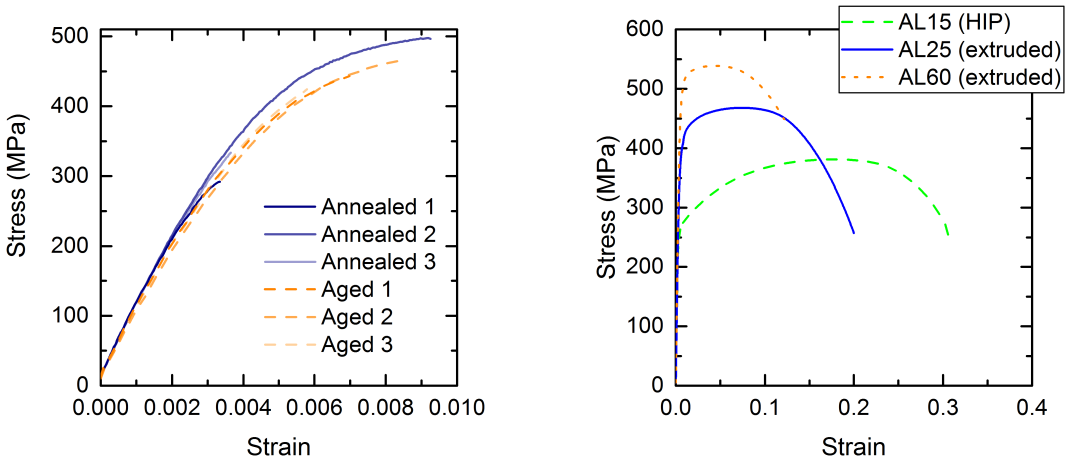

(a) (b)

Figure 7.8: Tensile stress-strain curves of annealed **(a)** CuYOTi dog-bones with 14 mm gauge length and ETMT geometry (as per Fig. 3.4), tested at a strain rate of 1×10^{-3} mm s^{-1}, and **(b)** GlidCop alloys (AL15, 0.3 wt.% Al_2O_3 prepared by HIP; AL25, 0.5 wt.% Al_2O_3 prepared by hot extrusion; AL60, 1.2 wt.% Al_2O_3prepared by hot extrusion) averaged from three room temperature tensile tests performed to ASTM E8 standard on TETRE 160 round specimens (as per Fig. 3.4). Samples were tested at a strain rate of 0.015 min^{-1} until yield and then at 0.4 min^{-1}

containing a particle(s) of 0.2 to 1 µm. The appearance was typical of void nucleation around a hard particle, some limited ductility before void coalescence and then failure. Figure 7.9(c) again shows a similar region of dimples, of scale similar to the grain size (100 to 200 nm). Similar features occurred in all samples, regardless of heat treatment. Figure 7.9(d) shows a fracture surface inclined at ∼45° to the tensile load, where the failure mode was not clear and might result from incomplete sintering with some limited necking between part-consolidated powder neck regions. The competing scales of the fracture structures and the generally brittle behaviour suggested that the primary failure mode was micro-void formation and then void coalescence at the PPBs and inside grains, associated with clusters of hard, irregular shaped particles.

Figure 7.10(a) shows quantified point EDS analysis of the tensile fracture surface, with the compositions given in Fig. 7.10(b). The majority of particles were rich in Fe and O, with both Ti and Y present but not on the dimple surface. As expected O

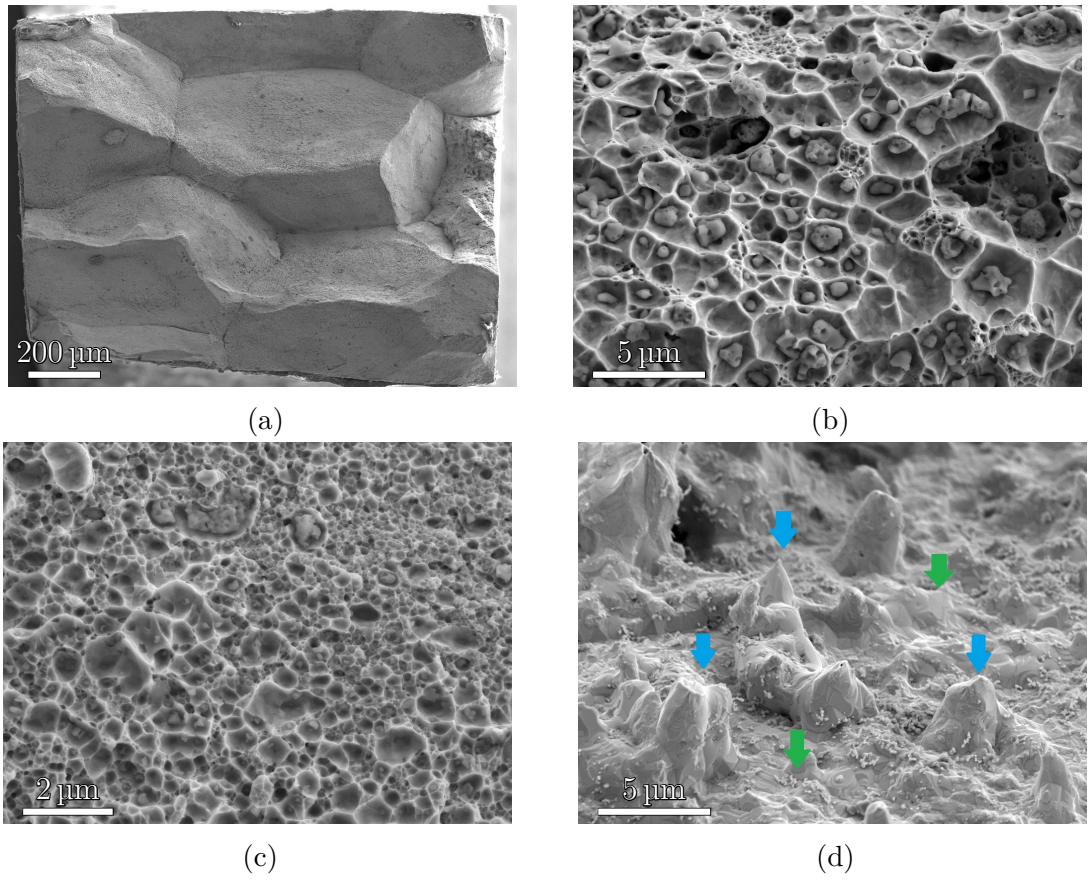

Figure 7.9: SE micrographs of fracture surfaces at room temperature of CuYOTi produced by FAST consolidation, cold-forging, and isothermal ageing. **(a)** Typical whole fracture surface perpendicular to tensile loading, **(b)**, **(c)** typical dimpled fracture surfaces perpendicular to loading direction, and **(d)** transgranular failure and ductile necking (arrowed) on fracture surface inclined at ∼45° to loading direction.

appeared across the surface due to inevitable minor surface oxidation. Particles 1-4, 6 and 7 contained O, Fe, Cr, Y and Ti with small amounts of Cu from scattered X-rays. The ratio of Fe to O was approximately 4:3, and Cr to O ratio was approximately 1:1. The ratio of Fe to Cr (co-located with Fe) was 83%, suggesting the source of contamination was the milling pot rather than the milling media which had a lower Cr concentration (see Table 3.1). Figure 7.11 shows the particle labelled 4 in Fig. 7.10, which consisted of a polycrystalline Fe and O-rich particle with separate crystals rich in Y and O. Ti was present but was not spatially resolved, and the overall composition of the particle could be interpreted as Fe_3O_4 with some Y_2O_3.

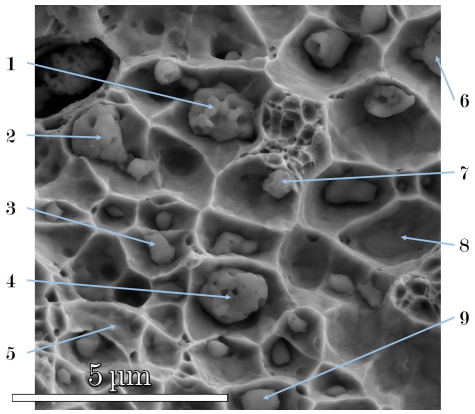

(a)

	Cu	O	Fe	Ti	Y	Cr	C
1	4.1	41.7	28.7	2.0	2.4	6.9	13.9
2	10.1	41.1	26.7	0.5		7.8	13.8
3	17.1	35.8	25.4	0.8	0.1	4.8	16.0
4	3.7	48.4	27.3	2.2	2.4	5.4	10.1
5	59.1	1.9					38.9
6	3.6	44.7	33.2	0.5	0.1	5.9	12.0
7	16.0	39.9	21.6	0.8	0.1	7.5	14.2
8	76.1	1.5	0.3				21.8
9	12.0	44.9	27.6	0.6	0.1		14.8

(b)

Figure 7.10: Point EDS of CuYOTi fracture surface prepared by FAST consolidation, cold-forging, and ageing: **(a)** SE micrograph of cup-and-cone fracture surface showing points of EDS analysis, and **(b)** table of EDS derived compositions with all values in at.%.

7.3.5 Thermal properties

Thermal conductivity

Laser flash analysis (LFA) of CuYOTi following forging and annealing was used to obtain the thermal diffusivity and hence thermal conductivity. Figure 7.12(a) shows the measured thermal diffusivity with respect to temperature from 300 to 825 K for FAST consolidated, forged, and annealed CuYOTi and CuYO, and annealed AL25.

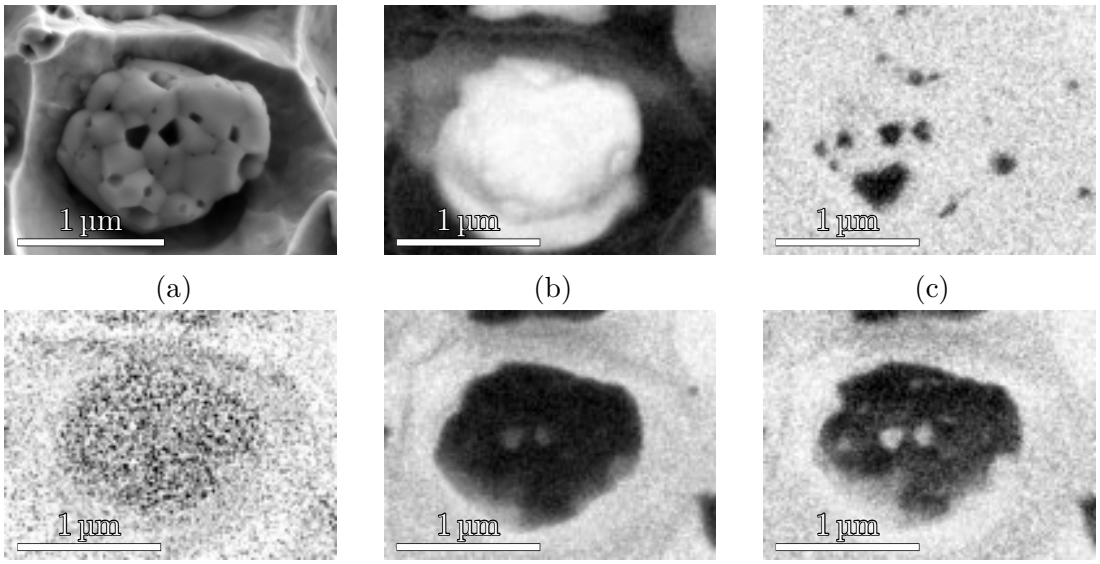

Figure 7.11: Inverse EDS maps of particle at tensile fracture surface of CuYOTi, marked 4 in Fig. 7.10: **(a)** Secondary electron micrograph, **(b)** Cu L map, **(c)** Y L map, **(d)** Ti L map, **(e)** O K map, and **(f)** Fe L map.

The diffusivity was expected to decrease with increasing temperature, as shown by AL25 and CuYO. CuYOTi, in contrast, exhibited an increase in diffusivity until 700 K, after which it decreased rapidly in line with the other alloys. The increase in diffusivity was attributed to Ti in solution which is known to increase Cu alloy thermal conductivity with increasing temperature [34, 35]. This arises as a result of Ti providing a reduction in the interface resistivity at grain boundaries and nanoparticle boundaries, which assists electron transport [36, 37]. The apparent coherent nature of nanoparticles in Cu-0.25Y_2O_3-0.25Ti, as shown in Fig. 6.17, supports this interpretation. Figure 7.12(b) shows the calculated thermal conductivity from the thermal diffusivity measurements. AL25 had no temperature dependence of thermal conductivity in the range 300 to 825 K. CuYOTi and AL25 showed an increasing thermal conductivity with temperature, which was more marked for CuYOTi.

Over the range of 400 to 700 K the mean thermal conductivity of CuYOTi was $332 \pm 16\,\mathrm{W\,m^{-1}\,K^{-1}}$. The mean thermal conductivity of AL25 over the same temperature range was $372 \pm 11\,\mathrm{W\,m^{-1}\,K^{-1}}$ which agreed with $\sim$364 $\mathrm{W\,m^{-1}\,K^{-1}}$ in [52, 129].

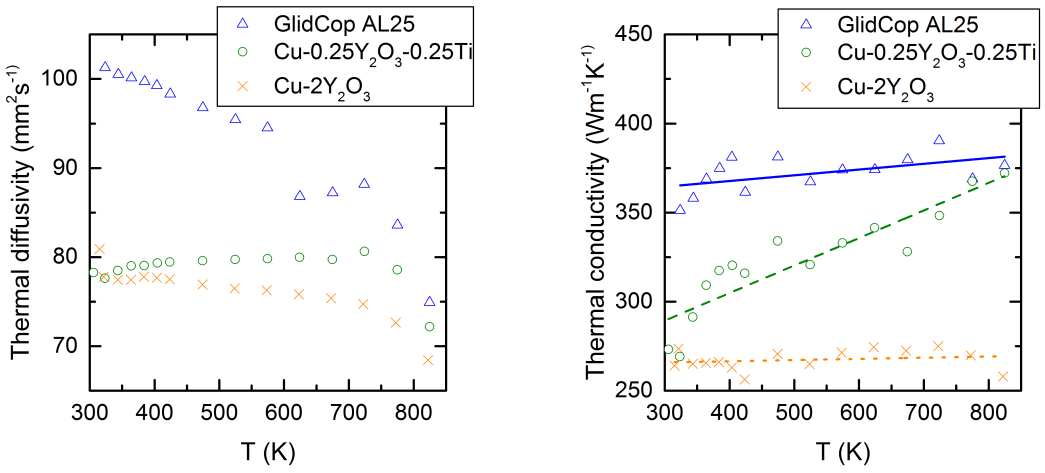

(a) (b)

Figure 7.12: **(a)** Thermal diffusivity, and **(b)** thermal conductivity of annealed Cu-0.25Ti-0.25Y_2O_3 and Cu-2Y_2O_3, and annealed GlidCop AL25 from 300 to 825 K obtained by LFA.

CuYO had a mean thermal conductivity over the same range of $267 \pm 6\,\mathrm{W\,m^{-1}\,K^{-1}}$, which compared favourably with a similar Cu-0.8Y-0.16O composite/ODS alloy produced by HIP consolidation that had a thermal conductivity of $\sim$240 $\mathrm{W\,m^{-1}\,K^{-1}}$ over the same temperature range [130]. Overall, given the challenges presented by Fe pick-up in the microstructures, thermal conductivity performance was encouraging when compared with published work.

Table 7.4 outlines the estimated individual contributions to the reduction of thermal conductivity compared with pure Cu, including grain diameter, volume fraction of particles and pores, and the presence of Fe impurities based on the assumptions presented in Section 2.4.2 and the applicability of the Wiedmann-Franz law. The single largest contributor to the reduction of thermal conductivity from that of pure Cu was expected to be 0.3 wt.% Fe (Table 7.1). If all Fe was retained in solid solution, an increase in the electrical resistivity of 34.5 $\mathrm{n\Omega\,m}$ would be expected, giving a total reduction in the thermal conductivity of $\sim$270 $\mathrm{W\,m^{-1}\,K^{-1}}$. However the total measured reduction was $<$130 $\mathrm{W\,m^{-1}\,K^{-1}}$, suggesting that relatively low concentrations of Fe

were retained in solution, and by implication, the majority of Fe was in the dispersed nanoparticles, as seen in EELS analysis in Fig. 7.7(e) and Fig. 7.17. The second largest contribution to the reduction in thermal conductivity was estimated to be the density of grain boundaries. The ultra-fine grained CuYO had the smallest mean grain diameter ($\sim$120 nm) and hence the highest density of grain boundaries leading to a possible reduction in the thermal conductivity of up to $\sim$80 $\mathrm{W\,m^{-1}\,K^{-1}}$. Table 7.4 also shows that as intended, the presence of the oxide nanoparticles had a relatively minor direct effect on thermal conductivity.

The thermal conductivity reductions in the CuYO and CuYOTi alloys were comparable to those for Cu-Al_2O_3 ODS alloys produced by reactive ball milling and HIP consolidation [22].

Table 7.4: Calculated contributions to thermal conductivity, κ, associated with presence of grain boundaries, particles, pores and Fe impurity solute atoms. All values in $\mathrm{W\,m^{-1}\,K^{-1}}$ at 20 °C, calculated using the approach in Section 2.4.2 [22, 47].

Contributing effect	CuYOTi	CuYO	AL25
$\Delta\kappa_{gb}$ (grain diameter, nm)	-42 (250)	-79 (120)	-27 (400)
$\Delta\kappa_{pa}$ (V_f particles)	-5.4 (0.0089)	-21 (0.0352)	-6.8 (0.0113)
$\Delta\kappa_{po}$ (V_f porosity)	-13 (0.022)	-35.4 (0.06)	-1.0 (0.001)
$\Delta\kappa_{Fe}$ (Fe impurity, wt.%)	-270 (0.3)	-25 (0.01)	-3 (0.001)
Expected κ	70	240	360

7.3.6 Thermal stability

Thermal stability is a primary consideration for any application as a Demonstration Power Plant (DEMO) heatsink material, and was evaluated by (i) microstructural assessment after isothermal ageing, and (ii) creep behaviour at elevated temperature.

Microstructural stability

Table 7.5 gives the measured microhardness of the as-sintered alloys and following isothermal ageing. AL25 was unaffected by isothermal ageing with any variation

considered to be within the error range because it was supplied in an already heat-treated and relatively stable condition. CuYO softened by 14%, while conversely CuYOTi hardened by 22% approaching a comparable hardness to CuYO. The AL25 and CuYOTi contained a similar fraction of alloying additions, so the increased hardness of CuYOTi may have implied further comparative precipitation of hardening and/or stabilising of particles occurred during ageing.

Table 7.5: Effect of isothermal ageing on hardness on CuYOTi, CuYO, and AL25

Alloy	Sintered hardness (MPa)	Aged hardness (MPa)
CuYOTi	1540 ± 240	1900 ± 140
CuYO	2440 ± 110	2100 ± 150
AL25	1430 ± 30	1400 ± 30

Figure 7.13 compares the microstructures of CuYOTi and AL25 following isothermal ageing. The microstructures were broadly similar with equiaxed grains of ∼250 nm and ∼500 nm respectively. Grain boundary pinning was implied to be more effective in CuYOTi, and there were fewer "abnormally" large grains (>800 nm).

Figure 7.14 shows the effect of isothermal ageing on the grain structure and textures of CuYOTi parallel to the forging direction (taken from thinned TEM specimens). Figure 7.14(a) shows the highly deformed microstructure after forging with flattened, plate-like grains shown in cross section. This contrasts with the equiaxed grain structure formed during recovery and recrystallisation in Fig. 7.14(b). Approximately, the grain diameter increased by a factor of ∼2 following ageing to 217 ± 17 nm, the aspect ratio of the grains changed from ∼0.3 to ∼1.

Figure 7.15(a) shows grain boundary pinning after ageing by nanoparticles of 8 to 25 nm in diameter, along with a fine dispersion of <10 nm nanoparticles within grains. Figure 7.15(b) shows remnant defect (dislocation) structures within the grains giving rise to contrast due to residual local strains.

Figure 7.16(a) shows nanoparticles residing in a comparatively large, coarsened grain of ∼600 nm by ∼1000 nm. The grain interior is largely defect free and Fig. 7.16(b)

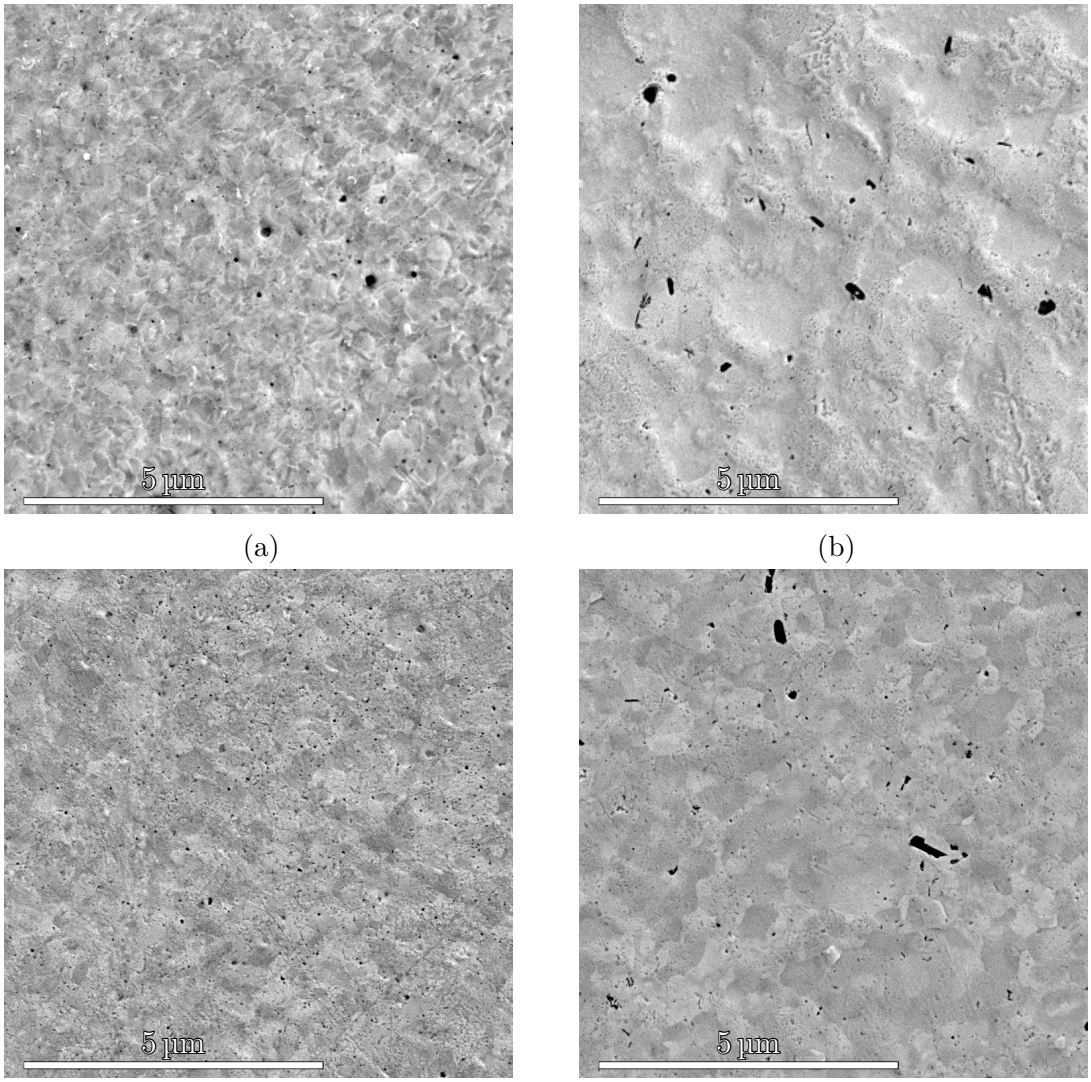

(a) (b)

(c) (d)

Figure 7.13: SE micrographs of the Cu-ODS alloys, imaged perpendicular to the forging and extrusion directions respectively. Prior to ageing **(a)** CuYOTi, **(b)** AL25, and 350 °C-545 h isothermally aged **(c)** CuYOTi, and **(d)** AL25.

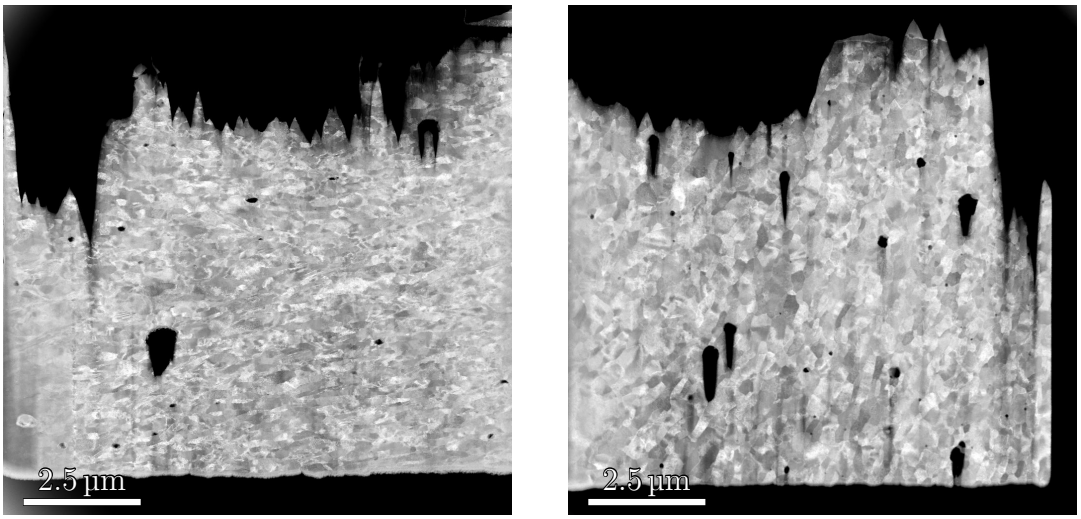

(a) (b)

Figure 7.14: ADF-STEM micrographs parallel to the forging direction from FIB liftouts of **(a)** CuYOTi prepared by FAST consolidated and cold-forging, and **(b)** following isothermal ageing.

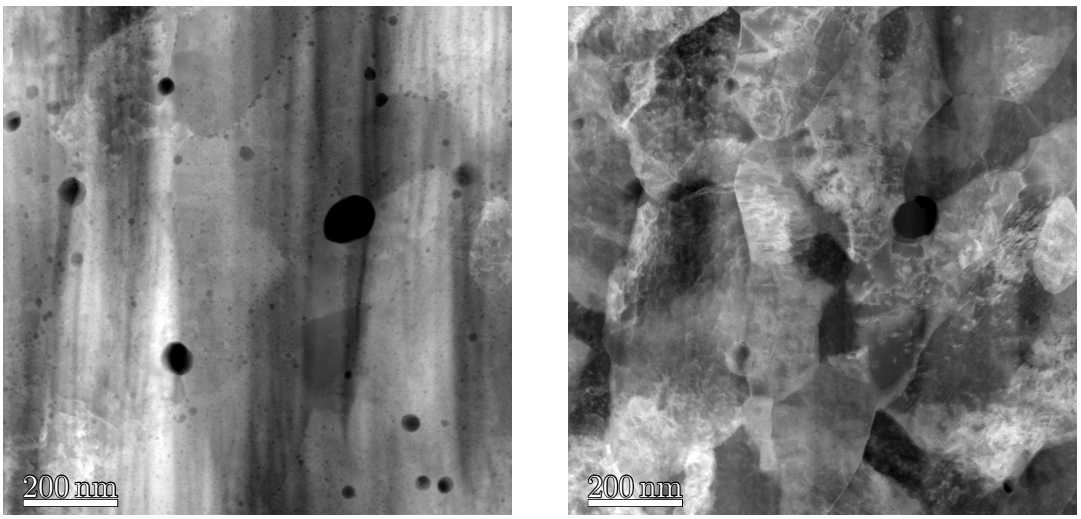

(a) (b)

Figure 7.15: STEM imaging from FIB liftout of CuYOTi following isothermal ageing: **(a)** HAADF micrograph, and **(b)** ADF micrograph.

shows the intragranular nanoparticles. 328 particles in the highlighted region in Fig. 7.16(a) had a mean diameter of 4.8 ± 1.5 nm. Particles with a diameter of less than 3.0 nm were considered to be unreliably resolved and were not included. In this case, despite the dispersion of particles, the driving force for grain coarsening overcame the Zener pinning force and the grain broke free, rapidly consuming comparably soluble grains nearby.

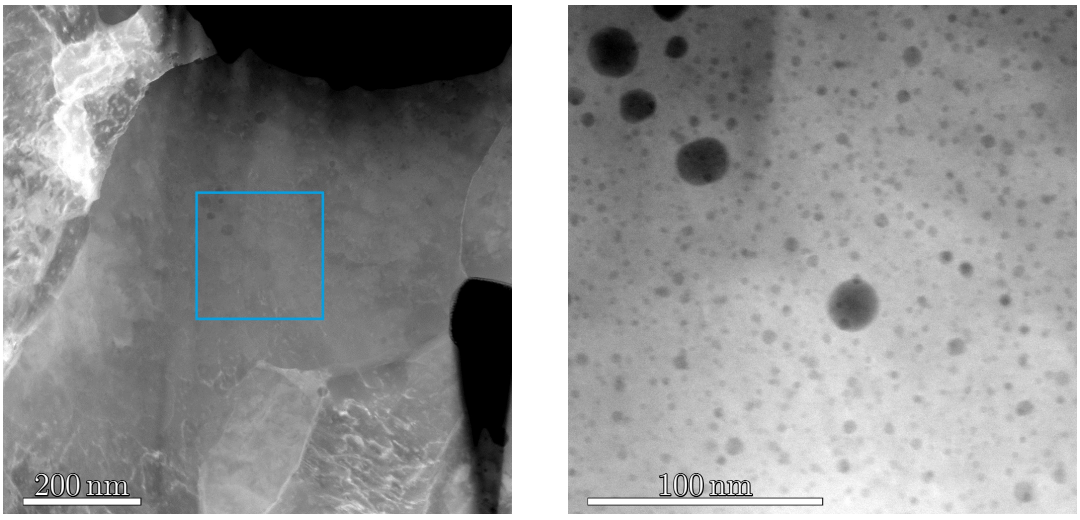

(a) (b)

Figure 7.16: STEM imaging of CuYOTi following isothermal ageing: **(a)** DF micrograph showing grain structure, and **(b)** HAADF micrograph showing nanoparticles within the region highlighted in (a), the average thickness of the matrix in this region was 19 nm.

Figure 7.17 shows EELS analysis of fine particles within a grain of CuYOTi. Here, imaging of the finest particles was optimum, with a mean nanoparticle diameter from 90 particles of 2.4 ± 0.9 nm. Figures 7.17(b) to 7.17(e) show the distribution of Y, Ti, O and Fe. There was near-complete overlap in the distributions of Ti, O and Fe obtained from core loss EELS analysis. It was not possible to deconvolute the plasmon peak overlap with the Y $N_{2,3}$ edges, however the Y map corresponded well with EDS data acquired simultaneously, and was co-located with the Ti, O and Fe. It was not possible to determine atomic ratios between the components of the EELS maps with required certainty.

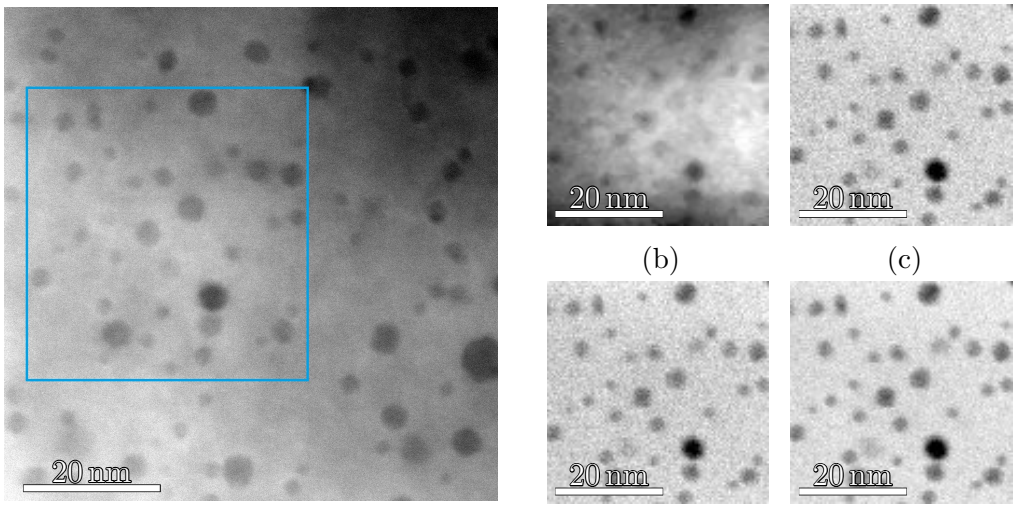

Figure 7.17: EELS analysis of particles in FAST consolidated and cold-forged Cu-0.25Ti-0.25Y_2O_3: **(a)** DF STEM showing the region of interest for EELS, the average thickness of the matrix in this region was 15 nm, **(b)** inverse Y $N_{2,3}$ map, **(c)** inverse Ti $L_{2,3}$ map, **(d)** inverse O K map, **(e)** inverse Fe $L_{2,3}$ map.

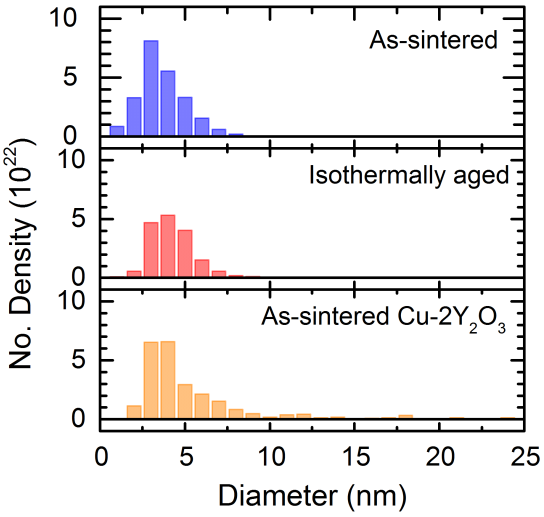

Figure 7.18: Nanocluster size distributions of Cu-0.25Y_2O_3-0.25Ti as-sintered (from 3489 particles in five regions measured from HAADF-STEM micrographs) and aged (from 1228 particles in five regions measured from HAADF-STEM micrographs) compared with Cu-2Y_2O_3 (taken from Fig. 4.19).

Table 7.6: Particle diameter, number density, and interparticle spacing for CuYOTi as-sintered (from 3489 particles in five regions measured from HAADF-STEM micrographs) and aged (from 1228 particles in five regions measured from HAADF-STEM micrographs) compared with CuYO (taken from Fig. 4.19

Sample	Mean diameter	Number density	Mean interparticle spacing
CuYOTi	3.2 ± 1.5 nm	2.36×10^{23} m^{-3}	16.2 nm
Aged CuYOTi	3.8 ± 1.7 nm	1.74×10^{23} m^{-3}	17.9 nm
CuYO	7.1 ± 6.0 nm	8.24×10^{22} m^{-3}	23.0 nm
AL25 [131]	4 to 25 nm	$\sim 1 \times 10^{21}$ m^{-3}	$\sim$100 nm

Figure 7.18 compares the measured nanoparticle/cluster size distributions of CuYOTi prior to and after isothermal ageing with as-sintered CuYO. The aged CuYOTi shifted the peak diameter slightly towards increased diameters. CuYO had a wider distribution of particle diameters, with a long tail of particles >20 nm in diameter. Changes in the particle diameter and size distribution after isothermal ageing were limited to an increase from 4.7×10^{22} to 8.1×10^{22} m^{-3} in particles between 3 nm and 4 nm in diameter, and a corresponding decrease in the number density of particles >3 nm in diameter. Again, this was attributed to incomplete particle formation during sintering, which was only completed during the longer ageing cycle. Table 7.6 gives the mean diameter, particle number density and interparticle spacing for CuYOTi prior to and after isothermal ageing, along with the as-sintered CuYO and literature measurements for as-extruded AL25 [131]. The CuYOTi showed a significant reduction in the mean particle diameter compared with CuYO, both of which had significantly reduced particle diameter, increased number density and reduced interparticle spacing when compared with AL25. The particle diameters in the CuYOTi were consistent with the idealised design requirement outlined in Section 6.1. CuYOTi also compared favourably in terms of particle size with recent Y_2O_3-containing Cu-ODS alloys in the literature prepared by MA of Cu with Y in an O-rich enivronment that yielded a Cu-0.8Y-0.16O alloy with a mean Y_2O_3 particle diameter of 920 nm [130, 132].

Creep resistance

Small punch testing of aged CuTiYO, CuYO and AL25 was undertaken at 350 °C in an Ar atmosphere to evaluate creep resistance. The technique does not provide creep data comparable with uniaxial creep testing on account of the loading geometry. However, as a comparative technique it offers significant benefits in the reduced sample size and simple planar nature of specimens allowing, for example, small and safe irradiated samples to be investigated quickly and conveniently. Creep results here are provided only for semi-quantitative ranking of the response of the various alloys and cannot be compared with literature values.

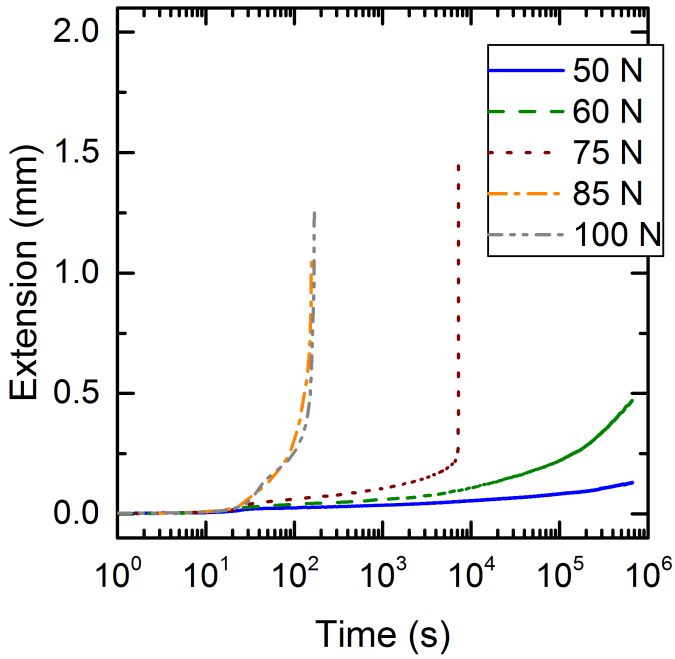

Figure 7.19: Small punch creep testing at 350 °C; of FAST consolidated, cold forged and thermally aged CuYOTi, showing the extension with time for loading at 50 N, 60 N, 75 N, 85 N and 100 N.

Figure 7.19 shows the effect of increasing load on the extension of CuYOTi with time. Higher loads led to breakthrough of the disc within minutes while at lower loads, the experiments had to be stopped before failure after 100 h as time constraints on

equipment access prevented continuation. The samples all reached a pseudo steady-state of increasing extension with time, indicative of secondary creep [88, 133], before the creep accelerated leading to failure, indicative of tertiary creep.

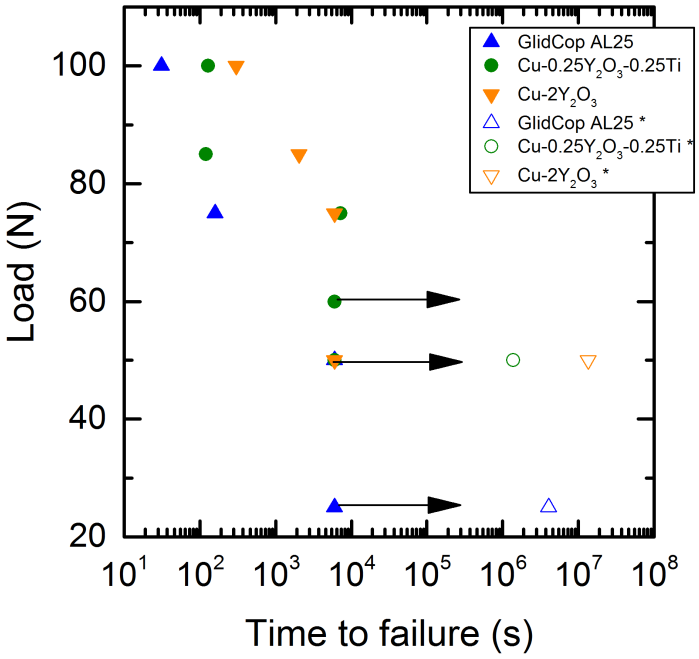

Figure 7.20: Small punch creep testing at 350 °C of FAST consolidated, cold forged and thermally aged Cu-0.25Ti-0.25Y_2O_3(CuYOTi), Cu-2Y_2O_3 (CuYO), and hot extruded GlidCop AL25. Testing was stopped after 3.6×10^5 s, indicated by an arrow, and extrapolation for estimated failure time for unfailed samples was made based on their pseudo steady-state creep rate, indicated by *.

Figure 7.20 shows the effect of load on the failure time for CuYOTi, CuYO and AL25. AL25 consistently failed at lower loads than CuYOTi, which in turn failed at lower loads than CuYO, and within the range studied CuYO was the most creep resistant.

Figure 7.21 shows the failure surfaces of the three samples, CuYO, CuYOTi and AL25. The CuYO had the greatest resistance to breakthrough of the punch, as evidenced by the limited failures in Figs. 7.21(a) and 7.21(b). The punch breakthrough was via radial fracture in all cases, with punch out of the disc centre in the less creep

resistant CuYOTi and AL25. It is hypothesised that the CuYO and CuYOTi exceeded the creep resistance of the AL25 for two primary reasons. First, the FAST process does not impart significant texture into the material, whereas the AL25 had typical extrusion texture, presenting a large number of long grain boundaries that promoted creep. Second, the distribution of oxide particles was narrower and finer in the CuYO and CuYOTi than in the AL25, so better grain boundary pinning was achieved. The largest oxide particles in the Cu-Y_2O_3 ODS alloys of around 40 nm are a factor of 100 smaller than those observed in AL25 which were as large as 5 µm on occasion - the distribution of more closely spaced particles provides more effective pinning points and enhanced creep resistance [51, 88].

7.4 Summary

Cu-0.25Y_2O_3-0.25Ti was produced from precursor powders of Cu-0.5Ti, Cu and Y_2O_3 by MA, consolidated by FAST, cold-forged, annealed and then aged. Properties were characterised by hardness evaluation, tensile testing, laser flash analysis, and elevated temperature small punch testing. The microstructure was characterised by SEM and TEM using EDS and EELS with a focus on Cu grain size and nanoparticle development.

It was found that:

- After ageing a near-homogeneous distribution of Ti and Y-rich nanoparticles was formed, which were very stable over the period investigated and were generally highly effective in pinning recrystallised grains so that the mean grain size coarsened only to ∼200 nm.
- The room temperature thermal conductivity of Cu-0.25Y_2O_3-0.25Ti was lower than the commercially available GlidCop AL25 ODS alloy, but higher than the

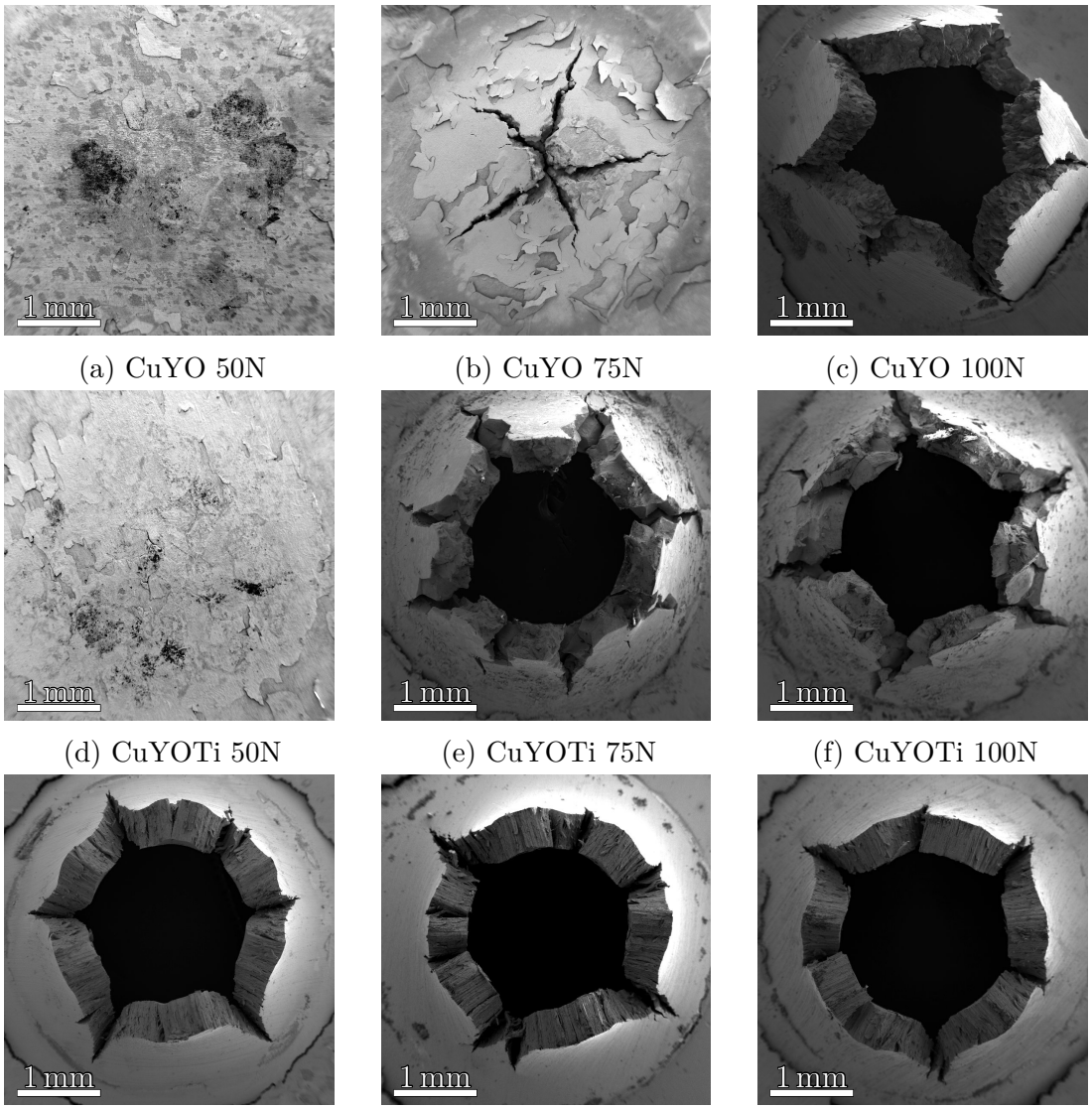

(a) CuYO 50N (b) CuYO 75N (c) CuYO 100N

(d) CuYOTi 50N (e) CuYOTi 75N (f) CuYOTi 100N

(g) AL25 50N (h) AL25 100N (i) AL25 75N

Figure 7.21: SE micrographs showing the effect of increasing load on failure surfaces of CuYO, CuYOTi and AL25 small punch test samples, tested at 350 °C until failure or 100 h.

in-house Cu-2Y_2O_3, However at the proposed DEMO operating temperature of 300 °C Cu-0.25Y_2O_3-0.25Ti had a similar thermal conductivity to AL25.

- Room temperature tensile properties of Cu-0.25Y_2O_3-0.25Ti were undermined by incomplete sintering and most particularly by a distribution of Fe-based inclusions at prior particle boundaries and within grains. In particular, room temperature tensile ductility was reduced to below useful levels.

- Despite poor room temperature tensile properties, the creep resistance of Cu-0.25Y_2O_3-0.25Ti was higher than commercially available GlidCop AL25 ODS alloy during small punch creep testing. The four times higher oxide fraction of Cu-2Y_2O_3 provided the best creep resistance.

Chapter 8

Conclusions and suggestions for further work

8.1 Conclusions

This thesis investigated the manufacture, microstructure and properties of Cu-based ODS alloys for possible fusion power applications as a heat sink material. Initially work concerned showing proof-of-principle, followed by various developments to incorporate alloying elements, followed by consolidation and property studies. At all stages high resolution microscopy was used to investigate the behaviour of the critical nano-scale dispersoids.

Objective 1

To investigate the relationship between the microstructure and properties, and their stability, in Cu-ODS alloys, with an emphasis on the dynamics and mechanism of any oxide dissolution and subsequent re-precipitation and ageing.

Planetary ball milling of Cu showed expected difficulties of cold-welding dominating over work-hardening. The addition of a minority of 20-40 nm Y_2O_3 improved particle refinement during MA and some of the Y_2O_3 was dispersed at fine-scale within the Cu matrix. With limited work-hardening (compared with Fe alloys) the capacity of the Cu for refining and absorbing Y_2O_3 fragments was low, so that perhaps less than 1% of the added Y_2O_3 was effectively distributed and refined. An addition of 2 wt.%

Y_2O_3 resulted in a bimodal distribution of Y_2O_3 nanoparticles in Cu, comprising "virgin" particles and a minority of those that had experienced some refinement and effective dispersion.

The proposed mechanism for distribution of the Y_2O_3 in Cu was by a combination of fragmentation followed by limited disassociation of Y and O. Y-rich nanoparticles of a refined size and comparatively even distribution formed on subsequent thermal exposure. Both HIP and FAST could be used to re-precipitate particles during consolidation, and relatively fast grain boundary diffusion paths gave rise to the formation of larger particles at grain boundaries than in the grain interiors.

Triple points and interfaces between prior particle boundaries (defined by surface oxides) that consolidated at high temperature formed microstructures that were denuded of the Y and O-rich nanoparticles which was suggested to be consistent with Y_2O_3 fragmentation and partial disassociation during milling. Similar particle denuded zones have not been reported in other ODS alloys, which tend to use more complex composition matrix alloys.

Thermal ageing of the alloys showed that consolidated microstructures were stable, with retained ultra-fine grain sizes below 200 nm and a dispersion of nanoparticles that showed only very slight Ostwald ripening during ageing. In general, the microstructures were finer than other Cu-ODS alloys made from comparable alloys, and showed promise for further investigation.

Objective 2

To investigate the relationship between the processing conditions and Cu-ODS microstructure in both as-milled powder and bulk consolidated material, and the effect of ternary alloying additions on microstructure.

Consolidation of Cu-Y_2O_3 alloys was not straightforward, with difficulty in achieving high densities resulting from the cold-welding of powder particles produced during

MA giving large particles that sintered poorly. Post-consolidation thermomechanical treatments of forging and annealing facilitated residual pore removal and gave final bulk densities >99% of the theoretical density.

Ternary additions of Ti were explored (i) to provide an improved Cu work-hardening response and thus improve the milling response, and (ii) to refine nano-oxides, in a similar fashion to its effect in Fe-ODS alloys. The most effective route for Ti addition during processing was identified as melt-alloying to prepare a Cu feedstock powder, which was then alloyed with Y_2O_3 and diluted with Cu powder during MA. However the addition of Ti always led to reaction and agglomeration with Y_2O_3 and facilitated pick-up of Fe contamination from the milling pot and media. Despite this, when the optimum route was used, Ti additions enabled a reduction by a factor of 2 of the mean oxide nanoparticle diameter, which was attributed to a reduction in the surface energy of the particle that was suggested by greater coherency of nanoparticles with the Cu matrix.

Objective 3

To compare in-house produced materials with competitor Cu alloys and Cu-ODS products suitable for the divertor application and to explore the relationship between processing route and properties, with particular emphasis on investigating the thermal stability of Cu-ODS alloys with respect to microstructure and creep.

Figure 8.1 compares fusion relevant Cu alloys suggested for divertor application according to their 0.2% proof strength and thermal conductivity. The principle alloys examined in this thesis are added to the figure: the model alloy system Cu-$2Y_2O_3$, and the best-design alloy Cu-$0.25Y_2O_3$-0.25Ti. In terms of the properties reported here, the ODS alloys showed a moderate strength-conductivity performance combination. The figure also suggests the further improvements that these alloys might achieve with further optimisation, most particularly by elimination of Fe contamination, which in

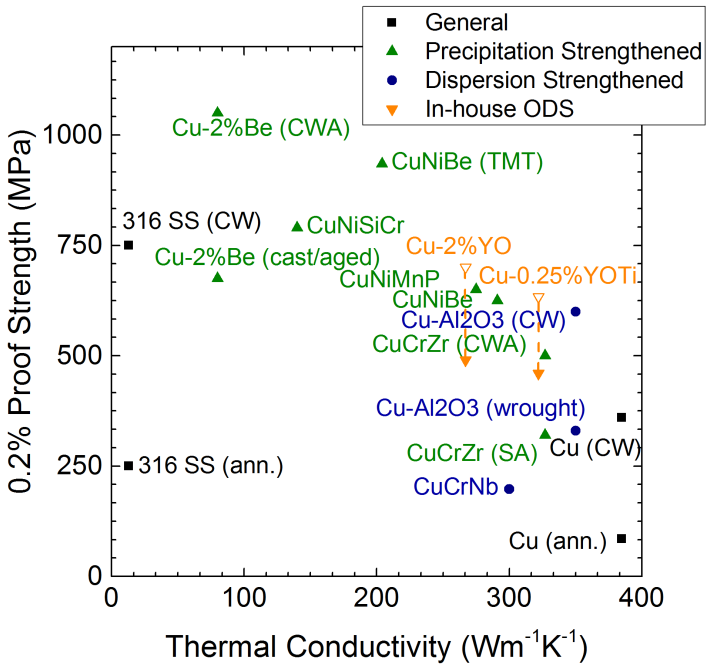

Figure 8.1: Room temperature 0.2% proof strength from tensile testing versus thermal conductivity of fusion Cu alloys, [11], including in-house consolidated, cold-forged and isothermally aged Cu-2Y_2O_3 and Cu-0.25Y_2O_3-0.25Ti, the upper bounds represent the potential alloy strength ignoring PPB sintering difficulties.

principle, should be relatively easy to achieve. These optimised alloys would then occupy property space unachievable by existing alloys. Further, on the basis of creep data in this thesis, it can be expected that strengths would be maintained to higher temperatures successfully, owing to the good stability and effective pinning that the nanoparticles provide.

The new Cu-ODS alloys microstructures had significant grain refinement compared with commercial Cu-ODS and other alloys, aided by generally even distribution of fine particles in the majority of the alloy volume. Abnormal grain growth following ageing was not observed.

Creep properties were evaluated by small punch testing and compared with commercial Cu alloy GlidCop AL25 and were shown semi-quantitatively to exceed those of AL25 under identical conditions.

Overall, despite some difficulties in identifying effective processing and alloying routes, new Cu-ODS alloys have been developed that allow equivalent, preliminary properties to commercially available comparable alloys, and given that obvious further improvements might be readily achieved, offer the potential for a new class of stable, higher performing Cu-ODS alloys for fusion applications.

8.2 Suggestions for further work

There are a number of opportunities for the further development of Cu-ODS alloys produced by MA.

Milling

The mechanical alloying process examined in this thesis suffered from the introduction of contamination in the form of Fe. Fortuitously the Fe generally re-precipitated with the other alloying elements (Ti, Y, O) to form complex oxides rather than potentially more mechanically damaging intermetallics or conductivity lowering solid solutions.

MA should be undertaken using milling pots and media constructed of the desired dispersoid compound, such as Y_2O_3, Al_2O_3, *et cetera*.

Scalability of planetary ball milling is generally considered poor by industry. Similar Cu-ODS alloy could now be investigated using attritor mills that are considered much more scalable, and can be actively cooled to improve the ratio of work-hardening and fracture to cold-welding of the ductile Cu powder. A reduction of the milling temperature toward cryogenic temperature could be considered in an attritor system, and can be expected to significantly improve the milling process in terms of time taken and effective alloying.

Investigation of process control agents as a method to introduce alloying elements and simultaneously improve the ratio of work-hardening and fracture to cold-welding, could offer opportunities for more rapid powder refinement.

Consolidation

Consolidation by FAST, VHP, and HIP each suffered from ineffective sintering, although the fine microstructural features necessary for strengthening could be retained. Industrially, the gold standard for consolidation of powder products is by direct powder extrusion, which is difficult to achieve at the laboratory scale owing to the large powder charge required (typically >10 kg). Powder forging of MA Cu-ODS might produce alloys with the best mechanical properties since powder surface oxides - shown here to be problematic - are sheared and ruptured in a manner unavailable in HIP, FAST, *et cetera*.

Mechanical property characterisation

There remain key mechanical properties for fusion divertor application that were not examined in this thesis. Particularly toughness, fatigue resistance, and elevated temperature properties. These must be evaluated and in particular, fatigue and

toughness properties are likely to be encouraging only in powder forged/extruded variants that promote the mechanical break-up of surface oxides.

Irradiation resistance

The alloy design has been considered for an active fusion environment based on the understanding of other Cu-ODS and precipitation hardening alloys. The properties that result from irradiation particularly in terms of the effectiveness of the nanoparticles in prevention of swelling by acting as He sinks should be evaluated. The effect of irradiation on the stability of the nanoparticles themselves might also be usefully evaluated.

Ternary additions

Whilst Ti was effective in improving some of the properties of the Cu-Y_2O_3 alloys, it was not possible to fully understand the mechanism for the improvements observed. There are multiple opportunities to further develop the understanding of the role of Ti in the Cu-ODS system perhaps drawing further on the more developed understanding in Fe-ODS alloys.

Overall

If the suggested further development works could be undertaken, the Cu-Y_2O_3-Ti system presents a promising alternative to the precipitation strengthened Cu alloys for divertor application. On the basis of the work in this thesis and the outstanding results seen particularly in creep resistance, thermal conductivity and microstructural control, in a less-than-perfect manufacturing parameter space, it is expected that the anticipated improved properties would allow ready adoption and improved performance for future fusion reactors.

References

[1] Garry M McCracken and Peter E Stott. *Fusion: the Energy of the Universe*. Academic Press, 2012.

[2] EUROfusion. Focus on limiters and divertors, 2014. "[Online; accessed 20-August-2014].

[3] AK Suri, N Krishnamurthy, and IS Batra. Materials issues in fusion reactors. In *Journal of Physics: Conference Series*, volume 208, page 012001. IOP Publishing.

[4] J. H. You, G. Mazzone, E. Visca, Ch Bachmann, E. Autissier, T. Barrett, V. Cocilovo, F. Crescenzi, P. K. Domalapally, D. Dongiovanni, S. Entler, G. Federici, P. Frosi, M. Fursdon, H. Greuner, D. Hancock, D. Marzullo, S. McIntosh, A. V. Müller, M. T. Porfiri, G. Ramogida, J. Reiser, M. Richou, M. Rieth, A. Rydzy, R. Villari, and V. Widak. Conceptual design studies for the european demo divertor: Rationale and first results. *Fusion Engineering and Design*, 109–111, Part B:1598–1603, 2016.

[5] M. Porton and W Timmis. The potential of ods copper alloys as the structural material for the demo divertor. Technical report, CCFE, 2013.

[6] Antonella Li-Puma, Marianne Richou, Philippe Magaud, Marc Missirlian, Eliseo Visca, and Vincenzo Pericoli Ridolfini. Potential and limits of water cooled divertor concepts based on monoblock design as possible candidates for a demo reactor. *Fusion Engineering and Design*, 88(9–10):1836–1843, 2013.

[7] Jack Robert Nicholas, Peter Ireland, David Hancock, and Dan Robertson. Development of a high-heat flux cooling element with potential application in a near-term fusion power plant divertor. *Fusion Engineering and Design*, 2015.

[8] J. H. You, E. Visca, Ch Bachmann, T. Barrett, F. Crescenzi, M. Fursdon, H. Greuner, D. Guilhem, P. Languille, M. Li, S. McIntosh, A. V. Müller, J. Reiser, M. Richou, and M. Rieth. European demo divertor target: Operational requirements and material-design interface. *Nuclear Materials and Energy*, 2016.

[9] W Timmis. Material assessment report on the use of copper alloys in demo (2012). Report, CCFE, 2013.

[10] H. Trinkaus and B. N. Singh. Helium accumulation in metals during irradiation – where do we stand? *Journal of Nuclear Materials*, 323(2–3):229–242, 2003.

[11] Steven J Zinkle. Applicability of copper alloys for demo high heat flux components. *Physica Scripta*, 2016(T167):014004, 2016.

[12] D. D. L. Chung. Materials for thermal conduction. *Applied Thermal Engineering*, 21(16):1593–1605, 2001.

[13] G. J. Butterworth and C. B. A. Forty. A survey of the properties of copper alloys for use as fusion reactor materials. *Journal of Nuclear Materials*, 189(3):237–276, 1992.

[14] L. Commin, S. Antusch, S. Baumgartner, D. Bolich, B. Dafferner, W. Goldacker, M. Hoffmann, P. Lukits, M. Rieth, and H. Zimmermann. Assessment of copper based materials for the water-cooled divertor concept of the demo european fusion reactor. In *Fusion Engineering (SOFE), 2013 IEEE 25th Symposium on*, pages 1–4, 2013.

[15] ITER. Iter structural design criteria for in-vessel components, appendix a g 74 ma 8 01-05-28 w0.2. Technical report, ITER, 2013.

[16] A. A. Ridha and W. B. Hutchinson. Recrystallisation mechanisms and the origin of cube texture in copper. *Acta Metallurgica*, 30(10):1929–1939, 1982.

[17] Yue Zhang, Jing Tao Wang, Chang Cheng, and Jinqiang Liu. Stored energy and recrystallization temperature in high purity copper after equal channel angular pressing. *Journal of Materials Science*, 43(23):7326, 2008.

[18] JR Groza and JC Gibeling. Principles of particle selection for dispersion-strengthened copper. *Materials Science and Engineering: A*, 171(1):115–125, 1993.

[19] J.W. Martin. *Micromechanisms in Particle-Hardened Alloys*. Cambridge University Press, 1980.

[20] D. J. Dunstan and A. J. Bushby. Grain size dependence of the strength of metals: The hall–petch effect does not scale as the inverse square root of grain size. *International Journal of Plasticity*, 53(0):56–65, 2014.

[21] Haiou Zhuo, Jiancheng Tang, and Nan Ye. A novel approach for strengthening cu–y2o3 composites by in situ reaction at liquidus temperature. *Materials Science and Engineering: A*, 584:1–6, 2013.

[22] S. Nachum, N. A. Fleck, M. F. Ashby, A. Colella, and P. Matteazzi. The microstructural basis for the mechanical properties and electrical resistivity of nanocrystalline cu–al2o3. *Materials Science and Engineering: A*, 527(20):5065–5071, 2010.

[23] Matthew J Alinger. *On the formation and stability of nanometer scale precipitates in ferritic alloys during processing and high temperature service*. Thesis, 2004.

[24] A. Hirata, T. Fujita, Y. R. Wen, J. H. Schneibel, C. T. Liu, and M. W. Chen. Atomic structure of nanoclusters in oxide-dispersion-strengthened steels. *Nat Mater*, 10(12):922–926, 2011.

[25] T Okuda and M Fujiwara. Dispersion behaviour of oxide particles in mechanically alloyed ods steel. *Journal of Materials Science Letters*, 14(22):1600–1603, 1995.

[26] M. Ratti, D. Leuvrey, M. H. Mathon, and Y. de Carlan. Influence of titanium on nano-cluster (y, ti, o) stability in ods ferritic materials. *Journal of Nuclear Materials*, 386-388:540–543, 2009.

[27] Sheng-Yi Zhong, Joel Ribis, Nicolas Lochet, Yann de Carlan, Vincent Klosek, Vincent Ji, and Marie-Hélène Mathon. The effect of y/ti ratio on oxide precipitate evolution in ods fe-14 wt pct cr alloys. *Metallurgical and Materials Transactions A*, 46(3):1413–1418, 2015.

[28] M. A. Thual, J. Ribis, T. Baudin, V. Klosek, Y. de Carlan, and M. H. Mathon. Relaxation path of nanoparticles in an oxygen-enriched ferritic oxide-dispersion-strengthened alloy. *Scripta Materialia*, 136:37–40, 2017.

[29] A. J. London, S. Santra, S. Amirthapandian, B. K. Panigrahi, R. M. Sarguna, S. Balaji, R. Vijay, C. S. Sundar, S. Lozano-Perez, and C. R. M. Grovenor. Effect of ti and cr on dispersion, structure and composition of oxide nano-particles in model ods alloys. *Acta Materialia*, 97:223–233, 2015.

[30] A. Hirata, T. Fujita, C. T. Liu, and M. W. Chen. Characterization of oxide nanoprecipitates in an oxide dispersion strengthened 14ywt steel using aberration-corrected stem. *Acta Materialia*, 60(16):5686–5696, 2012.

[31] Teruo Takahashi, Yasuhiko Hashimoto, Shinichiro Omori, and Koichiro Koyama. Dispersion hardening of cu–al–ti alloys by internal oxidation. *Transactions of the Japan institute of metals*, 26(4):271–279, 1985.

[32] Seung Zeon Han, Kwang Ho Kim, Joonhee Kang, Hongrae Joh, Sang Min Kim, Jee Hyuk Ahn, Jehyun Lee, Sung Hwan Lim, and Byungchan Han. Design of exceptionally strong and conductive cu alloys beyond the conventional speculation via the interfacial energy-controlled dispersion of al_2o_3 nanoparticles. *Scientific reports*, 5:17364, 2015.

[33] S Barzilai, M Aizenshtein, N Froumin, and N Frage. Y2o3/(cu–me) systems (me= al, ti): interface reactions and wetting. *Journal of materials science*, 41(16):5108–5112, 2006.

[34] S. Suzuki, K. Hirabayashi, H. Shibata, K. Mimura, M. Isshiki, and Y. Waseda. Electrical and thermal conductivities in quenched and aged high-purity cu–ti alloys. *Scripta Materialia*, 48(4):431–435, 2003.

[35] S Nagarjuna. Thermal conductivity of cu-4.5 ti alloy. *Bulletin of Materials Science*, 27(1):69–71, 2004.

[36] Tatsuo Oku, Akira Kurumada, Toshiaki Sogabe, Takeo Oku, Toshiharu Hiraoka, and Koji Kuroda. Effects of titanium impregnation on the thermal conductivity of carbon/copper composite materials. *Journal of Nuclear Materials*, 257(1):59–66, 1998.

[37] Yeram Sarkis Touloukian, RW Powell, CY Ho, and MC Nicolaou. Thermophysical properties of matter-the tprc data series. volume 10. thermal diffusivity. Report, DTIC Document, 1974.

[38] D. V. Kudashov, H. Baum, U. Martin, M. Heilmaier, and H. Oettel. Microstructure and room temperature hardening of ultra-fine-grained oxide-dispersion strengthened copper prepared by cryomilling. *Materials Science and Engineering: A*, 387-389:768–771, 2004.

[39] S. Cheng, E. Ma, Y. M. Wang, L. J. Kecskes, K. M. Youssef, C. C. Koch, U. P. Trociewitz, and K. Han. Tensile properties of in situ consolidated nanocrystalline cu. *Acta Materialia*, 53(5):1521–1533, 2005.

[40] Farideh Salimyanfard, Mohammad Reza Toroghinejad, Fakhreddin Ashrafizadeh, and Meysam Jafari. Ebsd analysis of nano-structured copper processed by ecap. *Materials Science and Engineering: A*, 528(16–17):5348–5355, 2011.

[41] JP Stobrawa, ZM Rdzawski, and WJ Głuchowski. Microstructure and properties of nanocrystalline copper-yttria microcomposites. *Journal of Achievements in Materials and Manufacturing Engineering*, 24(2):83–86, 2007.

[42] Abderrazak Daoud, Jean-Bernard Vogt, Eric Charkaluk, Jérémie Bouquerel, Lin Zhang, and Jean-Claude Biasci. Anisotropy effects on the tensile and fatigue behaviour of an oxide dispersion strengthened copper alloy. *Materials Science and Engineering: A*, 534(0):640–648, 2012.

[43] S. A. Fabritsiev, A. S. Pokrovsky, S. J. Zinkle, and S. E. Ostrovsky. Effect of helium on the swelling of glidcop al25 ig alloy. *Journal of Nuclear Materials*, 306(2–3):218–231, 2002.

[44] Ömer Güler and Ertan Evin. The investigation of contact performance of oxide reinforced copper composite via mechanical alloying. *Journal of Materials Processing Technology*, 209(3):1286–1290, 2009.

[45] C. Kittel. *Introduction to Solid State Physics*. Wiley, 2004.

[46] P. V. Andrews, M. B. West, and C. R. Robeson. The effect of grain boundaries on the electrical resistivity of polycrystalline copper and aluminium. *Philosophical Magazine*, 19(161):887–898, 1969.

[47] P. Sudharshan Phani, V. Vishnukanthan, and G. Sundararajan. Effect of heat treatment on properties of cold sprayed nanocrystalline copper alumina coatings. *Acta Materialia*, 55(14):4741–4751, 2007.

[48] S. Tähtinen, M. Pyykkönen, P. Karjalainen-Roikonen, B. N. Singh, and P. Toft. Effect of neutron irradiation on fracture toughness behaviour of copper alloys. *Journal of Nuclear Materials*, 258–263, Part 1(0):1010–1014, 1998.

[49] S Tähtinen, A Laukkanen, and BN Singh. Damage mechanisms and fracture toughness of glidcop cual25 ig0 copper alloy. *Journal of nuclear materials*, 283:1028–1032, 2000.

[50] Ronald R. Solomon, Jack D. Troxell, and Anil V. Nadkarni. Glidcop dsc properties in the temperature range of 20–350c. *Journal of Nuclear Materials*, 233–237, Part 1:542–546, 1996.

[51] G. Li, B. G. Thomas, and J. F. Stubbins. Modeling creep and fatigue of copper alloys. *Metallurgical and Materials Transactions A*, 31(10):2491–2502, 2000.

[52] M Li and SJ Zinkle. 4.20-physical and mechanical properties of copper and copper alloys. *Compr. Nucl. Mater., Elsevier, Oxford*, pages 667–690, 2012.

[53] JP Stobrawa and ZM Rdzawski. Thermal stability of functional properties in dispersion and precipitation hardened selected copper alloys. *Archives of Materials Science and Engineering*, 30(1):17–20, 2008.

[54] Amir Afshar and A Simchi. Abnormal grain growth in alumina dispersion-strengthened copper produced by an internal oxidation process. *Scripta Materialia*, 58(11):966–969, 2008.

[55] H. R. Brager, H. L. Heinisch, and F. A. Garner. Effects of neutron irradiation at 450c and 16 dpa on the properties of various commercial copper alloys. *Journal of Nuclear Materials*, 133–134(0):676–679, 1985.

[56] SA Fabritsiev and AS Pokrovsky. Effect of irradiation temperature on microstructure, radiation hardening and embrittlement of pure copper and copper-based alloy. *Journal of Nuclear Materials*, 367:977–983, 2007.

[57] BN Singh and S Tähtinen. *Final report on characterization of physical and mechanical properties of copper and copper alloys before and after irradiation.* 2002.

[58] JA Cahill and AD Kirshenbaum. The density of liquid copper from its melting point (1356 k.) to 2500 k. and an estimate of its critical constants. *Journal of Physical Chemistry (US)*, 66, 1962.

[59] LLC MatWeb. Matweb - materials properties database, 2017. [Online; accessed 03-January-2017].

[60] C. Suryanarayana and Nasser Al-Aqeeli. Mechanically alloyed nanocomposites. *Progress in Materials Science*, 58(4):383–502, 2013.

[61] C. Suryanarayana. Mechanical alloying and milling. *Progress in Materials Science*, 46(1):1–184, 2001.

[62] M. Samadi Khoshkhoo, S. Scudino, J. Bednarcik, A. Kauffmann, H. Bahmanpour, J. Freudenberger, R. Scattergood, M. J. Zehetbauer, C. C. Koch, and J. Eckert. Mechanism of nanostructure formation in ball-milled cu and cu–3wt.%zn studied by x-ray diffraction line profile analysis. *Journal of Alloys and Compounds*, 588(0):138–143, 2014.

[63] Viseslava Rajkovic, Dusan Bozic, and Milan T Jovanovic. Properties of copper matrix reinforced with various size and amount of al2o3 particles. *Journal of Materials Processing Technology*, 200(1):106–114, 2008.

[64] Michael S Nagorka, Carlos G Levi, and Glenn E Lucas. Novel oxide-dispersion-strengthened copper alloys from rapidly solidified precursors: Part 1. microstructural development. *Metallurgical and Materials Transactions A*, 26(4):859–871, 1995.

[65] Z. A. Munir, U. Anselmi-Tamburini, and M. Ohyanagi. The effect of electric field and pressure on the synthesis and consolidation of materials: A review of the spark plasma sintering method. *Journal of Materials Science*, 41(3):763–777, 2006.

[66] Zhao-Hui Zhang, Zhen-Feng Liu, Ji-Fang Lu, Xiang-Bo Shen, Fu-Chi Wang, and Yan-Dong Wang. The sintering mechanism in spark plasma sintering–proof of the occurrence of spark discharge. *Scripta Materialia*, 81:56–59, 2014.

[67] Olivier Guillon, Jesus Gonzalez-Julian, Benjamin Dargatz, Tobias Kessel, Gabi Schierning, Jan Räthel, and Mathias Herrmann. Field-assisted sintering technology/spark plasma sintering: mechanisms, materials, and technology developments. *Advanced Engineering Materials*, 16(7):830–849, 2014.

[68] Charles Hirlimann. Understanding the branly effect. *arXiv preprint cond-mat/0703495*, 2007.

[69] Pierre Guyot, Vincent Rat, JF Coudert, F Jay, Alexandre Maitre, and Nicolas Pradeilles. Does the branly effect occur in spark plasma sintering? *Journal of Physics D: Applied Physics*, 45(9):092001, 2012.

[70] Min Yu, Salvatore Grasso, Ruth Mckinnon, Theo Saunders, and Michael J Reece. Review of flash sintering: materials, mechanisms and modelling. *Advances in Applied Ceramics*, 116(1):24–60, 2017.

[71] Zuhair A Munir, Dat V Quach, and Manshi Ohyanagi. Electric current activation of sintering: a review of the pulsed electric current sintering process. *Journal of the American Ceramic Society*, 94(1):1–19, 2011.

[72] Niraj Chawake, Linford D Pinto, Ajeet K Srivastav, Karthik Akkiraju, BS Murty, and Ravi Sankar Kottada. On joule heating during spark plasma sintering of metal powders. *Scripta Materialia*, 93:52–55, 2014.

[73] Zhao-Hui Zhang, Fu-Chi Wang, Lin Wang, and Shu-Kui Li. Ultrafine-grained copper prepared by spark plasma sintering process. *Materials Science and Engineering: A*, 476(1-2):201–205, 2008.

[74] K. N. Zhu, A. Godfrey, N. Hansen, and X. D. Zhang. Microstructure and mechanical strength of near- and sub-micrometre grain size copper prepared by spark plasma sintering. *Materials and Design*, 117:95–103, 2017.

[75] MA Auger, V de Castro, T Leguey, A Muñoz, and R Pareja. Microstructure and mechanical behavior of ods and non-ods fe-14cr model alloys produced by spark plasma sintering. *Journal of Nuclear Materials*, 2013.

[76] Anselmi-Tamburini U., Z.A. Munir, and J.E. Garay. Preparation of dense nanostructured functional oxide materials with fine crystallite size by field activation sintering, 2009.

[77] Xue-Hui Zhang, Chen-Guang Lin, and Shun Cui. Microstructure and properties of al2o3 dispersion-strengthened copper fabricated by reactive synthesis process. *Rare Metals*, pages 1–5, 2013.

[78] Xiaoqiao Tang, Haibin Zhang, Daming Du, Dong Qu, Chunfeng Hu, Rongjun Xie, and Yi Feng. Fabrication of w–cu functionally graded material by spark plasma sintering method. *International Journal of Refractory Metals and Hard Materials*, 42:193–199, 2014.

[79] G. Cipolloni, M. Pellizzari, A. Molinari, M. Hebda, and M. Zadra. Contamination during the high-energy milling of atomized copper powder and its effects on spark plasma sintering. *Powder Technology*, 275(0):51–59, 2015.

[80] Daniel B Butrymowicz, John R Manning, and Michael E Read. Diffusion in copper and copper alloys. part i. volume and surface self-diffusion in copper. *Journal of Physical and Chemical Reference Data*, 2(3):643–656, 1973.

[81] SJ Rothman and NL Peterson. Isotope effect and divacancies for self-diffusion in copper. *physica status solidi (b)*, 35(1):305–312, 1969.

[82] R. M. Langford and C. Clinton. In situ lift-out using a fib-sem system. *Micron*, 35(7):607–611, 2004.

[83] C.C. Ahn and O.L. Krivanek. *EELS Atlas: A Reference Collection of Electron Energy Loss Spectra Covering All Stable Elements*. Gatan, 1983.

[84] D. B. Williams and C. B. Carter. *Transmission electron microscopy: a textbook for materials science*. 2009.

[85] AL Patterson. The scherrer formula for x-ray particle size determination. *Physical review*, 56(10):978, 1939.

[86] Luca Lutterotti. Total pattern fitting for the combined size–strain–stress–texture determination in thin film diffraction. *Nuclear Instruments and Methods in Physics Research Section B: Beam Interactions with Materials and Atoms*, 268(3–4):334–340, 2010.

[87] WJ Parker, RJ Jenkins, CP Butler, and GL Abbott. Flash method of determining thermal diffusivity, heat capacity, and thermal conductivity. *Journal of applied physics*, 32(9):1679–1684, 1961.

[88] Dobe, scaron, F., Mili, x10D, and K. ka. Small punch testing in creep conditions. *Journal of Testing and Evaluation*, 29(1):31–35, 2001.

[89] G Ressel, D Holec, A Fian, F Mendez-Martin, and H Leitner. Atomistic insights into milling mechanisms in an fe–y2o3 model alloy. *Applied Physics A*, 115(3):851–858, 2014.

[90] L. Toualbi, M. Ratti, G. Andre, F. Onimus, and Y. de Carlan. Use of neutron and x-ray diffraction to study the precipitation mechanisms of oxides in ods materials. *Journal of Nuclear Materials*, 417(1-3):225–228, 2011.

[91] Hongtao Zhang, Michael J. Gorley, Kok Boon Chong, Michael E. Fitzpatrick, Steve G. Roberts, and Patrick S. Grant. An in situ powder neutron diffraction study of nano-precipitate formation during processing of oxide-dispersion-strengthened ferritic steels. *Journal of Alloys and Compounds*, 582:769–773, 2014.

[92] A. M. Harris, G. B. Schaffer, and N. W. Page. The morphological evolution of hollow shells during the mechanical milling of ductile metals. *Scripta Materialia*, 34(1):67–73, 1996.

[93] JY Huang, YK Wu, and HQ Ye. Ball milling of ductile metals. *Materials Science and Engineering: A*, 199(2):165–172, 1995.

[94] Jianhong He, Kyung H. Chung, Enrique J. Lavernia, Xiaozhou Liao, and Yuntian T. Zhu. Mechanical milling-induced deformation twinning in fcc materials with high stacking fault energy. *Metallurgical and Materials Transactions A*, 34(3):707–712, 2003.

[95] H Bahmanpour. *Synthesis and Deformation Behavior of Nanocrystalline Copper Alloys*. Thesis, North Carolina State University, 2012.

[96] PS Gilman and JS Benjamin. Mechanical alloying. *Annual Review of Materials Science*, 13(1):279–300, 1983.

[97] JS Benjamin and TE Volin. The mechanism of mechanical alloying. *Metallurgical Transactions*, 5(8):1929–1934, 1974.

[98] Yuuji Kimura, Hideyuki Hidaka, and Setsuo Takaki. Work-hardening mechanism during super-heavy plastic deformation in mechanically milled iron powder. *Materials Transactions, JIM*, 40(10):1149–1157, 1999.

[99] L Takacs and JS McHenry. Temperature of the milling balls in shaker and planetary mills. *Journal of materials science*, 41(16):5246–5249, 2006.

[100] J. Y. Huang, Y. K. Wu, and H. Q. Ye. Deformation structures in ball milled copper. *Acta Materialia*, 44(3):1211–1221, 1996.

[101] H. Okamoto. Cu-y (copper-yttrium). *Journal of Phase Equilibria*, 19(4):398, 1998.

[102] P Zhang, SX Li, and ZF Zhang. General relationship between strength and hardness. *Materials Science and Engineering: A*, 529:62–73, 2011.

[103] P. P. Chattopadhyay, I. Manna, S. Talapatra, and S. K. Pabi. A mathematical analysis of milling mechanics in a planetary ball mill. *Materials Chemistry and Physics*, 68(1–3):85–94, 2001.

[104] G Ressel, P Parz, S Primig, H Leitner, H Clemens, and W Puff. New findings on the atomistic mechanisms active during mechanical milling of a fe-y2o3 model alloy. *Journal of Applied Physics*, 115(12):124313, 2014.

[105] Kenichi Kaminaga, Ryosuke Sei, Kouichi Hayashi, Naohisa Happo, Hiroo Tajiri, Daichi Oka, Tomoteru Fukumura, and Tetsuya Hasegawa. A divalent rare earth oxide semiconductor: Yttrium monoxide. *Applied Physics Letters*, 108(12):122102, 2016.

[106] Linus Pauling. Atomic radii and interatomic distances in metals. *Journal of the American Chemical Society*, 69(3):542–553, 1947.

[107] Daniel R Stull and Harold Prophet. Janaf thermochemical tables. Report, DTIC Document, 1971.

[108] Hongtao Zhang, Yina Huang, Huanpo Ning, Ceri A. Williams, Andrew J. London, Karl Dawson, Zuliang Hong, Michael J. Gorley, Chris R. M. Grovenor, Gordon J. Tatlock, Steve G. Roberts, Michael J. Reece, Haixue Yan, and Patrick S. Grant. Processing and microstructure characterisation of oxide dispersion strengthened fe–14cr–0.4ti–0.25y2o3 ferritic steels fabricated by spark plasma sintering. *Journal of Nuclear Materials*, 464:61–68, 2015.

[109] Kun Shen, Mingxing Guo, and Mingpu Wang. Recrystallization characteristics of a fine grained copper alloy. *Materials Chemistry and Physics*, 120(2–3):709–714, 2010.

[110] Su-Hyeon Kim and Dong Nyung Lee. Recrystallization of alumina dispersion strengthened copper strips. *Materials Science and Engineering: A*, 313(1–2):24–33, 2001.

[111] X. Boulnat, N. Sallez, M. Dadé, A. Borbély, J. L. Béchade, Y. de Carlan, J. Malaplate, Y. Bréchet, F. de Geuser, A. Deschamps, P. Donnadieu, D. Fabrègue, and M. Perez. Influence of oxide volume fraction on abnormal growth of nanostructured ferritic steels during non-isothermal treatments: An in situ study. *Acta Materialia*, 97:124–130, 2015.

[112] X. Boulnat, D. Fabregue, M. Perez, M. H. Mathon, and Y. Decarlan. High-temperature tensile properties of nano-oxide dispersion strengthened ferritic steels produced by mechanical alloying and spark plasma sintering. *Metallurgical and Materials Transactions a-Physical Metallurgy and Materials Science*, 44A(6):2461–2465, 2013.

[113] N. Sallez, X. Boulnat, A. Borbely, J. L. Bechade, D. Fabregue, M. Perez, Y. de Carlan, L. Hennet, C. Mocuta, D. Thiaudiere, and Y. Brechet. In situ characterization of microstructural instabilities: Recovery, recrystallization and abnormal growth in nanoreinforced steel powder. *Acta Materialia*, 87:377–389, 2015.

[114] G. Carro, A. Munoz, M. A. Monge, B. Savoini, R. Pareja, C. Ballesteros, and P. Adeva. Fabrication and characterization of y2o3 dispersion strengthened copper alloys. *Journal of Nuclear Materials*, 455(1-3):655–659, 2014.

[115] T. Yamada, H. Noto, Y. Hishinuma, T. Muroga, and H. Nakamura. Development of a dispersion strengthened copper alloy using a ma-hip method. *Nuclear Materials and Energy*, 2016.

[116] J. A. Choren, S. M. Heinrich, and M. B. Silver-Thorn. Young's modulus and volume porosity relationships for additive manufacturing applications. *Journal of Materials Science*, 48(15):5103–5112, 2013.

[117] James C. Wang. Young's modulus of porous materials. *Journal of Materials Science*, 19(3):801–808, 1984.

[118] M. K. Miller, K. F. Russell, and D. T. Hoelzer. Characterization of precipitates in ma/ods ferritic alloys. *Journal of Nuclear Materials*, 351(1–3):261–268, 2006.

[119] Pradyumna Kumar Parida, Arup Dasgupta, K. G. Raghavendra, K. Jayasankar, and S. Saroja. Structural studies of dispersoids in fe–15 wtmodel ods alloys

during milling and subsequent annealing. *Transactions of the Indian Institute of Metals*, pages 1–7, 2016.

[120] E. Yuasa, T. Morooka, R. Laag, W. A. Kaysser, and G. Petzow. Microstructural change of cu—ti—b powders during mechanical alloying. *Powder Metallurgy*, 35(2):120–124, 1992.

[121] H. Okamoto. Cu-ti (copper-titanium). *Journal of Phase Equilibria*, 23(6):549, 2002.

[122] C. Biselli, D. G. Morris, and N. Randall. Mechanical alloying of high strength copper-alloys containing tib2 and al2o3 dispersoid particles. *Scripta Metallurgica Et Materialia*, 30(10):1327–1332, 1994.

[123] D. L. Zhang, S. Raynova, C. C. Koch, R. O. Scattergood, and K. M. Youssef. Consolidation of a cu–2.5 vol.mechanical milling. *Materials Science and Engineering: A*, 410–411:375–380, 2005.

[124] Martin Stobik. Nanoval atomizing—capabilities, applications and related processes. In *Symposium Spray Forming*, pages 65–79, 2002.

[125] H. Okamoto. Cu-zr (copper-zirconium). *Journal of Phase Equilibria and Diffusion*, 29(2):204–204, 2008.

[126] S-H Kim and DN Lee. Annealing behavior of alumina dispersion-strengthened copper strips rolled under different conditions. *Metallurgical and Materials Transactions A*, 33(6):1605–1616, 2002.

[127] Ming-xing GUO, Ming-pu WANG, SHEN Kun, Ling-fei CAO, Ruo-shan LEI, and Shu-mei LI. Effect of cold rolling on properties and microstructures of dispersion strengthened copper alloys. *Transactions of Nonferrous Metals Society of China*, 18(2):333–339, 2008.

[128] Khushbu Dash, Bankim Chandra Ray, and Debasis Chaira. Synthesis and characterization of copper–alumina metal matrix composite by conventional and spark plasma sintering. *Journal of Alloys and Compounds*, 516:78–84, 2012.

[129] G. Kalinin and R. Matera. Comparative analysis of copper alloys for the heat sink of plasma facing components in iter. *Journal of Nuclear Materials*, 258–263, Part 1:345–350, 1998.

[130] G. Carro, A. Muñoz, M. A. Monge, B. Savoini, A. Galatanu, M. Galatanu, and R. Pareja. Thermal conductivity and diffusivity of cu-y alloys produced by different powder metallurgy routes. *Fusion Engineering and Design*, 2016.

[131] S. A. Fabritsiev and A. S. Pokrovsky. Effect of high doses of neutron irradiation on physico-mechanical properties of copper alloys for iter applications. *Fusion Engineering and Design*, 73(1):19–34, 2005.

[132] G. Carro, A. Muñoz, M. A. Monge, B. Savoini, and R. Pareja. Microstructural and mechanical characterization of cu-0.8 wt.%y. *Fusion Engineering and Design*, 2015.

[133] Roger C. Hurst, Robert J. Lancaster, Spencer P. Jeffs, and Martin R. Bache. The contribution of small punch testing towards the development of materials for aero-engine applications. *Theoretical and Applied Fracture Mechanics*, 86, Part A:69–77, 2016.

Glossary

ADF annular dark field

APT atom probe tomography

bcc body-centered cubic

BF bright-field

BPR ball-to-powder weight ratio

CCFE Culham Centre for Fusion Energy

DEMO Demonstration Power Plant

DF dark-field

dpa displacements per atom

DS dispersion strengthened

EBSD electron backscatter diffraction

EDS energy dispersive X-ray spectroscopy

EELS electron energy loss spectroscopy

EFTEM energy filtered transmission electron microscopy

ETMT electrothermal mechanical testing system

FAST field assisted sintering technique

fcc face-centered cubic

FEG field emission gun

FFT fast fourier transform

FIB focused ion beam

FWHM full width at half maximum

HAADF high angle annular dark field

HIP hot isostatic press

IACS international annealed copper standard

ITER International Tokamak Experimental Reactor

LFA laser flash analysis

MA mechanical alloying

mfp mean free path

ODS oxide dispersion strengthened

PCA process control agent

PID proportional–integral–derivative

PPB prior-particle-boundary

SE secondary electron

SEM secondary electron microscope

STEM scanning transmission electron microscope

TD theoretical density

TEM transmission electron microscope

UTS ultimate tensile strength

VHP vacuum hot press

XRD X-ray diffraction